

Faculty of Applied Engineering
Research Group Advanced Reactor
Technology (ART)

Faculty of Science
Research Group Antwerp X-ray analysis,
Electrochemistry and Speciation (AXES)

Electrosynthesis as an environmentally friendly production method

A screening methodology towards upscaling

Thesis submitted in fulfillment of the requirements for the degree of
Doctor in de Toegepaste Ingenieurswetenschappen
(Doctor in Applied Engineering)

Danny Pauwels

Promotors:

Prof. dr. Ing. Tom Breugelmans
Prof. dr. Karolien De Wael

Antwerp 2018



Faculty of Applied Engineering
Research Group Advanced Reactor
Technology (ART)

Faculty of Science
Research Group Antwerp X-ray Analysis,
Electrochemistry & Speciation (AXES)

**Electrosynthesis as an environmentally friendly production method
A screening methodology towards upscaling**

Danny Pauwels

Members of the jury

Prof. dr. Serge Tavernier

President of the jury
Universiteit Antwerpen
Faculty of Applied Engineering

dr. Ing. Jonas Hereijgers

Secretary of the jury
Universiteit Antwerpen
Faculty of Applied Engineering

Prof. dr. Ing. Tom Breugelmans

Promotor
Universiteit Antwerpen
Faculty of Applied Engineering

Prof. dr. Karolien De Wael

Promotor
Universiteit Antwerpen
Department of Chemistry

dr. ir. Thijs de Groot

External member of the jury
Technische Universiteit Eindhoven
Department of Chemical Engineering and
Chemistry
Innovation Technologist, AkzoNobel

Prof. dr. Sabine Van Doorslaer

External member of the jury
Universiteit Antwerpen
Department of Physics

Prof. dr. ir. Annick Hubin

External member of the jury
Vrije Universiteit Brussel
Department of Materials and Chemistry

Dankwoord

Na iets meer dan vijf jaar geleden af te studeren en ongeveer vier jaar geleden aan een doctoraat te zijn begonnen, ben ik nu beland in de laatste rechte lijn van het afronden van dit hoofdstuk in mijn leven. Een hoofdstuk met ups en downs, vertragingen en versnellingen, verwachtte resultaten en verrassingen, maar nooit met een periode van dagelijkse sleur. Een hoofdstuk dat ik succesvol kan afronden dankzij de steun en medewerking op zowel wetenschappelijk als persoonlijk vlak van verscheidene mensen. Deze mensen wil ik met dit schrijven hiervoor zeer graag en orecht bedanken.

Om te beginnen bedank ik graag mijn promotores, Tom en Karolien. Allereerst om mij de mogelijkheid te geven om te doctoreren, daarnaast ook voor de hulp en het bijstaan met raad en daad gedurende de afgelopen jaren. Tom, met jou heb ik net iets meer samengewerkt en graag bedank ik je om mij ook steeds in de juiste richting te wijzen wanneer dat nodig was. Door het vertrouwen dat je in mij stelde, heb ik naast het wetenschappelijke hierdoor ook veel bijgeleerd op persoonlijk vlak.

Vervolgens bedank ik ook graag mijn collega's en ex-collega's van ART. Doorheen de jaren is de groep aanzienlijk veranderd en vooral gegroeid. Waar we ooit met een handvol in Mechelen (en wat eenzaten in Brussel ;)) zijn begonnen, zijn we, na een tussenstop in Hoboken, beland op CDE met een velvoud van het ledenaantal. Ondanks de veranderingen heb ik altijd een zeer fijne sfeer ondervonden in onze groep, zowel op de werkvloer als daarbuiten. Hierbij bedank ik graag iedereen voor hun bijdrage hieraan en voor de hulp die ze mij direct of indirect hebben geboden doorheen mijn doctoraat. Dus bedankt, Bart G., Jonas, Bart V., Robbe, Kristof, Benny, Daniel en Sander, maar ook bedankt 'nieuwelingen', Nick, Lien, Joren, Jonathan, Oriol en Miguel voor het voortzetten van de goede sfeer tijdens de laatste weken/maanden van mijn verhaal bij ART.

I would also like to thank the colleagues at BIMEF. Thank you, Vincent, for all the help with the measurements in the last months and for having no problem with me shifting deadlines and disrupting your agenda to do experiments. Your positive attitude was a real motivator and I enjoyed working with you. Also thanks Mohammad, for the timely analysis of the data. Tevens wil ik ook Melissa bedanken voor de uitgebreide hulp bij de eerste experimenten.

Verder wil ik ook graag mijn vrienden en familie bedanken. De input voor het wetenschappelijke werk was misschien beperkt, maar des te groter was de invloed op persoonlijk vlak. Korte ontmoetingen of langdurige ontspanningsactiviteiten, het waren telkens zeer welkome afwisselingen met het doctoraatsleven. Daarnaast wil ik ook graag mijn schoonouders bedanken. Leo en Ria, jullie staan altijd klaar voor ons en helpen ons met zoveel zaken, of het nu gaat over grote verbouwingen, kleine klusjes of eender welke vraag die wij hebben. Dit wordt altijd gedaan met een lach en zonder probleem. Hierdoor heb ik mij vaak beter op het werk kunnen concentreren, waarvoor onzettend bedankt. Ook bedankt Urbain, voor de zeer welkome hulp afgelopen jaar, dat toch net iets drukker was dan gemiddeld.

In het bijzonder wil ik ook heel graag mijn ouders bedanken. Moeke en Vake, bedankt om mij de kans te geven om te gaan studeren waardoor ik uiteindelijk deze thesis heb kunnen verwezenlijken. Moeke, je hebt me altijd onvoorwaardelijk gesteund in mijn keuzes en mij ook bijgestaan tijdens de moeilijkere perioden. Daarnaast heb je steeds in mij geloofd wat mij altijd heeft gemotiveerd om nieuwe uitdagingen niet uit te weg te gaan, maar om te proberen en vol te houden. Vanuit de grond van mijn hart, ongelooflijk bedankt hiervoor.

Ten slotte gaat mijn grootste dank uit naar jou, Inez, mijn vriendin, mijn schat. Altijd ben je daar voor mij en het valt niet samen te vatten wat je allemaal al hebt gedaan voor mij en nog steeds doet, zeker in het afgelopen jaar. De impact hiervan op dit

werk en op mijn afgelegde traject valt niet te onderschatten en ik kan niet in woorden beschrijven hoeveel dit voor mij betekent. Voor dit en nog veel meer, bedankt!

Danny

Scientific contributions

Part III of this thesis was realized in a close collaboration with the Laboratory of Biophysics and Biomedical Physics (BIMEF). The *in situ* EPR spectroelectrochemical experiments were performed in cooperation with dr. Hong Yue Vincent Ching. The DFT computations were done by Vincent and Mohammad Samanipour under supervision of Prof. dr. Sabine Van Doorslaer.

Summary

Organic electrosynthesis is a field within electrochemistry that concerns the synthesis of organic products using the electron as a redox agent instead of chemical reductants or oxidants. It offers several important advantages to conventional synthetic methods, such as mild process conditions as reactions can be carried out at ambient temperature and pressure, higher selectivity due to precise control of the reaction by control of the electrode potential, ability to produce unstable or hazardous reagents *in situ* and less generation of pollutants and waste streams. It is a versatile and inherently environmentally friendly technique, and is labeled as a “clean” and “green” process. Its advantages make it an interesting alternative for industrial applications. However, despite its potential, its implementation is limited. A major drawback is the lack of the crucial combined knowledge on organic synthesis, electrochemistry and engineering aspects. This work aims to bridge the gap between the engineering aspects and the fundamental electrochemical mechanistic aspects of a reaction by developing an innovative screening approach towards industrial implementation.

In a first part, the electrochemical pathway of an industrial relevant reaction is studied: the aldol reaction of acetone to diacetone alcohol. The aldol reaction is a useful and common reaction for C-C bond formation, however, the conventional process exhibits drawbacks to which electrosynthesis offers an answer. A thorough electrochemical investigation is performed to screen this electrochemical reaction. Key parameters are identified and their influence on the reaction is quantified. The obtained information is subsequently used to develop a modular continuous flow electrochemical microreactor setup, which can be combined with analytical techniques to acquire a versatile research platform. The setup is used to investigate the capabilities of performing the electrosynthetic case study in flow. Electrochemical microreactors offer additional advantages such as a lower energy input and less auxiliaries while maintaining the same throughput and product yield as a batch setup.

The influence of reactor parameters such as inter-electrode distance and electrolysis configuration are investigated and described.

In a second part, a more mechanistic approach is applied. Sufficient knowledge of the reaction mechanism is essential to tune the electrocatalyst in order to increase the activity and to improve the viability of the electrochemical pathway. To unravel the underlying electrode reaction mechanisms, electron paramagnetic resonance (EPR) is a well-suited technique to acquire information on the chemical nature and electronic structure of the different intermediates. Even though EPR spectroelectrochemical experiments (i.e. *in situ* EPR studies performed during electrochemical reactions) were first reported in 1958, it is presently vastly underexploited in electrocatalytic research. On the one hand this can be attributed to the fact that EPR equipment is not widely available and requires specific knowledge, on the other hand there is a considerable lack or even absence of commercially available equipment for such combined experiments. To overcome this problem, a simple, inexpensive and versatile platform consisting of an innovative electrode construction is developed, specifically optimized for electrocatalytic research. The setup is validated on a case study: the reductive intramolecular cyclisation of allyl 2-bromobenzyl ether to 4-methylisochromane. Intermediate products are detected and identified, confirming the proposed mechanism.

Combining these two parts, a methodology comprising the different aspects of an in-depth investigation of an organic electrochemical pathway is developed. Necessary setups were constructed to provide versatile research platforms where available equipment was insufficient or non-existing.

Samenvatting

Organische elektrosynthese is een domein in elektrochemie waarin het elektron als redox agens wordt gebruikt om organische producten te synthetiseren. Deze techniek biedt verscheidene belangrijke voordelen ten opzichte van conventionele synthesemethoden, zoals milde reactieomstandigheden doordat reacties bij atmosferische druk en kamertemperatuur kunnen doorgaan, een hogere selectiviteit dankzij de nauwkeurige controle van de reactie door middel van de potentiaalcontrole, de mogelijkheid om instabiele of gevaarlijke reagentia *in situ* te genereren en een lagere hoeveelheid vervuilingen en afvalstromen. Het is een veelzijdige en inherent milieuvriendelijke methode die wordt aanzien als een “proper” en “groen” proces. De voordelen maken het een interessante alternatieve productieroute voor industriële toepassingen. Echter, ondanks het potentieel, blijven de toepassingen in de industrie beperkt. Een belangrijk nadeel is vaak het gebrek aan de noodzakelijke combinatie van kennis over organische synthese, elektrochemie en ingenieurstechniek. Dit werkt beoogd het overbruggen van de afstand tussen de ingenieurstechniek en de fundamentele elektrochemische mechanistische aspecten van een reactie door een innovatieve screeningsmethodiek naar verdere industriële implementatie te ontwikkelen.

In een eerste deel wordt de elektrochemische reactieweg van een industrieel relevante reactie bestudeerd: de aldolreactie van aceton naar diacetalcohol. De aldolreactie is een handige en veelgebruikte reactie om koolstof-koolstofbindingen te vormen. Het conventionele proces heeft echter een aantal nadelen waarop elektrosynthese een antwoord biedt. Een grondig elektrochemisch onderzoek wordt uitgevoerd om de elektrochemische reactie te doorlichten. Hierin worden sleutelparameters geïdentificeerd en hun invloed op de reactie wordt gekwantificeerd. De bekomen informatie wordt vervolgens aangewend om een modulaire continue elektrochemische microreactoropstelling te ontwikkelen. Deze opstelling wordt

gecombineerd met analytische technieken waarbij een veelzijdig onderzoeksplatform bekomen wordt. De opstelling wordt gebruikt om de mogelijkheid tot het uitvoeren van de elektrosynthetische casestudie in een continue reactor te onderzoeken. Elektrochemische microreactoren bieden bijkomende voordelen zoals een lagere energietoevoer en minder benodigde hulpmiddelen voor een gelijkaardige omzet en opbrengst dan een batchreactor. De invloed van parameters zoals de inter-elektrodeafstand en de elektrolysemethode wordt onderzocht en beschreven.

In een tweede deel wordt een meer mechanistische benadering toegepast. Voldoende kennis over het reactiemechanisme is essentieel om te elektrokatalysator te kunnen optimaliseren om de levensvatbaarheid van een elektrochemische route te verhogen. Om de onderliggende elektrodereacties te ontrafelen wordt elektronen paramagnetische resonantie spectroscopie (EPR) gebruikt, dat informatie schenkt over de chemische natuur en elektronische structuur van de verschillende intermediairen. Ondanks dat EPR spectro-elektrochemische experimenten al in 1958 gerapporteerd werden, wordt het vandaag de dag onderbenut in elektrokatalytisch onderzoek. Enerzijds kan dit worden toegewezen aan het feit dat EPR-uitrusting niet eenvoudig beschikbaar is en specifieke kennis vereist. Anderzijds is er een tekort aan commercieel verkrijgbare uitrusting voor dergelijke gecombineerde experimenten. Om dit probleem op te lossen wordt een eenvoudig, goedkoop en veelzijdig platform ontwikkeld dat specifiek geoptimaliseerd is voor elektrokatalytisch onderzoek. Het platform wordt gevalideerd aan de hand van een casestudie: de reductieve intramoleculaire cyclisatie van allyl-2-bromobenzylether naar 4-methylisochromaan. Intermediaire producten worden gedetecteerd en geïdentificeerd waardoor het voorgestelde mechanisme wordt bevestigd.

Door deze twee delen te combineren, wordt een methodologie verkregen die de verschillende aspecten omvat van een diepgaand onderzoek naar een organische elektrochemische route. De benodigde opstellingen werden ontwikkeld wanneer de beschikbare uitrusting onvoldoende of onbestaande was.

Table of contents

Dankwoord	III
Scientific contributions	VII
Summary	IX
Samenvatting	XI
Nomenclature	XXI
Part I Introduction	1
Chapter 1 Organic electrosynthesis.....	3
1.1 Sustainable development in the chemical processing industry....	4
1.2 Organic electrosynthesis as a green alternative production route in the industry	6
1.2.1 The origins of organic electrosynthesis.....	6
1.2.2 The green nature of organic electrosynthesis.....	8
1.2.3 The possibilities and advantages of an electrosynthetic route.....	10
1.3 Examples in the industry	13
1.3.1 Electrohydrodimerization of acrylonitrile	13
1.3.2 Paired electrosynthesis of phthalide and 4- <i>tert</i> - butylbenzaldehyde dimethylacetal.....	15
1.4 Upscaling and implementation of an electrosynthesis	16

Chapter 2	Scope and outline	19
2.1	Scope	20
2.2	Strategy	21
2.3	Outline	23
Chapter 3	Fundamental concepts and experimental techniques	27
3.1	Electrode reactions in organic electrochemistry.....	28
3.1.1	Charge transfer.....	28
3.1.2	Mass transfer.....	34
3.1.3	Electrolysis methods.....	40
3.2	Cell and electrode design	43
3.2.1	Cell design	43
3.2.2	Batch operation versus continuous flow operation	46
3.2.3	Electrodes for organic electrosynthesis	46
3.3	Electrochemical techniques.....	48
3.3.1	Chronoamperometry.....	48
3.3.2	Cyclic voltammetry	53
3.4	Electron paramagnetic resonance	55
3.4.1	Basics of EPR.....	55
3.4.2	Acquisition of a spectrum and interpretation of the data .	61
3.4.3	Combined EPR and electrochemistry.....	66

Part II	Engineering approach for an electrochemical study towards industrial implementation	71
Chapter 4	Literature review for the conversion of the aldol reaction to an electrosynthetic flow process	73
4.1	Introduction	74
4.2	The aldol reaction of acetone to diacetone alcohol.....	75
4.3	Flow chemistry and microreactors	81
4.4	Electrochemical microreactors for synthesis	84
4.4.2	Microreactors with solid plate-to-plate electrodes.....	86
4.4.3	ECMR for the aldol reaction of acetone.....	89
4.5	Mechanism of the chemical aldol reaction	89
4.6	Electrogenerated bases as initiator	91
4.6.1	Carbonyl compounds as probase.....	92
4.6.2	Oxygen as a probase.....	95
4.7	Proposed mechanisms in literature for the electrosynthetic aldol reaction	96
4.7.1	Combined mechanism proposed by Tsai	96
4.7.2	Radical mechanism proposed by Kumar et al.	97
4.7.3	EGB initiated mechanism proposed by Shono et al.	97
Chapter 5	Electrochemical aldol reaction of acetone to diacetone alcohol	99
5.1	Introduction	100
5.2	Experimental	100
5.2.1	Chemicals	100
5.2.2	Electrochemical experiments.....	101

5.2.3	Analysis.....	101
5.3	Results and discussion.....	102
5.3.1	Validation of the electrosynthetic pathway	102
5.3.2	Voltammetric investigation	104
5.3.3	Electrolysis potential	105
5.3.4	Influence of water in the electrolyte on the yield of DAA	110
5.3.5	Comparing the contribution of anode and cathode	113
5.3.6	Effect of the electrode material.....	115
5.3.7	Reaction crossover and cell setup.....	117
5.4	Conclusions	119
Chapter 6	The application of an electrochemical microflow reactor	121
6.1	Introduction	122
6.2	Experimental	123
6.2.1	Chemicals	123
6.2.2	Reactor design.....	123
6.2.3	Pt deposition	126
6.2.4	Mass transfer limitation measurements	127
6.2.5	Analysis.....	127
6.3	Results and discussion.....	128
6.3.1	Characterization and validation of the deposited platinum layer.....	128
6.3.2	Reactor setup considerations	131
6.3.3	Evaluation of the spacer design	135

6.3.4	Electrochemical aldol reaction of acetone in the microfluidic reactor	140
6.4	Conclusions	148
Chapter 7	Understanding the electrosynthetic aldol reaction	151
7.1	Introduction	152
7.2	Experimental	155
7.2.1	Chemicals	155
7.2.2	Setup	155
7.2.3	Analysis.....	155
7.3	Results and discussion.....	155
7.3.2	Reaction at the counter electrode	160
7.4	Conclusions	161
Part III	Mechanistic approach for an electrochemical study by in situ EPR spectroelectrochemistry.....	163
Chapter 8	Literature review on in situ EPR spectroelectrochemistry.....	165
8.1	Introduction	166
8.1.1	Practicalities of in situ EPR spectroelectrochemical experiments	166
8.2	Applications.....	169
8.3	Cell designs.....	170
8.3.1	The Adams cell	170
8.3.2	The Allendoerfer cell	172
8.3.3	The channel electrode cell.....	173

Chapter 9	Development of a versatile <i>in situ</i> EPR spectroelectrochemistry platform for electrocatalysis....	175
9.1	Introduction	176
9.2	Construction of the electrode.....	178
9.3	Electrochemical and spectroscopic validation	181
9.4	Conclusions	186
9.5	Supplementary Information	187
9.5.1	Mesh-electrode	187
9.5.2	Wire-electrode	192
Chapter 10	Elucidation of the mechanism of the electrosynthetic intramolecular cyclisation of allyl 2-bromobenzyl ether .	197
10.1	Introduction	198
10.2	Experimental	201
10.2.1	Chemicals	201
10.2.2	Setup and procedure	201
10.2.3	EPR simulations and density functional theory (DFT) computations	202
10.3	Results and discussion	202
10.3.1	Electrochemical validation.....	202
10.3.2	In <i>situ</i> EPR spectroelectrochemical study of the cyclisation reaction	204
10.4	Conclusions	213
10.5	Supplementary information	214

Part IV	Conclusions and future perspectives.....	223
Chapter 11	Conclusions and future perspectives.....	225
11.1	Conclusions	226
11.1.1	Engineering approach for an electrochemical study towards industrial implementation	226
11.1.2	Mechanistic approach for an electrochemical study by <i>in situ</i> EPR spectroelectrochemistry.	228
11.2	Future perspectives.....	230
List of figures	223
List of tables	247
Bibliography	249
Personal information	275

Nomenclature

List of acronyms

ACN	Chapter 1: acrylonitrile else: acetonitrile
ABBE	Allyl 2-bromobenzyl ether
ADN	Adiponitrile
CE	in schemes: Chemical Electrochemical else: Counter Electrode
CV	Cyclic Voltammetry
CW	Continuous Wave
DAA	Diacetone Alcohol
DISP	Disproportionation
DMF	Dimethylformamide
DMPO-OH	(5,5-dimethyl-2-hydroxyl-pyrrolin-1-yl)oxyl
EC	Electrochemical Chemical
ECC	Electrochemical Chemical Chemical
ECE	Electrochemical Chemical Electrochemical
ECMR	Electrochemical Microreactor
EEC	Electrochemical Electrochemical Chemical
EGB	Electrogenerated Base
EPDM	Ethylene Propylene Diene Monomer rubber
EPR	Electron Paramagnetic Resonance
GC	Glassy Carbon as technique: Gas Chromatography
GC-FID	Gas Chromatography-Flame Ionization Detector
HOMO	Highest Occupied Molecular Orbital
HPLC	High Performance Liquid Chromatography

ID	Inner Diameter
LUMO	Lowest Unoccupied Molecular Orbital
MO	Mesityl Oxide
MV	Methyl Viologen
PB	Probase
PBN	<i>N</i> -tert-Butyl- α -phenylnitronate
PEEK	Polyether Ether Ketone
PhPh	Phenolphthalein
POM	Polyoxymethylene
PP	Polypropylene
TEMPO	2,2,6,6-tetramethylpiperidin-1-yl)oxyl
RE	Reference Electrode
SCE	Saturated Calomel Electrode
SEESR	Simultaneous Electrochemical Electron Spin Resonance
SEM	Scanning Electron Microscopy
SHE	Standard Hydrogen Electrode
STR	Stirred Tank Reactor
TBAP	Tetrabutylammonium Perchlorate
UV-VIS	Ultraviolet-Visible Spectroscopy
WE	Working Electrode

List of symbols

A	hyperfine coupling constant [Hz]
A_s	specific electrode area $(\frac{A}{V_r})$ [$\text{m}^2 \text{ m}^{-3}$]
\vec{B}_0	(external) magnetic field
C	chemical step
c_b	bulk concentration [mol m^{-3}]
C_{dl}	differential capacitance of the double layer [F]
c_i	concentration of species i [mol m^{-3}]
C_0	concentration at the electrode surface [mol m^{-3}]
D_i	diffusion coefficient of species i [$\text{m}^2 \text{ s}^{-1}$]
δ	diffusion layer thickness [m]
δ_H	boundary layer thickness [m]
E	in schemes: electrochemical step else: potential [V]
E	energy level [eV]
F	Faraday constant [96485 C mol $^{-1}$]
Φ	electrical field or potential gradient
Φ_i	current efficiency of species i
g_e	electron g -factor [-2.002319304361(82)]
G_z	Graetz number
h	Planck constant [$6.626070040(81) \times 10^{-34}$]
\hbar	reduced Planck constant $(\frac{h}{2\pi})$ [$1.054571800(13) \times 10^{-34}$]
I	current [A]
\vec{I}	nuclear angular momentum
I_d	diffusional limiting current [A]
I_L	limiting current [A]
j	current density [A m^{-2}]
$J_{c,i}$	convective flux of species i [$\text{mol s}^{-1} \text{ m}^{-2}$]
$J_{d,i}$	diffusional flux of species i [$\text{mol s}^{-1} \text{ m}^{-2}$]

J_i	total flux of species i [mol s $^{-1}$ m $^{-2}$]
j_L	limiting current density [A m $^{-2}$]
$J_{m,i}$	migrational flux of a species i [mol s $^{-1}$ m $^{-2}$]
k_m	mass transfer coefficient [m s $^{-1}$]
L	characteristic linear dimension [m]
m_i	mass of species i [kg]
M_i	molar mass of species i [kg mol $^{-1}$]
m_s	spin angular momentum quantum number
μ	dynamic viscosity [N s m $^{-2}$]
μ_B	Bohr magneton [9.274009994(57) \times 10 $^{-24}$ J T $^{-1}$]
$\vec{\mu}_s$	spin magnetic moment
n	stoichiometric number of electrons involved in an electrode reaction
	amount of substance [mol]
ν	frequency [Hz]
ν_{kin}	kinematic viscosity [m 2 s $^{-1}$]
O	oxidized form of the standard system $O + ne^- \rightleftharpoons R$
Q	charge [C]
R	reduced form of the standard system $O + ne^- \rightleftharpoons R$
	universal gas constant [8.3144598(48) kg m 2 s $^{-2}$ mol $^{-1}$ K $^{-1}$]
Re	Reynolds number
R_u	uncompensated resistance [Ω]
ρ	volumetric mass density [kg m $^{-3}$]
ρ_{st}	space-time yield [kg m $^{-3}$ s $^{-1}$]
\vec{S}	spin angular momentum
Sc	Schmidt number
Sh	Sherwood number
t	time [s]
T	Tesla
T	temperature [K]

u_i	ion mobility [$\text{m}^2 \text{ V}^{-1} \text{ s}^{-1}$]
v	bulk fluid velocity or mean linear velocity [m s^{-1}]
\dot{V}	volumetric flow rate [$\text{m}^3 \text{ s}^{-1}$]
V_r	reactor volume [m^3]
z_i	valence number of ions of substance i

Part I

Introduction

CHAPTER 1

Organic electrosynthesis

THIS CHAPTER DISCUSSES THE PROGRESS AND THE CHALLENGES OF SUSTAINABLE DEVELOPMENT IN THE CHEMICAL INDUSTRY. IT ALSO GIVES AN INTRODUCTION TO ORGANIC ELECTROSYNTHESIS AND SHOWS ITS ADVANTAGES OVER TRADITIONAL CHEMICAL PRODUCTION PROCESSES AND ITS POSSIBILITIES AS A GREEN ALTERNATIVE PRODUCTION ROUTE. THE MOST PROMINENT INDUSTRIAL ORGANIC ELECTROSYNTHESIS PROCESSES ARE SHOWN AND TO CONCLUDE, THE CHALLENGES OF UPSCALING AND IMPLEMENTING AN ORGANIC ELECTROSYNTHESIS ARE DISCUSSED.

1.1 Sustainable development in the chemical processing industry

In today's society there is an increasing awareness that our current way of life, especially with the expanding world population, is not a sustainable system and improvements towards more sustainability in various domains is imperative. There are many direct and indirect arguments to this case, of which several correlate to the increase of the global population and the corresponding growing industrial demands. In 2011 the European Commission published a Eurobarometer (a public opinion survey) in which respondents were asked which they considered to be the single most serious problem facing the world as a whole. One in five (20%) considered climate change to be the most serious problem [1]. Another main concern listed was the availability of energy. These answers reflect years of awareness creation about issues that affect us all and which also gave rise to treaties as the Kyoto protocol [2]. The role of the industry in the preceding problems and the potential it has to drive the development necessary for improvement, is not to be underestimated. For example, in the Kyoto protocol 42% of the greenhouse gas reduction is expected to be achieved through measures in the industry [3]. Besides the greenhouse gas emission, the current industry entails many other major issues which contribute to the preceding problems, such as excessive energy consumption and waste production. One reason for these industrial problems is that after the Second World War, industrialization took place at a tremendous pace but its effects on the environment, flora and fauna, and people's safety and health were not given much attention. As a consequence, problems arose such as increased global warming, degradation of the ozone layer, contamination of land and water ways due to toxic chemicals released by industries, depletion of non-renewable resources, etc.

To overcome these problems or lessen the extent of it, the chemical processing industry has taken an interest in green chemistry and with it started the development towards more sustainability. Green chemistry is a concept that came to life in 1991

with the launch of the Green Chemistry Program [4,5]. This environmentally-conscious approach was further developed and in 1998 Paul Anastas and John Warner formulated the twelve principles of green chemistry [6]:

1. Prevention of waste.
2. Atom economy (reaction efficiency).
3. Safer synthesis (less hazardous chemical use).
4. Safer chemicals (less toxic products).
5. Safer solvents and auxiliaries.
6. Energy efficiency.
7. Renewable feedstocks.
8. Fewer derivatives (waste minimization).
9. Catalysis.
10. Design for degradation.
11. Real-time analysis (pollution prevention).
12. Safer chemistry for accident prevention.

These principles can be considered as guidelines or focus points to help improve the quality and sustainability of a process. In practice it may not always be possible to comply with all of the principles and compromises, which possibly even contradict the principles, may be unavoidable. This is especially true when existing processes are altered compared to designing new processes due to limitations that may already be imposed by the current process [7]. The twelve principles of green chemistry can be translated into twelve principles of green engineering, which together form a framework for scientists and engineers for designing new materials, products, processes and systems which are benign to human health and the environment [8].

There are multiple ways to fulfill each requirement and sometimes the successful application of one principle advances one or more of the others because they may be interdependent. One method that offers a promising approach is organic

electrochemistry. As will be shown in the following section, organic electrosynthesis agrees well with the principles of green chemistry and fulfills several criteria. Thanks to the developments in related fields such as electrocatalysis it is becoming an increasingly interesting and viable alternative. There is common agreement among scientists that the importance of electrochemically based processes will increase in the future [9].

1.2 Organic electrosynthesis as a green alternative production route in the industry

1.2.1 The origins of organic electrosynthesis

Organic electrosynthesis is a more narrow definition of electroorganic chemistry or organic electrochemistry which are synonyms for a field of research within electrochemistry which is concerned with oxidation and reduction reactions of organic molecules at electrodes. As the name implies, it uses the electron as a redox agent rather than chemical oxidants or reductants as in traditional chemistry. The origins of electrochemistry date back to well over two centuries ago, when in 1792 the Italian physicist Alessandro Volta showed that the contact of two dissimilar metals generated a current. In 1800 he designed a device based on this effect which could produce “inexhaustible electric charge”, now known as the *Volta pile* or *Voltaic pile* [10]. This device, an electrochemical power source and basically the first battery, could supply a continuous electric current, a feature unseen until then. A feature that was essential for the development of electrolysis due to necessity of a current running for an extended period of time and hence, the field of electrochemistry was born. Within the same year, the first electrochemical reaction was also realized when William Nicholson and Sir Anthony Carlisle reported the electrolysis of water to hydrogen and oxygen [11]. Many discoveries and inventions followed, but it was not until decades later, when in 1834 Michael Faraday wrote about the findings of his electrochemical experiments, that the first organic electrosynthesis was reported.

Faraday found that the electrolysis of an aqueous solution of an acetate salt lead to the gaseous products carbon dioxide and ethane [12] (Figure 1.1).

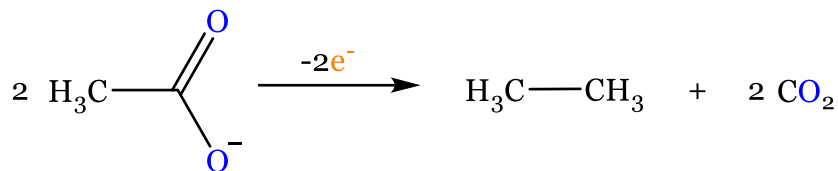


Figure 1.1: The first organic electrolysis, reported by Faraday.

A little more than a decade later Hermann Kolbe discovered probably the best known and the first useful organic electrosynthesis, which is now known as the Kolbe electrolysis or the Kolbe reaction. Kolbe found that the anodic oxidation of salts of a fatty acids (carboxylic acids) lead to decarboxylation and dimerization to hydrocarbons with loss of carbon dioxide [13–15] (Figure 1.2).

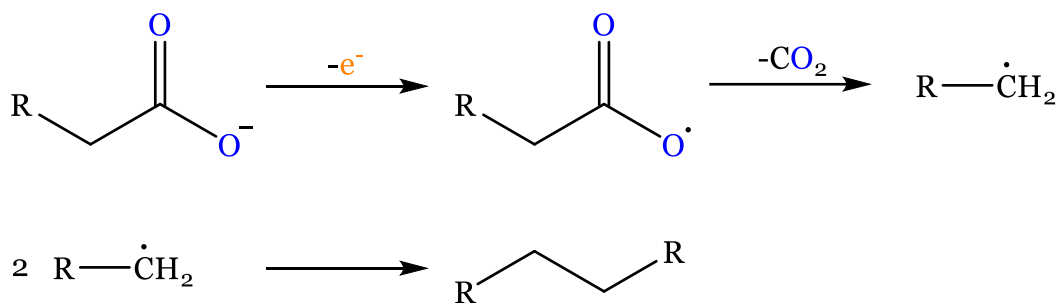


Figure 1.2: Reaction scheme of the Kolbe electrolysis.

Kolbe and Faraday are considered pioneers in the field of organic electrochemistry and established it as a research area in its own right. The field continued its steady development into the first half of the twentieth century. In the second half, from 1960 onwards, new electroanalytical techniques enabled a more profound and more efficient investigation of the mechanisms of the electrode reactions. Combined with technological advancements, appearance of new applications and developments in other areas the field underwent a rapid development. A summary of the progress

made in organic electrochemistry in the past century can be found in a review by Henning Lund [16]. More elaborate information on the history, developments, fundamentals and applications can be found in noteworthy literature on organic electrochemistry in references (non-exhaustive list) [17–22].

1.2.2 The green nature of organic electrosynthesis

Electrosynthesis is inherently an environmentally friendly technique since it uses the electron as a redox agent. The electron in electrolysis is one of the cheapest reagents in chemistry and is intrinsically a clean agent since it produces no waste in contrast with chemical oxidants or reductants, contributing to the environmental compatibility of electrosynthesis [23,24]. Electrosynthesis offers many other advantages. Hazardous or expensive reagents can be avoided because the redox agents can be stoichiometrically generated *in situ*. This not only lessens waste production and pollution, but also increases process safety. Further contributing to safety are the mild reaction conditions. Whereas chemical processes commonly require the addition of large amounts of heat and high pressures, electrochemical processes can be conducted at room temperature and ambient pressure. Besides process safety, this also positively impacts the energetic aspect of the process. Waste streams and the amount of by-products are further decreased by the high selectivity electrosynthesis offers due to the precise control of the oxidation or reduction level by control of the potential. New reaction pathways may be possible that are not achievable in regular chemistry thanks to the different functional group interconversions or *in situ* redox-umpolung which is a unique feature of electrosynthesis (see section 1.2.3) [25–27]. This allows reducing the number of steps and auxiliaries and opens new strategies in synthesis. Electrochemical routes clearly have their place as a promising green method with a very strong potential, although it is not a general solution [23,24,28–31]. How it exactly relates to the principles of green chemistry is shown by Frontana-Uribe in Figure 1.3.

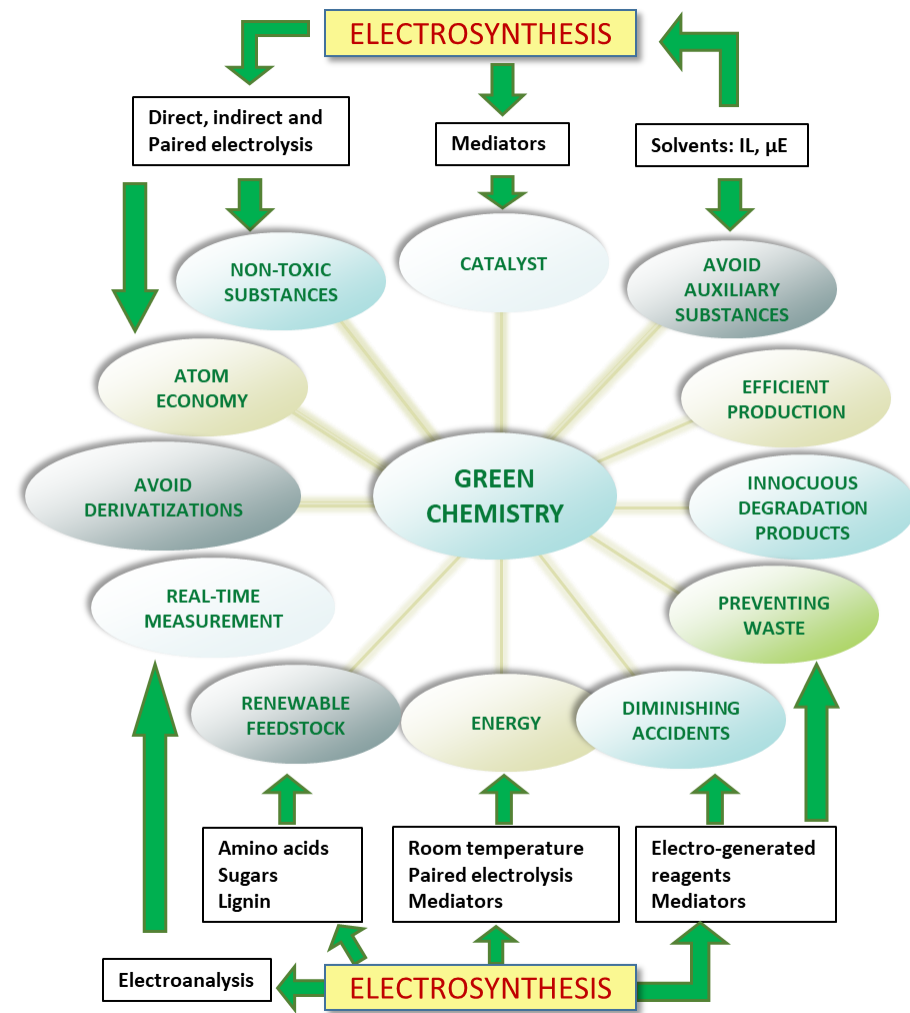


Figure 1.3: The direct relationship of organic electrosynthesis to the twelve principles of green chemistry [31].

A side-note has to be made about a general remark that is often made when an electrochemical route is concerned, which is the consumption of electricity. Though electrosynthesis has an inherently green character, the source of the necessary electricity might tip the balance to the other side. Although arguments can be made about the greenness of the electricity, it needs to be said that this often is much less of a problem than initially thought. It is a contemporary trend that the electricity production needs to become more sustainable, greener. As the global power consumption keeps rising, this becomes increasingly important. Many renewable sources are already applied today such as hydro, wind, solar and nuclear based power

generation and their share in the total power production will keep increasing. Besides the electricity production becoming greener as a whole, which benefits electrochemical routes, many of these renewable sources have a production cycle that does not necessarily correspond with the demand, such as solar and wind energy. Electricity storage on a large scale is still insufficiently developed and often there is a surplus of energy which is inadequately used or even wasted as there often is a minimum production capacity necessary for continuous operation. Electrosynthetic processes could be designed to be flexible to make optimal use of this energy, which would be a cheap source of green electricity. The current trend in society of an increasing consumption of electricity which is increasingly produced in a sustainable manner dictates that the concern of electricity consumption in an electrochemical process will be an issue of declining interest in the future.

1.2.3 The possibilities and advantages of an electrosynthetic route

Organic compounds are synthesized using two types of reactions: (i) C-C bond formations where larger structures are constructed from smaller units and (ii) functional group interconversions where functionality is added to the target molecule or for activation of the smaller building blocks. Electrosynthesis offers both types of reactions for all compounds that are electroactive or can react with electrogenerated reagents. This is achieved by the combination of heterogeneous electron transfers and chemical reactions (see Chapter 3 Section 3.1). The electron transfer step either transfers an electron from the electrode surface to the lowest unoccupied molecular orbital (LUMO) of the organic substrate (reduction at the cathode) or removes an electron from the highest occupied molecular orbital (HOMO) from the substrate (oxidation at the anode). Hereby the substrate is converted to a reactive intermediate (ion, ion radical or radical) or a reagent is generated (nucleophile, electrophile or acid and base). Examples of possible pathways are summarized in Figure 1.4.

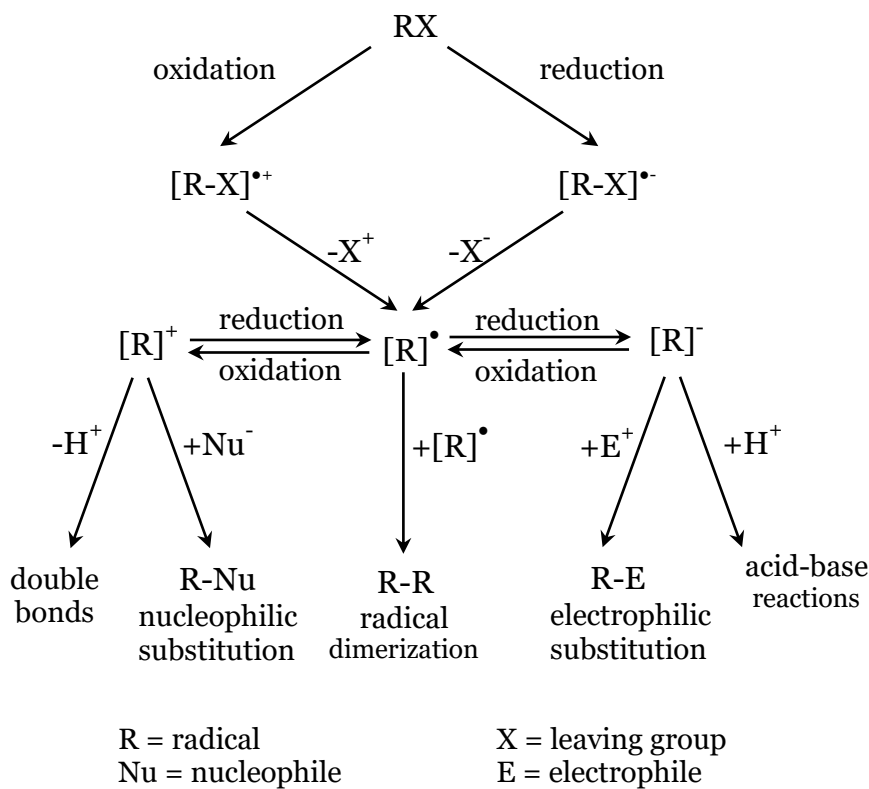


Figure 1.4: Possible pathways and intermediates of organic electrosynthesis. The radical anion and cation formed after the first oxidation or reduction step can also react directly. Additionally the radical R^\bullet can also react in a radical disproportionation or add to unsaturated bonds. Based on [24].

The dimerization in Figure 1.4 is a radical C-C bond formation while the nucleophilic substitution is a polar C-C bond formation. Besides these two types also pericyclic and transition metal-catalyzed reactions occur. In Figure 1.4 instead of undergoing a dimerization, the neutral radical can also react with a neutral substrate in an addition reaction in which a new radical is formed, or react with a radical from a different substrate in a coupling reaction. Different to the chemical radical chain addition where one C-C bond and one C-H or C-X bond is obtained, two C-C bonds can be obtained in the electrochemical pathway. In polar C-C bond formations activated donors react selectively with acceptors or vice versa. Here a unique feature of electrochemistry emerges: the possibility to reverse the polarity of functional groups, a phenomenon known as *umpolung*. Where chemically two or more steps are

required to achieve this, electrochemically this only requires one step. This is done by converting donors to acceptors by the oxidation of nucleophiles to electrophiles or vice versa. This way two donors or acceptors can be coupled as shown in Figure 1.5.

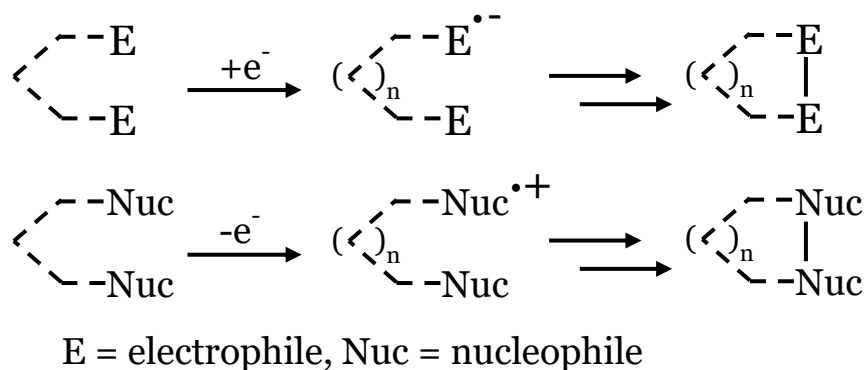


Figure 1.5: Electrochemically one-step in situ umpolung to couple two electrophiles or two nucleophiles [27].

It is obvious that organic electrosynthesis is a versatile technique that offers a wide range of possible reaction steps. Its capability to selectively add or remove electrons creates the potential for developing entirely new synthesis strategies. Besides its green character it has additional advantages such as the amenability to automation: the parameters of electrochemical processes such as the electrode potential and cell current are particularly suited for integration in automatic process control. Besides the precise control of the selectivity of the reaction also the reaction rate can be controlled by adjusting the current density or applied potential, and by monitoring and managing the charge the degree of transformation can be carefully controlled [31]. Furthermore, typically more pure products are obtained in an electrochemical process compared to those chemically synthesized [32]. If designed in a correct way, an electrochemical process can be a cost-effective option since cell constructions and peripheral equipment are generally simple. Of course there are more parameters which should be taken into the comparison of chemical and electrochemical routes, such as the relative economics, the market and so on.

1.3 Examples in the industry

Many companies and institutions have been or still are involved in organic electrochemistry and have developed knowledge and technology such as electrodes and cell setups [33]. In the past decades, many industrial electrosynthesis processes have emerged. Some have reached commercial status, others never went beyond pilot installation status. Of those that were operated commercially, many only operated for a period of time before becoming obsolete due to new routes or new technology. An overview and elaborate discussion of industrialized processes can amongst other sources be found in [19,22,29,34] and the references therein. Of the many processes that are described, two stand out. Both because of their success and prolonged application in the industry. These are the electrohydrodimerization of acrylonitrile (ACN) to adiponitrile (ADN) developed by Monsanto and the paired electrosynthesis of phthalide and 4-*tert*-butylbenzaldehyde dimethylacetal developed by BASF. These processes are briefly discussed.

1.3.1 Electrohydrodimerization of acrylonitrile

The electrohydrodimerization of acrylonitrile to adiponitrile is the best known and most likely the most successful organic electrosynthesis process (Figure 1.6). It was initiated by Manuel Baizer in 1960 while working at Monsanto [35] and the process is often referred to as “the Monsanto process”. The reaction yields adiponitrile, which is subsequently catalytically hydrogenated to obtain the hexamethylenediamine which by dehydration-condensation with adipic acid forms the well-known fiber Nylon-6,6.

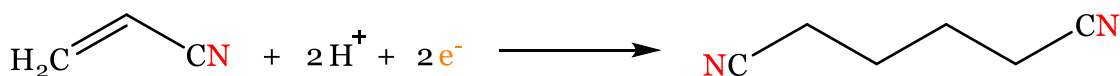


Figure 1.6: The Monsanto process: the electrohydrodimerization of acrylonitrile to adiponitrile.

Cathodic hydrocoupling of acrylonitrile had been known since the 1940s, but the yield was low. Baizer found that the use of quaternary ammonium salts increased both the current efficiency and the yield [36], leading to the breakthrough of the commercialization and intensive development by Monsanto followed [37]. Initially the process was performed in a divided cell with an aqueous solution of ACN and lead electrodes (with 1% silver in the anode) with an ion exchange membrane to separate catholyte and anolyte. One cell consisted of 24 bipolar units with each unit containing 16 electrode pairs. The setup included a stripper to remove the ADN and to recycle the unreacted ACN [19,22,34,38].

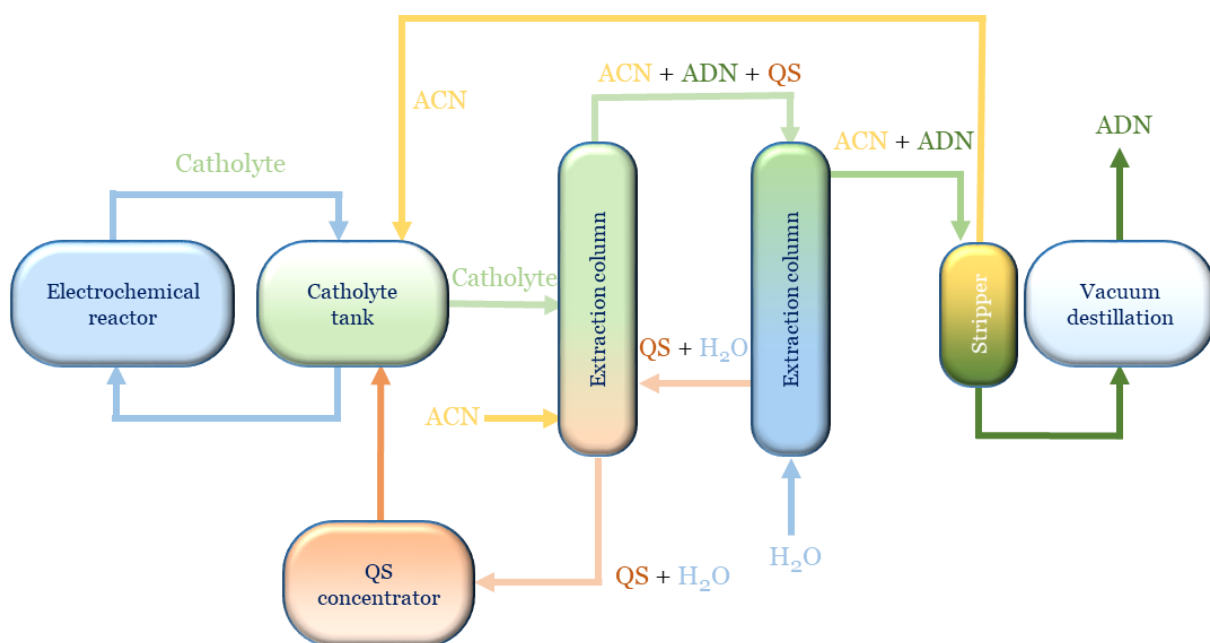


Figure 1.7: Scheme of the industrial electrosynthesis process for the electrohydrodimerization of acrylonitrile. ACN = acrylonitrile, ADN = adiponitrile, QS = quaternary ammonium salt [24].

Due to the high energy costs related to the higher cell voltage caused by the separator and high repair and maintenance costs the electrochemical reactor was converted to an undivided cell. Besides improving energy efficiency, the focus was directed on less corrosion, long-term stable operation, recovery of supporting electrolyte and process safety. After 15 years of development, a new process was introduced. In the current

process cadmium cathodes and steel anodes are used. Even though the current density was halved, the cell potential dropped by almost 70% causing the total power consumption to drop by 65%. A detailed overview of both processes can be found in [34]. At present time more than 300 000 ton is produced annually by this process. The Monsanto process is a prime example of how an electrochemical route can be a viable option even when it requires a nonlinear cost investment. For example the electrolytic part makes up less than 20% of the whole process while the corresponding costs are about 30%. For the chloralkali process the ratio is even worse [19]. Still the process remains to date the largest organic electrosynthesis (by volume).

1.3.2 Paired electrosynthesis of phthalide and 4-*tert*-butylbenzaldehyde dimethylacetal

A second process noteworthy of mentioning, is the BASF paired electrosynthesis process for the simultaneous production of phthalide and 4-*tert*-butylbenzaldehyde dimethylacetal (Figure 1.8). Much less of a milestone in industrial organic electrosynthesis, but still important as it is the first commercialized paired electrosynthesis, running for already almost two decades. In paired electrosynthesis useful products are produced at both electrodes, which is considered the holy grail of electrosynthesis since all the energy input in the process is used to obtain desired products [22,29,34].

A unique feature of this process is that methanol is both a solvent and a reagent. The reduction of methanol is suppressed by the quaternary ammonium salt supporting electrolyte and the reduction of phthalic acid dimethyl ester proceeds highly efficiently. The organic yield is over 90% for both the anodic and cathodic reaction and the current efficiency of the total process amounts to 70% giving it a better energy efficiency than the conventional process [34]. The process proceeds in a capillary gap cell consisting of bipolar carbon discs separated by narrow spacers. The discs have a center hole for the electrolyte inlet. This process shows what an organic electrosynthetic route is capable of. Of course developing a paired electrosynthesis is

not trivial and might not always be possible as the compatibility of both reactions depends on many parameters that have to fit.

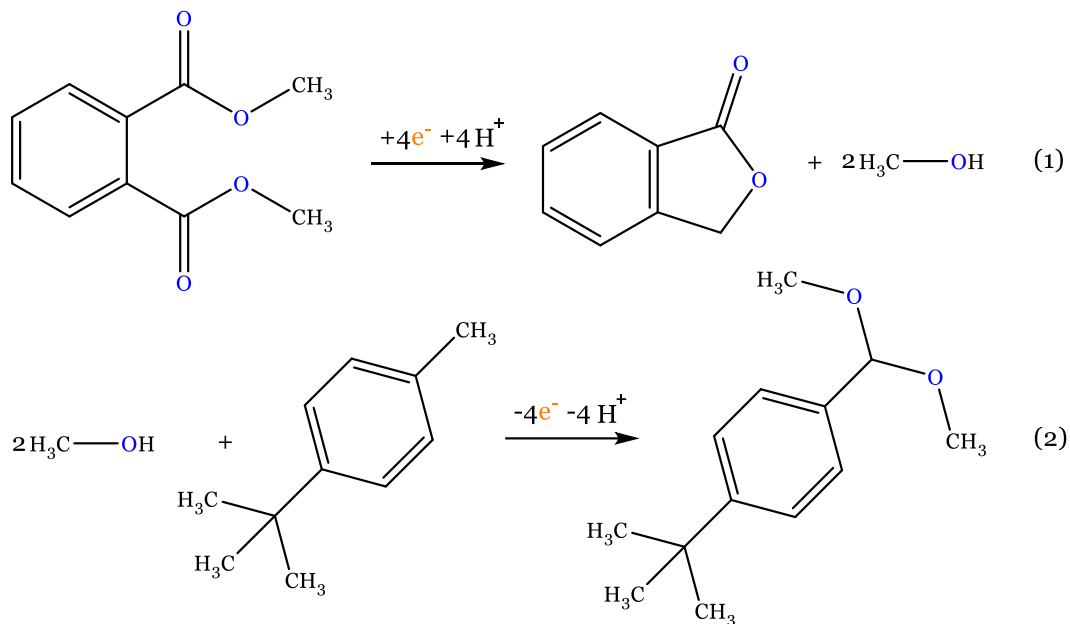


Figure 1.8: The BASF paired electrosynthesis process: (1) cathodic reduction of phthalic acid dimethyl ester to phthalide, (2) anodic oxidation of 4-*tert*-butyltoluene to 4-*tert*-butylbenzaldehyde dimethyl acetal.

1.4 Upscaling and implementation of an electrosynthesis

Similar to what chemical engineering is in chemistry, electrochemical engineering is the field concerned with the design, characterization and operation of electrolytic devices and processes. However, compared to chemical engineering, the progress of electrochemical engineering in implementation of electrosynthetic processes has been slow. Despite the successful implementation of processes such as these described above, the development to a commercial production level is the exception rather than the rule. An extensive list of processes that have reached commercial scale, piloted processes which have not yet reached commercialization and processes which have been discontinued is given by Sequeira et al. in [29]. They also listed

criteria for success based on what was common in the commercialized processes. Most of these are directly linked to the green character of electrosynthesis such as a higher product selectivity than chemical routes, lower energy costs, minimized pollution problems and a less hazardous route. Main reasons for failure (discontinuation) were assigned to the discovery of alternative chemical or catalytic routes and economic reasons such as disappearing markets or markets that may not have really existed.

Sequeira et al. also discuss reasons for the lack of new commercialized processes, most of which are also found in the criteria for competitiveness of organic electrochemistry stated by Weinberg [33]. One such reason is that a lot of attention has been devoted to high volume, low added value processes while electrochemical processes often are more competitive in low volume, higher added value processes, such as pharmaceutical and specialty chemicals. Another main reason is the lack of the necessary skills which is a combination of organic synthesis, electrochemistry and (electrochemical) engineering and as a consequence companies not familiar with electrochemistry are reluctant to venture into this area. This is also acknowledged by Pletcher et al. [34] who found several causes contributing to this problem. A major one is that electrochemical engineering has not been a recognized subject area and is often undertreated in electrochemical and engineering courses and textbooks, leading to a lack of appreciation of electrochemical routes. Furthermore much of the electrochemical technology has been developed in isolation with little interaction or transfer of concepts, experience and equipment. Examples of this can be found in the two electrosynthetic processes described in section 1.3 where for both processes extensive electrochemical engineering has led to specialized setups which are operated under specific conditions, both developed for the specific reaction.

It is clear that electrosynthesis is a method with a lot of potential from which the industry could benefit in its quest towards more sustainability, owing to its inherently green character, amount of controllability and chemical versatility. However, despite

being around for almost two centuries and having known successful commercial implementations for over half a century, it is still far too often not considered when alternative production routes are sought after. Furthermore, when it is considered at all, it often is approached as a final resort instead of an alternative with realistic economic feasibility. Many causes can be named that contribute to the general attitude towards electrosynthesis, of which several are technological and technical reasons. However, due to general technologic advances and progression made in several related fields, many of these reasons have become irrelevant. As explained, one major cause is the lack of the combined knowledge needed to completely develop an electrosynthetic route to an industrial viable application. As a consequence often only one aspect is investigated thoroughly and the electrosynthetic implementation is developed very case specific in isolation. A more general approach would facilitate the transfer of technology and knowledge and would benefit the applicability and perception of electrosynthetic pathways as a whole.

CHAPTER 2

Scope and outline

THIS CHAPTER DEFINES THE SCOPE OF THIS WORK, DESCRIBES THE STRATEGY FOLLOWED TO ACHIEVE THE GOALS SET IN THE SCOPE AND GIVES THE OUTLINE OF THIS DISSERTATION.

2.1 Scope

As the previous chapter shows, industrial electrosynthesis offers a great potential, however, implementation in industry is lacking. To further establish electrosynthesis as an interesting alternative for organic synthesis with industrial viability, it is necessary to pay more attention to bridging the gaps between the different concerned areas, i.e. electrochemistry, chemical engineering and organic synthesis. This requires screening strategies that involve multiple aspects and do not focus on one single facet of the complete process. The goal of this dissertation is to gain insights into different aspects crucial for the development of a robust and reproducible electrosynthetic pathway. This will help closing the gap between the fundamental electrochemical investigations and the engineering research conducted in the development of an electrochemical route. To achieve this goal, the attention is directed towards two main topics which are recognized as important steps in process development.

The first step is to develop the electrochemical reaction as a flow compatible process by means of electrochemical engineering. Such investigation comprises an electrochemical screening of the reaction to assess its capability as an electrosynthetic process and identify and quantify relevant parameters. The obtained information can subsequently be applied in the development of the reaction in continuous flow mode. Flow chemistry offers several advantages to batch operation such as typically a higher yield and selectivity and increased process safety and is becoming increasingly popular in the chemical industry. This first stage covers important (electrochemical) engineering aspects in the development of an electrosynthetic pathway.

In a second step a more fundamental approach is applied. As explained in Chapter 1 both the engineering aspects and the fundamental understanding of the reaction are vital aspects in the development of an electrosynthetic process. A profound understanding of the underlying mechanism and the impact of the electrocatalyst is

necessary to enable a thorough optimization of the electrosynthetic pathway. Consequently, the focal point of this second stage will be the elucidation of reaction intermediates, reaction mechanisms and the influence of catalyst properties on the pathway such as its material and the morphology. This allows tuning the electrocatalyst to increase its activity and selectivity.

After completing these two steps an innovative methodology is obtained that offers a unique combination of both an electrochemical engineering investigation and a fundamental study to gain insights into the important aspects in the development of an electrochemical pathway. This could be seen as a more general multi-aspect screening methodology.

2.2 Strategy

In accordance with the two steps of the scope, a two-folded strategy is applied. To reach the goal, industrial relevant reactions which exhibit problems to which electrosynthesis can offer an answer are used as case study reactions.

Firstly the aldol reaction of acetone to diacetone alcohol will be used in the electrochemical study. The aldol reaction is a common reaction in the chemical industry to create carbon-carbon bonds. However, the traditional chemical pathway often has problems concerning selectivity leading to large waste streams and costly purifications. In addition, the standardly employed homogeneous base catalysts cause corrosion problems. Both drawbacks are particularly relevant to the aldol reaction of acetone. Additionally diacetone alcohol is an important intermediate in the chemical industry, which makes it an interesting candidate for an electrosynthetic pathway. In the first step, the reaction will be thoroughly electrochemically screened and parameters such as the electrolyte composition, electrode material and electrolysis potential will be investigated. The obtained information will give important insights into the electrochemical pathway and allows assessment of this

route. In a following phase, to convert the electrochemical batch reaction to an electrochemical flow synthesis, a modular electrochemical microreactor screening setup will be built which will then be used to assess the reaction in flow. Reactor parameters such as electrolysis setup and inter-electrode distance will be described and investigated. The modular microreactor setup will offer a versatile research platform that can be combined with analytical techniques to be suited for a broad range of reactions.

Secondly a more mechanistic approach will be undertaken. To unravel the underlying electrode reaction mechanisms, electrochemical measurements will be combined in situ with electron paramagnetic resonance (EPR) spectroscopy. EPR is a technique that is well-suited to acquire information on the chemical nature and electronic structure of the different intermediates. Its unique feature to detect radicals make it particularly useful for organic electrochemistry in which radicals are common intermediates. It offers a strong potential in electrochemical research but is vastly underexploited and lacks commercially available equipment for combined studies. An innovative and versatile setup will be developed, specifically optimized for in-depth electrocatalytic research. To emphasize the generic character of this approach, another common and useful industrial reaction is selected as a case study. The setup and fundamental approach will be validated by the study of the reaction mechanism of the reductive cyclisation of allyl 2-bromobenzyl ether to 4-methylisochromane. The activation of R-X bonds knows many applications of which the synthesis of heterocyclic compounds is of particular interest due to the many important applications of the products it yields. More specific the benzopyran derivate 4-methylisochromane is an important building block in the pharmaceutical industry.

2.3 Outline

Corresponding to the two-folded strategy the experimental work in this dissertation is presented in two parts: (i) an engineering approach for an electrochemical study towards industrial implementation of the electrosynthetic aldol reaction of acetone and (ii) a mechanistic approach for an electrochemical study by in situ EPR spectroelectrochemistry of the reaction mechanism of the electrosynthetic intramolecular reductive cyclisation of allyl 2-bromobenzyl ether. A schematic illustration of the outline is shown in Figure 2.1.

In Part II a thorough electrochemical investigation is performed on the industrial relevant aldol reaction of acetone to diacetone alcohol. Chapter 4 describes the problems and disadvantages of the traditional chemically performed aldol reaction and the specifics of the case study. Furthermore the advantages of flow chemistry are discussed and a concise description of the state-of-the-art of microfluidic reactors for electrochemical synthesis is given. In Chapter 5 the reaction is electrochemically screened with industrial implementation in mind. The applicability of an electrosynthetic route for the reaction is assessed by determining and quantifying the relevant parameters. A versatile modular electrochemical microreactor platform is built in Chapter 6 which is then employed to perform the case study in flow. Important reactor parameters and their influence on the performance of the reaction are quantified and described. The mechanism of the electrochemically performed aldol reaction is looked into and compared with the traditional chemical mechanism in Chapter 7.

In Part III, a fundamental electrochemical study is performed to elucidate the reaction mechanism of another yet industrial relevant reaction by in situ EPR spectroelectrochemical measurements: the reductive cyclisation of allyl 2-bromobenzyl ether to 4-methylisochromane. Chapter 8 discusses of the combination of electrochemistry with EPR measurements and gives a brief overview

of contemporary cell and electrode design. In Chapter 9 an innovative versatile electrode construction is built and validated both electrochemically and spectroscopically by means of standard reactions, i.e. the reduction of methyl viologen and the reduction of *p*-benzoquinone. This setup is then employed in Chapter 10 to identify important intermediates in the case study reaction to confirm the proposed reaction scheme.

In the final part of this dissertation, Part IV, the general conclusions of this work are given together with perspectives towards future research.

Part I

Chapter 1

Organic electrosynthesis as a green alternative production route**Part II****Engineering approach for an electrochemical study towards industrial implementation**

Electrochemical screening

Chapter 4, 5 & 7

Electrosynthesis in continuous flow

Chapter 4 & 6

Part III**Mechanistic approach for an electrochemical study by in situ EPR spectroelectrochemistry**

Profound mechanistic investigation

Chapter 8, 9 & 10

Part IV**Conclusions and future perspectives**

Chapter 11

Figure 2.1: Schematic outline of this dissertation.

CHAPTER 3

Fundamental concepts and experimental techniques

THIS CHAPTER EXPLAINS THE THEORETICAL BACKGROUND OF THE ELECTROCHEMICAL AND SPECTROSCOPIC TECHNIQUES USED IN THIS WORK.

3.1 Electrode reactions in organic electrochemistry

This section provides a first insight into some of the fundamental concepts concerning organic electrochemistry. It is based on reference works in electrochemistry and organic electrochemistry listed in references [19–22,34,39–44]. For a more comprehensive explanation of these topics, the reader is referred there.

3.1.1 Charge transfer

Electrode reactions are redox reactions where an electron is transferred between a substrate molecule and an electrode, taking place at or near the electrode surface. A general electrode reaction presented by the following equation where an oxidized species O accepts an electron to form the reduced species R .



This seemingly simple conversion is composed of multiple steps, as shown in Figure 3.1. Four types of elementary steps can be distinguished:

1. Mass transfer of the reactant from the bulk solution to the electrode surface and mass transfer of the product from the electrode surface to the bulk solution.
2. Chemical reactions taking place before or after the electron transfer.
3. Adsorption of the substrate or intermediate and desorption of an intermediate or the product.
4. Electron transfer at the electrode surface.

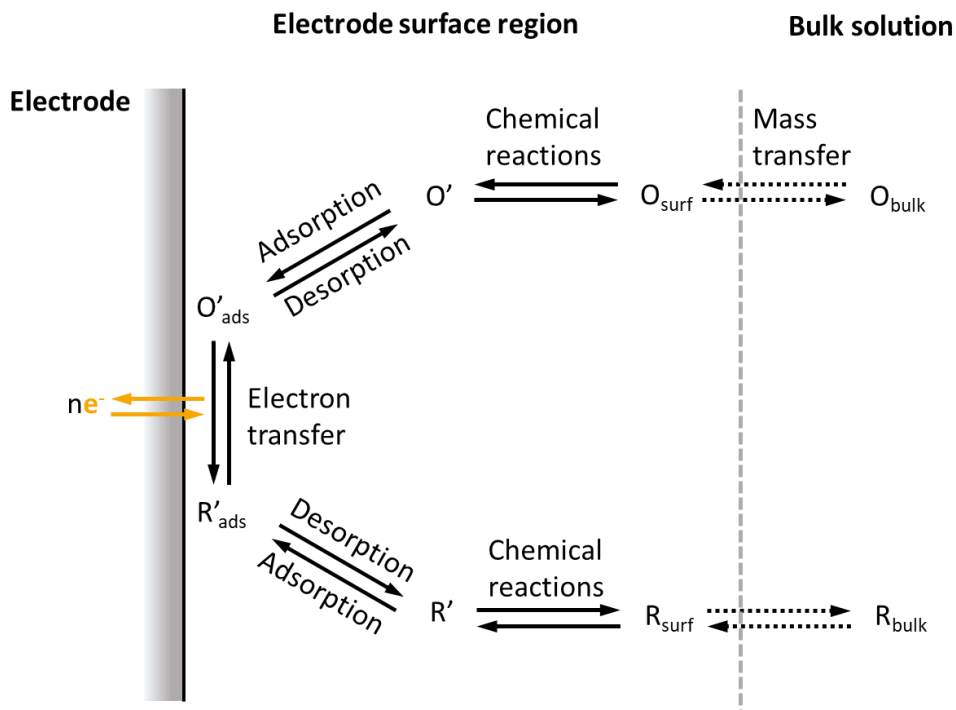


Figure 3.1: Possible reaction steps during a general electrochemical reaction.
Redrawn from [40].

A complete electrochemical reaction is comprised of a series of a combination of these steps. Each of the steps has its own rate of which some are potential dependent. At steady state, the rates of all steps are equal with the more facile steps being limited in their rate by the slower steps. The overall rate of the electrochemical reaction is determined by the slowest or rate-determining step. A simple reaction may only involve three steps: mass transfer from and to the bulk and an electron transfer in between, while a complex reaction can involve a series of electron transfers, chemical reactions and adsorption or desorption phenomena. In the case of organic electrochemical reactions, the electron transfer almost never takes place by itself and usually is accompanied by chemical reactions happening before and/or after the charge transfer step. This is quite different from inorganic electrochemistry where the opposite is true. Various different sequences of electron transfers and chemical steps are possible. In the electron transfer steps, electrons are considered to be transferred singly, i.e. a single electron is exchanged between substrate and electrode. However,

many reactions have an overall transfer of more than one electron. Such reactions are a process of a rapid succession of multiple single-electron steps instead of a multi-electron transfer since the energetic and activation requirements for any type of the latter process are too high to compete with the former process [19,44]. The chemical steps can involve multiple molecules and be of high-order and not only first-order or even be a succession of chemical reactions. A common nomenclature to classify mechanisms of organic electrochemical reactions is to refer to the electrochemical step (heterogeneous electron transfer) as E and the (homogeneous) chemical step as C.

3.1.1.2 Mechanisms involving a single electron transfer

The simplest mechanism for an organic electrochemical reaction consists of a single chemical and single electrochemical step and can either be EC or CE. An example of a CE process is the reduction of a weak acid (Figure 3.2).

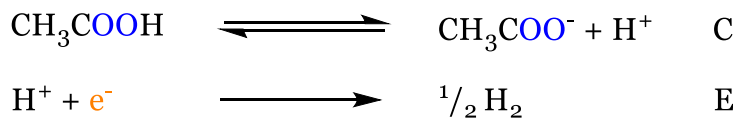


Figure 3.2: CE mechanism example: reduction of acetic acid.

An example of an EC mechanism is the electrohydrodimerization of an activated alkene (Figure 3.3).

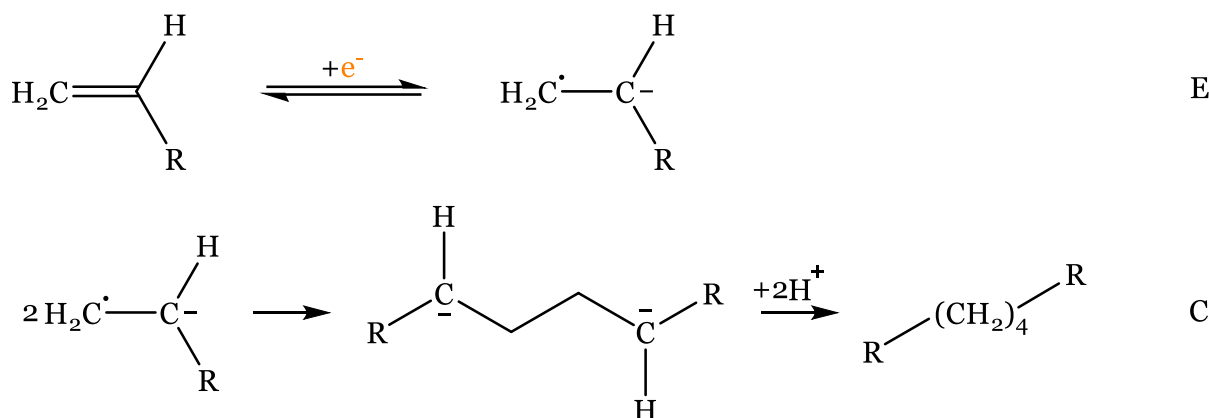


Figure 3.3: EC mechanism example: electrohydrodimerization of an alkene.

Sometimes this is also referred to as an ECC mechanism due to the two consecutive chemical steps, but as stated above, a single C notation can represent a succession of chemical steps and thus, the notation simplifies to EC.

3.1.1.3 Mechanisms involving multiple electron transfers

In some reactions, more than one electron is transferred. As explained above, the electron transfer is a series of single electron transfer steps which can happen consecutively or which are alternated by a chemical step. The first case would be described as an EEC mechanism and an example is the reduction of alkyl halides to alkanes (Figure 3.4).

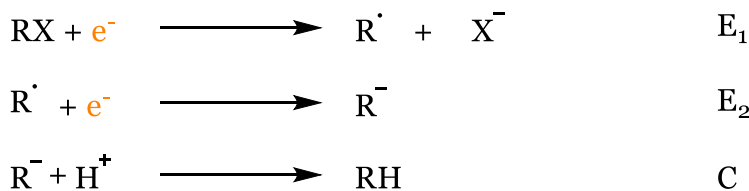


Figure 3.4: EEC mechanism example: reduction of alkyl halides to alkanes.

More common is that the electron transfers are alternated by a chemical step, resulting in an ECE mechanism, for example in the reduction of benzoquinone (Figure 3.5).

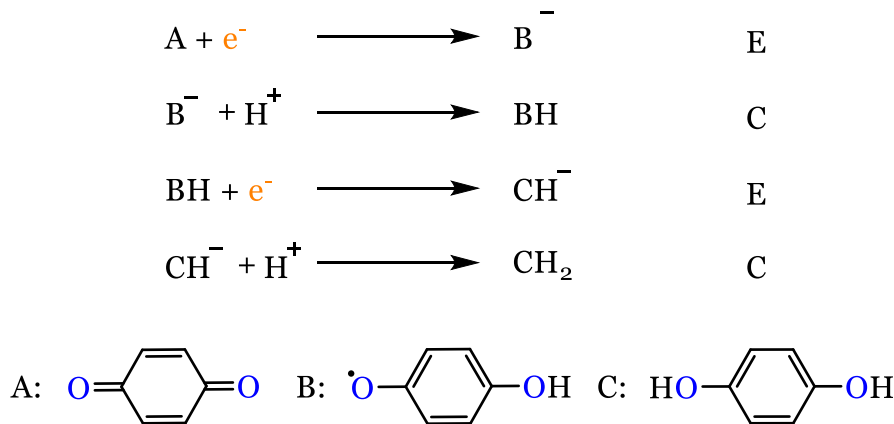


Figure 3.5: ECE mechanism example: reduction of benzoquinone in a protic solvent. A: 1,4-benzoquinone, BH: semiquinone, CH₂: hydroquinone.

However, if the second electrochemical step is a radical disproportionation step, the mechanism is referred to as a DISP. In fact, a DISP mechanism is an alternative pathway to ECE where in the ECE mechanism the disproportionation step is insignificant. This is explained by the reduction of aromatic halides (Figure 3.6).

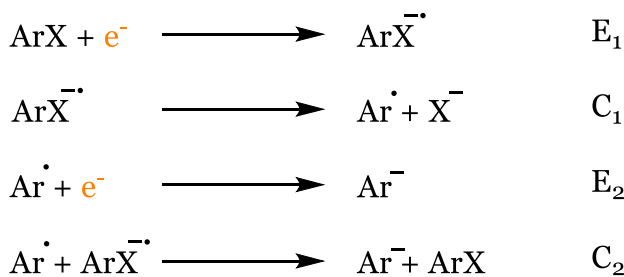


Figure 3.6: DISP mechanism example: reduction of aromatic halides.

If C₂ is insignificant, the result is E₁C₁E₂ which is the ECE pathway. However, if C₂ is important the alternative pathway becomes E₁C₁C₂, or DISP. In the latter case either C₁ or C₂ can be rate limiting which is then referred to as DISP1 or DISP2 respectively.

Since DISP2 involves a second-order rate-limiting step, it can easily be distinguished from ECE or DISP1. The distinction between ECE and DISP1 however, is in practice nearly impossible because of the identical rate-determining step C₁.

Besides the general cases listed here, a great variety of schemes is possible consisting of combinations or variations of these general cases. Sometimes further subclasses are defined, for example depending on the order of the chemical step which is then denoted as C₁ for a first order reaction, C₂ for a second order and so on (not to be confused with the suffixes in Figure 3.4 and Figure 3.6 where the suffix orders a series of similar steps), or depending on the (ir)reversibility of the chemical or electrochemical step, respectively denoted by suffixes *i*, *r* or *q* for quasi-reversible.

3.1.1.4 Indirect organic electrosynthesis

The mechanisms discussed above are direct electrochemical reactions, i.e. the substrate is directly involved in the heterogeneous electron transfer at the electrode surface. It is also possible to employ an electrogenerated reagent as a redox catalyst, to shift the electron transfer involving the substrate from a heterogeneous process occurring at the electrode to a homogeneous process: a so-called indirect or mediated electrolysis [45]. The mediator is activated at the electrode surface and then reacts in solution with the substrate wherein the mediator is regenerated. This process can offer several advantages over a direct electrolysis:

- Overpotentials can be avoided as the substrate is not oxidized or reduced at the electrode itself.
- Mediators can exhibit a higher or even different selectivity.
- Poisoning of the electrode by adsorption of intermediates or other ions can be avoided.
- The electrolysis is conducted at a potential lower than that necessary for a direct electrolysis of the substrate, leading to less energy input and

suppression of side reactions. In addition overoxidation or –reduction of the substrate is avoided.

An indirect electrolysis can proceed *in situ* or *ex situ*, but the former is usually more desirable since the electrogenerated species does not need to be stable enough to be transferred to another cell and its *in situ* regeneration allows the use of catalytic amounts. A mediated electrolysis may offer an interesting route if a direct electrolysis encounters major drawbacks or is not feasible. However, as it increases the complexity of the system, the total balance should be taken into account when deciding on this route. By introducing an additional component a more intensive and complex purification afterwards is required. Furthermore, the mediator needs to fulfill several requirements such as being chemically stable and not react with the solvent or the products and be initiated at a lower potential than the substrate itself. Hence, employing a mediator requires careful consideration.

3.1.2 Mass transfer

Since electrochemical reactions are surface processes, mass transfer plays an essential role in all fields of electrochemistry. As seen in Figure 3.1, it is a fundamental step in a general electrode reaction. The overall rate of an electrode reaction is not only influenced by the electrode kinetics, but also by the transfer of reactants from and products or intermediates to the bulk. Although the fundamentals remain the same, there are differences in how it is approached in different fields. In mechanistic research, where quantitative kinetic data is desired, it is essential to be able to precisely describe the mass transfer by mathematical equations. In an industrial setting however, it would be adjusted to maximize the economic potential of the process within the technical limitations. This permits mass transfer conditions which are not applicable in mechanistic research. Mass transfer occurs by diffusion, convection or migration. These are elaborated below where the equations given are valid for an infinitely (or ideal) diluted solution, as is often approximated in

electrochemistry. The derivation for a more general valid equation can be found in Chapter 12 in reference [42].

3.1.2.1 Migration

The movement of a charged species (ion) driven by an electrical field is called migration. Considering no concentration gradients, the migrational flux $J_{m,i}$ ($\text{mol s}^{-1} \text{ m}^{-2}$) for a species i is given by:

$$J_{m,i} = -u_i c_i \nabla \Phi \quad (3.2)$$

Where u_i is the ion mobility and Φ an electrical field or potential gradient. The minus sign arises because the direction of the flux opposes the direction of the increasing gradient. The mobility is a proportionality factor that denotes the average velocity of an ion in response to an electric field and can be linked to the diffusion coefficient by the Einstein relation:

$$u_i = \frac{|z_i| F D_i}{RT} \quad (3.3)$$

By inserting (3.3) in (3.2), $J_{m,i}$ can be expressed as:

$$J_{m,i} = -\frac{z_i F}{RT} D_i c_i \nabla \Phi \quad (3.4)$$

Normally, the conditions of the electrochemical experiment are chosen so that migration effects can be neglected, i.e. the solution is electroneutral ($\sum_i z_i c_i = 0$). This is accomplished by adding a significant amount of inert electrolyte, called the supporting electrolyte. In this case the effects of the electric field are limited to a very thin layer near the electrode's surface: the electrolyte double layer region.

3.1.2.2 Convection

Convection is the movement of species by bulk motion. The cause of the movement can be natural such as a density gradient caused by temperature or it can be forced in case a mechanical force is applied (e.g. stirring or agitating the solution). The convective flux of a species i is given by:

$$J_{c,i} = c_i v \quad (3.5)$$

Where v is the velocity of the bulk fluid.

3.1.2.3 Diffusion

Diffusion is the natural movement of species in solution without the influence of an electric field, driven by a concentration gradient. Natural diffusion occurs when there is a chemical change, causing a concentration difference. The diffusional flux for a species i is expressed by Fick's first law:

$$J_{d,i} = -D_i \nabla c_i \quad (3.6)$$

The change of concentration with time due to diffusion is given by Fick's second law, which is derived from the first law:

$$\frac{\partial C_i}{\partial t} = D_i \Delta c_i \quad (3.7)$$

Solving Fick's second law with the correct initial and boundary conditions for the system under study gives an expression for the variation of the diffusion-limited current with time.

3.1.2.4 Total flux

The total flux of a species i in solution is given by the combination of equations (3.4), (3.5) and (3.6):

$$J_i = J_{m,i} + J_{c,i} + J_{d,i} = -\frac{z_i F}{RT} D_i c_i \nabla \Phi + c_i v - D_i \nabla c_i \quad (3.8)$$

Due to excess of supporting electrolyte, the migration term can be neglected:

$$J_i = c_i v - D_i \nabla c_i \quad (3.9)$$

Or corresponding to Fick's second law:

$$\frac{\partial C_i}{\partial t} = -v \nabla c_i + D_i \Delta c_i \quad (3.10)$$

This equation is called the convective diffusion equation (as noted on p. 35 only valid for an infinitely (or ideal) diluted solution) and forms the basis in the study of hydrodynamic systems. In such systems hydrodynamic electrodes are used, which are electrodes that function in a regime of forced convection to rule out the effects of natural convection. In steady-state conditions, i.e. constant forced convection and constant applied potential or current, the convective-diffusion equation may be solved which allows inferring kinetic information about the system. Many hydrodynamic systems have been studied and their corresponding limiting current equations have been derived [40,41]. The most extensively used hydrodynamic electrode is the rotating disk electrode, other examples include the wall-jet electrode and the channel electrode.

In hydrodynamic systems the bulk solution remains well mixed due to the convection and diffusion is negligible. In a region near the electrode surface there is convective diffusion where both convection and diffusion play a role. This thin layer directly

adjacent to the electrode is retained by molecular forces and appears relative stagnant. Herein the fluid velocity increases from zero at the surface to the bulk fluid velocity v at a certain distance from the surface. This zone within which the velocity changes is called the hydrodynamic boundary layer of thickness δ_H :

$$\delta_H \approx \sqrt{\frac{\nu_{kin}y}{v}} \quad (3.11)$$

Where ν_{kin} is the kinematic viscosity and y the distance from the surface. Within this layer, in the direction of the bulk to the surface, convection gradually becomes less important and the effects of diffusion increase. In a thin stagnant layer near the electrode surface, convection is absent and diffusion dominates, all concentration gradients occur within this layer which is called the diffusion layer of thickness δ . It has been shown [46] that:

$$\delta \approx \sqrt[3]{\frac{D}{\nu_{kin}}} \delta_H \quad (3.12)$$

Equations (3.11) and (3.12) implicitly show the influence of forced convection on the diffusional mass transfer and how it benefits an electrochemical reaction by governing the diffusion-layer thickness. The more convection, i.e. the higher the fluid velocity, the thinner the hydrodynamic boundary layer and by extension the thinner the diffusion layer. The thinner the diffusion layer, the steeper the concentration gradient and hence, the larger the diffusional flux.

3.1.2.5 Mass transfer in industrial processes

As mentioned in Section 3.1.2, mass transfer is approached differently in laboratory setups and industrial settings. In the latter it is possible to find examples of processes with dormant solutions such as in electroplating or batteries, but it is much more common to find processes which utilize stirred or flowing solutions such as

electrosynthesis, fuel cells and water treatment. In addition much more complex cell and electrode geometries are used as the simplification of both is usually necessary for analytical description and does not necessarily result in the most optimal design. Where laboratory setups often are designed so that mass transfer is one dimensional, in industry it rarely is and as a result, the preceding mass transfer equations all develop in three dimensions. Moreover, the applied conditions often render the equations invalid, such as highly concentrated solutions or turbulent flows. Turbulence is usually advantageous since it increases mass transfer and promotes exchange of species between the bulk solution and the boundary layer. It is not uncommon to see turbulence promoters in industrial setups, which can even be the electrode itself. Consequently, the approach taken is to treat the setup as a unified whole and express the mass transfer in terms of space-averaged quantities. Dimensional groups which are useful and therefore often used are:

The Reynolds number Re , which describes the ratio of inertial forces to viscous forces within a fluid and is used to describe flows and predict flow patterns:

$$Re = \frac{vL}{\nu_{kin}} = \frac{\rho v L}{\mu} \quad (3.13)$$

The Schmidt number Sc , which is the ratio of momentum the kinematic viscosity (momentum diffusivity) to mass diffusivity and is used to characterize fluid flows.

$$Sc = \frac{\nu_{kin}}{D} \quad (3.14)$$

The Sherwood number Sh , which is the ratio of the rate of convection to the rate of diffusion for a species in a flow and is used to characterize mass transfer.

$$Sh = \frac{k_m L}{D} \quad (3.15)$$

The Sherwood number is proportional to the mass transfer coefficient k_m and is often used as a measure of the rate of mass transfer, calculated from the limiting current density (see Section 3.3.1.2) by the relationship:

$$Sh = \frac{I_L L}{nFADc^\infty} \quad (3.16)$$

It is also possible to define Sherwood as a function of Reynolds and Schmidt:

$$Sh = C Re^a Sc^b \quad (3.17)$$

Where C , a and b are constants which are system dependent and can be experimentally obtained. It can be shown that for a specific system equations for the limiting current derived from (3.10) and from (3.17) are essentially equivalent (see [34], Chapter 1). The former is mostly used in analytical electrochemistry while the latter is common in electrochemical engineering.

3.1.3 Electrolysis methods

Analytical electrochemical experiments are typically designed for repeated measurements and do not intend to achieve large conversions. However, this is often desirable in preparative electrochemistry or electrosynthesis. Electrolysis experiments where a large amount or even all of the reactant is converted are called bulk or exhaustive electrolysis. Where the time scale of analytical experiments usually is on the order of seconds to minutes, it is not uncommon for bulk electrolysis experiments to be on the time scale of minutes to hours. Despite the differences in setup and intention, the fundamentals governing both types of experiments remain the same. There are two ways of performing an electrolysis based on the parameter that is controlled, which is either the potential (E) or the current (I). Respectively these are called controlled-potential electrolysis or controlled-current electrolysis whereas in analytical experiments employing the same technique these would be

called chronoamperometry and chronopotentiometry respectively, after the parameter that is measured.

3.1.3.1 Controlled-potential electrolysis

The method of electrolysis employed has a consequence on the setup. In potential-controlled or potentiostatic electrolysis the potential of the working electrode is kept constant relative to a reference electrode. The reference electrode should be currentless, hence there is a necessity of a third electrode, the auxiliary or counter electrode, resulting in a three electrode system. Since the potential determines which reactions can occur and since it can be adjusted accurately, this technique has the advantage of being highly selective. By correctly setting the potential, the desired oxidation/reduction reaction can proceed and possible side reactions can be suppressed. This of course depend on the relative reaction potentials and may not always be achievable, if for example side reactions occur at potentials lower than necessary for the targeted reaction. However, overoxidation or –reduction is always avoided if the product does not react at a potential lower than that of the substrate since the potential will never increase. The disadvantage of this method is that the rate of the electrolysis is not controlled directly. The potential is set to the chosen value and the current corresponds to the electrode reaction. Consequently, exhaustive electrolysis by controlling the potential may take a long time. The current is proportional to the amount of reactant that is consumed and can be the limiting current at the beginning of the electrolysis. Towards the end of the electrolysis, when a significant amount is converted, less of the reactant is being consumed, the current drops and the rate of the reaction slows down (Figure 3.7).

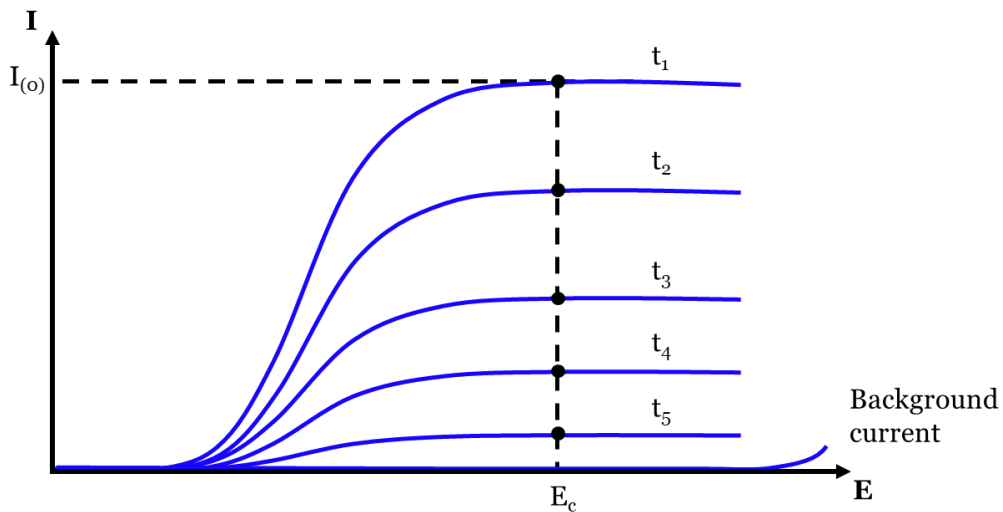


Figure 3.7: Current-potential curves at different times (increasing from t_1 to t_5) during a stirred controlled-potential bulk electrolysis at potential E_c . The current at the applied potential drops as time passes. Redrawn from [40].

3.1.3.2 Controlled-current electrolysis

In a controlled-current or galvanostatic electrolysis, logically the current flowing through the cell is controlled. This is achieved by adjusting the potential of one of the electrodes until the desired current is obtained. As a consequence, a much simpler setup is required as there is no need for a separate reference electrode and a two electrode system suffices. The simpler instrumentation requirement is one of the main reasons for the popularity of this technique in large scale electrolysis. Contrary to the controlled-potential electrolysis, the rate of the reaction remains constant throughout the electrolysis. However, as more reactant is consumed, the potential gradually increases to sustain the current flowing, possibly reaching values where undesired side reactions can occur (Figure 3.8). Therefore measures should be taken to ensure that the potential does not drift into such regions.

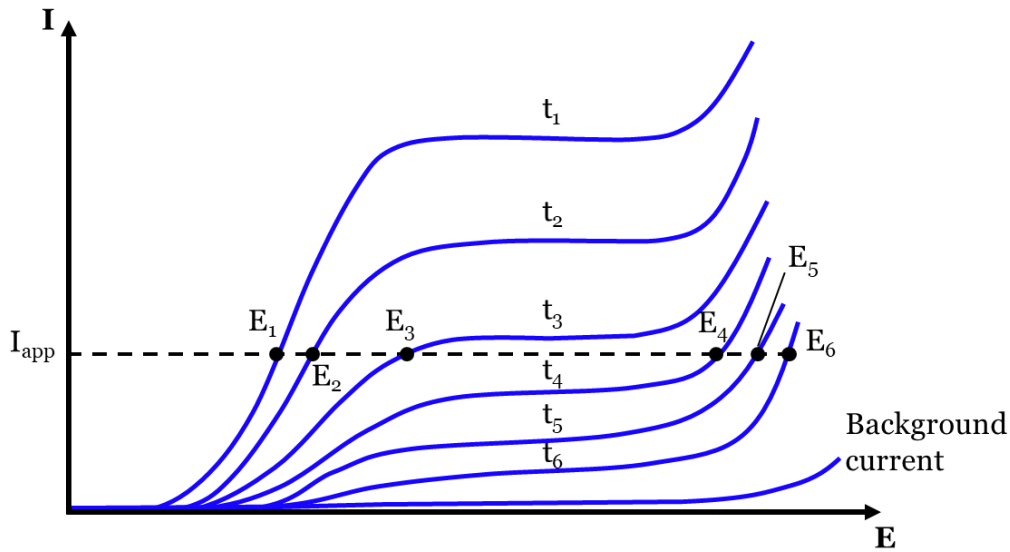


Figure 3.8: Current-potential curves at different times (increasing from t_1 to t_6) during a stirred bulk electrolysis with an applied constant current I_{app} . The potential to maintain I_{app} shifts from E_1 to E_6 as time passes. The largest shift between E_3 and E_4 occurs when I_{app} is equal to the limiting current. Redrawn from [40].

3.2 Cell and electrode design

3.2.1 Cell design

Cell setups for bulk electrolysis differ slightly from analytical setups because of the longer duration of the experiments and the often larger currents that are involved. In analytical electrochemical research, the cells and electrodes are designed for optimal response in analytical experiments. Consequently this usually means a small electrode surface area and a large solution volume, or at least a small ratio of the electrode surface area to the cell volume. These conditions minimize the effects of the uncompensated resistance and allow repeated experiments over an extended period of time without noticeable changes in concentration of reactants or products, so the semi-infinite boundary condition holds. However, for electrosynthetic experiments, it is often desired to convert large amounts of the reactant, hence the cells are adapted

appropriately and a large electrode surface area to cell volume is common. An aqueous solution is the standard electrolyte for electrochemical experiments, however, many organic electrosyntheses proceed in non-aqueous media due to the poor solubility of many organic compounds in water. Solvents as acetonitrile, dimethylformamide and dimethyl sulfoxide are common. When designing a cell for a specific process, the materials should always be checked for their compatibility with the solvent. Many different designs are possible depending on the specifics of the reaction. Specifications to take into consideration include: two or three electrode setup depending on the electrolysis method, divided or undivided cell, presence of a stirring device, temperature control, possibility to purge gas, etc. In any case, a good electrolysis cell should be designed to exhibit a uniform current distribution and a uniform mixing and mass transfer.

The possible separation of the electrodes is a common classification for cells, i.e. divided or undivided cells. If the reactions at both electrodes do not interfere or can be avoided by tuning the electrolyte and electrode material, an undivided cell is the most straight-forward setup. In some cases, so-called coupled reactions, the interaction of the products or intermediates generated at both electrodes is even desired to obtain the product of interest [47]. In an undivided cell the electrodes are placed as close to each other as possible to reduce cell resistance. Stirring can be introduced to increase mass transfer, however, because no laminar flow over the electrode surface is obtained, such setups are not considered hydrodynamic electrodes. Quite often it is necessary to separate both electrodes in compartments. For example to prevent the interaction of the products generated at both electrodes which can impede the desired reaction. Or to prevent the re-oxidation or -reduction of the target product at the auxiliary electrode. If the anolyte and catholyte are different, divided cells can be used to prevent intermixing and simplify the work-up. The compartments can be separated by diaphragms such as sintered glass or ceramics or by membranes. The separator can be tuned to allow passage of certain ions or species. Divided cells can lead to very complicated cell designs, however, mostly they

are of the H-type. Another not uncommon design is a concentric cell. An example of both is shown in Figure 3.9.

H-type cell



Concentric cell

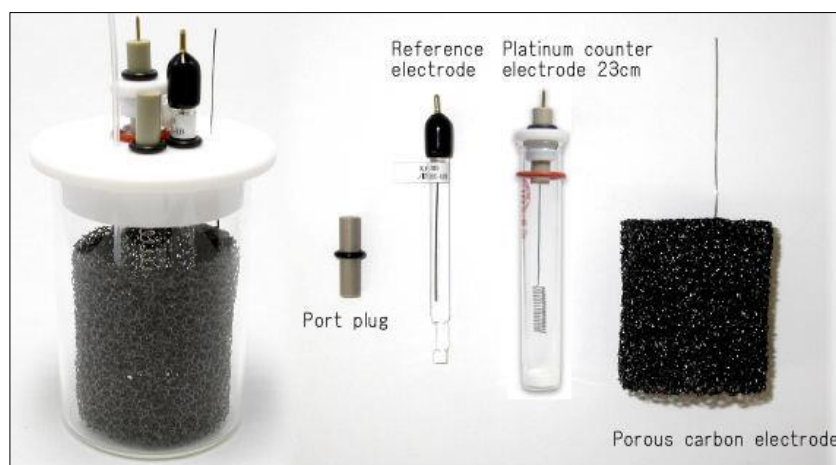


Figure 3.9: Top: example of an H-type cell. The clamp holds the two parts together between which the membrane is inserted. Models with an incorporated glass frit are also available. Bottom: Concentric bulk electrolysis cell. The counter electrode is positioned in the center in a concentric tube with a glass frit.

3.2.2 Batch operation versus continuous flow operation

Besides the classification in divided and undivided cells, another important parameter is the operation method which divides setups into batch cells or continuous flow cells. Batch operation is the simplest way and therefore mostly applied in laboratory scale electrosyntheses. Since the process conditions change during the experiment, reactions are often carried out until a certain amount of charge has passed to reach a given conversion. Constant process conditions can be realized in a flow through setup operating in steady state. Reactants are continuously replenished and products removed. Flow through cells entail a more complex setup and a higher cost however, since additional equipment is required, such as pumps. A batch cell can also operate in a flow through method. This is realized by adding reservoirs and recirculating the electrolyte solution, as is frequently seen in larger scale setups.

3.2.3 Electrodes for organic electrosynthesis

A component of major importance in a cell is the electrode as it has decisive influence on the success of the electrosynthesis. The electrode material and surface will influence many of the steps in an electrode reaction such as the adsorption and desorption, the electron transfer and the preceding and/or subsequent chemical reactions. On the one hand physical properties such as the size, geometry and surface morphology play a role, on the other hand the intrinsic properties of the material are important. Generally in bulk electrolysis an as large as possible surface area is desired. Complex electrode constructions such as three-dimensional electrodes and porous electrodes may improve space-time yield and mass transfer, however they may lead to an asymmetrical placement of working and auxiliary electrodes which leads to non-uniform potential distributions. Since the electrode reaction is dependent on the local potential gradient, this causes non-uniform current densities which has its influence on the reaction rate and selectivity and can cause undesired side reactions or ineffective use of the electrode area. To prevent this, often concentric cylindrical or parallel planar electrodes are used (Figure 3.10).

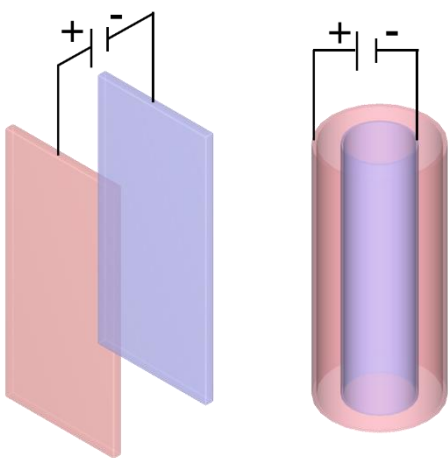


Figure 3.10: Representation of parallel planer electrodes (left) and concentric cylindrical electrodes (right).

Besides the geometrical aspect, the electrode material can have a tremendous effect on the outcome of the reaction and is a parameter to optimize for each reaction separately. General considerations include its physical and chemical stability in the environment of the system, its electrocatalytic activity (rate and selectivity) for the desired reaction and the cost and durability of the material. The last criterion might not be as important in laboratory scale setups, but becomes of increasing importance in larger scale setups and might be of decisive importance in commercial or industrial applications. An electrode may consist of a homogenous material, but it is not uncommon in electrocatalysis to combine materials to increase the catalytic effect. An overview of different materials, their properties and applications in organic electrochemistry can be found in [19] and [48] and in an extensive review by Walsh et al. [49].

3.2.3.2 Non-aqueous reference electrodes

Reference electrodes are a vital component in an electrochemical three electrode setup. The purpose is to provide a stable and reproducible voltage to which the potential of the working electrode can be controlled. As the potential of an electrode changes as current runs through it, a reference electrode ideally is currentless. The

redox couple chosen for the reference should have a high resistance against polarization. Usually a metal and a slightly soluble salt of this metal is applied. Common reference electrodes for aqueous solutions are the saturated calomel electrode (SCE, $\text{Hg}/\text{Hg}_2\text{Cl}_2$, $E = +242 \text{ mV}$ versus SHE (25°C)) and the silver chloride electrode ($\text{Ag}/\text{AgCl}/\text{saturated KCl}$, $E = +0.197 \text{ mV}$ versus SHE (25°C)). However, organic electrosyntheses often proceed in non-aqueous environments and although aqueous reference electrodes are applicable in solvents to a certain extent, there are some drawbacks. These include liquid junction potentials, possible contamination of the solvent solution by water and precipitates at the reference electrode frit causing noise or even failure of the reference electrode. For these applications it is advised to use a non-aqueous reference electrodes. A common type is based on the Ag/Ag^+ couple where the silver ion is provided by AgNO_3 , AgClO_4 or another silver salt which is soluble in the solvent of the system. These types of reference electrodes are less stable over time and should regularly be checked or refreshed. Besides these common types, reference electrodes can be tuned for solvent or ion compatibility for a specific reaction and many different variations are available [50].

3.3 Electrochemical techniques

3.3.1 Chronoamperometry

Chronoamperometry is a potentiostatic pulse method, i.e. the potential is stepped and the variation of the current in time is measured. In controlled conditions, analysis of the current response allows inferring information about the electrode reactions and their rates. When a potential step is applied in an unstirred solution containing an electroactive species from a potential where no reaction occurs to a potential in the mass-transfer-limited region, initially a large current is obtained due to the instantaneous step and the abundance of electroactive species at the electrode surface, after which the current decays over time. The current response consist of a faradaic current I_f which is due to the faradaic process (the electron transfer) and a

capacitive current I_c due to the charging of the electrochemical double layer. On a planar electrode, for a potential step experiment from a value where no electrolysis occurs to a value where there is mass-transfer-controlled electrolysis, there is semi-infinite linear diffusion and the current is:

$$I = nFAD \left(\frac{\partial c}{\partial x} \right)_0 \quad (3.18)$$

Solving Fick's second law for this case produces an equation that expresses the faradaic current-time response, better known as the Cottrell equation:

$$I(t) = I_d(t) = \frac{nFA\sqrt{D}c_b}{\sqrt{\pi t}} \quad (3.19)$$

The faradaic current decays proportionally to the inverse of \sqrt{t} while the capacitive current decays exponentially with time and the inverse of the cell constant $R_u C_{dl}$. In practice, the capacitive current usually decays to zero in the order of tens of microseconds to milliseconds and can be neglected for longer times. The square root time dependence of the current is a mark of diffusive control over the rate of electrolysis and this kind of dependence is also seen in other techniques (see section 3.3.2). Because the electroactive species gets depleted at the electrode surface natural convection sets in after a certain time and higher currents than those predicted by equation (3.19) can be observed. The timescale for convective interference depends on a number of parameters but in most fluid solvents macroscopic effects become noticeable from 20 seconds to 300 seconds [40,41]. When forced convection is applied, a steady state current is obtained which decreases as the bulk concentration of the electroactive species decreases over time. In this case, the technique is referred to as potentiostatic bulk electrolysis (see section 3.1.3.1).

3.3.1.1 Current efficiency and space-time yield

Important performance criteria that can be derived from the current response of the electrolysis are the current efficiency and space-time yield. The definition of the current efficiency is based on Faraday's law of electrolysis. He found that there was a quantitative relationship between the charge passed in a cell during an electrolysis and the amount of substance that had reacted [12]:

$$n = \frac{Q}{zF} \quad (3.20)$$

Where Q is the amount of charge passed, z is the number of electrons transferred per molecule and F is the Faraday constant ($96\ 485\ C\ mol^{-1}$) which is the electric charge of one mole of electrons. Since current is the change of charge in time, the charge can be found by integrating the current response over the total runtime of the electrolysis. The current efficiency Φ of a product i relates the moles of product i formed in the reaction to the moles of electrons consumed:

$$\Phi_i = \frac{m_i F z_i}{M_i Q_{exp}} = \frac{Q_{used\ in\ forming\ product}}{Q_{experimental}} = \frac{n_{experimental}}{n_{formed\ if\ \Phi_i=1}} \quad (3.21)$$

Where $Q_{experimental}$ is the amount of charge passed during the electrolysis. Thus, the current efficiency is the charge needed to form the amount of substance that the electrolysis yielded divided by the charge that was effectively used in the electrolysis, or from another point of view, the amount of product that was effectively formed divided by the amount of product that theoretically could have been formed. A current efficiency of 1 or 100% would mean that all charge was involved in the production of substance i . Current efficiencies lower than unity means either that back-reactions have occurred or more likely, that by-products were formed. Logically current efficiencies larger than 1 are impossible in pure electrochemical experiments, however they are sometimes observed when there are coupled chemical reactions.

Another important performance criterion which can be inferred from the current efficiency is the space-time yield ρ_{st} , which is the amount of product formed per unit of time and per reactor volume V_r :

$$\rho_{st} = \frac{1}{V_r} \frac{dm_i}{dt} \quad (3.22)$$

Filling in Faraday's law of electrolysis leads to:

$$\rho_{st} = \frac{M_i}{z_i F} \Phi_i A_s j \quad (3.23)$$

Where A_s is the specific electrode area $A_s = \frac{A}{V_r}$, which is the electrode surface area divided by the reactor volume (cm^2/cm^3). In a mass transfer controlled regime, the limiting current density j_L can be expressed as a function of the mean mass transfer coefficient k_m :

$$j_L = k_m n F C_b \quad (3.24)$$

Where C_b is the bulk concentration of the reactant. Inserting (3.24) in (3.23) gives:

$$\rho_{st} = v_i \Phi_i A_s k_m C_b \quad (3.25)$$

Where v_i is the stoichiometric ratio of the product i to the reactant. The space-time yield contains a design factor (A_s) and is proportional to the mass-transfer coefficient which can be increased by changing process conditions (stirring or agitating the solution). Equations (3.25) and (3.23) are important in the optimization of electrochemical cell design and are key formulas in electrochemical engineering.

3.3.1.2 Mass transfer measurements by the limiting-current technique

The rate of mass transfer can be measured by steady-state hydrodynamic voltammetry by a technique known as the limiting-current technique. This technique is well-established and an extensive discussion can be found in [51]. The technique is based on the principle of measuring the diffusion limiting current under well-known conditions from which the global mass transfer coefficient k_m can be derived. According to Faraday's law, the magnitude of the current density for an electrochemical reaction corresponds to:

$$j = nFJ \quad (3.26)$$

Inserting equation (3.26) in Fick's first law (equation (3.6)) and considering the Nernst model, the current density can be written as:

$$j = -nFD \frac{\partial C}{\partial x} = -nFD \frac{(C_b - C_0)}{\delta} \quad (3.27)$$

Where C_b is the bulk concentration and C_0 the concentration at the electrode surface. Since the global or mean mass transfer coefficient k_m is defined by:

$$J = k_m \Delta C = k_m (C_b - C_0) \quad (3.28)$$

And considering that $C_0 = 0$ when the reaction is diffusion-controlled, the limiting current I_L can be written as:

$$I_L = k_m nFAC_b \quad (3.29)$$

When employing equation (3.29) to determine the mass transfer coefficient, the results are influenced by several factors such as the state of the electrode, the change of bulk ion concentration in long channels and the thickness of the diffusion layer

[52,53]. Influences can be minimized by refreshing the electrolyte for each measurement and by careful preparation of the electrodes. The change of bulk ion concentration should be taken into account if necessary and the diffusion layer thickness should be calculated to verify the results.

3.3.2 Cyclic voltammetry

Cyclic voltammetry (CV) is one of the most widely used electrochemical techniques. It is often used for the initial electrochemical study of a system to diagnose electrode reactions and identify species in solutions. In cyclic voltammetry the potential is linearly swept from an initial potential E_i in one direction and after a certain time, or at a certain potential, the direction of the scan is reversed and then swept until a second switching potential is reached upon which the direction is reversed again. This cycle is often repeated several times and ended at a final potential E_f . The limit potentials between which the potential is swept can be called E_{min} and E_{max} and the initial direction of the scan can be positive or negative.

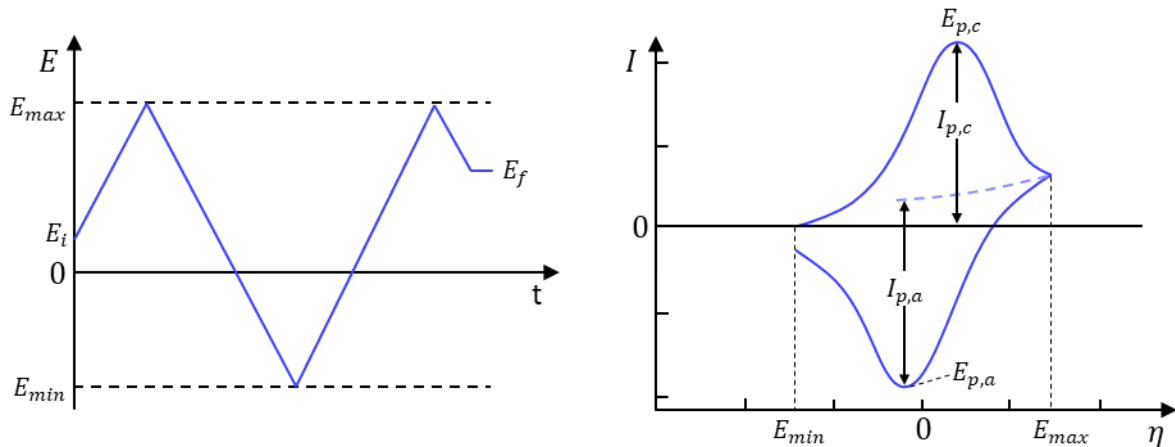


Figure 3.11: Left: variation of the applied potential with time in cyclic voltammetry, showing the initial potential E_i , switching potentials E_{min} and E_{max} and the final potential E_f . Right: Cyclic voltammogram of a reversible system, showing the peak potentials $E_{p,c}$ and $E_{p,a}$ and the corresponding peak currents $I_{p,c}$ and $I_{p,a}$.

The current response which is measured consists of a faradaic current I_f due to electron transfers and a capacitive current resulting from the charging of the double layer:

$$I = I_c + I_f = C_d \frac{dE}{dt} + I_f = \nu C_d + I_f \quad (3.30)$$

Where ν is the scan rate. As equation (3.30) shows, the capacitive current is proportional to the scan rate, which means that its contribution increases with increasing scan rate. An expression for the total current requires thorough mathematical labor and was obtained by John Randles and Augustin Sevcik in 1948:

$$I = -nFA[O]_\infty \sqrt{(\pi D_O \sigma)} \chi(\sigma t) \quad (3.31)$$

Where $\sigma = \frac{nF}{RT} \nu$

$\chi(\sigma t)$ is a dimensionless current function that gives the relationship between the current at any point on the curve and the relevant variables and can be seen as a normalized current for a reversible reaction. Values of χ have been calculated and tabulated for different electrode types and can be used to compare the shapes of experimental and simulated curves [41,44]. Equation (3.31) shows that the total current is proportional to $\sqrt{\nu}$. This property indicates diffusion control and is analogous to the \sqrt{t} dependency of the current in section 3.3.1.

From equations (3.30) and (3.31) it is obvious that the sweep rate or scan rate has a direct influence on the peak current. In order to extract kinetic information the contribution of the capacitive current must be subtracted. This is one of the reasons why usually other techniques such as linear sweep voltammetry are used to obtain kinetic data. The peak potential however, is independent of ν and tells something about the electroactive species in solution, as does the number of peaks, their shape and relative position. For a reversible reaction the anodic and coupled cathodic peak

(resulting from the reversed scan of the anodic peak) are well-defined and have a peak-to-peak separation deviating slightly from the mathematical calculation due to uncompensated resistance effects. In general for (electrochemically) quasi-reversible and irreversible systems, the peaks are broader and lower and shifted towards more negative (for a reduction) or more positive (for an oxidation) potentials, giving larger peak-to-peak separations. The appearance of electrochemically reversibility however, is also dependent on the scan rate as reactions that seem reversible at slow sweep rates can be quasi-reversible or even irreversible at high sweep rates. Voltammograms of systems with a coupled chemical reaction might not display a peak on the reverse scan due to the products of the initial scan being converted to an electrochemically inactive species. Likewise additional peaks may arise depending on the electrochemical activity of the formed products.

3.4 Electron paramagnetic resonance

Electron paramagnetic resonance (EPR) is a magnetic resonance technique that is used for the study of systems containing an unpaired electron. An example of such a system is an organic radical. This makes the technique particularly useful for the study of electrosynthetic processes as organic radicals are commonly found as intermediates. The paramagnetic property implies that the system is susceptible to magnetic fields. Exploiting this property forms the basis of the experimental technique, which is explained below. This section is based on references [54–60] and gives an introduction to the technique and its application in electrochemistry. For a more extensive discussion of the theory, relevant equipment and many examples of its applications in electrochemical research, the reader is referred to those references.

3.4.1 Basics of EPR

Electrons have an intrinsic angular momentum property called “spin”, indicated with a quantum number called the electron-spin quantum number S with a value $n/2$

where n is any integer ≥ 0 and equal to 1 for an electron. For a visual interpretation an electron and its spin can be thought of as a little bar magnet rotating around its axis:



Figure 3.12: Visual representation of a free unpaired electron in space. Its spin is represented by the black arrow, the resulting magnetic moment by the blue arrow pointing up.

Because the electron is charged this generates a magnetic field with magnetic moment $\vec{\mu}_s$, proportional to the electron-spin vector \vec{S} :

$$\vec{\mu}_s = \gamma \vec{S} \quad (3.32)$$

The length or magnitude of \vec{S} is quantized in units of the reduced plank constant $\hbar = \frac{h}{2\pi}$: $|\vec{S}| = \hbar \sqrt{S(S+1)}$, γ is the gyromagnetic ratio which for a system is the ratio of its magnetic moment to its angular momentum and is given by:

$$\gamma = \frac{q}{2m} \quad (3.33)$$

Where q is its charge and m is its mass. Or for an isolated electron:

$$\gamma = \frac{|-e|}{2m_e} g_e \quad (3.34)$$

Where g_e is the electron g -factor, a dimensionless factor that corrects the magnetic moment of the quantum electron from the classical result as the electron-spin cannot be attributed to mass distributed identically to the charge. g_e is known to an extraordinary precision and is roughly equal to 2.002319 [61]. Equation (3.34) is

commonly expressed in terms of the Bohr magneton μ_B which expresses the magnetic moment of an electron:

$$\mu_B = \frac{e\hbar}{2m_e} \quad (3.35)$$

Inserting equation (3.35) in equation (3.34) gives:

$$\gamma = \frac{\mu_B}{\hbar} g_e \quad (3.36)$$

So equation (3.32) can be written as:

$$\vec{\mu}_s = -g_e \frac{\mu_B}{\hbar} \vec{S} \quad (3.37)$$

With $|\vec{\mu}_s| = g_e \mu_B \sqrt{S(S+1)}$. Note that due to the negative charge of the electron the direction of $\vec{\mu}_s$ is opposite to that of \vec{S} .

In presence of an external magnetic field \vec{B}_0 a second (magnetic) quantum number comes into effect, also called the magnetic electron-spin quantum number or the spin angular momentum quantum number m_s which takes on values in integral steps between $+S$ and $-S$, thus giving $2S + 1$ values. Visually the spin can be represented by the spin angular momentum vector \vec{S} precessing about \vec{B}_0 along an arbitrarily chosen axis, defined as the z-axis (Figure 3.13). The time-averaged vector can either be aligned with or aligned against the magnetic field, labeled by the projection of \vec{S} on the direction of the magnetic field. The spin vector and the magnetic moment have an opposite direction, so for the spin up state \vec{S} is aligned with \vec{B}_0 and $\vec{\mu}_s$ is aligned against the direction of \vec{B}_0 . m_s takes the values of $\pm S$ so an electron has two possible states: $m_s = +\frac{1}{2}$ and $m_s = -\frac{1}{2}$ respectively denoted as spin up or α-spin and spin down or β-spin. In the absence of a magnetic field, both states have the same energy and the electron has an equal probability to be in either state.

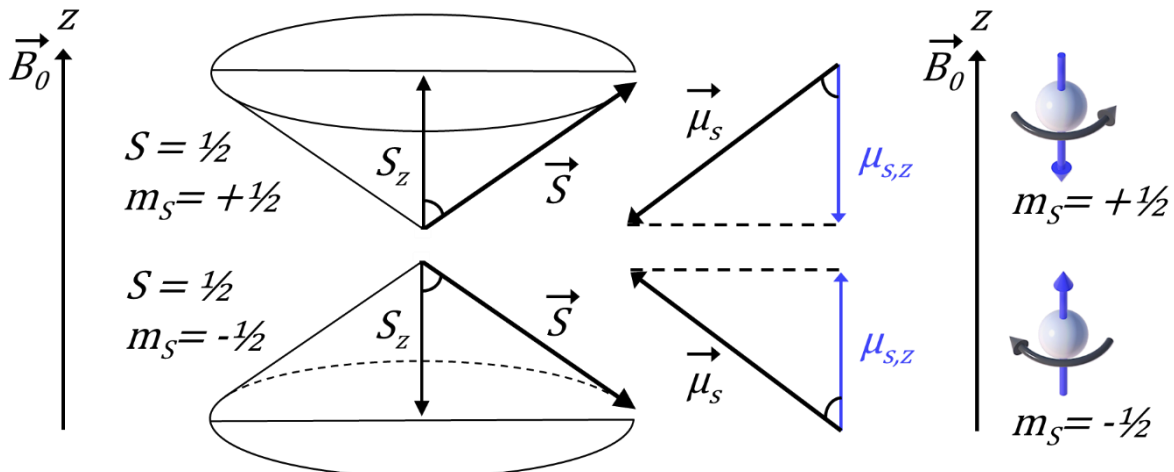


Figure 3.13: Left: Precession of the spin vector \vec{S} about the magnetic field \vec{B}_0 . Note that the direction of the $\vec{\mu}_s$ is opposite to that of \vec{S} [55]. Right: Visual representation of the minimum and maximum energy orientations of $\vec{\mu}_s$ with respect to the magnetic field \vec{B}_0 .

The interaction energy of the electron magnetic moment with B is given by the negative value of their scalar product. Since the z-axis is taken to be aligned along the axis of the external magnetic field this results in:

$$E = \vec{\mu}_s \cdot \vec{B}_0 = \mu_{s,z} \cdot B_0 = g_e \mu_B m_s B_0 \quad (3.38)$$

Where $\mu_{s,z} = -g_e \mu_B m_s$ is the z-component of the magnetic moment which is related to the m_s spin states, resulting in two different energy levels for the electron in the external magnetic field, corresponding to the two spin states:

$$E_+ = +\frac{1}{2} g_e \mu_B B_0 \quad (3.39)$$

$$E_- = -\frac{1}{2} g_e \mu_B B_0 \quad (3.40)$$

Visually represented by:

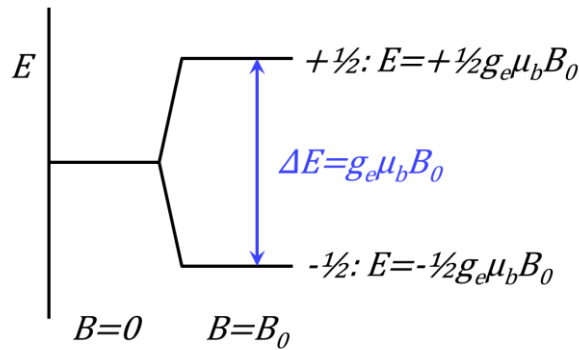


Figure 3.14: Electron Zeeman splitting as a function of the magnetic field \vec{B}_0 and the corresponding spin state energies.

This splitting into levels is called the electron Zeeman splitting and the two states of different energy are referred to as the electron Zeeman levels which are proportional to B , the strength of the applied external magnetic field \vec{B}_0 . The unpaired electron will be in the state of lowest energy when the electron magnetic moment is aligned with the applied magnetic field (spin down) and the state of highest energy when $\vec{\mu}_s$ is aligned against the field (spin up). In EPR spectroscopy a sample is irradiated with electromagnetic radiation ($h\nu$) in the presence of an external field. This radiation may induce transitions between the two levels (spin inversion $\alpha \leftarrow \beta$) since they comply with the selection rule to conserve angular momentum $\Delta m_s = \pm 1$, provided that the direction of the magnetic field associated with this radiation is perpendicular to that of the external magnetic field and that the energy of the radiation is equal to that of the Zeeman splitting:

$$h\nu = \Delta E = g_e \mu_B B_0 \quad (3.41)$$

This relation is known as the resonance condition and the frequency at which these transitions occur is called the resonance frequency. Rearranging equation (3.41) gives:

$$\nu = g_e \frac{\mu_B}{\hbar} B_0 \quad (3.42)$$

Since $\omega = 2\pi\nu$

$$\omega = g_e \frac{\mu_B}{\hbar} B_0 = 2\pi\gamma_e B_0 \quad (3.43)$$

ω is the angular frequency of the spin \vec{S} precessing about \vec{B}_0 at resonance, also known as the Larmor frequency. An electron in isolation only has its intrinsic spin angular momentum \vec{S} , but an electron in a molecule also possesses some orbital angular momentum \vec{L} . For an s-orbital electron in ground state the orbital angular momentum is (approximately) zero, however, due to interaction between the ground state and excited states there is a non-zero contribution to the total angular momentum. This is called spin-orbit coupling. In practice this contribution is assumed proportional to \vec{S} and both terms are combined and g is introduced as an effective g -factor to balance the contribution:

$$h\nu = g\mu_B B_0 \quad (3.44)$$

The additional angular momentum can also be seen from the point of view of the electron. The electron experiences the nucleus as an orbiting positive charge causing a local magnetic field $\Delta\mu$ that also affects the electron. And equation (3.44) could be written as:

$$h\nu = g_e\mu_B(B_0 + \Delta B) \quad (3.45)$$

Since only the spectrometer value of B_0 is known, this is usually written in terms of g :

$$h\nu = (g_e + \Delta g)\mu_B B_0 \quad (3.46)$$

Equation (3.44) implies that there are infinite pairs of ν and B that fit this relationship. Therefore the magnetic field of resonance is not unique to the system under study as spectra can be acquired at different frequencies. Δg however (or for simplicity g), is a unique feature that contains information on the interaction of the electron and the electronic structure of the molecule. The value of g can be taken as a fingerprint of the molecule.

3.4.2 Acquisition of a spectrum and interpretation of the data

In an EPR experiment, a sample is radiated with electromagnetic radiation (microwaves) and when the resonance condition is fulfilled, absorption of the incident radiation is observed (Figure 3.15).

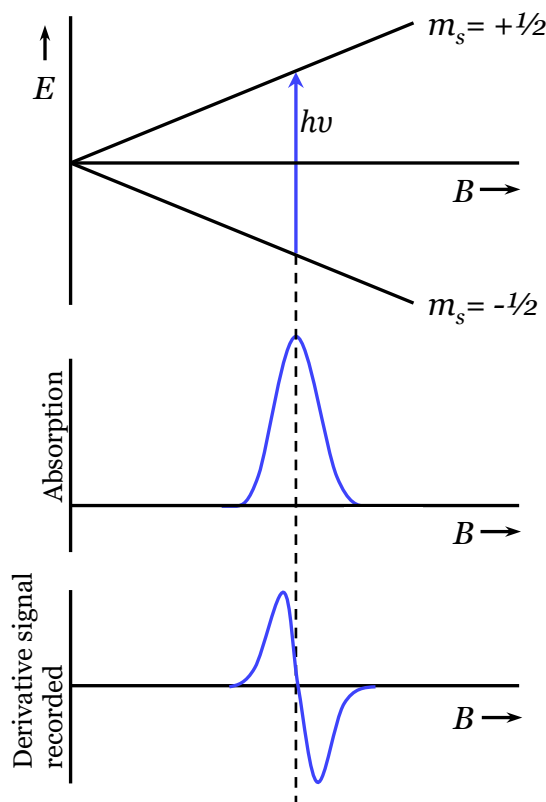


Figure 3.15: (a) Energy-level diagram of an unpaired electron in a magnetic field.
(b) Absorption signal when the resonance condition is fulfilled.
(c) Resulting first derivative of the absorption curve, recorded by the detector. [56]

The resonance condition can be accomplished by varying either ν or B . Because of technical reasons, in practice it is much easier to fix the frequency to a set value and sweep the magnetic field.

To improve the sensitivity a phase-sensitive detector is used and a small additional oscillating magnetic field B_m is applied to the external field B in the same direction of the main field (Figure 3.16). As a result, the detector output also oscillates. The detector only detects output signals with the same modulation frequency as applied, suppressing signals arising from noise and giving a greater signal-to-noise ratios. If the magnitude of B_m is small relative to the line width, the detector signal peak-to-peak value approximates the slope of the absorption curve and thus the output of the detector is the first derivative of the absorption curve.

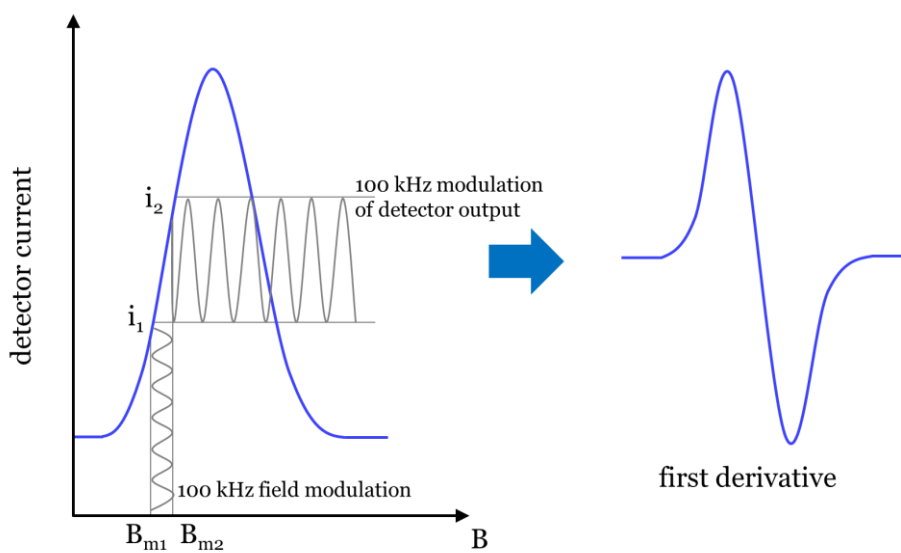


Figure 3.16: Schematic representation of the phase sensitive detection. As the magnetic field is swept a small oscillating magnetic field is applied (commonly 100 KHz) in the same direction as the main field. As the modulation B_m increases from B_{m1} to B_{m2} the detector output increases from i_1 to i_2 . If the magnitude of B_m is sufficiently small relative to the line width, the detector current's peak-to-peak value approximates the slope of the absorption curve and consequently, the first derivative of the absorption curve is obtained [60].

Important information about the system under study can be obtained by interpreting key features of the spectrum such as the line separation, the number of lines, the linewidth and the intensity. The position is determined by the *g*-factor, the number of lines is dictated by the nuclear spin \vec{I} of the interacting nuclei and the line separation is determined by the hyperfine interactions. These will be briefly discussed below. The linewidth and intensity have numerous factors influencing both and discussion of these of these is out of the scope of this dissertation. The interested reader is referred to the references above.

3.4.2.2 *g*-factor

As stated above, one important value that can be derived is the *g*-factor or *g* value which can be calculated from ν and \vec{B}_0 . For an isolated electron which has $g_e = 2.002319$ we can calculate from (3.44) that for a frequency of ca. 9500 MHz which is typical for X-band, the field strength B_0 at resonance is ca. 340 mT. In molecules generally and organic molecules particularly, the orbital contribution to the total angular momentum is quenched (lost) because the existence of covalent bonds lift the degeneracy of the orbitals. The effective *g*-factor will be close to the “spin-only” g_e , slightly altered via spin-orbit coupling. Hence, sweeping the field of resonance that would correspond to g_e is a good starting point to detect organic radicals.

3.4.2.3 Nuclear spin and hyperfine interaction

The interactions of the spins of unpaired electrons and magnetic nuclei of a paramagnetic organic molecule in a magnetic field B can be represented by:

$$g_e \mu_B \vec{S} \cdot \vec{B} + g_n \mu_n \vec{I} \cdot \vec{B} + \vec{S} \cdot \vec{D} \cdot \vec{S} + \vec{S} \cdot \hat{\vec{A}} \cdot \vec{I} + \vec{I} \cdot \hat{\vec{Q}} \cdot \vec{I} \quad (3.47)$$

From left to right these terms represent the electron Zeeman interaction, the nuclear Zeeman interaction, the fine splitting which is relevant for species with more than one unpaired electron, the hyperfine splitting which is due to electron-nuclear

interaction and spin-spin coupling due to nuclear-nuclear interactions. $|\vec{\mu}_n|$ is about three orders of magnitude smaller than $|\vec{\mu}_e|$ which is reflected in the relative sizes of these terms. For species with more than one unpaired electron the terms in $\vec{S} \cdot \vec{B}$, $\vec{S} \cdot \vec{S}$, $\vec{I} \cdot \vec{B}$ and $\vec{S} \cdot \vec{I}$ have to be considered and for radicals $\vec{S} \cdot \vec{B}$, $\vec{I} \cdot \vec{B}$ and $\vec{S} \cdot \vec{I}$ are sufficient.

The electron Zeeman interaction is much larger than the hyperfine interaction and therefore it can be treated as a perturbation of the larger Zeeman interaction (this is called the strong-field approximation). The energies associated with the different states are summarized as:

$$E = g_e \mu_B m_S B_0 - g_n \mu_n m_I B_0 + a m_S m_I \quad (3.48)$$

Where a is called the hyperfine coupling constant. Since there are $2I + 1$ possible values of m_I , the nuclear Zeeman interaction term splits the Zeeman interaction into $2I + 1$ lines (Figure 3.17) and the hyperfine interaction causes a perturbation in the associated energy levels. The separation between the two lines is the hyperfine splitting which is field-independent and a characteristic of the nucleus-electron interaction given by a . The selection rules $\Delta m_S = \pm 1$ and $\Delta m_I = 0$ dictate the allowed transitions which are shown by the blue arrows.

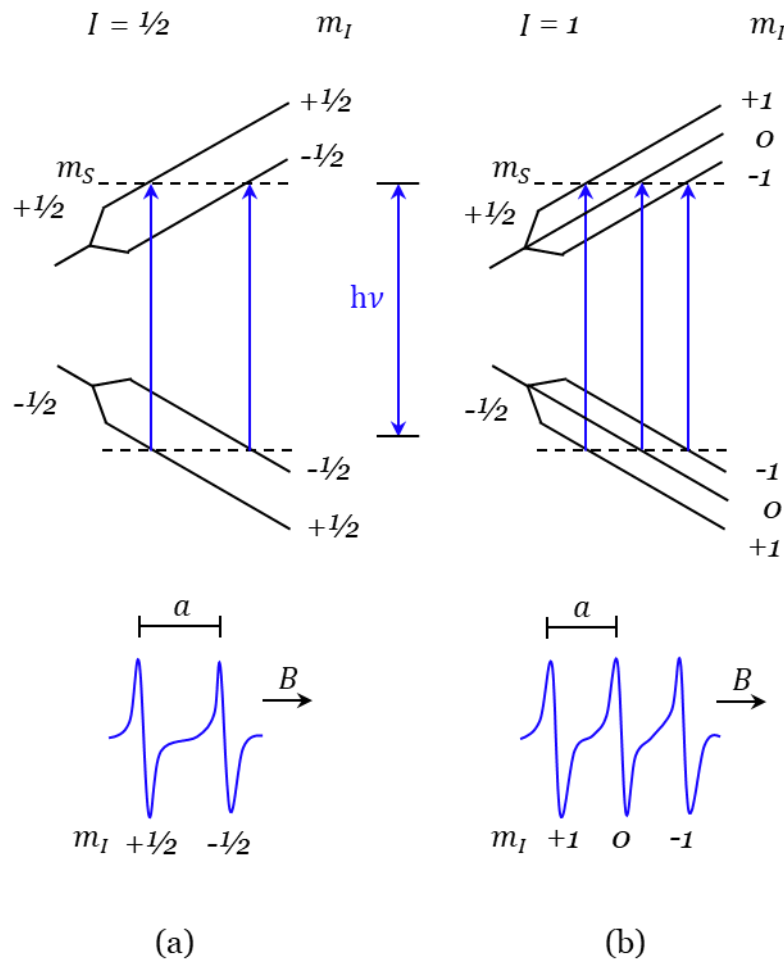


Figure 3.17: Splitting of an EPR signal by hyperfine interactions between the unpaired electron and a nucleus with spin quantum number (a) $I = 1/2$ and (b) $I = 1$ and the anticipated EPR spectra for both cases [57].

For a radical containing more than one nucleus which the electron interacts with, additional $a m_I$ terms arise in equation (3.48). For example for coupling to two nuclei equation (3.48) becomes:

$$E = m_S(g_e \mu_B B + a_1 m_{I1} + a_2 m_{I2}) - g_n \mu_n m_I B_0 \quad (3.49)$$

Where m_{I1} and m_{I2} are the nuclear spin quantum numbers of the two nuclei and a_1 and a_2 the corresponding hyperfine coupling constants. If $a_1 = a_2$ the nuclei are

referred to as being equivalent. Hyperfine interactions can make an EPR spectrum look very complex but they unveil important information about the detected species.

3.4.3 Combined EPR and electrochemistry

The ability of EPR to detect and identify radicals make it a technique particularly useful to combine with electrochemical research to study and elucidate reaction mechanisms. This potential has long been recognized and the first combined EPR and electrochemical experiments were reported by Ingram et al. in Nature over half a century ago [62]. In that work, the combination of the two techniques was not inspired by interesting (organic) electrochemical reactions, but rather by the convenient way of generating radicals by means of electrolysis. The electrolysis was performed separately and samples were taken, frozen and transferred to an EPR spectrometer. The radicals could be detected, but the solid-state spectra precluded any conclusions being drawn about their nature. It was not for long until Maki and Geske first demonstrated the potential of the combined techniques by performing the electrolysis *in situ*, i.e. in the spectrometer cavity [63–65]. The two different approaches of Ingram et al. and Maki and Geske can respectively be referred to as external generation and internal generation. The latter is in older literature often referred to by the acronym SEESR which stands for Simultaneous Electrochemical Electron Spin Resonance spectroscopy. Electron spin resonance (ESR) and EPR are equivalent terms¹ and nowadays the same technique is often referred to as *in situ* EPR spectroelectrochemical experiments. The difference between *in situ* and *ex situ* methods originally existed due to the severely limiting constraints of *in situ* cells and the sacrifice of well-defined electrochemistry that came with it. However, decades of research and development since the first experiments have led to significant progression and contemporary *in situ* cell designs now show satisfactory electrochemical performance. Although in specific situations *ex-situ* generation might have its advantages, the requirement of long-term stability of the radicals

¹ Historically there was a semantic difference between both, but in recent times the terms are considered equivalent with a slight preference for the more general term EPR.

because of the significant transfer time of the electrochemical cell to the spectrometer have largely made the technique obsolete. The measurements reported in this dissertation were all performed *in situ*. The details of the cell and electrode designs that were used can be found in Chapter 9 were the construction of a suitable platform is discussed.

3.4.3.1 Instrumentation

This section will briefly discuss the instrumentation of an EPR spectrometer relevant to the design of electrochemical cells and electrodes. An extensive explanation of all components and features can be found in the literature referenced on page 55. Figure 3.18 shows a schematic illustration of an EPR spectrometer setup.

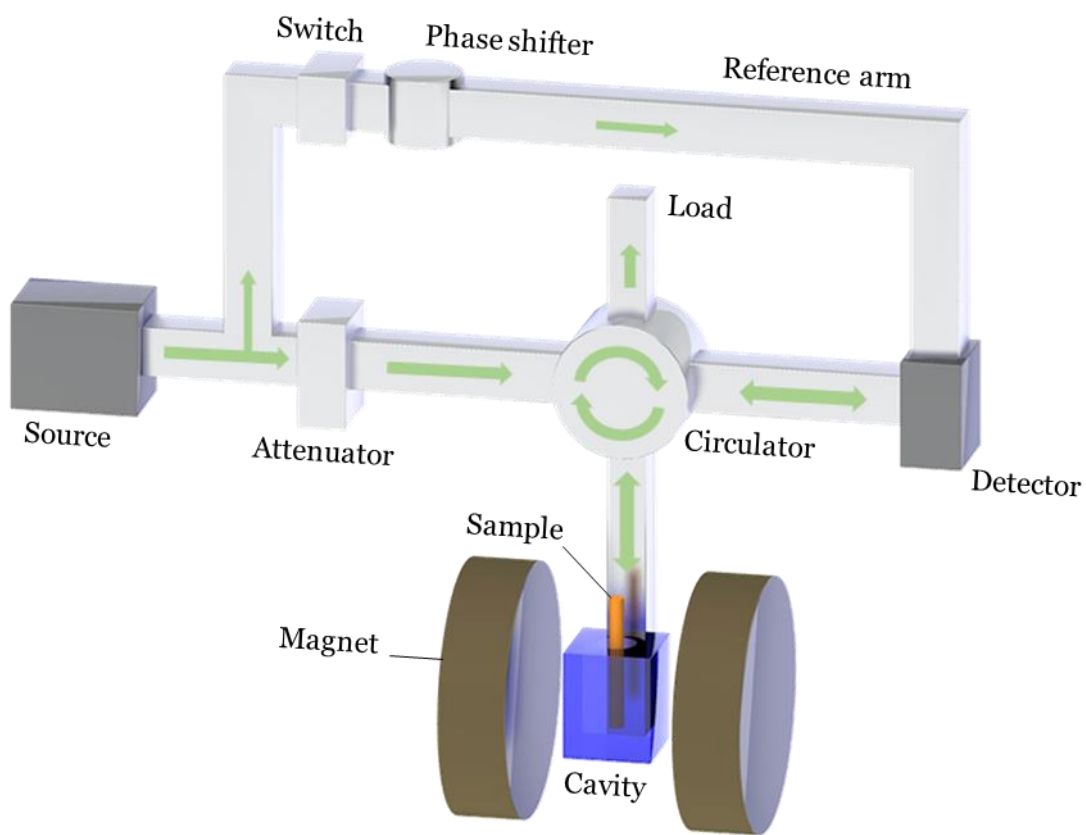


Figure 3.18: Schematic illustration of an EPR spectrometer. The flow of the microwaves is represented by the green arrows. Redrawn from [59].

The microwave bridge generates microwaves which are used to radiate the sample. Because of the absorption by water, microwaves are produced at small frequency windows called bands. The measurements in this dissertation were conducted at X-band which corresponds to a frequency of ca. 10 GHz. The microwaves are directed from the bridge through a wave guide towards the cavity or resonator in which the sample under study is situated. The cavity is positioned between two magnets which are used to generate the magnetic field necessary for the measurements. Simply said the cavity is a metal box which resonates the microwaves. There are several different cavities available but the by far most common, also the one most often reported in literature on combined EPR and electrochemical measurements, is the rectangular TE_{102} cavity, shown in Figure 3.19.

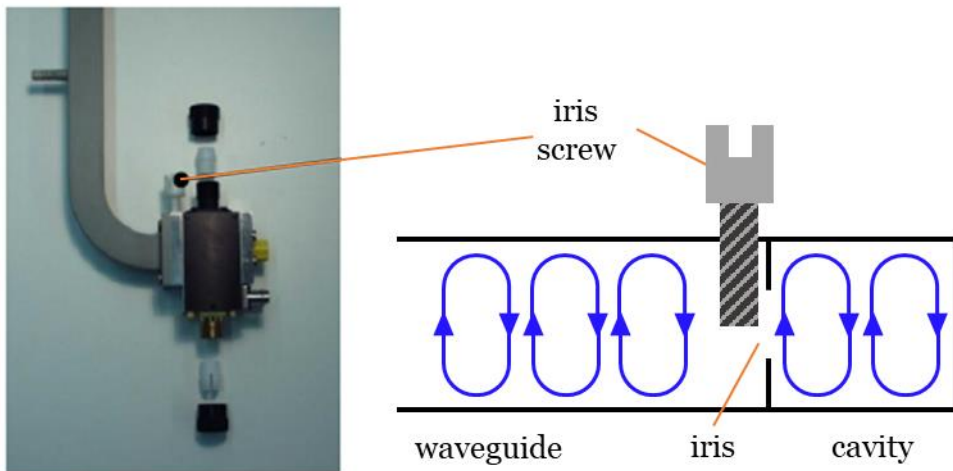


Figure 3.19: Left: part of the waveguide and a TE_{102} cavity. Right: schematic illustration of the microwaves entering the cavity. The iris screw is used to adjust the iris to achieve critical coupling [66].

The microwaves enter the cavity through a small opening called the iris. The size of the iris can be adjusted and controls the amount of microwaves entering the cavity and the amount that will be reflected. Finely adjusting this opening will lead to a unique position where the cavity is critically coupled. In this situation standing waves inside the cavity are realized so that all microwaves enter the cavity and none are

reflected. During the experiment, when the resonance condition is fulfilled (see section 3.4.1), the paramagnetic species absorbs the microwave energy, changing the coupling. As a result the microwave is no longer critically coupled and microwaves will be reflected back, resulting in an EPR signal. In combined *in situ* electrochemical and EPR measurements, the electrochemical cell resides in the cavity which imposes strict limitations on its geometry and dimensions. These requirements and relevant designs are discussed more in detail in Chapter 9 where a setup is constructed for combined *in situ* measurements.

Part II

Engineering approach for an electrochemical study towards industrial implementation

The electrosynthetic aldol reaction of
acetone

CHAPTER 4

Literature review for the conversion of the aldol reaction to an electrosynthetic flow process

THE PROBLEMS OF THE TRADITIONAL CHEMICALLY PERFORMED ALDOL REACTION ARE EXPLAINED BY THE HAND OF THE CASE STUDY ALDOL REACTION OF ACETONE. ADDITIONALLY THE STATE-OF-THE-ART FOR THE CASE STUDY IS PROVIDED. SUBSEQUENTLY A CONCISE LITERATURE REVIEW OF FLOW CHEMISTRY AND MICROREACTORS RELEVANT TO ELECTROCHEMICAL SYNTHESIS IS GIVEN. FINALLY, THE SCATTERED AND SCARCE INFORMATION IN LITERATURE ON THE MECHANISM OF THE ELECTROCHEMICAL ALDOL REACTION IS COMPILED AND THE PROPOSED MECHANISMS ARE LISTED.

4.1 Introduction

The aldol reaction is a useful reaction in organic chemistry to construct carbon-carbon bonds [67,68]. It is a reaction in which an enolizable carbonyl compound reacts with another carbonyl compound that is an aldehyde or ketone to form a β -hydroxycarbonyl compound (Figure 4.1). The resulting product has both an *aldehyde* and an *alcohol* functionality, hence the name *aldol*. The β -hydroxycarbonyl can undergo an elimination of water to form a α,β -unsaturated carbonyl compound. This first step in which the aldol is formed is called the “aldol addition” whereas the reaction that includes the elimination process is denoted “aldol condensation”. In the aldol reaction, the enolizable carbonyl compound has at least one acidic proton in its α -position which is abstracted in the first step, rendering the α -carbon nucleophilic. The α -carbon then attacks an unreacted carbonyl compound which is slightly electrophilic at the carbonyl carbon, initiating the aldol reaction. The classic aldol reaction is a reversible reaction which proceeds under thermodynamic control and is found to be slightly exergonic [69,70]. Generally, the equilibrium is located slightly towards the reactant side in the aldol reaction of two aldehydes and slightly to the product side for ketones. The traditional aldol reaction is performed in protic solvents and is acid or base-mediated. A more detailed description of the mechanism and a comparison to the proposed electrochemical mechanism can be found in Chapter 7.

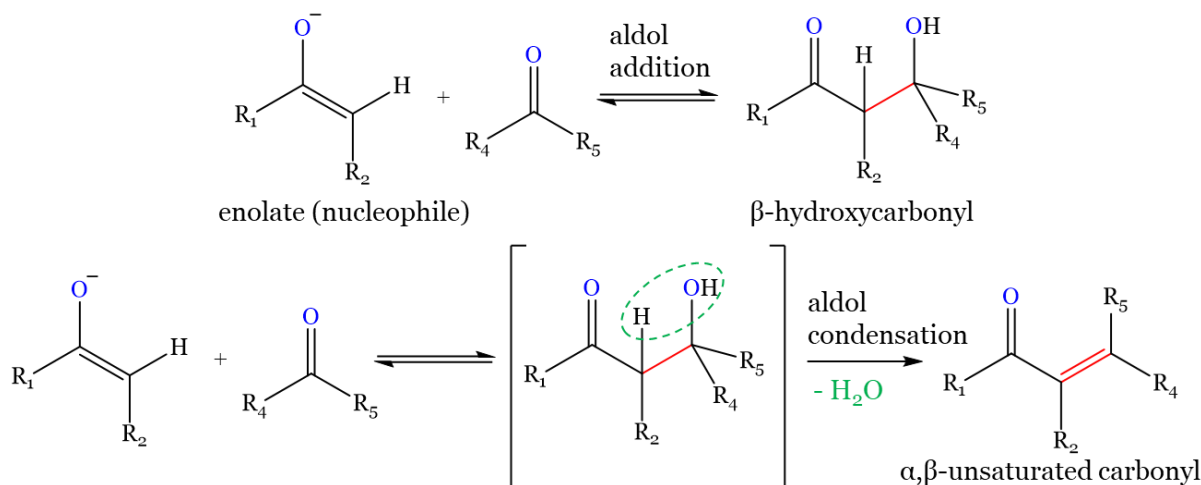


Figure 4.1: Base mediated aldol addition and aldol condensation of an enolate (aldehyde enolate if R₁ = H, ketone enolate if R₁ ≠ H) and a carbonyl compound (aldehyde if R₃ or R₄ = H, ketone if R₃ and R₄ ≠ H). The red bond depicts the resulting carbon-carbon bond.

4.2 The aldol reaction of acetone to diacetone alcohol

Acetone is the starting material to a broad range of useful products and intermediates [71,72]. The aldol condensation of acetone initially produces 4-hydroxy-4-methyl-pentan-2-one, commonly known as diacetone alcohol (DAA) (see Figure 4.3). Diacetone alcohol is an industrially useful and important product with a number of industrial applications. It is used as a solvent in varnishes, paints, cellulose acetate lacquer, thinners and in cleaning compounds and is considered to be an environmentally friendly alternative to other materials such as acetone due to its much lower volatility [73]. It is also an intermediate to other industrially important products. The dehydration of diacetone alcohol yields mesityl oxide (MO), a useful compound with various applications but primarily it is the precursor of methyl isobutyl ketone (MIBK), a popular solvent used mainly in the paint and coating industry [74] and the largest volume aldol reaction product of acetone [72].

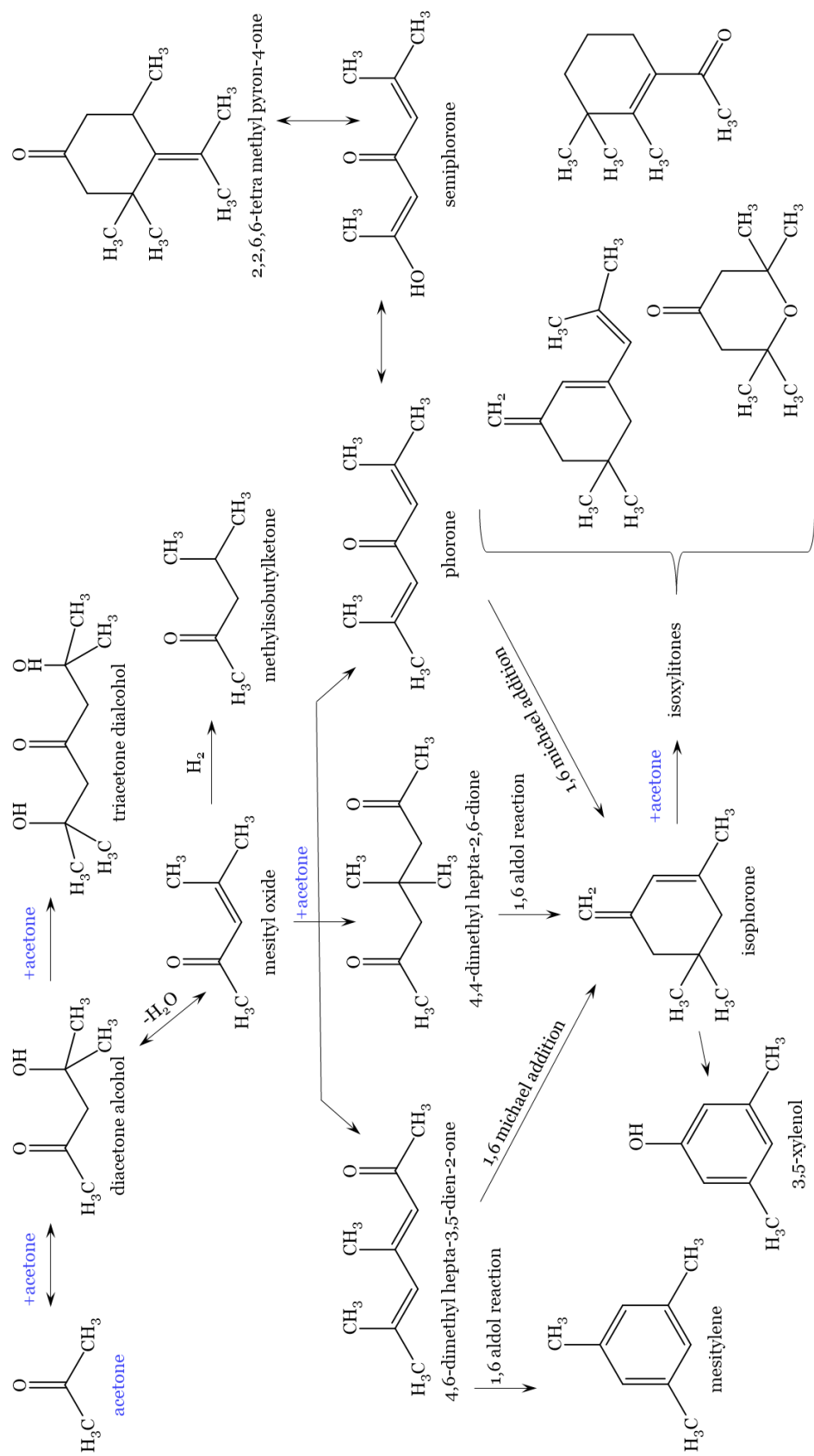


Figure 4.2: Scheme of the pathways in the self-condensation of acetone [71].

Heavier products from acetone such as phorone, isophorone and 3,5-xylenol are formed by self-condensation or cross-condensation between the same or different ketones that are formed in the reaction and also find many industrial applications (Figure 4.2). These possible further condensation reactions give rise to selectivity problems as they make it difficult to promote the desired pathway. Industrially, many of these products are formed during the same process where intense separation processes are used to extract the product of interest. Depending on what product is targeted the products of a lower condensation level are recycled to further react to the target product. Products that have undergone condensation beyond the target product are recovered as much as possible by converting them to smaller molecules again or valorized if recovery is not possible. To optimize the yield of the desired product DAA, further condensation reactions have to be prevented without shifting the equilibrium towards the dehydration product mesityl oxide.

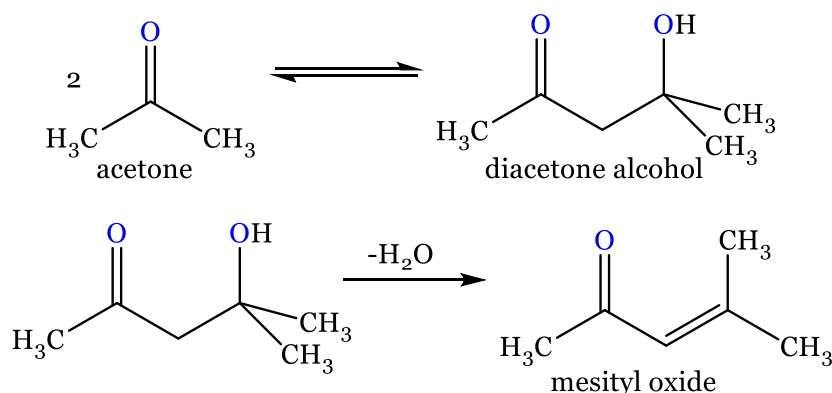


Figure 4.3: Self-aldol addition of acetone to diacetone alcohol and subsequent dehydration to mesityl oxide to complete the aldol condensation.

Conventionally, the aldol condensation of acetone is conducted using a homogeneous base catalyst such as NaOH and KOH [72,75]. Some major drawbacks are associated with the homogeneity and basic nature of the catalysts. The strong bases require specific measures to prevent corrosion problems which leads to high capital costs. The homogeneity of the catalyst requires intense purification afterwards in which the catalyst often is destroyed. In the conventional process, phosphoric acid is added to

neutralize the catalyst and stabilize DAA, after which DAA is recovered by evaporation and stripping of the acetone, which is then recycled [71,76]. This neutralization step must be accurately controlled as an excess of acid causes facile dehydration of DAA to MO [77]. The neutralization process and subsequent purification steps by distillation entail a high cost and produce large amounts of waste streams. It has been estimated for these compounds that product purification, recovery and waste treatment account for 30 % of the selling price [78].

Because of the disadvantages inherent to the homogeneous catalysts, such as the salt waste generated by the neutralization and the corrosion problems, heterogeneous systems offer a viable alternative. Solid acid-base catalysts are becoming increasingly important in chemical and life science industry as they have many advantages over homogeneous liquid acid-base catalysts [78,79]. Separation of the product stream is much easier, reducing purification costs and increasing catalyst life. They are more environmentally friendly than the homogeneous catalysts and are non-corrosive, making safe handling and disposal easier. Zeolites, oxides and ionic exchange resins make up about 80 % of the types of solid acid-base catalysts used in industrial processes while dehydration and condensation reactions most often use these types of catalysts [79]. Some commercial installations for the production of DAA use fixed-bed reactors employing solid alkaline catalysts such as $\text{Ba}(\text{OH})_2$ and $\text{Ca}(\text{OH})_2$. However, self-condensation of acetone to diacetone alcohol is a reversible exothermic reaction which is equilibrium limited with the equilibrium strongly favoring acetone (see Table 4.1). To obtain a reasonable yield, commercial operations are conducted at 10-20 °C with typical residence times of 20-60 minutes. A lower temperature has a favorable effect on the equilibrium of the reaction, but results in slower kinetics, giving a maximum possible conversion of acetone of 15 m% per pass at 15 °C [76]. Furthermore, many of the catalysts are susceptible to alkali dissolution and end up in the product stream.

Table 4.1: Equilibrium conversions of acetone to DAA.

Temperature (°C)	0	10	20	30	45	54
Conversion (wt%)	23.1	16.9	12.1	9.1	5.6	4.3

0–30 °C: Data from Craven [80].

45 & 54 °C: Data from Podrebarac [81].

To meet the requirements of the toughening environmental regulations and economical demands of the industry, lots of attention has been directed towards improving the catalyst of the reaction to increase the yield of diacetone alcohol or mesityl oxide. Different types of basic catalysts have been proposed for the condensation of acetone to diacetone alcohol, such as metal hydroxides [82,83], metal oxides [82,84–87], metal oxides promoted with alkali or alkaline earth metal ions [88], mixed metal oxides [89,90], layered double hydroxides [91,92] and anionic and cationic exchange membranes [81,93–96]. Besides improving the catalyst, some research also focuses on a different reaction technique instead of conventional batch reactors or fixed-bed reactors, such as catalytic distillation [87,93–96]. Catalytic distillation is a process where chemical reactions and distillation occur simultaneously in a distillation column. The major benefits include improved reaction rate and selectivity and its ability to increase conversion beyond its equilibrium limit. Despite its apparent benefits, the application of catalytic distillation in the production of DAA seems limited. Nicol [94] compared conventional separate reaction and distillation to catalytic distillation for the production of DAA and concluded that catalytic distillation is the inferior option compared with the conventional separate process for DAA production because it has no significant advantages in terms of catalyst productivity, product selectivity and separation costs. Podrebarac et al. [93] came to a similar conclusion that in a conventional batch reactor, a more efficient use of the catalyst and an increased selectivity towards DAA was observed. Both mention the low external catalyst-liquid mass transfer as an important factor contributing to the low reaction rate and low product selectivity and indicate that improving the external mass transfer is

necessary. This is also concluded by Huang et al. [97] who state that a new design of catalyst packing with reduced mass transfer resistance is required to achieve a high yield and a high selectivity towards DAA. However, Nicol further notes that the decoupled temperature and pressure dependence is a major advantage of the separate process and that the reactor costs will be minimal because of the mild reaction temperature and pressure.

The findings by Nicol, Podrebarac, Huang and others make way for an alternative production process for diacetone alcohol that combines the benefits of mild reaction conditions and heterogeneous catalysis, namely electrosynthesis. Furthermore, the characteristic high selectivity of electrosynthesis and the lesser waste corresponding with it are of particular importance in this specific case considering the problems these topics entail in the conventional routes. The advantages of an electrosynthetic pathway compared to a classic chemical pathway are discussed more in detail in Chapter 1. The electrochemical aldol condensation has been investigated by Shono et al. [98]. They report the self- and cross-condensation of a small number of aldehydes at a platinum electrode in dimethylformamide (DMF) with a quaternary ammonium salt as supporting electrolyte. The reactions proceed at reduction potentials of -1.8 to -2.1 V vs. the saturated calomel electrode (SCE) with yields of about 75 %. Shono et al. suggest that the reaction proceeds indirectly through the formation of an electrogenerated base (EGB) (see Section 4.7). A similar investigation was performed by Kumar et al. [99] who studied the aldol condensations of propanal with itself and with a small number of other aldehydes. They also used a platinum electrode, but the electrolyte consisted of 50 % DMF and 50 % water with KCl as supporting electrolyte. The reactions take place in a potential range of -1.55 to -2.20 V vs. SCE with yields of 55 - 80 %. Kumar et al. also suggest that the reaction proceeds through the formation of an EGB, but proposes a more detailed possible mechanism (see Section 4.7). The electrochemical aldol condensation of diacetone alcohol was also briefly investigated by Tsai et al. who reported the results in three papers [100–102]. Similar to Shono et al. and Kumar et al. these papers describe a preliminary investigation to the feasibility

of the reaction, which confirms the possibility of the electrochemical pathway, but offers no information towards industrial development or implementation. In the first investigation [100], a solution of 4 M acetone in water with 2.5 M KCl was galvanostatically electrolyzed, which resulted in millimolar concentrations of diacetone alcohol and cell potentials ranging from 3.2 to 5.2 V. When the acetone concentration was increased to 10 M in the set-up used, the potential further increased to 14 V. The high potentials correspond with a high energy consumption and the high concentration of support electrolyte requires thorough purification. These conditions, together with the low concentration of DAA that is obtained, are far from those that are required for an industrial feasible process. In the second investigation [102], pure acetone was galvanostatically electrolyzed with lower concentrations of supporting electrolyte and lower cell potentials due to the lower current applied to the cell (though potentials up to 30 V are mentioned when the batch set-up is slightly altered and the inter-electrode distance approaches 2 cm). This resulted in a 2.8 % yield of DAA after a 2 hour run. Though a maximum begin concentration of reactants is desirable from a production point of view, such a low yield is insufficient when contemplating further industrial relevant development.

It is clear that the first steps towards the development of an electrosynthetic route for the aldol reaction of acetone have been taken and further development awaits. The results of the reported preliminary investigations provide a starting point, but to move towards industrial implementation, a more detailed screening and description of the key parameters is required. As a continuation of this beginning, a more targeted investigation is presented in Chapter 5.

4.3 Flow chemistry and microreactors

In recent times the application of flow chemistry for organic syntheses has become increasingly popular due to the progress made in the field and development of relevant technology which allows an increasing number of chemical methodologies

to be combined with flow-through processes [103–105]. There are several advantages to flow chemistry compared to batch operation. Typically, a higher yield and selectivity are obtained as a result of increased process control and the steady-state conditions of the reactor. The combination of the latter with the typically smaller reactor volumes of flow reactors increases the safety of the overall process, which might be negligible in laboratory conditions, but is a vital aspect in a process of industrial scale. The fact that the reactor operates under steady-state conditions also allows easier automation of the process which in turn allows operation for an extended period of time with little to no intervention. An advantage particularly useful for organic synthesis is the unique aspect of flow chemistry to carry out a multistep synthesis continuously by utilizing a flow setup composed of several reactors, enabling the efficient preparation of complex substances [103,105]. Another important reason for the rapid growth of flow chemistry research is the potential it has to play an important role in the search of the chemical industry for sustainable and green processes. Besides the increased safety and improvements in multistep synthesis, advantages such as improved mixing and heat management, energy efficiency, scalability, waste generation, access to a wider range of reaction conditions and reproducibility potentially benefit the twelve principles of green chemistry (see Section 1.1).

The benefits of the properties and inherent advantages of flow synthesis have also been recognized in the field of electrosynthesis. Batch reactors of the stirred-tank-reactor (STR) type suffer from inhomogeneities of the current distribution and mass- and heat transfer [106]. Figure 4.4 shows a comparison of conventional electrochemical batch reactors with continuous flow electrochemical microreactors. The large geometric differences in a STR reactor leads to divergent current paths and varying local current densities (Figure 4.4 (a)). A parallel plate arrangement of the electrodes leads to a homogeneous current distribution and minimizes inhomogeneities caused by edge-effects [106,107]. Therefore advanced industrially used electrochemical reactors are mostly build as the filter-press type. Problems can

also arise from random flow patterns in the reactor as illustrated in Figure 4.4 (b). Different flow velocities in the flow pattern can lead to large differences in residence times and even partially dead volumes which may result in the formation of by-products. Reactors which employ a well-defined homogeneous (laminar) flow prevent this.

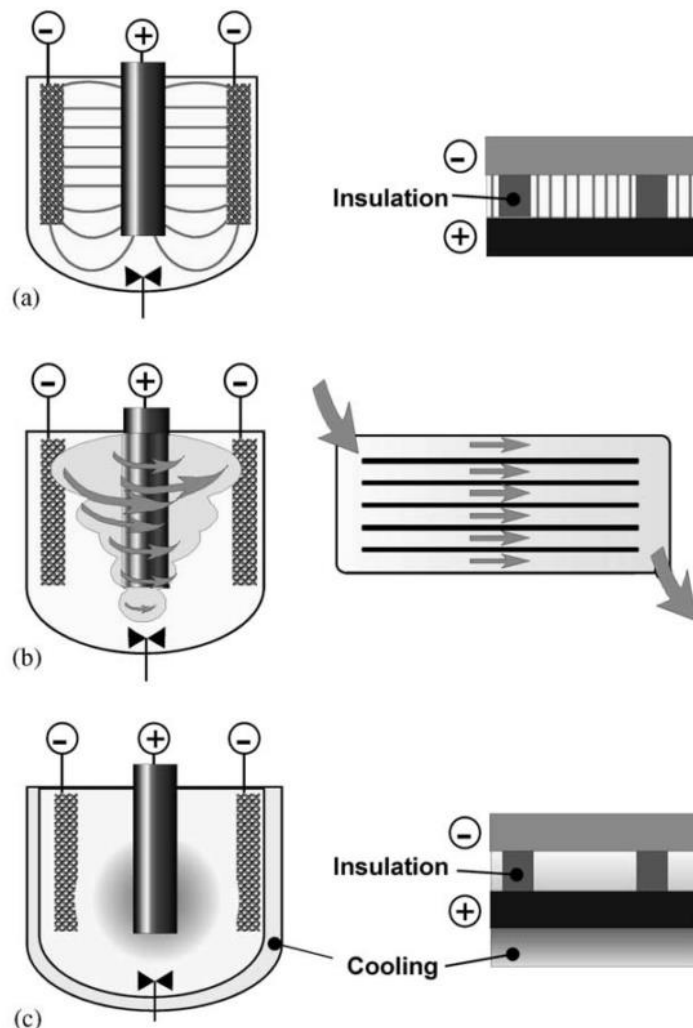


Figure 4.4: Comparison of the current distribution (a), mass transfer (b) and heat transfer (c) of conventional batch (STR) and micro electrochemical reactors [106].

In industrial reactors often large currents flow and possible hot-spots in the reactor can arise due to ohmic losses and the Joule reaction heat (Figure 4.4 (c)). Edge-effects

as a consequence of improper geometric design attribute to this problem. In turn this might have a significant influence on local reaction rates and electrolytic conductivity, leading to a loss of selectivity and yield. Planar electrode geometry and small channel dimensions as achieved in microreactors allow efficient and fast heat transfer preventing these problems.

4.4 Electrochemical microreactors for synthesis

From Section 4.3 it is clear that a continuous flow microreactor setup offers several advantages compared to a batch setup. Thanks to technological advancements in microfabrication techniques such as 3D-printing and micromilling, the miniaturization of flow devices has become more affordable and increasingly available [108]. Although these techniques are mostly employed in electroanalytical devices and microfluidic fuel cells, the implementation of microfluidic electrosynthetic systems is receiving a growing interest in literature. Consequently the application of an electrochemical microreactor (ECMR) for electroorganic synthesis is a rising topic [109]. Microreactor technology further improves the benefits of flow chemistry because of the process intensification and the associated advantages [110–113]. The recent reinvention of microflow cells for electrochemical synthesis builds on a long history of microflow cell design and electrochemical engineering in the laboratory and industry and is a logic extension of the progress made in both fields [34,114–116]. The use of microreactor technology in flow chemistry is extensively treated in literature. In this section the focus is mainly directed on its advantages in electrosynthetic applications. A more comprehensive discussion of microreactors in flow chemistry can be found in the aforementioned literature and the references therein.

The definition of the electrochemical microfluidic reactor as intended here, comprises electrochemical microsystems with characteristic dimensions in the millimeter and sub millimeter range, hence a small distance between the electrodes. Devices with

characteristic dimensions of this size sometimes are also called mesoreactors or millireactors, but these terms are not common practice and most often such devices are included in the definition of microreactors, as is the case in the classification of electrochemical microsystems by Ziogas et al. shown in Figure 4.5.

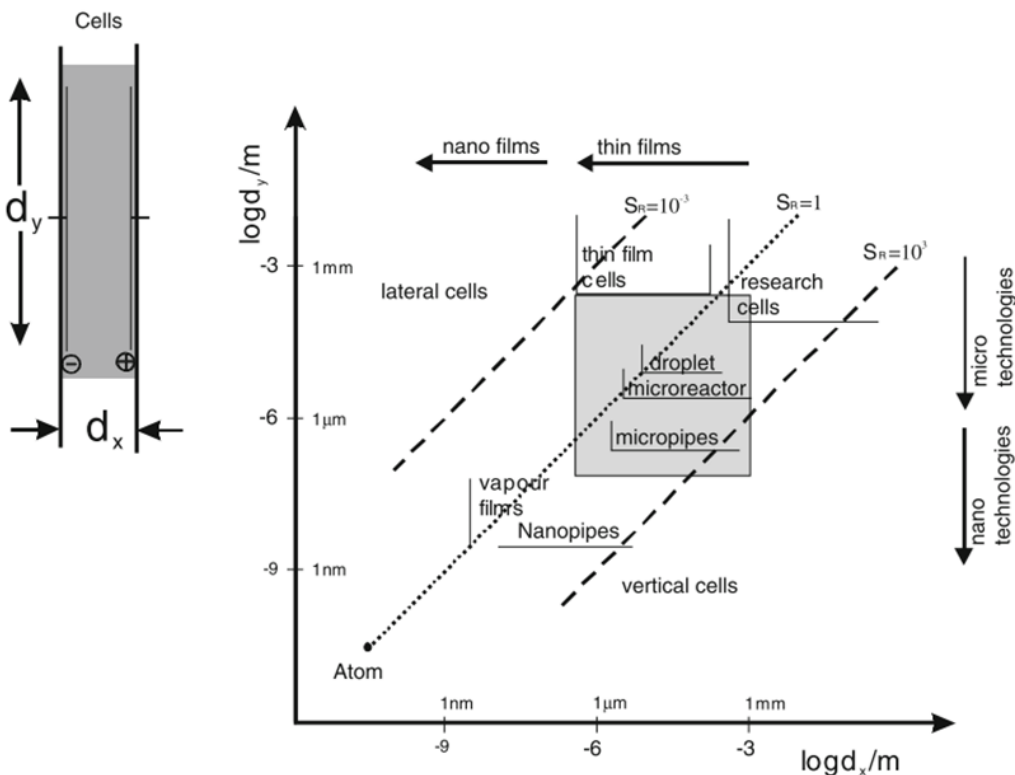


Figure 4.5: Classification of electrochemical microsystems with respect to the distance relationship $S_v = \frac{d_x}{d_y}$. The dashed lines mark an S_v of 10^{-3} , 1 and 10^3 respectively [109].

Electrochemical microreactors have several inherent advantages. The close proximity of the electrodes and often associated laminar flows lead to an intensification of the kinetics and mass transfer to the electrodes, resulting in higher yields and faster conversions [117,118]. Additionally, the laminar flow ensures a stable homogeneous flow which prevents partially dead volumes which result in loss in selectivity [119]. The small inter-electrode distance also allows operation with low concentrations or

even in absence of supporting electrolyte at low cell voltages due to the coupling (overlapping) of the diffusion layers of both electrodes at sufficiently small distances [120–122]. Furthermore, due to the laminar flow, the mass transfer of species in the direction perpendicular to the electrode's surface is governed only by diffusion so that in a well-dimensioned setup, separation of reaction products is possible (opposed to coupling of the electrodes) without the addition of a membrane [123]. The high specific interfacial area (electrode surface area to volume ratio) allows high conversions after a single pass [124,125]. These aspects, combined with the advantages associated with the small dimensions, make microfluidic reactors well-suited for fast screening of operative parameters or process optimization [126]. The addition of the precise control of reactive intermediates that electrosynthesis can offer due to the control of the potential, have made the application of electrochemical microfluidic reactors a viable and noteworthy alternative to batch processes in synthesis chemistry. This is reflected in the increasing attention it receives in literature in recent years. The list of electrochemical microreactors for continuous flow synthesis reported in literature is extensive. Several recent designs and their performance are covered in a comprehensive review by Watts et al. [124].

4.4.2 Microreactors with solid plate-to-plate electrodes

The most basic and most common type of microreactor design is a parallel plate electrode design [127–131]. This type of design is simple, often inexpensive to construct and offers a tremendously versatile platform to tune the design to the specific demands of a reaction, hence the large variety of designs that is seen in literature. As stated earlier, a parallel plate design provides a homogeneous current density distribution (if designed properly). The most common design consists of two parallel solid electrodes separated by a non-conducting spacer and the electrolyte flows between the electrodes (Figure 4.6 (a)). The spacer can be used to adjust the interelectrode distance which may range from tens of micrometers in setups in which the reactions at both electrodes are coupled to perform coupled electrolysis or to run

the reactor without added electrolyte [120,121,132–134] to millimeters in reactors for preparative scale synthesis [128,135].

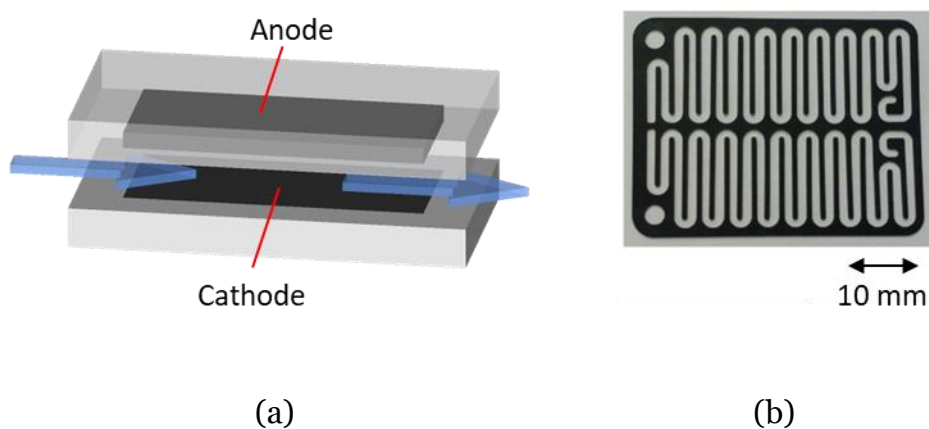


Figure 4.6: (a) Principle of a parallel plate flow-through electrochemical microreactor. (b) Serpentine reaction channel design to increase the channel length [136].

To achieve high conversion after a single pass, a designed pattern can be fabricated in the spacer to increase the channel length, such as a serpentine design in Figure 4.6 (b). An example of an inexpensive design of a parallel plate electrochemical microreactor is shown in Figure 4.7. This reactor was developed by Green et al. [128] in which the methoxylation of N-formylpyrrolidine and 4-tert-butyltoluene was performed. The reactor consisted of a circular design with a carbon plate anode and a stainless steel cathode, separated by a perfluoropolymer spacer in which a spiral reaction channel was cut. The plates were 150 mm in diameter resulting in a 2000 mm reaction channel with an active electrode area of 100 cm^2 . They were able to obtain 100 % conversion with >95 % selectivity and a product formation rate of ~24 g/h after a single pass.

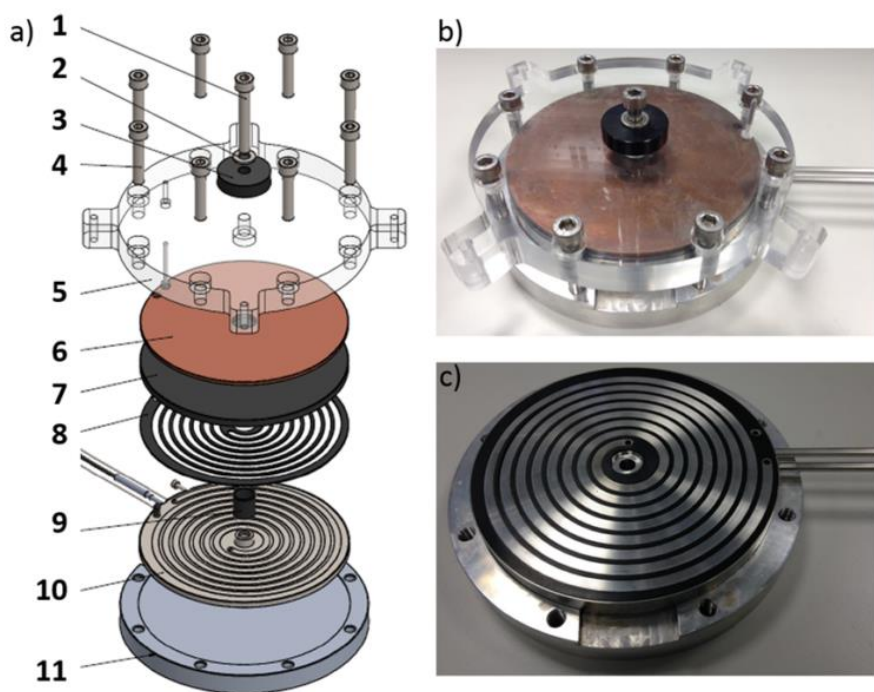


Figure 4.7: Electrochemical microreactor designed by Green et al. for preparative synthesis. 1. Central bolt. 2. Washer. 3. Insulating tube. 4. Peripheral bolt. 5. Perspex top plate. 6. Cu backing plate. 7. Carbon/polymer anode plate. 8. Perfluoroelastomer gasket. 9. Insulating tube around central bolt. 10. Stainless steel cathode plate with spiral groove. 11. Al base plate. (b) Photograph of reactor with Perspex top. (c) Photograph of reactor with gasket fitted into cathode plate to create the spiral channel [128].

The simplicity of this type of reactors allows for an easy upscaling to increase conversion by connecting multiple reactors in series or stacking multiple cells in one device [137]. The electrodes in the different cells of such a stack can be connected in series (bipolar configuration) or in parallel. This type of design where multiple cells are stacked is common in industrial type cells of the filter-press type (plate-and-frame cells) of which also commercial laboratory scale setups are available, such as the extensively studied FM01-LC laboratory flow reactor [135,138–140] and the electrochemical flow cells available from ElectroCell A/S [141–144]. These commercial cells often include spacers that have integrated turbulence promoters to

increase mass transfer [145–147]. The latter can also be achieved by incorporating porous flow-through electrodes [148,149], however this is not commonly done as complex designs are required and such electrodes easily lead to non-uniform potential distributions which can cause undesired side reactions or ineffective use of the electrode area. In case the cell compartments of both electrodes need to be separated, several parallel plate ECMR designs can be adjusted to incorporate a membrane or diaphragm to fulfill the requirement. However, this adds complexity to the setup and also yields an additional junction resistance over the separator.

4.4.3 ECMR for the aldol reaction of acetone

Microreactor setups are more commonly employed for fine chemicals or pharmaceuticals than for commodity chemicals since they are often associated with high capital and operating costs and small production capacities and thus they need products with a high added value to render them economically viable. However, due to the ease of scale-up and the increased selectivity and conversion which lead to a less intensive and less costly purification, the use of a microreactor setup can become industrially applicable for certain commodities or specialties such as diacetone alcohol. For a successful implementation it is thus important to achieve an adequate production rate and a high selectivity in the reactor. In Chapter 6 a microreactor setup is developed. To be able to comply with the aforementioned requirements, simplicity and modularity of the design is a key criterion which is why the reactor is based on a parallel plate configuration. Further details are discussed in Section 6.2.2.

4.5 Mechanism of the chemical aldol reaction

The reaction mechanism of the conventional chemical aldol reaction has been studied extensively and is well understood [67,68,75]. Fundamentally there are two different mechanisms for the aldol reaction denoted the acid-catalyzed aldol reaction and base-catalyzed aldol reaction depending on the nature of the catalyst. These are also

referred to as the enol or enolate mechanism respectively, named after the active species generated in the mechanism. In the enol mechanism the electrophile is activated while in the enolate mechanism the nucleophile is activated. In both mechanisms, condensation occurs under harsh conditions, hence mild conditions prevent this from happening.

The enol mechanism is shown in Figure 4.8. It proceeds via the acid-catalyzed keto-enol tautomerization of the carbonyl compound to the corresponding enol, rendering it nucleophilic at the α -carbon. The parallel protonation of another carbonyl by the acid activates the carbon towards attack. The nucleophilic enol then adds to the protonated carbonyl, completing the aldol reaction after deprotonation.

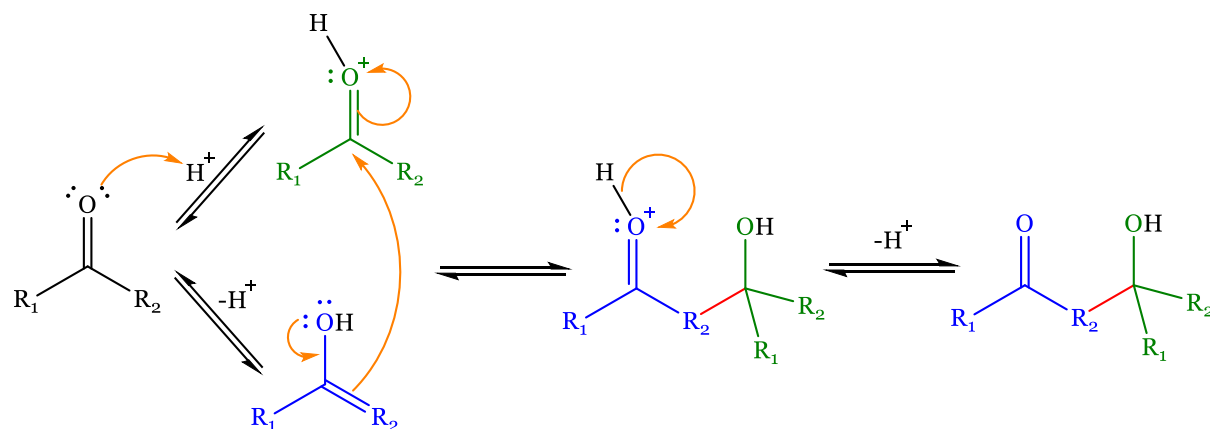


Figure 4.8: Mechanism of the acid-catalyzed aldol reaction (enol mechanism).

In the enolate mechanism (see Figure 4.9) the first step is the loss of an α -hydrogen of a carbonyl compound yielding the corresponding resonance stabilized enolate. This feature offers control of the reaction in cross-aldol reactions by controlling the relative acidity of the α -hydrogens of both carbonyl compounds. If one compound is non-enolizable, the possible products are limited. The enolate generated in the first step is nucleophilic and will attack the carbonyl group of another molecule. The aldol reaction is completed by the protonation of the aldol anion by the protonated base.

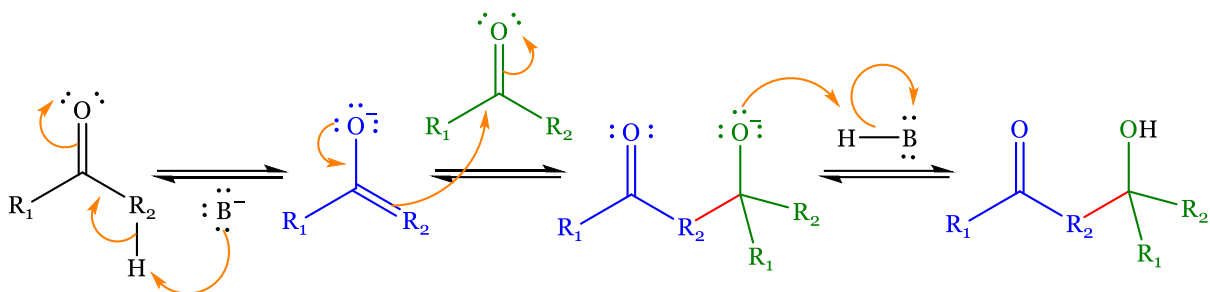


Figure 4.9: Mechanism of the base-catalyzed aldol reaction (enolate mechanism).

4.6 Electrogenerated bases as initiator

From the previous section it is clear that the aldol reaction is initiated by acids and bases and thus, generating these species *in situ* can induce the aldol reaction. The few mechanisms of the electrochemical aldol reaction that have been reported are mostly based on such an indirect or electrochemically induced pathway and mention electrogenerated bases (EGBs) which initiate the reaction (see Section 4.7). Electrogenerated bases are radical anions, anions or dianions which are derived from a probase (PB) [150,151]. This section discusses EGBs and their properties which are relevant to the aldol reaction and is based on the information found in references [150–153].

The use of EGBs in organic electrochemistry is well-known and documented and many systems with different probases have been developed for a wide range of reactions (see the previously mentioned references). Depending on the basicity an EGB can act as a base, as a nucleophile or as a single electron transfer agent which will determine in what type of reactions the specific EGB is useful. Some EGBs, such as the EGB derived from 2-pyrrolidone, are so stable that they can be generated *ex situ* and transferred to a reaction vessel to induce a reaction. Such procedure for the aldol reaction would be no different than using conventional chemical bases and is not considered here. EGBs are commonly classified according to the atom to which the proton transfer takes place which is typically nitrogen, oxygen or carbon.

Despite the established use of EGBs in organic electrochemistry, very little work has been done on EGBs and the aldol reaction. The little information that is available on its mechanism is fragmented throughout literature. This section aims to combine the available knowledge on EGBs relevant to the electrochemical aldol reaction to shed some light on its mechanism.

4.6.1 Carbonyl compounds as probase

The carbonyl group is an electrophile which is electroreducible. Reduction of a carbonyl group happens by the addition of an electron to the LUMO of the carbonyl group leading to the formation of a radical anion known as a ketyl radical ((1) Figure 4.10). This radical anion is quickly reversibly protonated on the basic oxygen center by the excess carbonyl compound ((2) Figure 4.10).

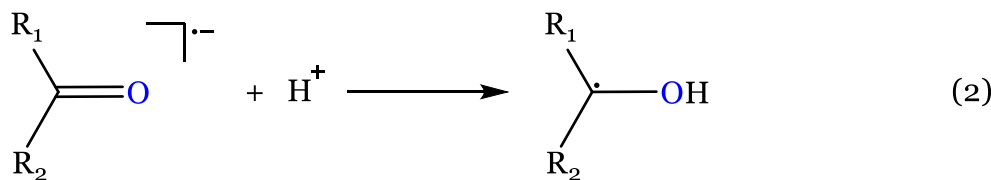
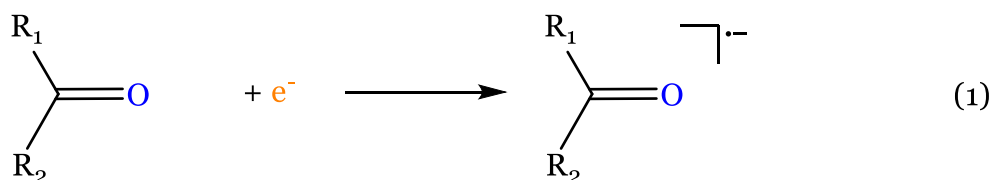


Figure 4.10: Formation (1) and protonation (2) of a radical anion EGB derived from a carbonyl compound as PB [152].

The protonated neutral radical can react with another neutral radical or with the ketyl radical to form a diol (Figure 4.11).

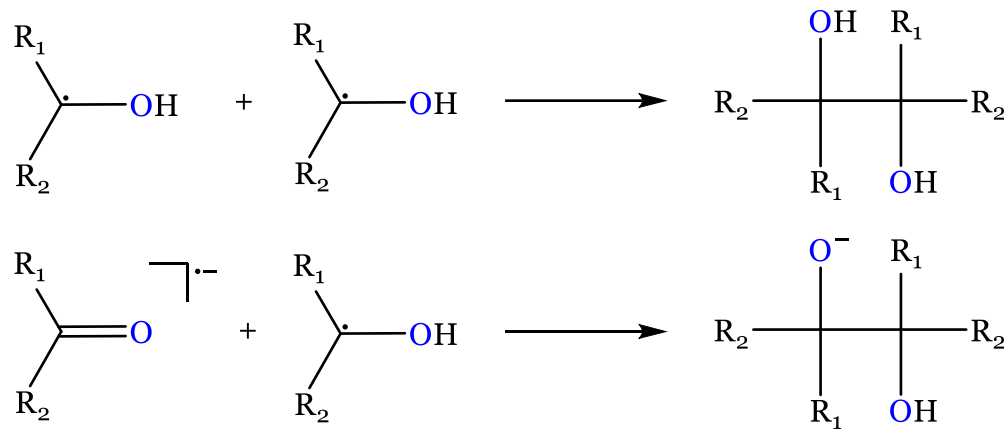


Figure 4.11: Formation of the diol by reaction of two radicals or between a radical and a radical anion.

The neutral radical can also be reduced directly ((1) Figure 4.12) or by radical disproportionation with the ketyl radical ((2) Figure 4.12) since it is normally more easily reduced than the corresponding radical anion [151]. Protonation of the reduced neutral radical generates the corresponding alcohol ((3) Figure 4.12).

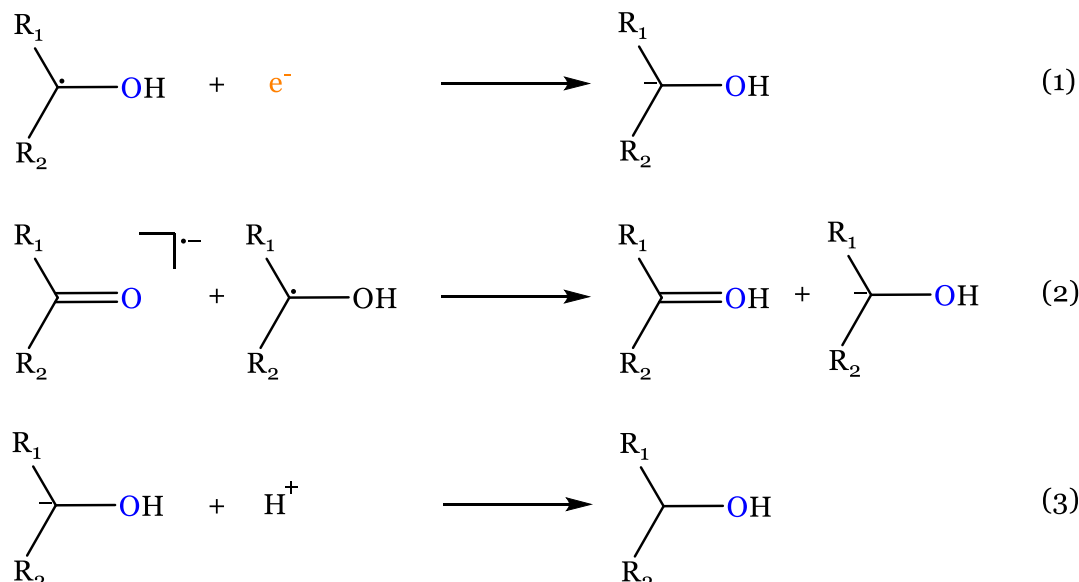


Figure 4.12: Direct reduction (1) and reduction by disproportionation (2) of the radical to the alkoxide. Protonation of the alkoxide to the alcohol (3).

The reaction between two radical anions is relatively slow [152] and would lead to the dimer dianion or a dianion of the carbonyl compound by radical disproportionation (Figure 4.13).

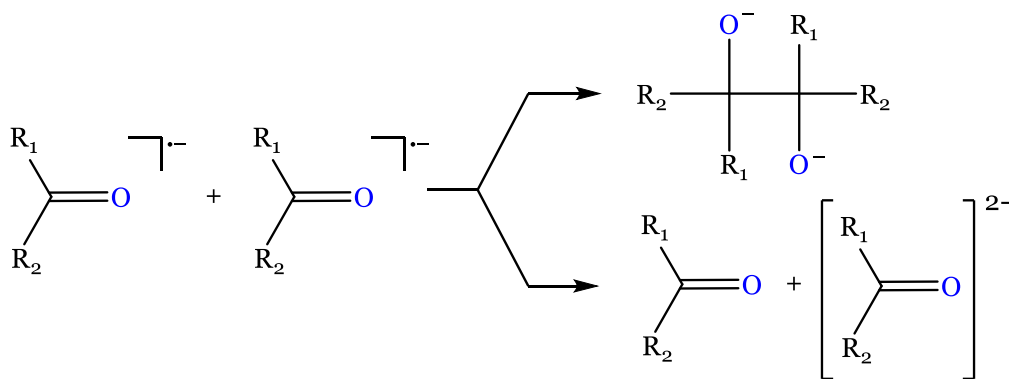


Figure 4.13: Formation of the dimer dianion or carbonyl dianion by reaction of two ketyl radicals.

To which extent the reactions in Figure 4.11, Figure 4.12 and Figure 4.13 take place and their relative competitiveness is not known as very little work has been done in this area [154–156]. It will also differ depending on the carbonyl compound. For example, the electrochemical behavior of an EGB of a quinone methide has been studied to some extent [157]. In this case the protonated ketyl radical is slightly more difficult to reduce than the corresponding PB, suppressing the reactions shown in Figure 4.11 and Figure 4.12.

Very few reports mention reactions in which the EGB derived from a carbonyl compound reacts with the same compound in a coupling reaction [98,158–160]. It is suggested [151] that the actual EGB is the dimer anion or dianion. Where most reactions involving EGBs require stoichiometric amounts of the EGB, the carbonyl coupling reaction can become catalytic when the product anion is protonated by the reactant, generating another nucleophile that propagates the reaction. This is a major advantage to the conventional route.

4.6.2 Oxygen as a probase

Dissolved oxygen is reduced to the superoxide anion $O_2^{-\cdot}$ at potentials of about -1 V in several aprotic solvents [150,151,153]. In the presence of nonacidic cations such as those of quaternary ammonium salts, the corresponding superoxide salt is formed. The use of alkali metal salts is discouraged as the corresponding superoxide salt is often insoluble and may precipitate at the electrode surface, strongly inhibiting its activity. The tetraalkylammonium superoxide can act as a nucleophile, as an electron donor and as a base. The properties and use of the superoxide anion EGB has been studied and reviewed (see [150,151,153] and the references therein). A common method is to bubble oxygen through the solution so an excess is available. The $O_2^{-\cdot}$ is a relatively weak base and its most dominant characteristic is its tendency to disproportionation via abstraction of protons of solvents and substrates resulting in the formation of a hydroperoxyl radical and the substrate anion ((1) Figure 4.14) [161].

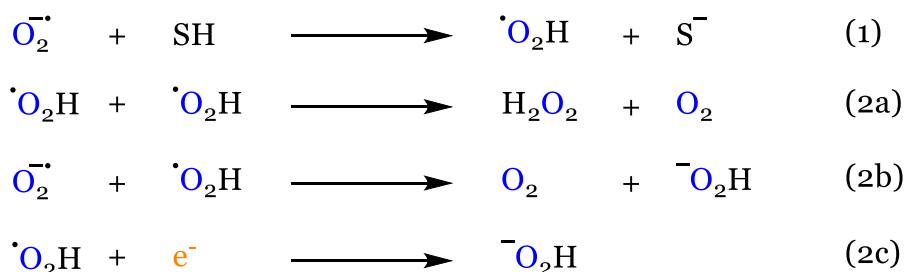


Figure 4.14: Disproportionation of superoxide anion with a proton donor (1) and termination reactions of the hydroperoxyl radical (2).

However, the O_2 regenerated in steps 2 cause oxidative follow-up reactions to occur. This can be prevented by not inserting additional oxygen in the system. Although reactions which are initiated by weak EGBs can benefit from the dissolved oxygen present in the system, its complicated chemistry can cause large discrepancies in both the coulometric measurement and the product distribution of an electrolysis in an aprotic solvent.

4.7 Proposed mechanisms in literature for the electrosynthetic aldol reaction

As stated in the Section 4.6, the electrochemical aldol reaction has received little attention and only a few mechanisms have been reported in literature. These mechanisms are presented in this section and their plausibility is evaluated in Chapter 7.

4.7.1 Combined mechanism proposed by Tsai

The first mechanism is the scheme proposed by Tsai in [102] (Figure 4.15). In that work the electrolysis of water is mentioned as a source of the in situ acids and bases in the form of H^+ and OH^- which induce the aldol reaction. In addition to the initiation by water electrolysis, the combined scheme suggests a direct activation of the reactant leading to an anion on the one hand and a cation on the other hand. Subsequent attacks on the generated species are suggested to complete the aldol reaction.

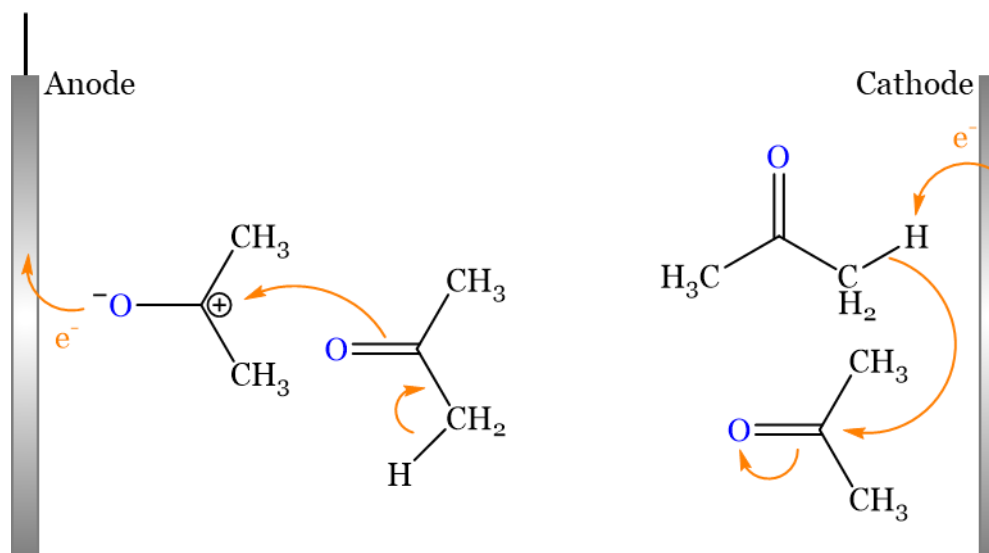


Figure 4.15: Mechanism of the electrochemical aldol by direct activation of the reactant as proposed by Tsai [102].

4.7.2 Radical mechanism proposed by Kumar et al.

The mechanism proposed by Kumar et al. in [99] is a detailed mechanism (Figure 4.16). In the first step a carbonyl molecule receives an electron and forms a radical anion. In a parallel reaction a similarly formed radical anion loses a hydrogen free radical to rearrange to an enolate. This enolate combines with one of the formed radical anions and loses an electron to rearrange to the alkoxide of the aldol product. Subsequently this species loses another electron to form a free radical which combines with the earlier lost hydrogen free radical and forms the aldol product.

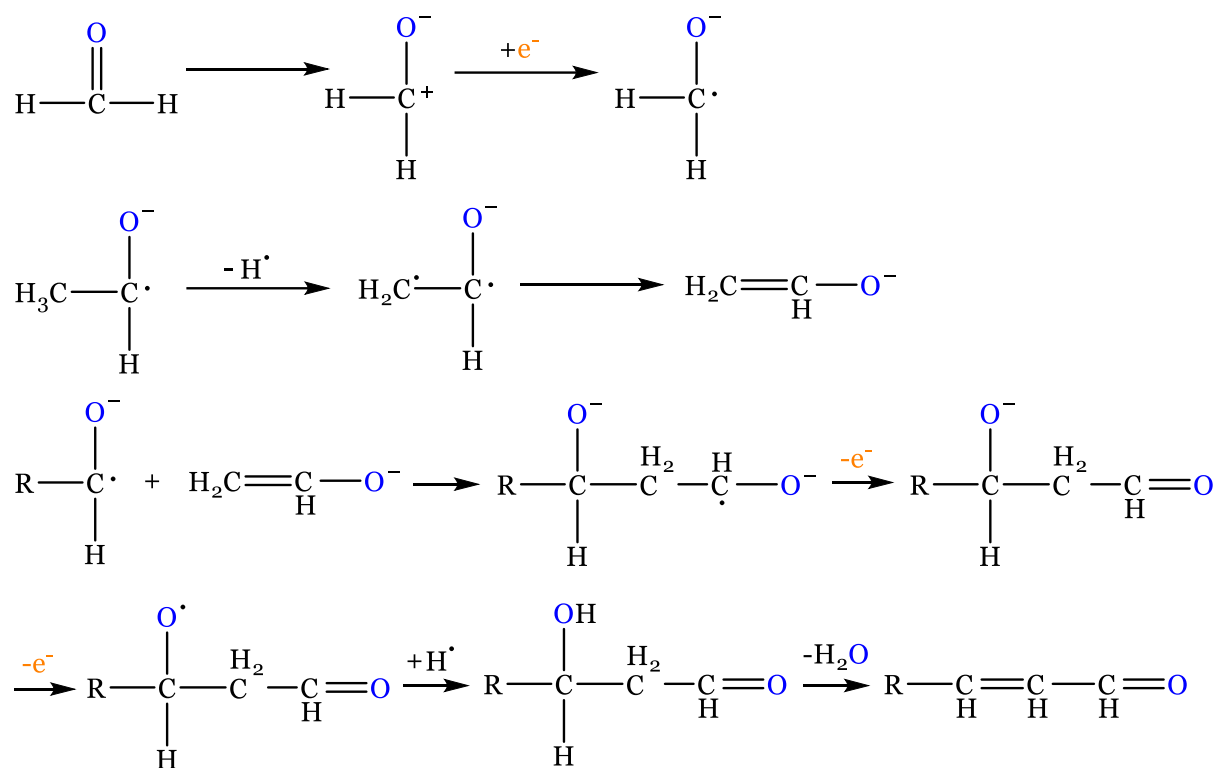


Figure 4.16: Mechanism of the electrochemical aldol reaction by reaction of independently formed radical anion and enolate as proposed by Kumar et al. [99]. Reformatted and errors corrected.

4.7.3 EGB initiated mechanism proposed by Shono et al.

A third mechanism is proposed by Shono et al. in [98], where the generation of an EGB derived from the carbonyl compound induces the reaction as shown in

Figure 4.17. In the first step of the mechanism the EGB is generated by reduction of a carbonyl molecule. This EGB then reacts with another unreacted carbonyl molecule to yield an enolate. The aldol reaction is then completed by the reaction of the enolate with an unreacted carbonyl compound.

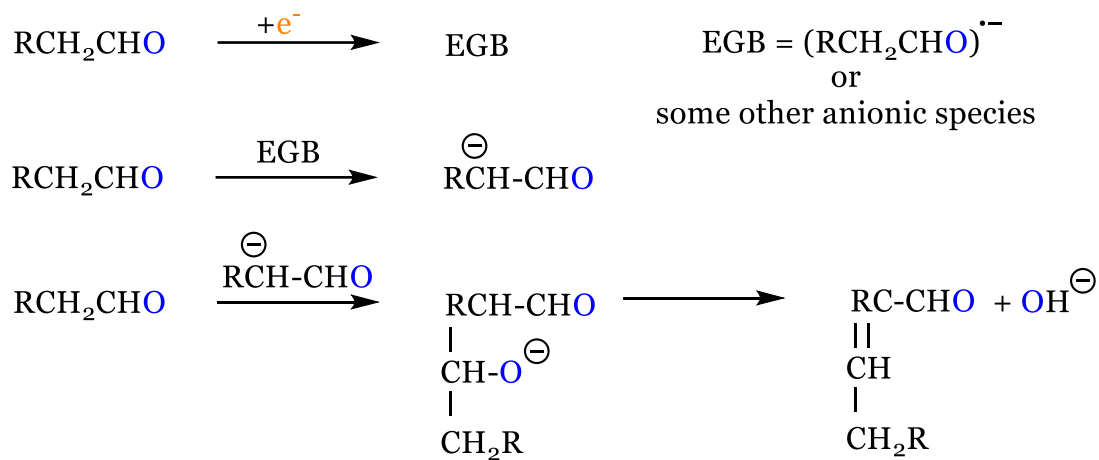


Figure 4.17: Mechanism of the electrochemical aldol reaction by generation of an EGB derived from the reactant as proposed by Shono et al. [98].

CHAPTER 5

Electrochemical aldol reaction of acetone to diacetone alcohol

THE POTENTIAL OF AN ELECTROSYNTHETIC ROUTE FOR THE ALDOL REACTION OF ACETONE TO DIACETONE ALCOHOL IS STUDIED. KEY PARAMETERS OF THE ELECTROLYSIS ARE IDENTIFIED AND QUANTIFIED AND THE MOST OPTIMAL CONDITIONS ARE DESCRIBED. FROM A PRESELECTED LIST OF MATERIALS, THE MOST PERFORMANT ELECTROCATALYST IS SELECTED.

This chapter is published as: D. Pauwels, J. Hereijgers, K. Verhulst, K. De Wael, T. Breugelmans, Investigation of the electrosynthetic pathway of the aldol condensation of acetone, Chemical Engineering Journal, 289 (2016) 554-561.

5.1 Introduction

In this section a first investigation towards the efficiency of the production of diacetone alcohol from acetone by electrosynthesis is presented. This means an evaluation of the parameters that influence the reaction, such as the electrolyte composition, the electrolysis potential and the electrode material in regards to the yield of DAA while keeping the industrial viability in mind. Thus optimization towards a high yield and high selectivity in a reasonable time span is desirable, but with attention given to factors such as material cost, energy consumption and simplicity of the reaction in regards to the setup and further purification. Shono et al. [98] and Kumar et al. [99] have demonstrated the possibility of an electrochemical aldol condensation (albeit indirectly) and Tsai et al. [100–102] have confirmed this for the aldol reaction of acetone to diacetone alcohol. Though, besides the confirmation, no further effort has been made towards the optimization of the reaction, especially with further industrial development in mind. This is shown by the fact that the reaction is conducted by galvanostatic electrolysis instead potentiostatic electrolysis with no attention given to the resulting potentials. They could perform the desired reaction but with very large potentials which connotes high energy costs or very low yields. In this work, the electrolysis is potential-controlled to ensure that this important factor that contributes to the viability is always taken into account.

5.2 Experimental

5.2.1 Chemicals

Acetone (HPLC grade, $\geq 99.9\%$ purity) was purchased from Biosolve BV (The Netherlands). The supporting electrolyte tetrabutylammonium perchlorate (TBAP, $n\text{-Bu}_4\text{NClO}_4$, electrochemical analysis grade, $\geq 99.0\%$ purity) was purchased from Sigma-Aldrich (Belgium). The water used in this study was ultrapure water ($18.2\text{ M}\Omega\text{ cm}$) purified in the laboratory (Milli-Q, Millipore, USA).

5.2.2 Electrochemical experiments

The controlled-potential electrolysis experiments were conducted in a batch setup in a conventional three-electrode configuration. A saturated Ag/AgCl was used as the reference electrode (all potentials in this chapter are reported versus Ag/AgCl) and a platinum sheet electrode (8 cm^2) was used as counter electrode (CE). The potential was controlled by a VSP-300 potentiostat from BioLogic (France). For every setup the uncompensated resistance was determined by impedance measurements and compensated using positive feedback. Commonly the uncompensated resistance was $50 - 100\ \Omega$. In the standard setup the electrodes were placed in an undivided glass recipient at a fixed inter-electrode distance, which was 1 cm between the working electrode and the reference electrode and 2 cm between the working electrode (WE) and the counter electrode. In the divided cell setup, a glass container with a fritted glass disc bottom (4-15 μm pores, 3 mm thick) was used to separate the cathode half-cell and anode half-cell. The resistance of this junction was found to be $100\ \Omega$, which was accounted for. To prevent sampling errors due to local differences in electrolyte composition during the electrolysis, the cell was stirred thoroughly for 10 seconds before a sample was taken from the center of the cell.

5.2.3 Analysis

Analysis of the samples was performed by GC-FID (Thermo Scientific Trace 1300) on a polar capillary column (Restek RTX-Wax 30 m \times 0.25 mm, PEG 0.25 μm). The carrier gas flow (N_2 , 5.0 purity) was controlled at $1.0\ \text{ml min}^{-1}$. The temperature of the column was held constant at $40\ ^\circ\text{C}$ for 3 minutes and then ramped to $200\ ^\circ\text{C}$ at $40\ ^\circ\text{C min}^{-1}$. This gave excellent separation of the target products allowing easy quantification. High temperature favors the equilibrium of the reaction to acetone [80], leading to possible decomposition of DAA during the analysis. However, all samples were analyzed four times with a corresponding standard deviation of less than 5 %. Calibration curves could be reproduced within the same standard deviation. Contrary to the expected effect of the high analysis temperature, a small amount of

acetone is converted to diacetone alcohol during the GC analysis yielding 0.1 m% DAA in a blank sample. This is accounted for in the results.

5.3 Results and discussion

5.3.1 Validation of the electrosynthetic pathway

Prior to the investigation and optimization of the parameters that influence the reaction, a validation of the electrochemical aldol condensation was performed by means of a batch electrolysis in the standard setup as described in Section 5.2.2. Both the working and counter electrode were platinum sheet electrodes of 8 cm^2 , the electrolyte consisted of 100 ml acetone with 0.1 M tetrabutylammonium perchlorate (TBAP). The potential was set at -2.5 V. This potential was chosen similar to the potentials reported by Shono et al. [98] and Kumar et al. [99] and also considering that organic reductions often proceed in this potential range [19]. The experiment ran for seven hours and each hour a sample was taken from the cell. During the experiment, the solution turns from colorless to pale yellow and finally even a dark orange or brownish color. Such a discoloration is also reported by Kumar et al. In all experiments, this discoloration was observed. This effect could not be directly assigned to a certain product in the GC-analysis results as there were no obvious correlations with any of the identified peaks. To find the origin of this color change, additional experiments in the same configuration were performed, but instead of homogenizing the solution before sampling, local samples were taken close to the electrode (where the discoloration originates) and in the bulk. GC-analysis of these samples showed a positive correlation between mesityl oxide, the dehydration product of DAA and the amount of discoloration in the solution. To confirm this result and the cause of the color change, UV-VIS-spectroscopy measurements were performed on the samples and compared to literature and analytical standards. Literature reports a mesityl oxide absorption peak at 235 nm (NIST) which shifts to 230-232 nm in hexane. Measurement of an analytical standard of mesityl oxide in

heptane gave an absorption peak at 231 nm. Measurements of the samples in heptane gave a distinct absorption peak at 231.5 nm agreeing well with both the analytical standard and literature. These results confirm that mesityl oxide, though obtained in very small concentrations, is the cause of the discoloration of the solution during the experiments. Figure 5.1 shows the analysis results of the electrolysis experiment.

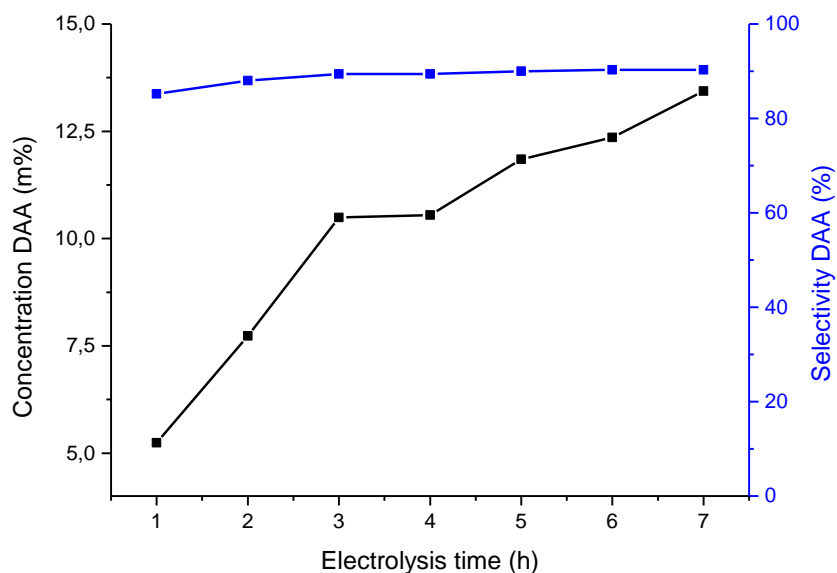


Figure 5.1: Concentration of DAA (m%) per hour of electrolysis (black line, left y-axis) and corresponding selectivity (blue line, right y-axis) during a batch electrolysis in the standard setup. WE and CE: 8 cm² platinum sheet, potential: -2.5 V, runtime: 7 h.

The concentration of DAA increases steadily over the time of the experiment, though with a less steep inclination after the first three hours. This is reflected in the formation rate of DAA which over the course of the entire experiment is 2.20×10^{-3} M min⁻¹, but is as high as 4.01×10^{-3} M min⁻¹ in the first 3 hours and as low as 1.15×10^{-3} M min⁻¹ in the last 3 hours. The selectivity towards DAA increases from ~85 % after the first hour to ~90 % after three hours and then remains about constant (selectivity calculated from relative peak area in GC-FID analysis). The final concentration of DAA after seven hours was 13.4 m%. An experiment that ran under the same conditions for 32 hours showed that no significant increase in the concentration of

DAA was noticeable after eight hours (results not shown). After two hours the concentration of DAA was 7.7 m%, which is more than half of the final concentration. In further experiments, the runtime will be limited to two hours as then sufficient DAA has formed to evaluate the result.

5.3.2 Voltammetric investigation

A standard electrochemical investigation often starts with a voltammetric investigation to identify and quantify basic electrochemical parameters. To investigate the electrosynthetic aldol reaction of acetone, cyclic voltammetry was performed on different electrode materials (Pt, Au, Ag, Cu) and in different solvents (water, dimethylformamide (DMF), dimethyl sulfoxide, tetrahydrofuran, acetonitrile). All results showed a similar behavior which is explained by one example shown in Figure 5.2.

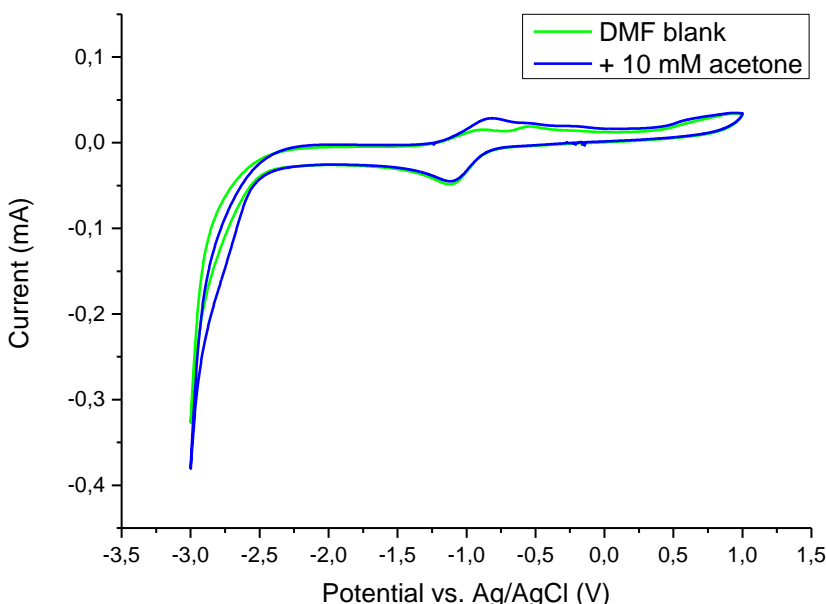


Figure 5.2: Cyclic voltammetry of 10 mM acetone in DMF + 0.1 M TBAP and of blank DMF (+ 0.1 M TBAP). Scanned at 100 mV s⁻¹.

Figure 5.2 shows the results of a CV in DMF. The redox couple visible in the center of the CV in both the blank and the 10 mM acetone sample is due to dissolved oxygen

and is not (directly) related to the reaction. On the far negative end of the scan, the solvent peak of DMF is visible which means that DMF itself is starting to react. Furthermore no obvious redox couple can be discerned in the voltammogram. This is also the case for all combinations of solvents, materials, scan rates and scan method (CV/LSV) applied. These results imply that acetone is stable in the window measured, however, the validation experiment clearly shows that acetone does react in this potential window resulting in the aldol reaction. Taking into account both observations, this means that the aldol reaction of acetone is an indirect or an electrochemically induced reaction. Considering the potential window in which the reaction takes place, the reaction is initiated by the activation of acetone itself and by the reduction of the dissolved oxygen to the superoxide radical anion. The direct activation occurs at the very negative potential limit of acetone. This is not visible in the CV's in the different solvents since this is obscured by the solvent peaks and considering the small concentration of acetone versus the abundance of solvent. The electrochemically induced nature of the electrosynthetic aldol reaction is further investigated in Chapter 7. Since a standard voltammetric investigation to derive kinetic parameters and such is not possible, the reaction is investigated using a more applied approach in the following sections.

5.3.3 Electrolysis potential

The first major parameter to be investigated is the electrolysis potential since it is directly linked to the energy requirement of the system. A high(er) potential implies a high(er) energy demand for the system and vice versa. A lower potential is thus desirable, but a lower potential means slower kinetics for a process under electrical charge transfer control and hence a balance has to be found between the potential applied to the cell and the amount of product that can be formed in a certain time. Seven experiments were conducted with the potential varying from -1 V to -4 V in steps of 0.5 V. The current responses of the different experiments are plotted in Figure 5.3.

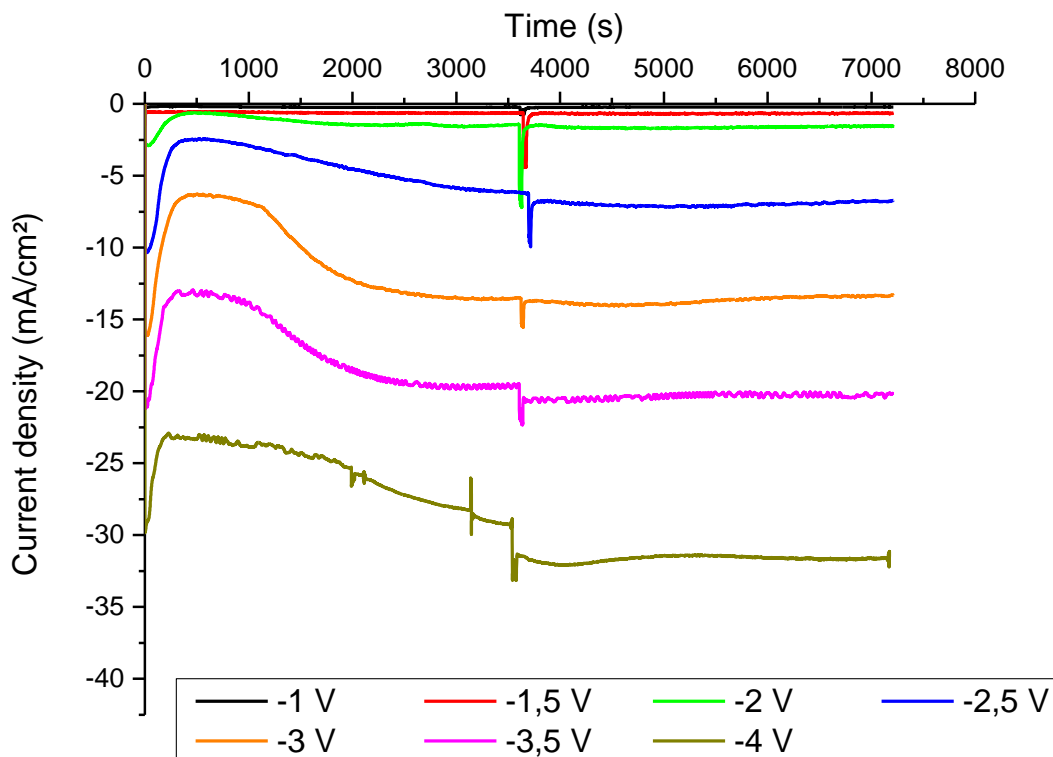


Figure 5.3: Current densities of separate batch electrolysis experiments at different potentials of WE versus RE in the standard setup. WE and CE: 8 cm² platinum sheet, runtime: 2 h.

It is immediately clear that the current density increases as the potential increases to a more negative value, i.e. for each potential step from -1 V to -4 the resulting current density is larger. All plots also display the same behavior: a larger (cathodic) current in the beginning, which rapidly decreases to a minimum and then slowly increases to a steady value. The large current in the beginning is due to the abundance of electroactive species at the surface of the electrode, which can react immediately at the beginning of the experiment. After this immediate reaction, more molecules need to be transferred to the electrode from the bulk and the current decreases to a minimum. A concentration gradient will drive molecules from the bulk to the electrode until the reaction is mass transfer-controlled and hence, the current slowly increases to a steady value. Since the solvent provides the electroactive species, there is no decrease of the current over time in the measured time frame as would be expected when using a small concentration of electroactive species due to the

abundance of molecules in proximity of the electrode. At about one hour into the experiment, a sharp peak of the cathodic current toward more negative values can be discerned. The cause of this peak is the sampling procedure (see Section 5.2.2). A sample was taken after one hour of electrolysis and at the end of the experiment and analyzed as described in Section 5.2.3).

Figure 5.4 shows the results of the analyses. The DAA concentration increases as the potential increases to a larger negative value up to -2.5 V and then remains more or less constant up to -3.5 V, at -4 V the final concentration decreases a little. During the experiments, a discoloration is observed, going from a barely noticeable pale yellow color at -1 V to a dark orange/brownish color at -2.5 V, this discoloration is known to be caused by the formation of mesityl oxide (see Section 5.3.1). At -3 V and further, the solution gets a very dark brown color and at -4 V small amounts of precipitation become visible.

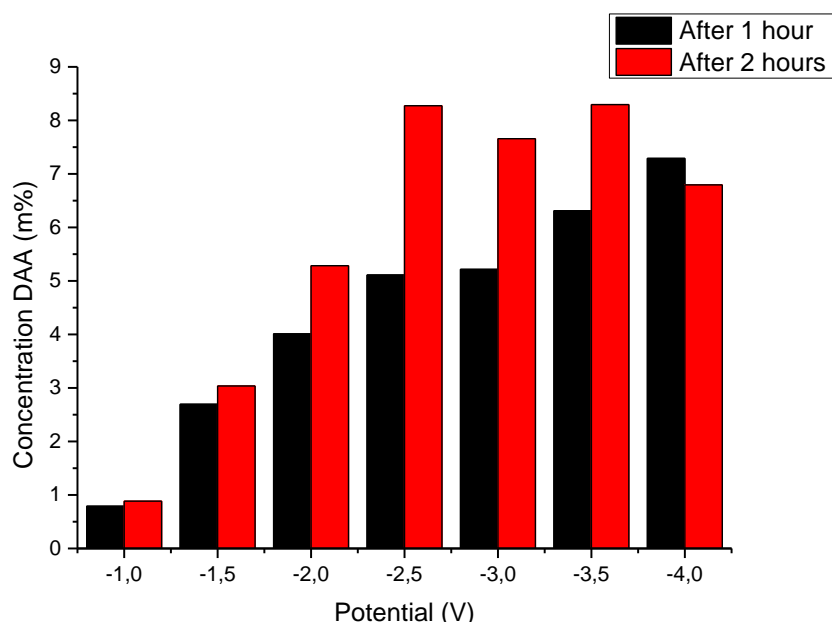


Figure 5.4: The concentration of DAA (m%) after 1 h of electrolysis (black columns) and after 2 h of electrolysis (red columns) in separate experiments in the standard setup with a different potential applied each experiment. WE and CE: 8 cm² platinum sheet, runtime: 2 h.

Larger potentials give a larger drive for the reaction and faster kinetics but also give rise to several side reactions, as indicated by the increasing discoloration and decreasing selectivity towards DAA as shown in Figure 5.5. The selectivity shows a maximum of about 95 % at -1.5 V and -2 V and decreases rapidly at higher potentials to a minimum of 70 % after 2 hours at -4 V. In addition, from [162] it is known that, at potentials of -3 V and more negative, the boundary of the potential window of the supporting electrolyte is reached and its stability is compromised. The supporting electrolyte can then be reduced or oxidized itself and react with the solvent. The decrease in DAA concentration at -4 V can be the result of the competition of the side reactions or due to breakdown of the molecule by these reactions.

It is also clear that in the first hour more DAA is formed than in the second hour of the electrolysis while this is not immediately visible in the current response. It is possible that products of the reaction or a side-reaction adsorb on the electrode and block the surface. From the analyses (not shown) it is also clear that more DAA converts to MO in the second hour, which logically follows from the fact that the DAA concentration increases as well (except for -4 V). When looking at the relative increments of the DAA concentration between the different experiments it is obvious that these are smaller than the relative increments of the corresponding current densities in Figure 5.3, e.g. the current more than doubles between the -2 V and -2.5 V experiments while the final DAA concentration increases only by slightly more than 50 %. This is even more obvious at the higher potentials as the current keeps increasing, but the final concentration does not. This is a first indication of occurring side-reactions, which do not contribute to the formation of DAA. The extent of this effect can be seen by plotting the current efficiency of each experiment. Since the exact reaction mechanism is not known here, the current efficiency cannot be calculated by means of stoichiometric calculations. However, a measure for the current efficiency can be used by dividing the DAA concentration by the charge passed in the cell since both are connected through Faraday's law of electrolysis (see Section

3.3.1.1). In this thesis this approximation is referred to as the (pseudo) current efficiency.

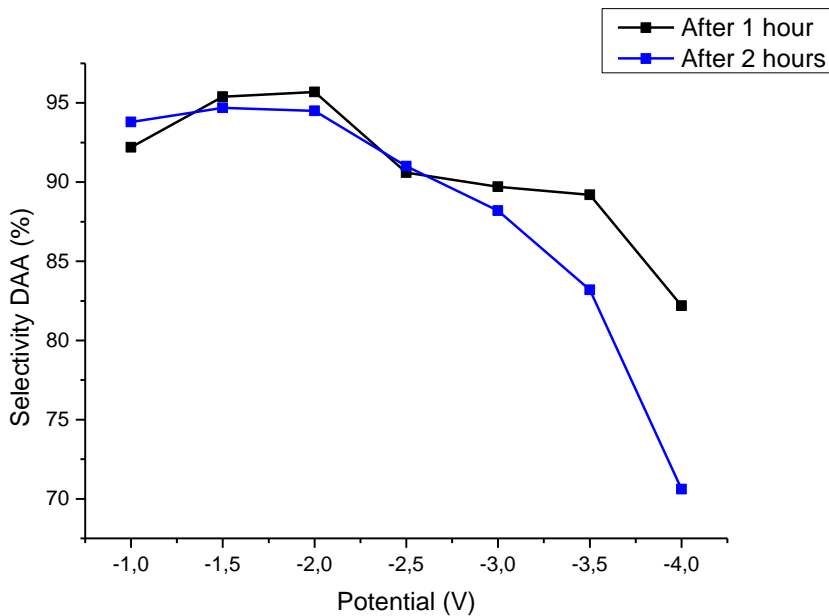


Figure 5.5: The selectivity towards DAA after 1 h of electrolysis (black line) and 2 h of electrolysis (blue line) in separate experiments in the standard setup with a different potential applied in each experiment. WE and CE: 8 cm² platinum sheet, runtime: 2 h.

Figure 5.6 shows the current efficiency for each experiment. The current efficiency is always the highest in the first hour, which corresponds to the earlier noted observation that the increase in DAA concentration is less in the second hour than in the first hour. The ratios of the current efficiencies between the experiments stays the same for both hours with the maximum efficiency obtained at -1.5 V. After 2 hours of electrolysis, -1 V and -2 V have a similar efficiency, which is about 20 % lower than the -1.5 V efficiency. The current efficiency decreases rapidly at potentials more negative than -2.5 V. From an energy-efficiency point of view -1.5 is the optimal potential as it has the highest current efficiency while from a production point of view -2.5 V is preferable since, compared to -1.5 V, it still has a significant increase in DAA concentration while not exhibiting the drawbacks of numerous side reactions and stability issues as encountered at potentials of -3 V and more negative. Combining

both concerns, -2 V is the golden mean as the final DAA concentration is about halfway between -1.5 V and -2.5 V while the efficiency leans more towards the maximum of -1.5 V, additionally the selectivity towards DAA is also the highest at this potential (see Figure 5.5).

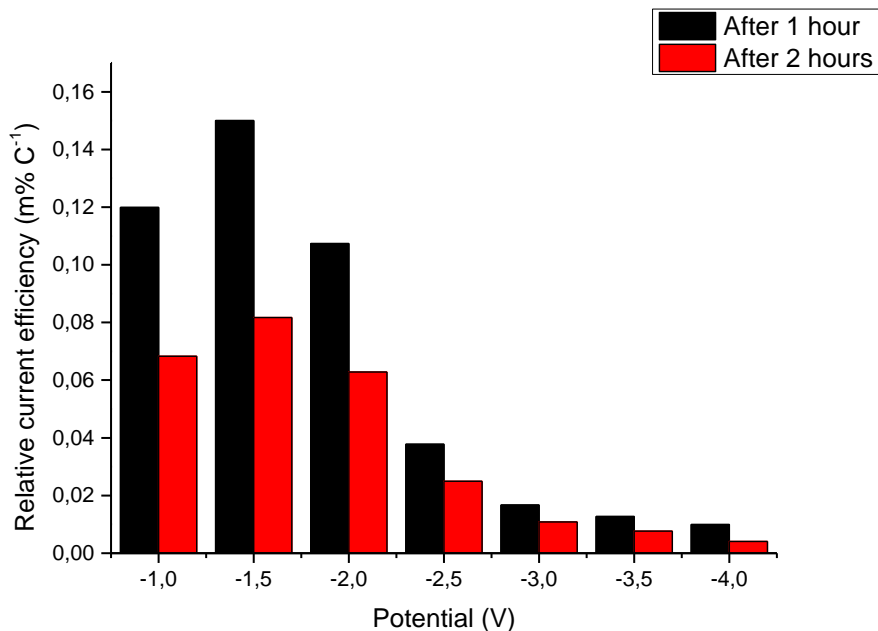


Figure 5.6: Relative (pseudo) current efficiencies for DAA formation after 1 h of electrolysis (black columns) and 2 h of electrolysis (red columns) in separate experiments in the standard setup with a different potential applied each experiment. WE and CE: 8 cm² platinum sheet, runtime: 2 h.

5.3.4 Influence of water in the electrolyte on the yield of DAA

The aldol addition or condensation can be catalyzed by either an acid or a base [75] and thus, adding water to the electrolyte can be beneficial as the electrolysis of water generates in situ acids and bases in the form of H⁺ and OH⁻. The possible advantage of water in the electrolyte is also mentioned by Tsai et al. [102]. To investigate this effect, a series of experiments was conducted in the standard setup with different amounts of ultrapure water added to the electrolyte in following concentrations: 0, 0.5, 1, 2, 5, 8, 10 and 12 m%. Figure 5.7 shows the results of the experiments. Acetone

is a hygroscopic substance and always contains a small amount of water unless dried thoroughly. The acetone used in this work has a maximum water content of 0.1 %, thus the 0 m% described in the experiments contains this amount of water. To evaluate the influence of this tiny amount of water, an experiment with dried acetone (Extra Dry, Acroseal®, ≥99.8 % pure, H₂O <0.005 %, obtained from Acros) was conducted under inert atmosphere and in presence of molecular sieves (3A). The difference between the regular HPLC acetone and the dried acetone was negligible (results not shown).

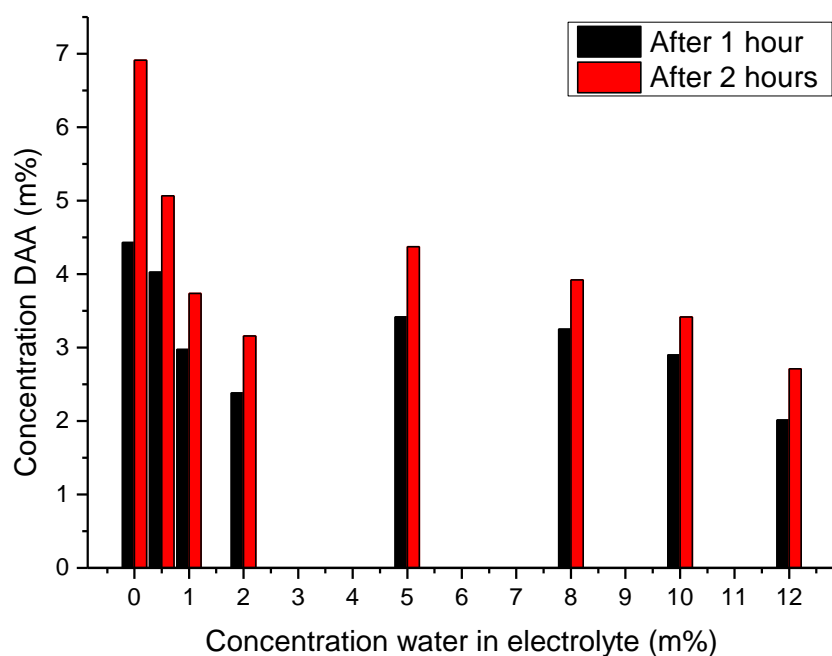


Figure 5.7: The concentration of DAA (m%) versus different amounts of water added to the electrolyte in separate experiments, after 1 h of electrolysis (black columns) and after 2 h of electrolysis (red columns). WE and CE: 8 cm² platinum sheet, runtime: 2 h.

In Figure 5.7 it is clear that adding water does not have a beneficial effect for the production of DAA. The maximum DAA concentration is obtained when no water is added to the electrolyte. For any amount of water added, the resulting DAA concentration is significantly lower. The possible beneficial effect of the in situ generated base in the form of OH⁻ is non-existent or much smaller than the

disadvantageous effect of the water electrolysis. The electrolysis of the water is also observed visually during the experiment. The addition of water causes the formation of bubbles at the cathode and higher concentrations of water increase the amount of bubble formation, indicating the evolution of hydrogen on the cathode. Besides causing a competitive electrochemical reaction to the aldol addition of acetone (or to the generation of the required EGB), the water also slows down the rate of the chemical aldol addition of acetone [81,96], which could be a possible additional inhibition for the reaction via the EGB. Tsai et al. propose reactions at both the cathode and anode for the indirect reaction via the electrolysis of water [100]. The effect of the addition of water described by Tsai et al. does not correspond with the results obtained in this work and the indirect reaction by the electrolysis of water is therefore disputed.

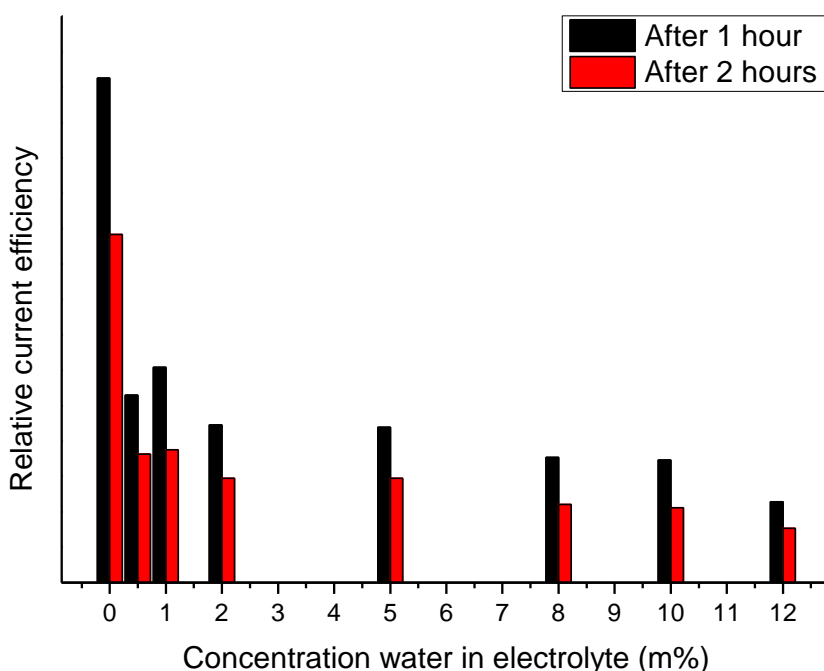


Figure 5.8: Relative (pseudo) current efficiencies for DAA formation versus different amounts of water added to the electrolyte in separate experiments, after 1 h of electrolysis (black columns) and after 2 h of electrolysis (red columns). WE and CE: 8 cm² platinum sheet, runtime: 2 h

5.3.5 Comparing the contribution of anode and cathode

Although the electrosynthetic aldol condensation is usually approached as purely an organic reduction, there are possible contributions of the anode to the reaction. In addition to the indirect reaction via the electrolysis of water, Tsai et al. also propose reactions at both the cathode and anode for the reaction via an EGB. Therefore, it is still interesting to investigate both electrodes separately to see the contribution of each towards the reaction through the formation of an EGB. To this end two experiments were conducted in the divided setup as described in Section 5.2.2. The reference electrode was placed close the working electrode in the same compartment. To investigate the contribution of the anode +2.5 V was applied to the working electrode. In a second experiment -2.5 V was applied to investigate the contribution of the cathode. Figure 5.9 (a) shows the current responses of both experiments.

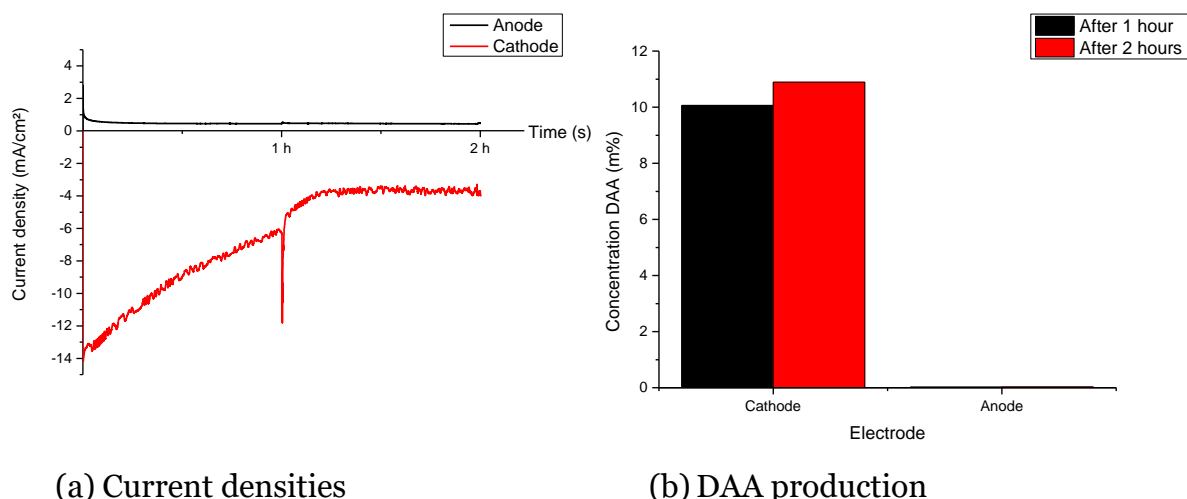


Figure 5.9: (a) Current densities of the anode (black line) and cathode (red line) in separate experiments and (b) resulting DAA concentration after 1 h (black columns) and 2 h (red columns). Experiments in divided setup with respectively -2.5 V and +2.5 V applied to the cathode and anode in separate experiments. WE: 0.156 cm² platinum wire, CE: 8 cm² platinum sheet, runtime: 2 h.

The anodic current density peaks at about 2.8 mA cm^{-2} in the beginning and quickly declines to 1 mA cm^{-2} after which it steadily decreases over the course of two hours to less than 0.5 mA cm^{-2} in the end. The cathodic current on the other hand, peaks at -14 mA cm^{-2} in the beginning, then decreases to about -4 mA cm^{-2} and remains constant around this value. As expected, the current response of the cathode is much larger than that of the anode. Again, the sharp peak due to the sampling after one hour is visible in both plots, though it is more pronounced in the cathode plot. Figure 5.9 (b) shows the results of the analyses from both experiments. The DAA concentration found in the anode experiment was 0.1 m\% , which corresponds with the amount of DAA found in a blank acetone sample after analysis. This small amount is not visible on the scale of Figure 5.9 (b).

It can be concluded that the anode does not contribute to the formation of DAA. The current measured at the anode indicates that some reaction takes place, but the qualitative analysis did not display any clear distinction of a possible product. At the cathode, the formation of DAA is evident. The increase in concentration from one to two hours is very small, even less than what was observed during the potential experiments (see Figure 5.4). It is possible that, similar to the pure chemical reaction, an equilibrium is reached. In the validation experiment (see Section 5.3.1) a final concentration of 13.4 m\% was obtained, running this experiment for 32 hours showed no significant increase in the concentration, indicating a possible equilibrium. In this divided setup, the equilibrium might be reached faster. The discrepancy in final concentration (11 m\% vs. 13.4 m\%) could be due to uncontrolled parameters such as the ambient temperature since the setup is not temperature-controlled. Despite no increase in the DAA concentration in the second hour, the current density does not decrease to zero, but rather stays at a constant value. This means that either an equal amount of DAA is produced as there is converted to MO, other products or being broken down or that side-reactions with the EGB still proceed. As in the anode experiment, no clear distinction of one product was observed in the analysis. However, on the chromatograms of experiments that reached the equilibrium fast or

in long experiments, more variation of the baseline (several very small peaks, not the noise) was observed. The resulting peaks were not pronounced and not separable enough to be identified, but they do indicate numerous products due to further condensation reactions and breakdown products.

5.3.6 Effect of the electrode material

In the previous experiments platinum electrodes for both the working and counter electrode were employed. Platinum was chosen as it has proven to have a good activity towards the electrochemical aldol condensation [98–102]. From Section 5.3.5 it is clear that the reaction proceeds at the cathode. To investigate if the reaction is independent on the electrode material or if the material plays an important role in the generation of the EGB, two other materials beside platinum are tested as the cathode: gold and glassy carbon. The experiments were conducted in the divided setup with a potential of -2.5 V applied to the working electrode.

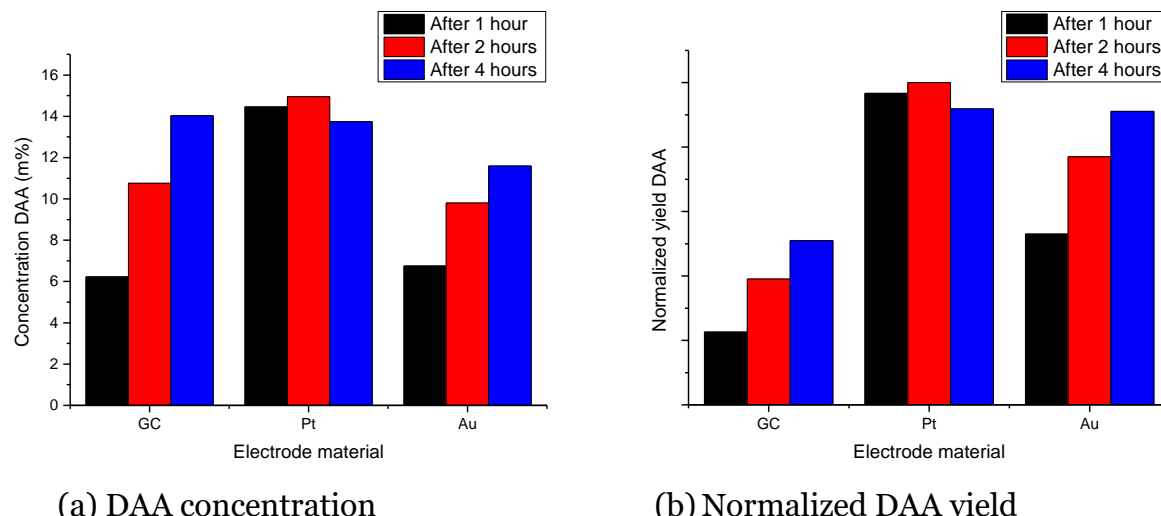


Figure 5.10: DAA concentration (a) and surface area normalized yield (b) after 1 h (black columns), 2 h (red columns) and 4 h (blue columns) of electrolysis in separate experiments with different working electrodes: 0.287 cm^2 glassy carbon disk, 0.156 cm^2 platinum wire and 0.133 cm^2 gold disk, CE: 8 cm^2 platinum sheet. Potential: -2.5 V.

Figure 5.10 (a) shows the DAA concentration after one, two and four hours for each experiment. While for both gold and glassy carbon the concentration steadily increases over the 4 hours, for platinum the concentration remains about constant, even slightly decreasing after 4 hours. This corresponds to earlier observations described in Section 5.3.1 and 5.3.5 that an equilibrium is reached. For gold this concentration is also reached after four hours, but for glassy carbon this concentration does not get reached in the same time span, making it the least active material for this reaction. Though the same final concentration is obtained by both platinum and glassy carbon electrodes, platinum remains the better choice as it reaches this concentration in a much shorter time span. In Figure 5.10 (a) the concentration is used as a measure for the performance which is an intensive property, but does not take into account the surface area of the electrode. As an electrochemical reaction is a surface process, this is an important parameter. Therefore, in Figure 5.10 (b) a normalized yield is used as a measure for the performance, which is the amount of DAA produced per unit of surface area taking platinum as a reference. It can be seen that gold outperforms glassy carbon which can also be derived from Figure 5.10 (a) since it reached almost the same concentration as glassy carbon, but has less than half the surface area.

It is clear that in this setup, for platinum, the maximum DAA concentration is reached within the first hour. To further investigate the course of the reaction in the first hour, the experiment for platinum was repeated and sample was taken each ten minutes. Figure 5.11 shows the analysis result. 0 minutes is not shown as this is the start of the experiment and no DAA has formed yet. The big increase between 10 and 20 minutes seems unlikely and is possibly due to experimental error. More important is that the concentration seems to increase to its final value with a declining increase. 80 % of the final concentration is already reached after 30 minutes and after 50 minutes the maximum concentration is obtained. The data describes the course of an exponential curve: the concentration increases over the course of the reaction, but the increments between two measurements decrease. The selectivity towards DAA increases from

~93 % after 10 minutes to ~97 % after 20 minutes after which it remains constant. The reaction on platinum shows the same behavior as gold or glassy carbon, but it proceeds much faster.

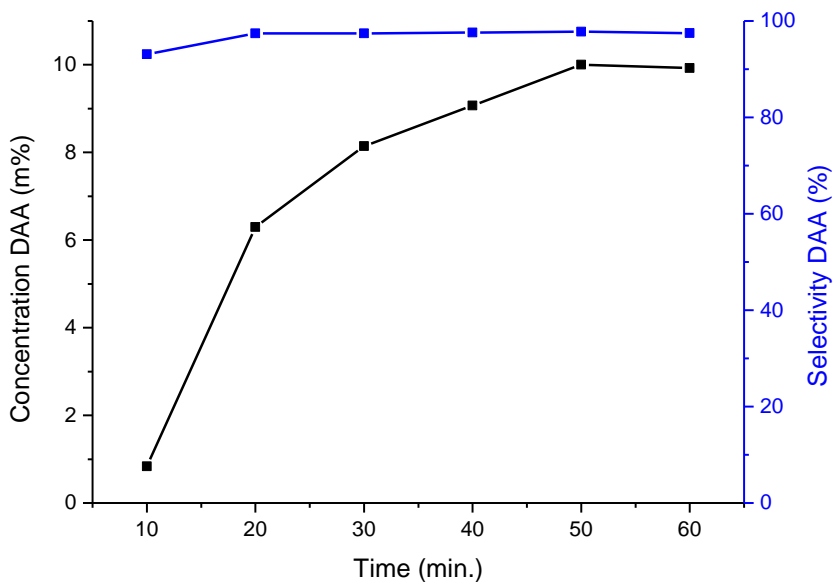
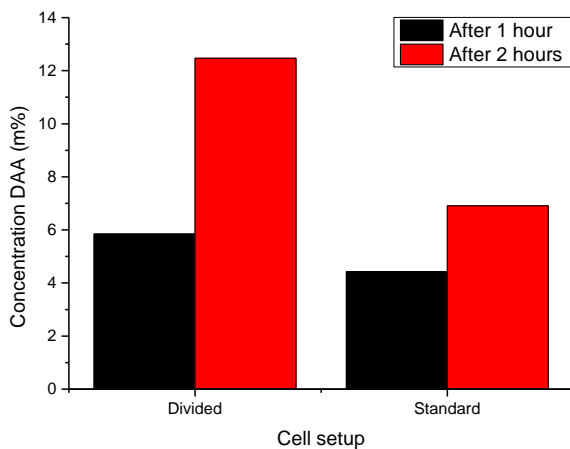


Figure 5.11: The DAA concentration (black line, left y-axis) and corresponding selectivity (blue line, right y-axis) during a 1 h experiment in the divided setup, sampling each 10 min. WE: 0.156 cm^2 platinum wire, CE: 8 cm^2 platinum sheet. Potential: -2.5 V. Runtime: 1 h.

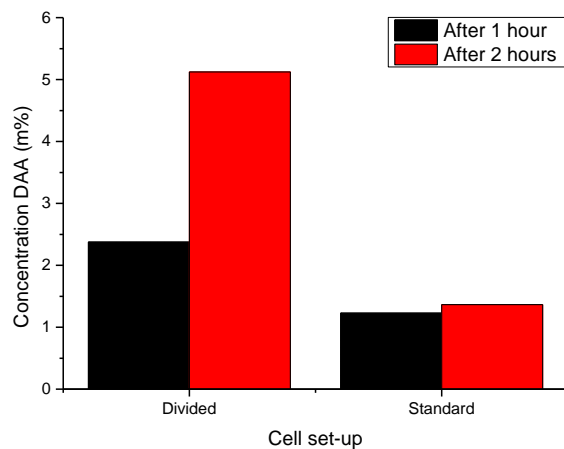
5.3.7 Reaction crossover and cell setup

During the experiments in the divided setup (Section 5.3.5 and Section 5.3.6) it was noticed that the resulting DAA concentration was higher than expected when compared to the standard (undivided) setup, based on the surface to volume ratio. More specific a higher concentration per electrode surface area was reached in the same timespan compared to the standard setup. This effect is also noticeable in the difference in formation rates of DAA between the two setups. In the standard setup the formation rate was $2.20 \times 10^{-3} \text{ M min}^{-1}$ (see Section 5.3.1) while in the divided setup the formation rate amounts to $11.38 \times 10^{-3} \text{ M min}^{-1}$ after one hour and even to $18.66 \times 10^{-3} \text{ M min}^{-1}$ if only the first 30 minutes are considered. To investigate this effect, two experiments were performed which were identical besides the setup. The

same two experiments were repeated with another working electrode. The working electrode was a platinum wire (0.156 cm^2) in the first two experiments and a platinum sheet (8 cm^2) in the other two, the counter electrode in all experiments was a platinum sheet (8 cm^2). The surface to volume ratio was equal between two experiments with the same working electrode.



(a) WE: sheet electrode.



(b) WE: wire electrode

Figure 5.12: DAA concentration for a Pt sheet electrode (a) and Pt wire electrode (b) after 1 h (black columns) and 2 h (red columns) of electrolysis in a divided and standard (undivided) setup. CE: 8 cm^2 Pt sheet. Potential: -2.5 V.

Figure 5.12 shows the distinct difference between the standard setup and the divided setup, which is the same for both electrodes: in both cases, the divided setup leads to a higher DAA concentration. For the wire electrode (Figure 5.12 (b)) the difference in final concentration between the two setups is much larger and the increase after the first hour in the standard setup is very small. Considering the results from previous experiments this is likely due to an experimental error. However, it is obvious that the divided setup leads to better yields. This can be attributed to crossover of intermediates or products, which has a negative effect on the DAA production.

5.4 Conclusions

The electrosynthetic pathway of the aldol reaction of acetone has been investigated. Voltrammetric research showed that the reaction is an electrochemically initiated reaction. Therefore an applied approach was taken to investigate the reaction. Even though no thorough optimization was done, it was possible to obtain DAA concentrations of 10-11 m% in the standard setup up to 15 m% in the best case in the divided setup in two hours of electrolysis. This is significantly more than the 2.8 % after two hours of galvanostatic electrolysis reported by Tsai et al. and similar to the commercial fixed-bed reactors operating at 15 °C. The parameters for this maximum concentration were a platinum working electrode, separation of both electrodes and -2.5 V potential applied, although a better trade-off between yield and current efficiency is obtained at -2 V. The potential-controlled electrochemical aldol condensation of acetone to diacetone alcohol was performed in a batch setup. A number of parameters was screened. The results show that, contrary to the findings of Tsai et al., adding water to the electrolyte has a disadvantageous effect on the production of diacetone alcohol. The possibility of an indirect reaction via the electrolysis of water is hereby disputed. Furthermore it is confirmed that platinum is the most active for this reaction and that the reaction proceeds exclusively via the cathode. However, it is also found that separation of the cathode and anode compartments of the cell prevents breakdown of diacetone alcohol and thus, has a beneficial effect on the production.

CHAPTER 6

The application of an electrochemical microflow reactor

THE CONSTRUCTION AND DESIGN OF AN ELECTROCHEMICAL MICROFLOW REACTOR FOR THE ELECTROCHEMICALLY INDUCED ALDOL REACTION OF ACETONE IS DESCRIBED. THE SETUP IS BUILT MODULAR TO PROVIDE VERSATILITY IN THE ELECTRODE MATERIAL AND ELECTROLYSIS SETUP. THE MODULAR SETUP IS APPLIED TO INVESTIGATE THE CONVERSION OF THE ELECTROSYNTHETIC ROUTE ESTABLISHED IN THE PREVIOUS CHAPTER TO A CONTINUOUS FLOW PROCESS. IMPORTANT REACTOR PARAMETERS ARE SCREENED AND DISCUSSED.

This chapter is published as: D. Pauwels, B. Geboes, J. Hereijgers, D. Choukroun, K. De Wael, T. Breugelmans, The application of an electrochemical microflow reactor for the electrosynthetic aldol reaction of acetone to diacetone alcohol, Chemical Engineering Research & Design, 128 (2017) 205-213.

6.1 Introduction

In this chapter the construction and application of a microfluidic system for the electrochemically induced aldol reaction of acetone to diacetone alcohol is discussed. Industrial viability and implementation requires a robust design with focus on the ease of operation and high rate of product formation. Therefore, the design is uncomplicated and is based on a parallel plate electrode arrangement where both electrodes directly face each other, separated by a single flow channel. All benefits of the microfluidic reactor are maintained while a simple, yet performant device is acquired. This type of reactor design for electrochemical synthesis with rectangular flow channels is a widely used design in both industrial and laboratory applications and has been characterized extensively [135,138], demonstrating its viability.

Microreactors imply characteristic dimensions in the micrometer range, however, the device developed in this chapter has characteristic dimensions in the millimeter range and volumes in the milliliter range. Such devices sometimes are also called mesoreactors or millireactors, but these terms are not common practice and most often such devices are included in the definition of microreactors (see Figure 4.5). In this thesis the broader definition of microreactors is used.

The setup is validated by evaluating different configurations with varying reactor and reaction parameters. This is done by checking the flow and the mass transfer on the one hand and assessing the performance (maximum obtainable concentration and selectivity), production rate capacity (yield per unit of time and space time yield) and efficiency (here: yield per unit of charge) on the other hand. Calculating the dimensionless current efficiency requires knowledge of the exact reaction mechanism, which for this reaction is not known. As a measure for the apparent current efficiency the ratio of the yield to the charge passed in the cell is used as both are related through Faraday's law of electrolysis. The space time yield ρ_{ST} is calculated using the reactor volume over the electrode. The aforementioned figures of merit are

always interpreted with respect to the electrode surface area and the specific interfacial area, as these parameters determine for a large part the cost of the construction of the reactor.

6.2 Experimental

6.2.1 Chemicals

Acetone (HPLC grade, 99.8+ %) was purchased from Chem-Lab (Belgium). The supporting electrolyte tetrabutylammonium perchlorate (TBAP, *n*-Bu₄NClO₄, 99.0 %), potassium ferricyanide (K₃[Fe(CN)₆]), potassium ferrocyanide (K₄[Fe(CN)₆]) and sodium sulphate (Na₂SO₄) was purchased from Sigma-Aldrich (Belgium). The platinum plating solution (Platinum Q Salt® Pt 5Q) was obtained from Alfa Aesar (Germany). The ultrapure water (18.2 MΩ cm⁻¹ at 25 °C) was prepared in the laboratory (Milli-Q, Millipore). To minimize the effects of the uncompensated resistance in the reactor, a value was determined by impedance spectroscopy for different configurations of the reactor which could be compensated by positive feedback. Typically the value for the uncompensated resistance was less than 10 Ω owing to the small distance between the reference and working electrode.

6.2.2 Reactor design

To be suitable for industrial implementation, the electrochemical microreactor needs certain design criteria besides the performance requirements such as high yields, high productivity, high selectivity and a good reaction control. In particular, it should provide a platform that is easy to operate by non-specialists, a modular setup to fit specific operating conditions and a robust design that is capable of an extended runtime. Furthermore it is also beneficial if the construction is easy and cheap. The most basic type of cell construction that is able to meet the specifications consists of an undivided setup with a solid electrode plate-to-plate geometry. Hence, this is the design the electrochemical microreactor is based upon with focus on a high specific

electrode surface area and a low inter-electrode distance. The reactor is schematically illustrated in Figure 6.1 and one reactor half is illustrated in Figure 6.12.

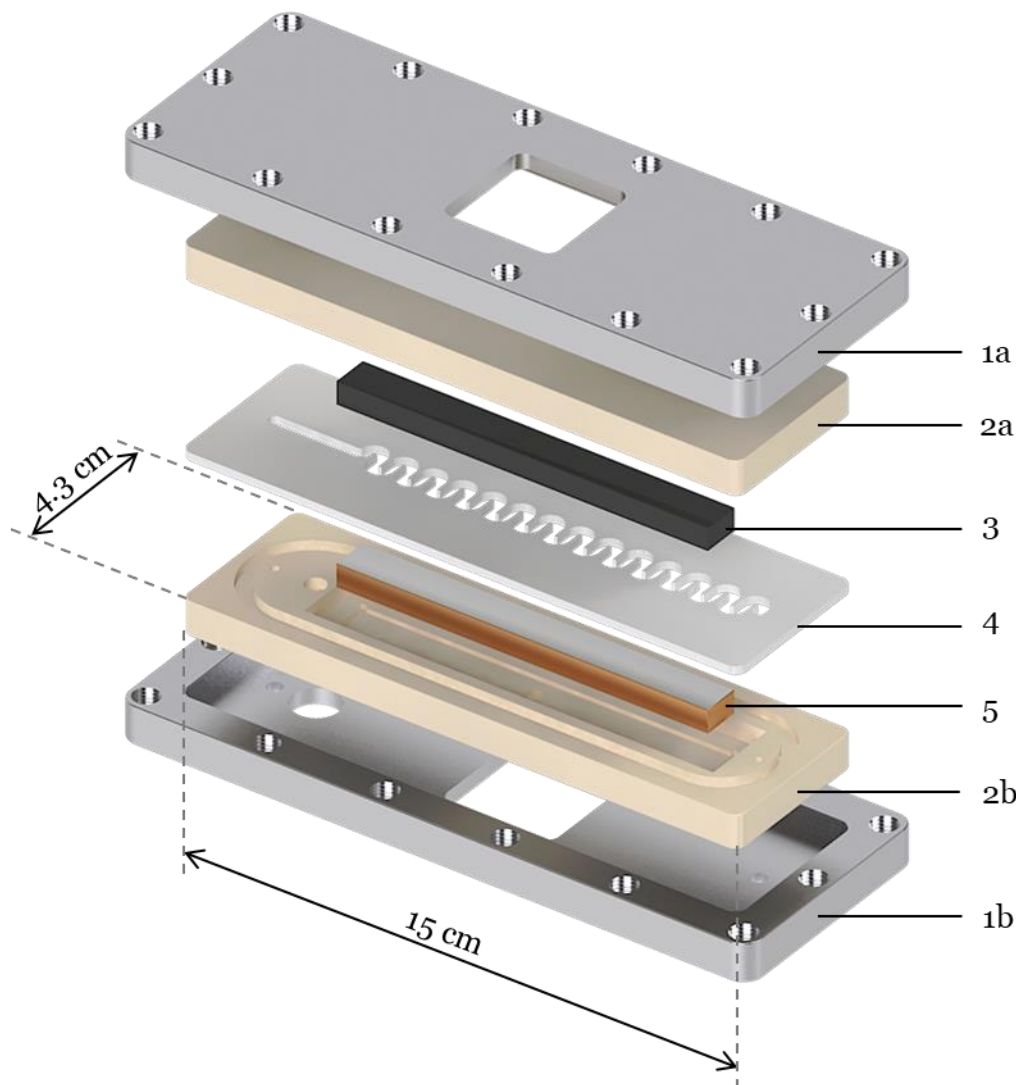


Figure 6.1: Exploded view of the electrochemical microreactor. **1** Aluminium housing with holes for the in- and outlet tubing, electrode connections and reference electrode (1b only). **2** PEEK housing in which the electrodes are embedded with epoxy with in- and outlet ports, reference electrode port (2b only), hole for the electrode connection and groove for the EPDM O-ring. **3** Glassy carbon counter electrode. **4** POM spacer with serpentine reaction channel. **5** Working electrode consisting of a copper substrate with a deposited platinum layer on top.

The reactor consists of two parts which hold the electrodes. The electrodes are solid bars (Figure 6.1 no. 1) embedded with an epoxy resin in a PEEK (polyether ether ketone) housing (Figure 6.1 no. 2). The PEEK material ensures an excellent chemical resistance to solvents and inorganic acids in the common concentrations as well as a high temperature resistance (if needed) and excellent adhesion to the epoxy resin. The PEEK housing has ports for the inlet and outlet of the flow channel and a threaded opening for the Ag/Ag⁺ reference electrode (RE-7VP, ALS Co., Ltd, Japan). An electrical connection to the electrodes is glued with conductive silver epoxy in an opening in the back through which the electrodes are accessible. The electrodes are separated by a POM (polyoxymethylene) spacer in which the flow channel is machined (Figure 6.1 no. 3). The thickness of the spacer determines the distance between the electrodes (inter-electrode distance) and the reactor volume. In this work the spacer thickness is set to 4 mm giving a total reactor volume of 3.88 ml and a volume of 1.42 ml over the electrode for one channel in the divided setup. In order to achieve a good sealing, a groove was milled in the PEEK housing to incorporate an EPDM (ethylene propylene diene monomer rubber) O-ring which is compressed between the housing and the spacer. The two parts are held together in an aluminium holder which is secured by 14 bolts to 4 Nm (Figure 6.1 no. 4). The setup is easily and quickly dismantled and reassembled, unlike many designs reported in literature which are sealed completely. Swapping electrodes is done by using different housing parts in which other materials are embedded. A membrane can be incorporated in the reactor by fixing it between two identical spacers. The electrolyte flow was provided by a HPLC pump (DeltaChrom P102 double piston pump). When a measurement is started it takes some time for a concentration profile to develop in the reactor which depends on the flow rate of the electrolyte. This is noticeable in the current response where initially a large current is observed which gradually decreases to a steady value. When steady state is reached, a sample is taken by filling a vial at the outlet. Each experiment is performed at least three times, unless specified otherwise.

6.2.3 Pt deposition

The deposition of the platinum layers was done from a commercial plating solution (see Section 6.2.1) which is a 26×10^{-3} M solution of $\text{Pt}(\text{NH}_3)_4\text{HPO}_4$ in a dilute phosphate buffer ($\text{pH} \sim 10.6$). The deposition parameters were based on a literature report on plating bath conditions [163]. To optimise the deposition and characterise the deposited platinum layer, a solid copper disk electrode ($d = 6$ mm) was used as a substrate. For the working electrode in the reactor, a $10 \times 1 \times 0.6$ cm copper plate embedded in a PEEK casing as described in Section 6.2.2 was used. Prior to the deposition the electrodes were mechanically polished (Struers LaboPol-5) with $1 \mu\text{m}$ alumina slurry and rinsed with ultrapure water. The deposited platinum layer was also polished with subsequently 1 , 0.3 and $0.05 \mu\text{m}$ alumina slurry and rinsed. The plating was performed in a three electrode configuration with a Pt counter electrode and Ag/AgCl reference electrode. For the reactor electrode, a special holder was machined and multiple platinum plate counter electrodes were combined and placed under the copper plate working electrode, covering the entire electrode. This ensures a uniform current distribution over the electrode so a uniform deposit is obtained. Several constant current and constant potential depositions were performed and the best results were obtained with a constant potential deposition at -720 mV vs. Ag/AgCl and at 365 K until a charge of 1 C cm^{-2} was passed. The high temperature has no direct influence on the deposited layer, but a limited influence on the efficiency and thus the rate of the deposition. A strict control of the temperature ensures a good reproducibility of the deposits. When glassy carbon (GC) was used as a substrate, visually identical platinum layer deposits were obtained but the deposited layers could easily be wiped off with the slightest touch. Contrarily the copper substrate depositions showed excellent adhesion and could only be removed by sanding down or polishing the electrode.

6.2.4 Mass transfer limitation measurements

To evaluate the different designs of the spacers used in this work, the effect of the channel design on the mass transfer was investigated using the limiting-current technique (see Section 3.3.1.2). This technique and its application on micro- and minichannels is well documented in literature [52,164–166].

If a well-known electrochemical system is used the mass transfer coefficient can easily be calculated from $I_L = k_m nFAC_b$. In this work the reduction of ferricyanide to ferrocyanide is used. The electrolyte used in the measurements consisted of 1×10^{-3} M potassium ferricyanide, 5×10^{-3} M potassium ferrocyanide and 0.5 M sodium sulphate as supporting electrolyte in ultrapure water. The electrodes in the reactor have the same dimensions, so to ensure that the limiting reaction is the cathodic reaction of ferricyanide, a 5 times higher concentration of ferrocyanide was used. The diffusion coefficient is 6.532×10^{-10} m² s⁻¹ and the Schmidt number 1479 [145]. To perform the measurements, the inlet flow was held constant and the potential was stepped over a range. At each potential step the current was allowed to converge to a steady value before it was measured. This was done for a series of fixed values for the inlet flow.

6.2.5 Analysis

Analysis of the samples was performed by GC-FID (Thermo Scientific Trace 1300) on a polar capillary column (Restek RTX-Wax 30 m × 0.25 mm, PEG 0.25 µm). The carrier gas flow (He, 5.0 purity) was controlled at 1.4 ml min⁻¹. The temperature of the column was held constant at 40 °C for 1 minute and then ramped to 200 °C at 40 °C min⁻¹. This resulted in excellent separation of the target products allowing easy quantification. A calibration curve between 1 and 20 m% was established with a correlation coefficient of 0.9939. All samples were analysed at least three times with a standard deviation of no more than 5 % and usually much less.

6.3 Results and discussion

6.3.1 Characterization and validation of the deposited platinum layer

In Chapter 5 it was established that, from a selected number of materials, platinum showed the best activity towards the aldol reaction of acetone as the equilibrium concentration is reached in the shortest amount of time. To incorporate platinum as a working electrode in the reactor, electrodeposition was used as a convenient and cost-effective method compared to using a solid platinum electrode. In case a larger surface area is desired, a similar deposition on a 3-dimensional electrode can be performed [167]. The depositions were performed as described in Section 6.2.3. Scanning electron microscopy (SEM) was used to characterise the surface of the deposited layer and a batch experiment was performed to compare the platinum deposit to a solid platinum disk electrode of equal size (Figure 6.3). After the deposition, the platinum layer has a dull metallic appearance with a darker tint compared to a polished solid platinum disk electrode. The SEM image shows a roughened surface. Polishing the deposited layer gives a very bright and highly reflecting metallic appearance making the electrode indistinguishable from a polished solid platinum disk electrode. The SEM image reveals a uniform layer with no cracks and very little inconsistencies, similar to the solid electrode. The deposited layer also shows very good adhesion to the copper substrate and can be polished until the substrate becomes visible. To evaluate the performance of the deposited platinum electrode, the performance in a standard batch experiment is compared to that of a solid platinum disk electrode of equal size (Figure 6.2). It is clear that both electrodes perform similarly.

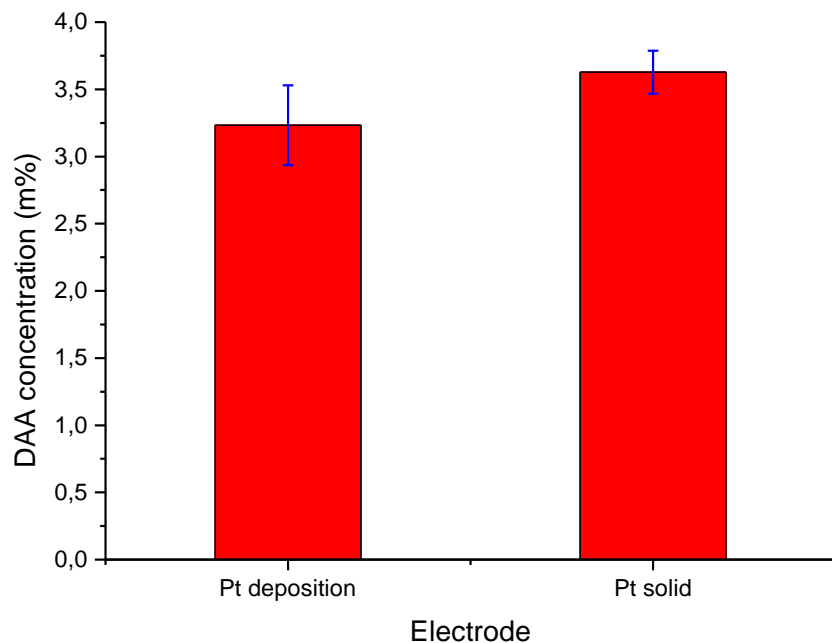


Figure 6.2: Comparison of a deposited platinum electrode (Pt deposition) and a solid platinum electrode (Pt solid). DAA concentration after two hours of electrolysis in batch setup. Electrolyte = 50 ml acetone + 0.1 M TBAP, $E = -2.35$ V vs. Ag/Ag⁺, Selectrodes: 0.28 cm². Experiments performed in triplicate.

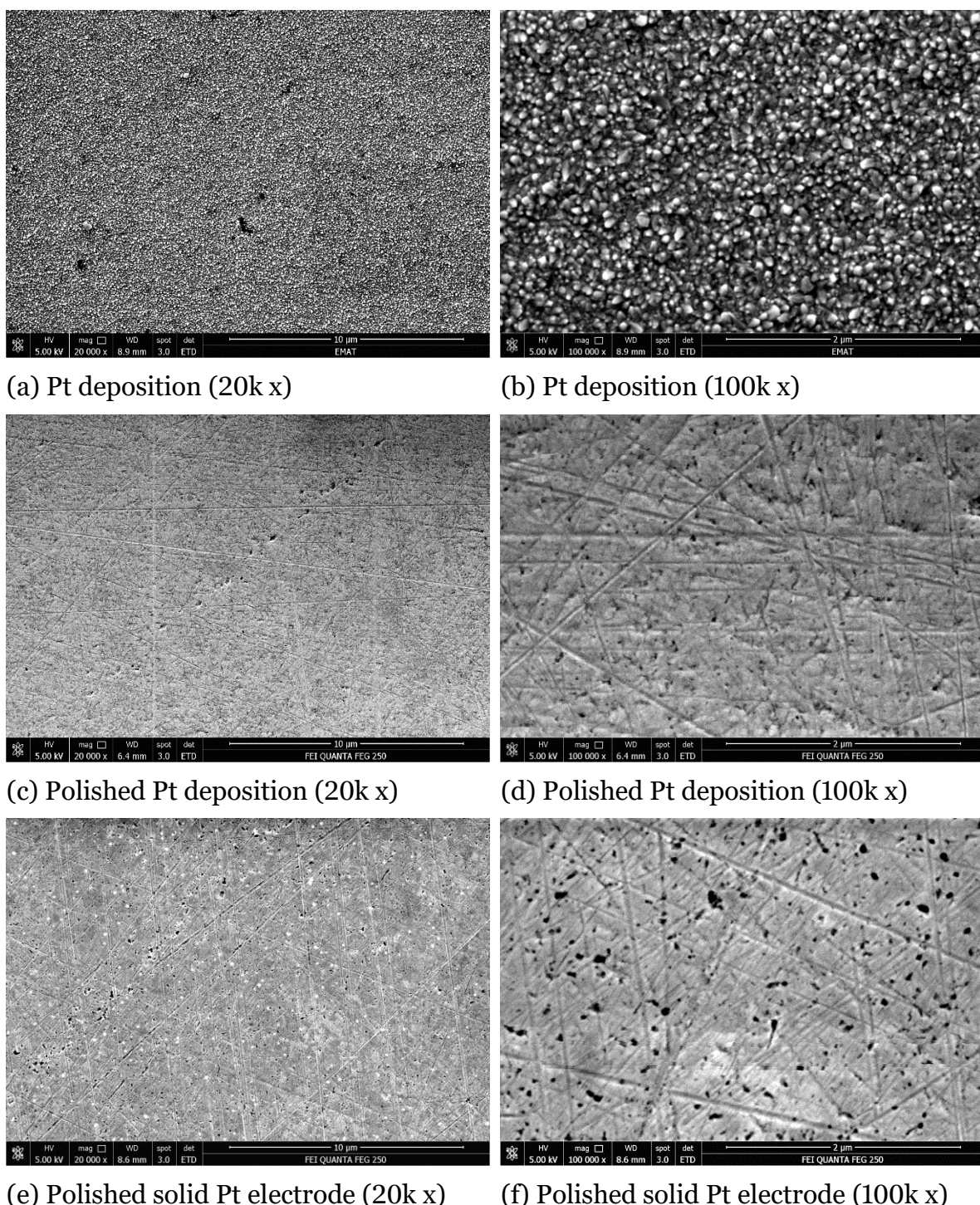


Figure 6.3: SEM images for the platinum layer deposition on copper and a solid platinum electrode. Constant potential deposition in Pt 5Q plating solution with T: 365 K, pH: 10.5, E: -720 mV vs. Ag/AgCl, Q: 1 C cm⁻²

6.3.2 Reactor setup considerations

The aldol reaction is an indirect reaction initiated by an anionic species generated at the cathode. In an undivided batch setup the reaction is impeded by the cationic species generated by the anode, which can react with the anionic species generated at the cathode. This cross-over of cathodic species can be driven by forced convection or diffusion. An easy way to prevent this in a batch setup is to separate anode and cathode. To prevent the cross-over in the microreactor setup, the spacer is designed carefully, so that a laminar flow in the reaction channel is obtained. Due to this laminar flow, the mass transfer of species in the direction perpendicular to the electrode's surface is only realised by diffusion. If the ratio of the residence time to the inter-electrode distance is set appropriately, cross-over and the mixing of electrogenerated species in the reactor is prevented. This circumvents the need for a membrane which entails a higher cost and a more complex setup. However, when performing the reaction in continuous flow in the microreactor, it becomes immediately clear that in this setup, the cross-over is not sufficiently prevented by the laminar flow solely. This can be explained by the development of the diffusion layer in the reactor. The parallel plate design with a rectangular reaction channel effectively creates a channel electrode. The current-potential behaviour deviates from ideal channel electrode behaviour due to the electrode dimensions relative to the channel dimensions, i.e. the electrode width and length equals the channel width and almost length. A channel electrode is non-uniformly accessible because the diffusion layer thickness varies along the electrode as $L^{1/3}$ where L is the electrode length [168]. A mean linear diffusion layer thickness δ can be calculated according to the Nernst model by:

$$\delta = \frac{D}{k_m} \quad (6.1)$$

Or considering equation (3.29), this becomes:

$$\delta = \frac{nFAC_bD}{I_L} \quad (6.2)$$

This equation might yield a value for the diffusion layer thickness which is much smaller than half of the reaction channel height but, due to the non-uniformity of the electrode, the diffusion layers can still overlap in the downstream end of the reaction channel. As explained earlier, this leads to cross-over of the generated species which limits the reaction. The consequence is that the concentration of DAA in the product stream is considerably less when no membrane is used compared to when a membrane was used, in which case the equilibrium concentration could be achieved (Figure 6.4).

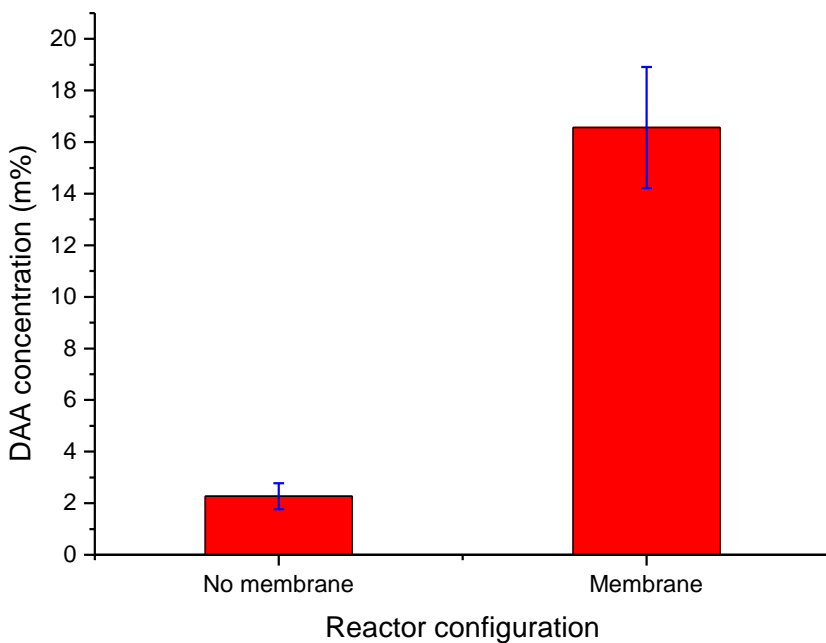


Figure 6.4: Comparison of the DAA concentration in the product stream in the reactor setup with no membrane (left) and membrane employed (right). Electrolyte = acetone + 0.1 M TBAP, $E = -2.35$ V vs Ag/Ag⁺, GC working and counter electrode, $\dot{V} = 0.5$ ml min⁻¹, $v = 0.18$ mm s⁻¹. Experiments performed in triplicate.

Hence, the setup requires the use of a membrane to separate the electrodes adequately. The membrane used in this work is a commercial polypropylene

microporous monolayer membrane (Celgard® 2500) with a thickness of 25 µm and 64 nm pores (Figure 6.5).

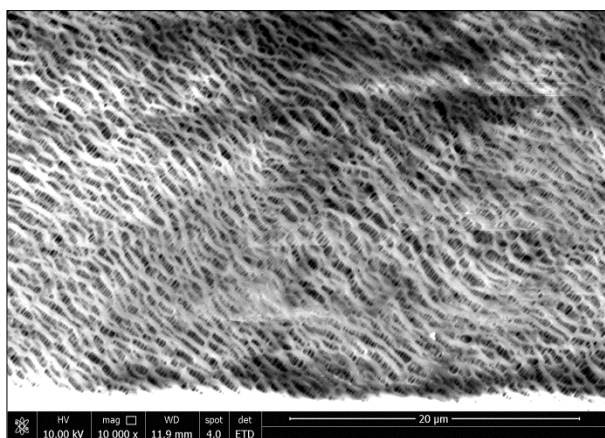


Figure 6.5: SEM picture (20k magnification) of the Celgard® 2500 membrane.

When a membrane is incorporated in the reactor, attention should be given to the spacer design. The spacer channel was designed to ensure an easy definable laminar flow in the reactor. The most straightforward design is a rectangular channel such as spacer A in Figure 6.6. When a membrane was fixed between two identical spacers of design A, sometimes the outlet flow of one of the two channels was significantly less than the other. This can be attributed to the fact that the membrane bends in the reactor due to a lack of support and partially or completely blocks one of the channels. To increase the support of the membrane, a second spacer with a serpentine channel design was machined (Figure 6.6, spacer B). The bends in the reaction channel support the membrane. When this spacer is used in combination with a membrane, no difference is observed in the flow rate of both product streams. As an additional advantage, this design offers a much longer reaction channel compared to spacer A.

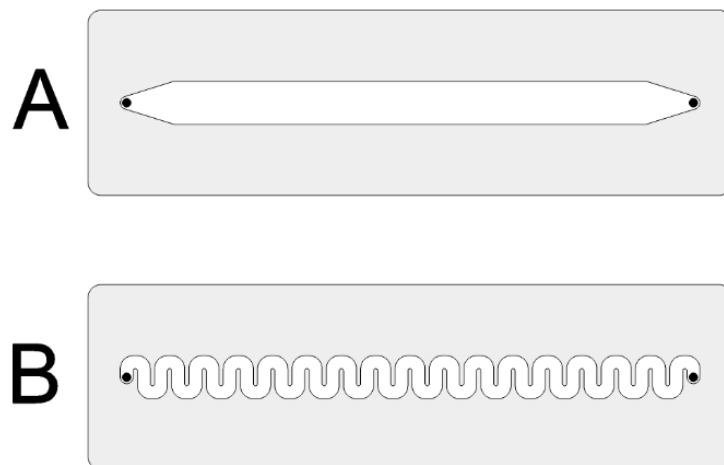


Figure 6.6: Representation of the spacer design, outer dimensions = 50 x 150 mm. Spacer A: rectangular channel with channel length 130 mm and channel surface area 1252 mm². Spacer B: serpentine channel with channel length 318 mm and channel surface area 971 mm². The dots represent the electrolyte inlet and outlet.

Both the total surface area of the reaction channel and the accessible electrode surface area are slightly smaller for spacer B compared to spacer A. Therefore spacer B has a slightly smaller reactor volume but still a similar electrode surface area to volume ratio (specific electrode area) at equal spacer thickness compared to spacer A. The total surface area of the channel in spacer A is 1252 mm² with an electrode surface area of 1000 mm². The corresponding channel length is 130 mm with a path length over the electrode of 100 mm. In spacer B the total surface area is 971 mm² with an electrode surface area of 730 mm² and a total channel length of 318 mm with a path length over the electrode of 232 mm. These numbers yield a specific electrode area of 5 cm⁻¹ for both spacers. The spacer thickness is 4 mm in the undivided setup and 2 mm in the divided setup for each spacer with the membrane clamped in between. Both setups provide an inter-electrode distance of 4 mm.

6.3.3 Evaluation of the spacer design

It is obvious that the spacer design influences the mass transfer of the electrochemical active species to the electrode surface, which is an important parameter with regards to the efficiency. In the electrosynthetic aldol reaction as performed, the electroactive species is the solvent itself, which is abundant at the electrode's surface. Hence, it could be said that mass transfer towards the electrode is of lesser interest. However, the radical species generated at the electrode are very reactive and increasing the mass transfer is important to prevent the reaction of the active species with the formed aldol which leads to further condensation products. In addition the increased mass transfer of the generated active radicals into the bulk increases the amount of possible radicals that can be formed, further increasing efficiency.

To evaluate the performance of both spacers, the global mass transfer was determined as described in Section 6.2.4. A single spacer was used with a thickness of 4 mm. Measurements of the limiting current were performed for volumetric flow rates $\dot{V} = 0.5, 1, 2$ and 3 ml min^{-1} which corresponds to a mean linear flow velocity of the electrolyte $v = 0.21, 0.42, 0.83$ and 1.25 mm s^{-1} respectively for spacer A and $v = 0.68, 1.36, 2.73$ and 4.09 mm s^{-1} for spacer B. Corresponding current-potential plots as illustrated in Figure 6.7 are obtained.

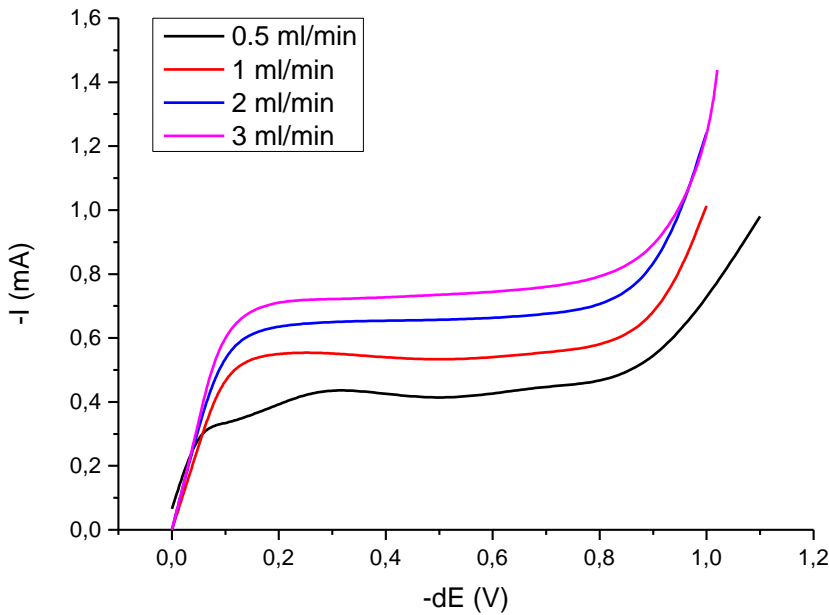


Figure 6.7: Current-potential plots of the limiting current region for the reduction of ferricyanide in the reactor with spacer A.

The plots show an initial steep increase of the current until a well-defined plateau is reached. This is the limiting current plateau from which the limiting current is derived. When the potential is stepped further, at a certain moment the current increases again, this is due to the onset of hydrogen evolution. For channel electrodes the limiting current is given by

$$I_L = 0.925nFAC_b D^{2/3} \left(\frac{V}{h^2 d} \right)^{1/3} wx^{2/3} \quad (6.3)$$

Where d and h are respectively the channel width and half the channel height and w and x the electrode width and length. Equation (6.3) is valid when $h \ll d$ and the electrode width w is sufficiently smaller than the channel width d to prevent edge effects. In addition the equation does not hold for sufficiently low flows or long electrodes as in such case, the Levêque approximation that is used (and in extension equation (6.3)) is no longer valid [168]. From equation (6.3) it is clear that for channel electrodes there is a linear correlation between the limiting current I_L and the cube

root of the flow rate \dot{V} . As explained in Section 6.3.2, the spacer design and resulting reaction channel geometry does not represent an ideal channel electrode since the electrode width is equal to the channel width and the length is almost equal. Nevertheless plotting I_L versus $\dot{V}^{1/3}$ gives a Pearson's correlation coefficient of 0.996 for spacer A and 0.892 for spacer B which indicates that the limiting current behaviour of the reactor for both spacers is still comparable to that of an ideal channel electrode.

From the limiting currents, the global mass transfer coefficients k_m were estimated using equation (3.29) and subsequently the Sherwood number Sh was calculated by:

$$Sh = \frac{k_m D_H}{D} \quad (6.4)$$

Where k_m is the global mass transfer coefficient, D_H is the hydraulic diameter and D the diffusion coefficient. The Sherwood number represents the ratio between the mass transfer by convection and mass transfer by diffusion and is the dimensionless version of the mass transfer coefficient. To characterise the performance of the spacers, Sh is plotted versus Re in Figure 6.8.

The fact that for the same volumetric flow rates the Re number for spacer B is higher than for spacer A is a logical consequence from the difference in aspect ratio and channel length between the two spacers. The hydraulic diameter is 40% less for spacer B compared to spacer A, but the channel length increases by more than 140%, which leads to higher fluid velocities (and thus Re numbers) for the same volumetric flow rates.

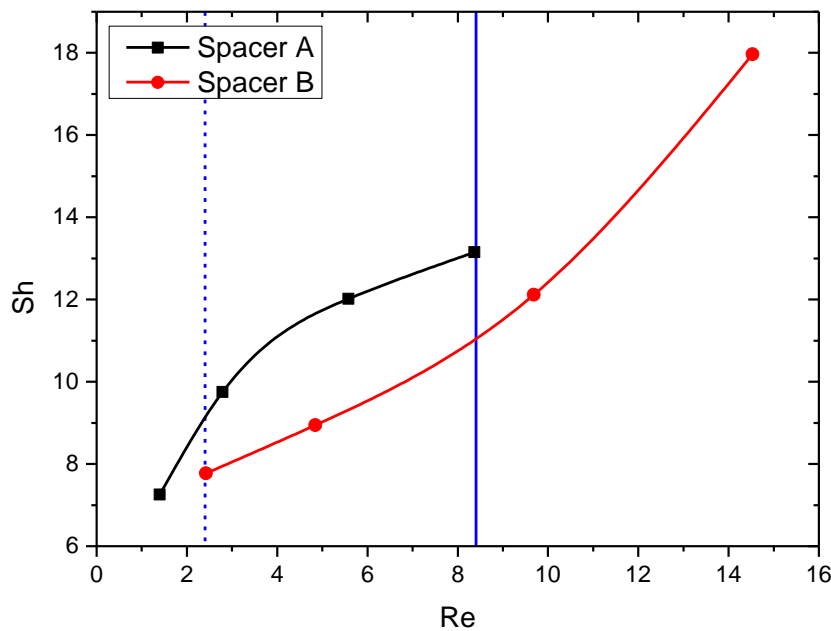


Figure 6.8: Sh versus Re plot for the two spacers. Squares connected by solid line: spacer A, dots connected by dashed line: spacer B. The horizontal lines mark the area of equal Re , which is referred to in Figure 6.9.

A more interesting observation is that in the range of equal Re numbers, the mass transfer in spacer A is higher than in spacer B. To a certain extent, this is the consequence of the development of the flow profile, which can be checked by calculating the Graetz number as follows:

$$Gz = \frac{D_H}{L} Re Sc \quad (6.5)$$

Where D_H is the hydraulic diameter, L the length and Re and Sc the well-known Reynolds and Schmidt numbers. A Graetz number of 20 or less (or $Gz^{-1} \geq 0.05$) is the point at which the flow profile is considered fully developed [169]. A less developed flow profile has a thinner hydrodynamic boundary layer at the electrode surface and hence by extension, a beneficial effect on the mass transfer. This correlation is shown in Figure 6.9, where Sh is plotted versus Gz^{-1} .

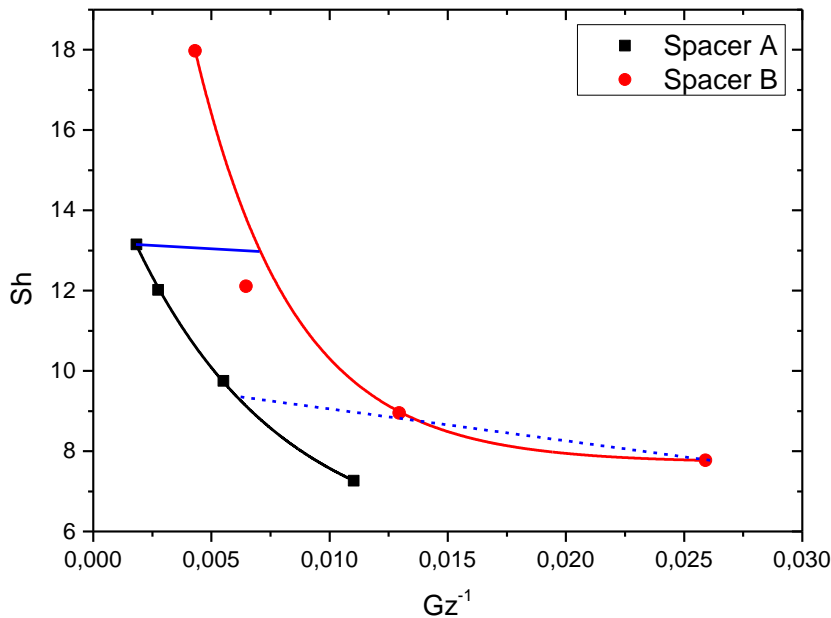


Figure 6.9: Sh versus Gz^{-1} plot for both spacers. Squares and solid line: experimental values and fitted curve for spacer A. Dots and dashed line: experimental values and fitted curve for spacer B. The horizontal lines represent the points of equal Re on both curves and correspond to the values marked by the vertical lines on Figure 6.8.

If Gz is calculated for a fixed length for both spacers in the range of overlapping Re , it is obvious from equation (6.5) that Gz for spacer A is higher than for spacer B for each value of Re , which is a direct consequence of the difference in aspect ratio. This means that the flow profile is less developed in spacer A at equal channel lengths and equal Re , which contributes to a better mass transfer as explained above. However, even though spacer A shows a better mass transfer at equal Re , the higher fluid velocities for the same volumetric flow rate in spacer B compensate for this effect. So for the same electrode surface area and equal reactor volume, spacer B offers an equal or better mass transfer than spacer A for each volumetric flow rate. In addition spacer B offers a better support for the membrane, which prevents bending of the membrane that causes the possible blocking of one of the channels.

6.3.4 Electrochemical aldol reaction of acetone in the microfluidic reactor

The reaction was performed in the reactor setup as displayed in Figure 6.1. Spacer B was used to create the reaction channel and a membrane was incorporated to separate the electrodes with an inter-electrode distance of 4 mm. The counter electrode was a glassy carbon electrode and the reference electrode was Ag/Ag⁺ (0.01 M AgNO₃). The reagent stream consisted of acetone + 0.1 M *n*-Bu₄NClO₄. Two working electrodes were investigated: a catalytic platinum deposit and an inert glassy carbon electrode. Earlier work [170] showed that the reaction reaches an equilibrium concentration of approximately 15 m% DAA, the exact value varies a bit due to parameters such as temperature and dissolved oxygen. The fractional conversion is not explicitly calculated, but for all experiments, the selectivity is consistently very high (generally $\geq 95\%$) meaning that the fractional conversion correlates strongly to the yield of the product and in this case even is comparable in numerical value. A flow rate of 0.5 ml min⁻¹ corresponding to a mean linear velocity of 0.68 mm s⁻¹ and a residence time of 340 s was set. Figure 6.10 (a) shows that for this flow rate, both materials reach the same maximum equilibrium concentration of ± 18 m% which corresponds to a space time yield of $\rho_{ST} = 0.23$ for Pt and 0.22 for GC. Decreasing the residence time would logically at one point cause the concentration (and consequently the yield) to drop. This effect is demonstrated in Figure 6.10 (b) which shows the results for an electrolysis of the same electrolyte in a smaller commercial thin layer cell with a platinum working electrode, which was used as a microfluidic reactor. The internal volume of the cell is 36 μ l and the surface area of the working electrode is 7 mm² which gives it a similar electrode surface area to volume ratio than the constructed reactor reported in this work. The electrodes in this cell are embedded in the same plane with a distance of 4 mm between them. This is a disadvantage because there is no possibility to separate the electrodes giving it a worse performance than the constructed device. In Figure 6.10 (b) the normalized yield is plotted versus the residence time. Due to the smaller volume of the commercial reactor, much shorter residence times are achievable with the same pump installation.

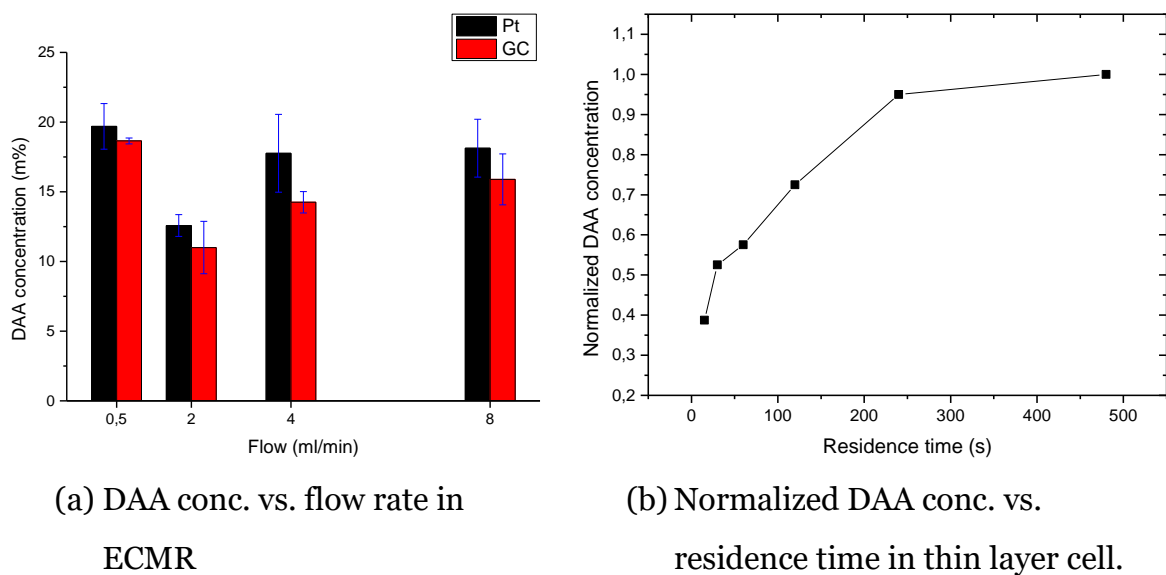


Figure 6.10: (a): DAA concentration at different flow rates in the divided reactor setup with Pt (black columns) or GC (red columns) WE, GC CE, electrolyte = acetone + 0.1 M TBAP, $E = -2.35$ V vs Ag/Ag⁺, inter-electrode distance = 4 mm. Experiments performed in triplicate. (b): normalised DAA concentration as a function of residence time for a platinum working electrode in a commercial thin layer cell employed as ECMR.

Figure 6.10 (b) clearly shows that for shorter residence times the concentration decreases and for longer residence times the concentration increases until the equilibrium concentration (or the maximum achievable concentration) in the given reactor setup is reached. In Chapter 5 it was seen that in the same batch setup a GC electrode can also reach the maximum concentration as a Pt electrode does, but it takes a much longer electrolysis time, suggesting a lower activity for the reaction. Taken into account this difference, it is expected that the tipping point at which the equilibrium concentration is no longer achievable, is different for the two materials. Logically this would happen at a higher residence time for GC than for Pt. To evaluate to what extent the flow rate can be increased before this happens, the reaction was performed in a range of volumetric flow rates of 0.5 to 8 ml min⁻¹ (close to the maximum flow rate of the pump), corresponding to mean linear velocities of 0.66 to 10.6 mm s⁻¹ and residence times of 350 to 22 s. The results are also plotted in

Figure 6.10 (a). A first observation is that in the range of volumetric flow rates applied, taken the error bars into account, there is no significant difference in concentration that was obtained in the product stream between the different flow rates. A remark needs to be made on the noticeable decrease at a flow rate of 2 ml min⁻¹. This might suggest a pattern, however, this is more likely due experimental variation or error. A second observation is that within the measured range of flow rates there is no significant difference noticeable between the two electrode materials.

6.3.4.2 Production rate

Figure 6.11 shows a plot of the production rate versus the flow rate for these experiments. Because similar concentrations are achieved at different flow rates, it is logical that a linear correlation exists (Pearson's $r = 0.996$ for Pt and 0.989 for GC) between the two, hence the larger flow rates correspond to a larger production rate.

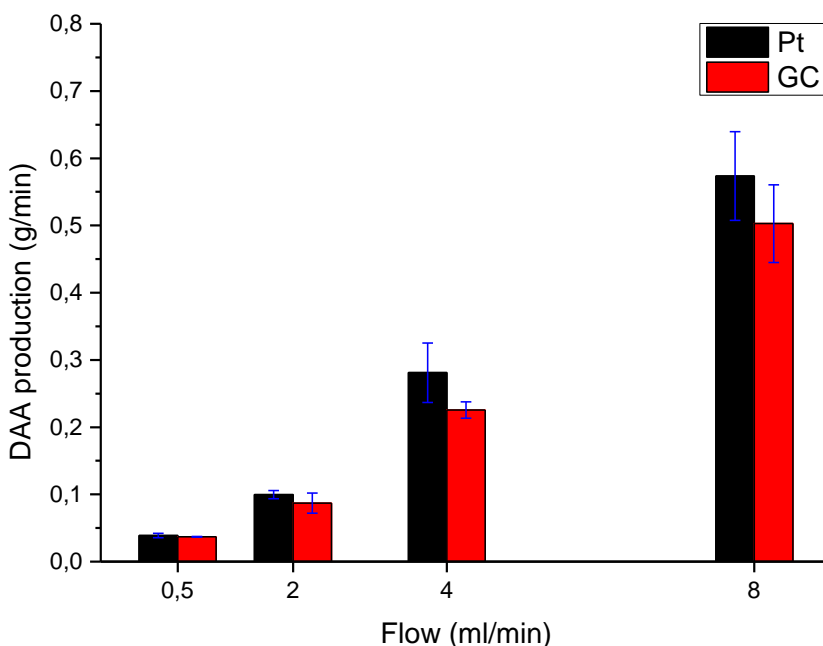


Figure 6.11: The DAA production rate versus volumetric flow rate for the divided reactor setup for a Pt (black columns) and GC (red columns) WE, GC CE, electrolyte = acetone + 0.1 M TBAP, E = -2.35 V vs Ag/Ag⁺, inter-electrode distance = 4 mm. Experiments performed in triplicate.

As Figure 6.10 implies, the maximum production rate and corresponding space time yield might not be reached in this setup. To further investigate this matter, the reactor was adjusted to a smaller volume. The working electrode was shortened and the spacer was adapted properly to create a serpentine channel over the working electrode (see Figure 6.12). The total channel surface area in the new setup is 504 mm² with an electrode surface area of 184 mm², giving a specific electrode area of 5 cm⁻¹, which is the same as in the larger setup (see Section 6.3.2). The path length of the channel over the electrode is 61 mm. The inter-electrode distance remains the same at 4 mm. A second HPLC pump was used to feed each channel separately so a larger total flow rate could be accomplished. The smaller volume and larger range of flow rates means that shorter residence times are achieved in the reactor, but because of the identical channel aspect ratio, the mean linear flow velocity is the same at equal flow rates for this smaller volume setup and the previous setup.



Figure 6.12: Adjusted ECMR with a smaller working electrode and adapted spacer leading to a smaller reactor volume, but equal specific electrode area compared to the larger volume setup.

Electrolysis experiments were conducted with a platinum working electrode in a range of volumetric flow rates of 1 to 20 ml min⁻¹ which corresponds to mean linear flow velocities of 1.4 to 27.7 mm s⁻¹ and residence times of 44.2 to 2.2 s. The results are shown in Figure 6.13.

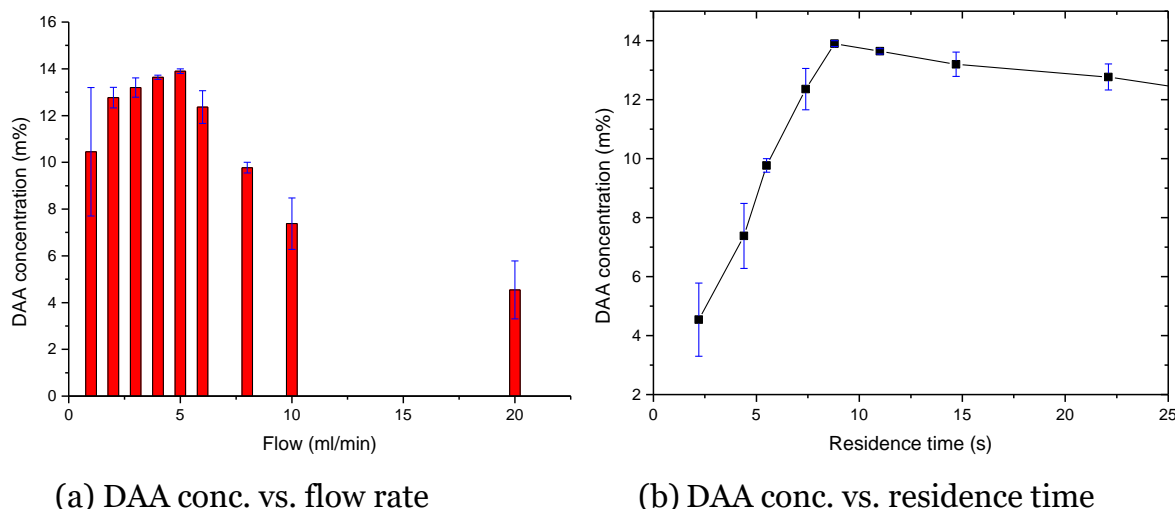


Figure 6.13: Experiments in the smaller divided ECMR with Pt WE, GC CE, electrolyte = acetone + 0.1 M TBAP, $E = -2.35$ V vs Ag/Ag⁺, inter-electrode distance = 4 mm. Experiments performed in triplicate. DAA concentration in the product stream at different flow rates (a) and versus the corresponding residence times (b). Experiments performed in triplicate.

Similar to the previous experiments, taken the error bars into account, the DAA concentration remains constant up to a certain flow rate, which in this case is 6 ml min⁻¹ corresponding to a mean linear velocity of 8.3 mm s⁻¹ and a residence time of 7.4 s. At higher flow rates or shorter residence times the concentration of DAA in the product stream starts to decline strongly. At a volumetric flow rate of 20 ml min⁻¹ which corresponds to a mean linear velocity of 27.7 mm s⁻¹ and a residence time of merely 2.2 s, the concentration drops to 4.5 m%. Since the concentration is about the same up to 6 ml min⁻¹, the maximum production rate and thus the best space time yield is achieved at this flow rate. However, at higher flow rates the loss of concentration is proportional to the increase in flow rate. As a consequence from 6 ml min⁻¹ onwards, the production rate and space time yield is almost constant. For the larger ECMR the maximum production rate is achieved at the maximum applied flow rate of 8 ml min⁻¹ which is 0.57 g min⁻¹ corresponding to a space time yield of 3.4 mmol cm⁻³ min⁻¹. Interestingly the production rates in the smaller ECMR from 6 ml min⁻¹ onwards range from 0.58 to 0.71 g min⁻¹ where the latter is at 20 ml min⁻¹ and

might be an overestimation considering the relatively large error bars. Not considering this result, the maximum production rate for the smaller ECMR is obtained at 8 ml min^{-1} and is 0.61 g min^{-1} which is very close to that of the larger ECMR. However, due to the much smaller setup, this corresponds to a space time yield of $14.3 \text{ mmol cm}^{-3} \text{ min}^{-1}$ which is more than fourfold increase compared to the larger ECMR.

To compare the performance of the continuous flow reactor against the batch setup, the absolute yield for both is calculated for a time frame of two hours, which was the duration of the batch experiments. The electrode surface area for the larger ECMR and the batch setup is comparable as the difference between both is less than 10 % (8 cm^2 in the batch setup versus 7.3 cm^2 in the reactor setup with serpentine spacer). For the batch experiments an absolute yield of 11.9 g with $\rho_{ST} = 0.0085 \text{ mmol cm}^{-3} \text{ min}^{-1}$ was achieved after this time while for the reactor the total amount of DAA was 68.8 g with $\rho_{ST} = 3.4 \text{ mmol cm}^{-3} \text{ min}^{-1}$, which is almost a six fold increase in absolute yield and 400 fold increase in space time yield. The continuous replenishing of reactant in proximity of the electrode and the large electrode surface area to volume ratio has a significant beneficial effect on the DAA production.

6.3.4.3 Reaction efficiency in the ECMR

Another parameter that was checked is the apparent current efficiency, for which an interesting observation is notable. From the current curves which are recorded during the experiment (not shown), it is clear that for the glassy carbon working electrode the current density rises less than linear with increasing flow rate, increasing from 0.60 mA cm^{-2} at 0.5 ml min^{-1} to 0.95 mA cm^{-2} at 8 ml min^{-1} . This means that the faradaic efficiency increases with the flow rate as the production capacity rate does increase linearly with the flow rate. This is obvious in Figure 6.14 where the yield per charge passed increases from 0.14 g C^{-1} at 0.5 ml min^{-1} to 1.20 g C^{-1} at 8 ml min^{-1} which is a tenfold increase in current density but a 16 fold increase in volumetric flow rate (or mean linear flow velocity). In the batch setup, glassy carbon after two hours had

an overall efficiency of 0.34 g C^{-1} , which is higher than the efficiencies obtained in the reactor at 0.5 and 2 ml min^{-1} , but much lower than the efficiencies at 4 and 8 ml min^{-1} . Higher flow rates might prevent certain side reactions taking place on the glassy carbon electrode, increasing its efficiency. In addition, faster removal of DAA from the electrogenerated base limits the reverse reaction, leading to a higher apparent current efficiency.

For the platinum deposit working electrode the current density in the reactor increases linearly from 0.93 mA cm^{-2} at 0.5 ml min^{-1} to 4 mA cm^{-2} at 2 ml min^{-1} and then remains constant around that value for higher flow rates. Consequently the efficiency increases only slightly from 0.10 g C^{-1} at 0.5 ml min^{-1} to 0.33 g C^{-1} at 8 ml min^{-1} . The value of 0.33 g C^{-1} is comparable to the divided batch setup with a platinum working electrode where the efficiency was 0.35 g C^{-1} after two hours. The faradaic loss for the platinum deposit working electrode is not completely clear, but is probably related to gas evolution (possibly hydrogen evolution). This is noticeable during operation where gas bubbles are visible in the outlet tubing on the cathodic side. The formation of these bubbles not only lowers the faradaic efficiency, but also leads to possible blocking of the electrode, reducing the available electrode surface area. The formation of gaseous products on the anodic side is not observed and for a glassy carbon working electrode, no gaseous products are observed at all.

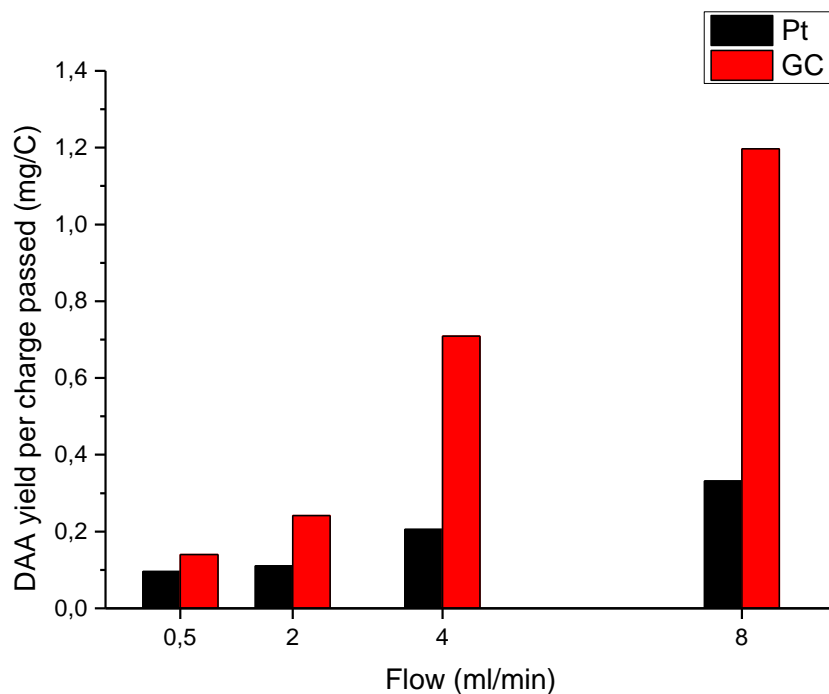


Figure 6.14: Apparent current efficiency (yield per charge passed) versus volumetric flow rate for the experiments shown in Figure 6.10 and Figure 6.11.

In the range of flow rates measured, the same concentration is reached on both materials up to the highest flow rate. This gives glassy carbon a better performance than platinum due to the higher efficiency. In the batch setup the efficiency of both materials was comparable while the activity of platinum was much higher, resulting in a higher yield. However, further lowering residence time will most probably lower the maximum obtainable concentration as seen in Figure 6.10 (b) and Figure 6.13 (b) and this presumably happens at a longer residence time for glassy carbon than for platinum. A parameter which plays a role here is the inter-electrode distance. A smaller distance can have a beneficial effect on the total power input of the setup due to the decreasing ohmic losses between the two electrodes (which can be quite large in non-aqueous solvents). However, this also decreases the total volume and thus for the same volumetric flow rates, the residence time decreases. This has its effect on the space time yield and the absolute yield. Optimisation depends on tuning the setup to find a balance between yield and efficiency. The fact that for this configuration up until the highest applicable flow rate the maximum concentration is achieved on both

materials, highlights the ease by which this reaction can be performed in an electrochemical microreactor.

6.4 Conclusions

The electrochemically induced aldol reaction of acetone to diacetone alcohol was performed in an electrochemical microfluidic reactor. The reactor design was focused on a modular, robust setup which is easy to (dis)assemble and to operate. The implementation of a membrane was necessary to prevent the mixing of electrogenerated species which has a negative impact on the reaction. Due to the modular setup, inserting or removing a membrane is fast and easy. To prevent blocking of the electrode chambers caused by bending of the membrane, a spacer with serpentine flow channel was used to support the membrane. This spacer, while providing nearly the same available electrode surface area and reactor volume as a similar sized rectangular flow channel, has a beneficial effect on the mass transfer in the reactor due to the increased channel length. In the divided setup, a maximum productivity of 0.57 g min^{-1} of DAA ($\rho_{st} = 3.4 \text{ mmol cm}^{-3} \text{ min}^{-1}$) at an efficiency of 0.33 g C^{-1} was achieved on a platinum working electrode at -2 V vs Ag/AgCl and a volumetric flow rate of 8 ml min^{-1} which corresponds to a mean linear velocity of 10.9 mm s^{-1} and a residence time of 22 s . This is a six fold increase in yield compared to the batch setup described in Chapter 5 and a 400 fold increase in space time yield. However, even at the maximum flow rate of the pump, the reactor was still not operating at the point where the maximum obtainable DAA concentration is less than the equilibrium concentration. Therefore no significant difference in DAA production rate or concentration was noticeable between the two electrode materials tested. Adjusting the reactor to a smaller volume so shorter residence times could be achieved lead to nearly the same production rate as in the larger volume reactor, but due the much smaller volume the space time yield increased to $14.3 \text{ mmol cm}^{-3} \text{ min}^{-1}$ which is a fourfold increase compared to the larger volume reactor. This result shows the potential of the application of an ECMR for this reaction. The efficiency of

platinum of 0.33 g C^{-1} in the reactor setup is similar to the 0.35 g C^{-1} in batch setup. This efficiency is limited due to the gas formation on the platinum electrode and the lack thereof on the glassy carbon electrode gives it a better efficiency as platinum in the reactor setup. Though further optimisation of the electrode surface area and the reactor volume for a maximum productivity is still possible, it has been demonstrated that the application of a simple electrochemical microreactor for the aldol reaction of acetone to diacetone alcohol leads to a high rate of product formation, a high selectivity and a high current efficiency. Furthermore, the microreactor setup combines the advantages of electrosynthesis with those of flow chemistry and offers a stable, robust and easy to scale up system. These promising results provide a next step for the implementation of electrosynthesis in an industrial application as a green and clean alternative for the existing chemical processes.

CHAPTER 7

Understanding the electrosynthetic aldol reaction

THIS CHAPTER GIVES AN INSIGHT INTO THE MECHANISM OF THE ELECTROSYNTHETIC ALDOL REACTION. THE MECHANISMS THAT ARE PROPOSED IN LITERATURE AND WHICH ARE LISTED IN CHAPTER 4 ARE CRITICALLY EXAMINED AND DISCUSSED. THE SCHEME PROVIDED BY THE MOST PROBABLE CANDIDATE IS VALIDATED BY A CONCISE VOLTAMMETRIC INVESTIGATION.

This chapter is in preparation for publication as: D. Pauwels, K. De Wael, T. Breugelmans, Insights into the mechanism of the electrosynthetic aldol reaction of acetone, Journal of Electroanalytical Chemistry (2018)

7.1 Introduction

In the previous chapters the electrochemically induced aldol reaction of acetone was screened in batch and in continuous flow operation. Several important parameters for each process could be identified and quantified. The electrochemical route exhibited excellent performance with yields comparable to the traditional chemical route. However, further optimization remains possible. An example is a profound study of the electrocatalyst material. A thorough and targeted optimization could lead to a more efficient reaction, a lower energy input and less amount of (expensive electrocatalyst) material used. Several strategies for such optimization are possible [171]. For a successful optimization it is useful to know the precise mechanism through which the reaction proceeds. This allows identifying important steps and intermediates and determining the influence of several parameters on the mechanism. However, as is discussed in Section 4.6, there is no confirmed reaction mechanism for the electrochemical aldol reaction and little research has been devoted to this. The few mechanisms that have been reported are shown in Section 4.7. However, they are not equally probable and a critical evaluation of each mechanism allows selecting the most probable mechanism which can then be investigated.

The first mechanism by Tsai et al. proposed an indirect mechanism initiated by the electrolysis of water. However, in Chapter 5 it was shown that the addition of water in the electrolyte had a detrimental effect on the yield and that the indirect aldol reaction by electrolysis of water is unlikely. The mechanism also proposed a reaction by direct activation on both anode and cathode. However, careful examination of the proposed steps reveal an unlikely scheme. On the cathode side the direct activation occurs by abstraction of an α -hydrogen which would form an enolate as in the base-catalyzed mechanism. This route seems plausible but would be accompanied by significant gas evolution, which in a water free electrolyte is not observed. Of course with a significant amount of water present, this observation would be impossible to make due to the water electrolysis. The activation on the anode side occurs by

abstraction of an electron of the carbonyl compound leading to a positively charged carbonyl carbon (depicted as a carbocation in the scheme). Since a single electron transfer would result in a radical cation, the abstraction of an electron pair is assumed. The reaction then completes by the attack of a neutral molecule. This mechanism is significantly less plausible than the cathodic reaction suggestion due to the reactivity of the neutral carbonyl molecule. In addition, in Chapter 5 it was shown that no product formation could be detected on the anode side in a divided cell, making it more unlikely to occur as presented. Furthermore, in the work of Tsai et al. [102] the cell potential is reported to be less than 1 V which means that the electrode potential is even lower and well within the stability window of both solvent and supporting electrolyte, making the direct activation as presented and therefore the proposed mechanism improbable.

A second, more detailed mechanism was provided by Kumar et al. Although the mechanism is a detailed stepwise scheme which implies a sound reasoning, there are some unlikely steps involved. The hydrogen free radical released in the formation of the enolate would easily combine with another hydrogen free radical or react with a ketyl radical, rendering the later recombination with the aldol radical improbable. The loss of an electron by the combination product is a step that needs to proceed via an outer shell electron transfer in solution of the radical anion to a neutral carbonyl molecule which is highly unlikely [172]. Equally unlikely is the formation of the free radical of the aldol product by spontaneous electron loss for which the previous reasoning also applies. Summarized this scheme offers an interesting mechanism, but besides the first step which corresponds to the reactions shown in Section 4.6.1 it consists of a series of improbable steps for which no fundamental basis is provided or can trivially be assumed.

The last mechanism, proposed by Shono et al. is the most interesting. Only providing a scheme that consists of a few steps without many details, it is a good basis for the mechanism of the electrosynthetic aldol reaction as it corresponds with the properties

of a carbonyl derived EGB as discussed in Section 4.6.1 and with experimental results as shown further in this chapter.

Applying this information to the acetone reaction, a mechanism can be proposed. The initiation step is the formation of the acetone ketyl radical which then is reversibly protonated by another acetone molecule, generating an enolate. The enolate attacks another acetone molecule as shown in the chemical mechanism in Figure 4.9. The protonation of the aldol anion happens either by the protonated ketyl radical ($pK_a \sim 11-12$ [152]) or by another acetone molecule ($pK_a \sim 19.2$) which in both cases propagates the reaction. Termination happens by a combination of the terminating steps shown in Figure 4.12. Another source for the protonation of the ketyl radical or the protonation of the aldol anion is the supporting electrolyte. The quaternary ammonium salt can protonate the EGB in a Hofmann elimination [173] (Figure 7.1).

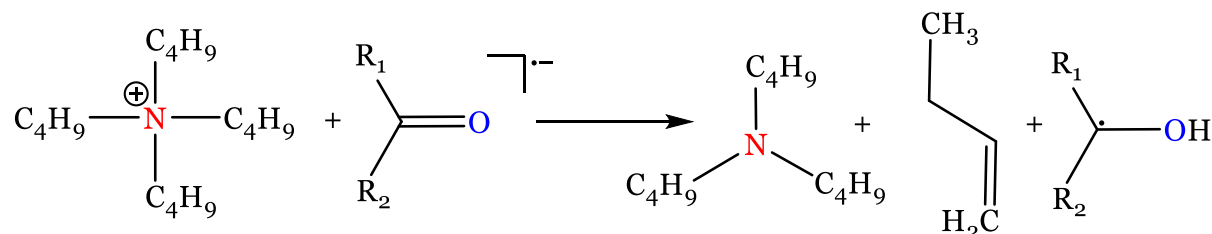


Figure 7.1: Protonation of an acetone ketyl radical by the tetrabutyl ammonium cation of the supporting electrolyte.

To check the EGB initiated mechanism by deprotonation of an acetone molecule as compared to a complete radical mechanism a series of measurements is performed in a standard batch setup. The role of the superoxide anion as EGB is also checked by isolating its contribution. The mechanism can be checked by intercepting the initiating deprotonation step by adding a compound that is more easily deprotonated than acetone, for example phenolphthalein (PhPh, $pK_a \sim 9.7$). In addition the deprotonated form of PhPh has a pink to fuchsia color which offers a visual confirmation of the reaction.

7.2 Experimental

7.2.1 Chemicals

Acetone (HPLC grade, 99.8+ %) was purchased from Chem-Lab (Belgium). The supporting electrolyte tetrabutylammonium perchlorate (TBAP, *n*-Bu₄NClO₄, 99.0 %) and phenolphthalein (ACS reagent) was purchased from Sigma-Aldrich (Belgium). The gas used to deoxygenize the solutions was high purity (5.0) nitrogen obtained from Praxair.

7.2.2 Setup

The experiments were conducted in an undivided airtight batch cell in a conventional three-electrode setup. A saturated Ag/AgCl was used as the reference electrode (all potentials in this chapter are reported versus Ag/AgCl). A platinum sheet electrode was used as counter electrode and a platinum wire was used as working electrode.

7.2.3 Analysis

Analysis of the samples was performed by GC-FID (Thermo Scientific Trace 1300) on a polar capillary column (Restek RTX-Wax 30 m × 0.25 mm, PEG 0.25 µm). The carrier gas flow (He, 5.0 purity) was controlled at 1.4 ml min⁻¹. The temperature of the column was held constant at 40 °C for 1 minute and then ramped to 200 °C at 40 °C min⁻¹. This resulted in excellent separation of the target products allowing easy quantification. All samples were analysed at least three times with a standard deviation of no more than 5 % and usually much less.

7.3 Results and discussion

Figure 7.2 shows CVs measured of acetone (with 0.1 M TBAP as supporting electrolyte) with and without dissolved oxygen. To remove the oxygen, nitrogen was

bubbled through the solution for a period of time and during the measurement a blanket of nitrogen was kept over the solution. In the CV with dissolved oxygen a peak can be discerned at about -1.15 V, which is the reduction of the dissolved oxygen to the superoxide anion. In both CVs the start of the solvent peak is visible from -1.7 V onwards which means that at this potential the solvents starts to reduce, which can be seen as the direct activation of acetone.

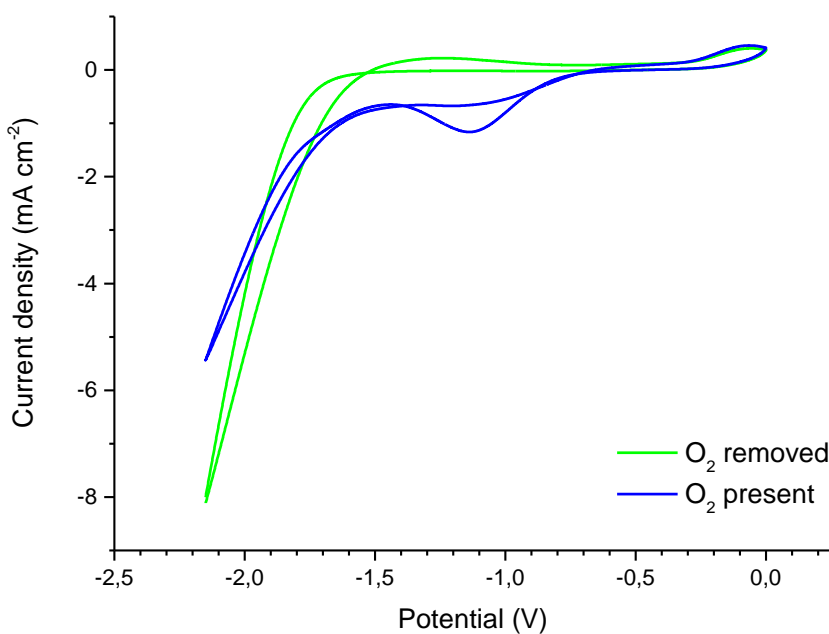


Figure 7.2: CVs for acetone with and without dissolved oxygen present. Pt WE and Ag/AgCl RE. Supporting electrolyte 0.1 M TBAP. $v = 100 \text{ mV s}^{-1}$.

When PhPh was added to the acetone an additional peak is visible at -1.9 V and a purple discolouration can be noticed at the electrode (Figure 7.3). To check whether this was the electrochemical reaction of PhPh and not due to the reduced solvent reacting with PhPh, the same measurement was done in DMF which has a much wider stability window. In DMF PhPh also clearly showed a peak at -2 V accompanied with the purple discolouration (CV not shown).

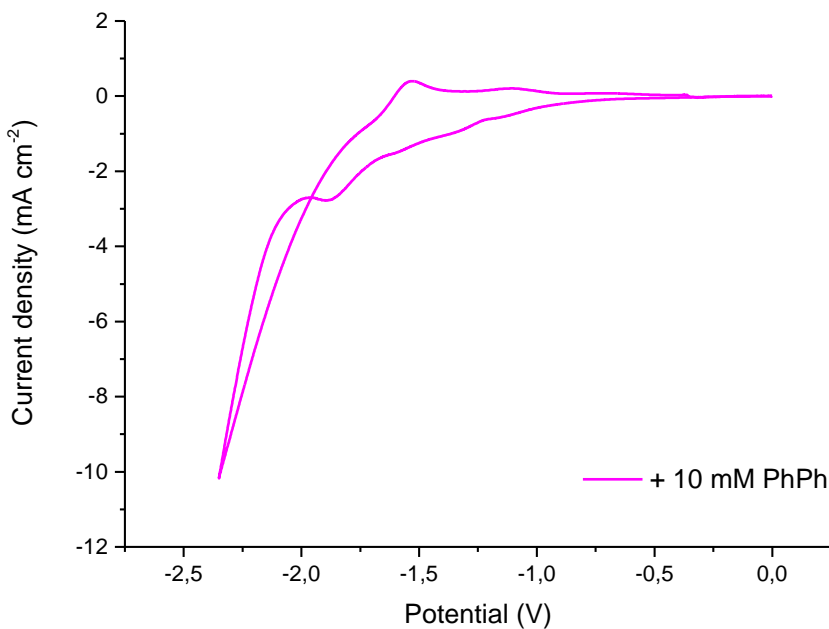


Figure 7.3: CVs for acetone with 10 mM PhPh added (no dissolved oxygen). Pt WE and Ag/AgCl RE. Supporting electrolyte 0.1 M TBAP. $v = 100 \text{ mV s}^{-1}$.

The CVs show that at a potential of -1.6 V oxygen is reduced, but acetone and PhPh are electrochemically inactive. Any DAA formed in an electrolysis at this potential is the result of the aldol reaction initiated by the superoxide anion EGB.

Figure 7.4 shows the results of controlled-potential electrolysis experiments at -1.6 V in the presence and absence of dissolved oxygen. The small amount of DAA formed when no dissolved oxygen should be present is probably because of an incomplete deoxygenation as acetone should not react at this potential. It is clear that when the oxygen is not removed, a significant amount of DAA is formed. However, when PhPh is added the same experiment yields no DAA at all, confirming the suggestion that the deprotonation of acetone is stopped in favor of the deprotonation of PhPh. In accordance with this reasoning a purple discolouration is seen at the electrode surface, indicating the presence of deprotonated PhPh. When an electrolysis is performed at -1.6 V in absence of dissolved oxygen but with PhPh added no discolouration is observed, as expected.

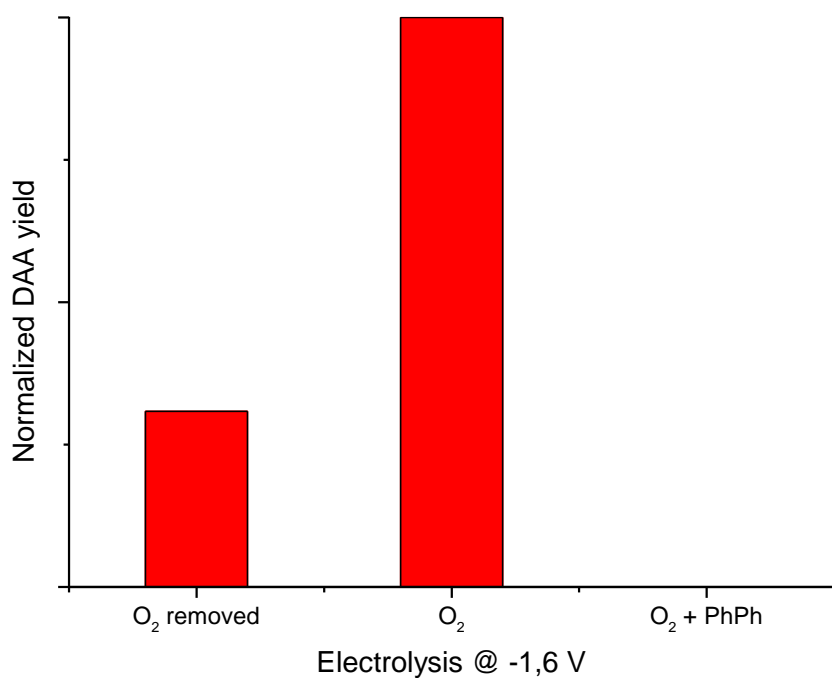


Figure 7.4: Relative concentrations of DAA for the controlled-potential electrolysis of acetone + 0.1 M TBAP at -1.6 V vs. Ag/AgCl with and without dissolved oxygen present and with PhPh added.

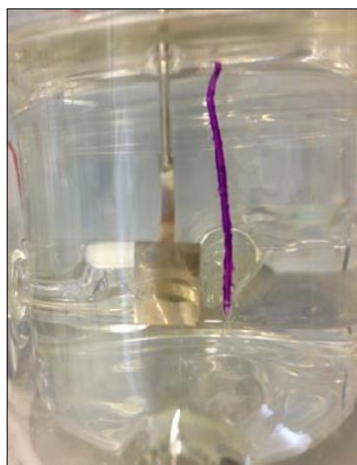


Figure 7.5: Purple discoloration noticeable at the working electrode due to the disprotonation of PhPh during the controlled-potential electrolysis of acetone + 0.1 M TBAP at -1.6 V vs. Ag/AgCl with dissolved oxygen present.

When performing the electrolysis at -2.1 V acetone itself will react and is expected to initiate the reaction. Figure 7.6 shows the results of controlled-potential electrolysis experiments at -2.1 V. The difference between the presence and absence of dissolved oxygen is small. Considering the abundance of acetone near the electrode surface, this is expected. Comparable to the experiments at -1.6 V no DAA is formed when PhPh is added.

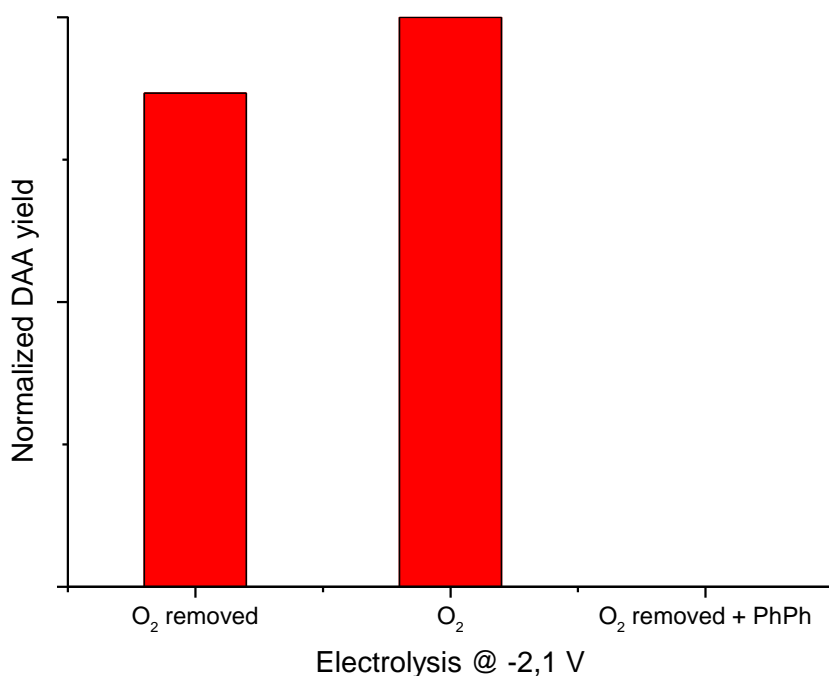


Figure 7.6: Relative concentrations of DAA for the controlled-potential electrolysis of acetone + 0.1 M TBAP at -2.1 V vs. Ag/AgCl with and without dissolved oxygen present and with PhPh added.

These results are in agreement with the proposed mechanism in which the acetone EGB initiates the reaction by deprotonation of another acetone molecule. Another observation made in these experiments that can also be made in the experiments in Chapter 5 and Chapter 6 further confirms this. If considered as a pure electrochemical mechanism where it is assumed that a single electron transfer takes place, the calculated current efficiencies of the experiments easily surpass thousand and ten thousand percent, even reaching as high as one hundred thousand percent.

As explained in Section 3.3.1.1 a purely electrochemical experiment can by definition not have a current efficiency higher than 100%. This means that the reaction is initiated electrochemically, but proceeds by a chemical (radical) chain reaction. Of course the single electron transfer assumption might be optimistic, but the magnitude of the current efficiency is too large to have the number of transferred electrons account for this. This observation confirms the propagation of the reaction, making the electrosynthetic aldol reaction a catalytic process.

7.3.2 Reaction at the counter electrode

Questions rise about the counter reaction in the acetone and TBAP system. Generally when no species is present that is easily oxidized, the counter reaction is the oxidation of the solvent or supporting electrolyte, depending on the electron donor strength of the solvent [162]. If the solvent is a weak electron donor such as acetonitrile or acetone, the oxidation of the anion of the supporting electrolyte is the more likely reaction. It has been shown that for perchlorate ions in acetonitrile the oxidation product of the perchlorate ions react with the solvent resulting in perchlorate acid and a solvent dimer [63]. Other frequently used quaternary ammonium salts such as the salts of tetrafluoroborate and hexafluorophosphate are presumed to react similarly resulting in the formation of tetrafluoroboric acid and hexafluorophosphoric acid respectively. Considering the solvent similarity of acetonitrile and acetone (both are dipolar protophobic aprotic solvents with a relatively high relative permittivity) a similar reaction is assumed to proceed in the acetone and TBAP system. The formation of a strong acid at the anode underlines the importance of separating anode and cathode in the electrosynthetic aldol reaction as demonstrated in Chapter 5 and Chapter 6. The presence of an acid species at the anode is also confirmed in the electrolysis experiments with PhPh where an orange-yellowish discoloration was observed. In a strongly acidic environment PhPh colors orange.

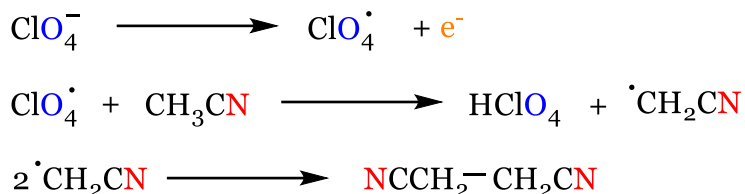


Figure 7.7: Oxidation of the perchlorate ion and reaction with solvent in an ACN/TBAP system [63].

7.4 Conclusions

The mechanisms proposed in the literature for the electrochemical aldol reaction were critically examined and evaluated. This allowed selecting the most probable mechanism which was subsequently checked by a concise voltammetric investigation. The results confirm the possibility of the proposed mechanism that states that the electrosynthetic aldol reaction proceeds via a radical initiated chemical chain reaction.

Part III

Mechanistic approach for an electrochemical study by *in situ* EPR spectroelectrochemistry

The electrosynthetic intramolecular reductive cyclisation of allyl 2-bromobenzyl ether

CHAPTER 8

Literature review on in situ EPR spectroelectrochemistry

THIS CHAPTER DISCUSSED THE PRACTICAL DIFFICULTIES AND CHALLENGES ASSOCIATED WITH THE COMBINATION OF ELECTROCHEMICAL TECHNIQUES AND ELECTRON PARAMAGNETIC RESONANCE SPECTROSCOPY. SUBSEQUENTLY PROMINENT CELL AND ELECTRODE DESIGNS FOR IN SITU EPR SPECTROELECTROCHEMICAL EXPERIMENTS ARE DISCUSSED.

8.1 Introduction

As noted in Section 3.4.3, the combination of electrochemical techniques with EPR spectroscopy is not new. Since the first experiments over half a century ago, a lot of progress has been made in the instrumentation and in the application of the combined technique. This chapter discusses the practical side of in situ EPR spectroelectrochemical experiments and covers noteworthy cell and electrode designs that have been developed throughout the history of the technique. The cells mentioned here are relevant to the experiments in this thesis. Many more different designs have been created, ranging from (more) simple designs which are generally applicable to complex designs with a more limited applicability. A comprehensive list and discussion thereof can be found in [57] and the references therein.

8.1.1 Practicalities of in situ EPR spectroelectrochemical experiments

In in situ EPR spectroelectrochemical experiments, the dimensional limitations of the cell setup are dictated by the EPR requirements. The principle of EPR is the irradiation of a sample by microwaves whereby standing microwaves are established in a cavity in which the sample resides. Hence, in combined experiments, the electrochemistry needs to take place in a cell inside this cavity. The shape and size of the cavity put restrictions on the geometrical dimensions of the cell. Most EPR spectrometers come equipped with the rectangular TE₁₀₂ cavity and consequently, it is the most frequently encountered cavity in reports on in situ EPR spectroelectrochemical experiments. Most cell designs are based on this cavity.

The standing wave inside the cavity allows the spatial separation of the electric and magnetic component of the microwaves (Figure 8.1). The standing waves have their electric and magnetic field components exactly out of phase, i.e. where the magnetic field is at maximum, the electric field is at a minimum and vice versa. Since the

magnetic field drives the absorption in EPR, the sample has to be placed in the magnetic field maximum to obtain the best signal and highest sensitivity.

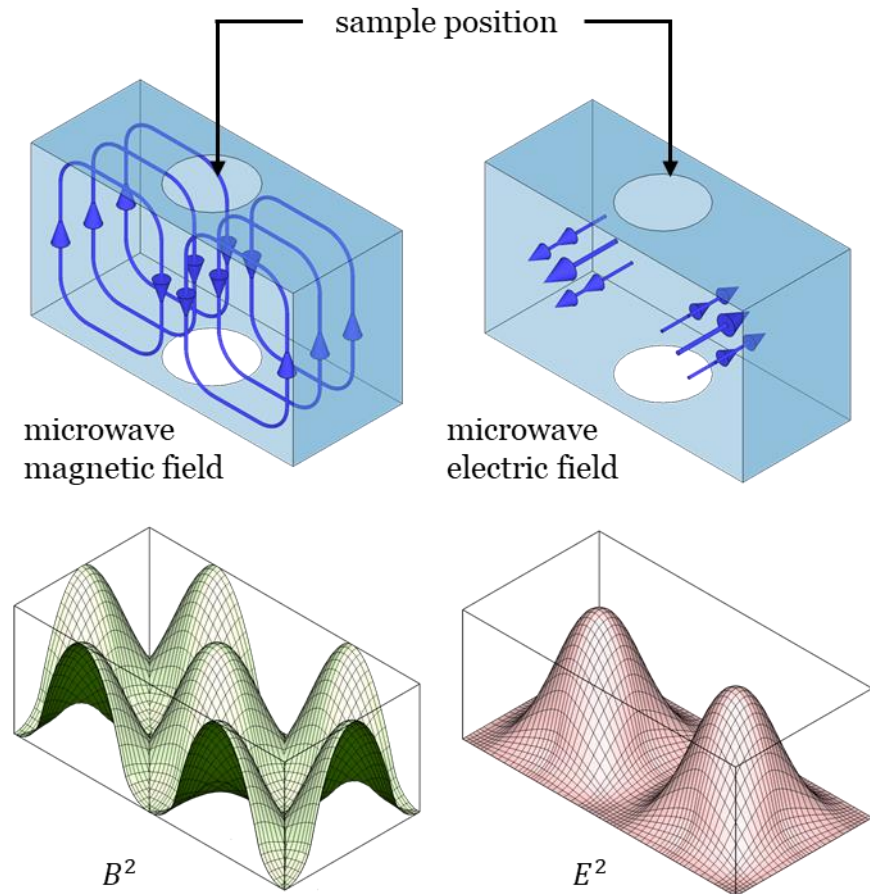


Figure 8.1: (a) schematic representation of the magnetic and electric field vector (redrawn from [66]) and (b) 3D representation of the field distribution inside a TE_{102} cavity (redrawn from [174]).

Additionally, interaction of the sample with the electric field causes a loss of microwaves due to non-resonant absorption known as dielectric loss. This loss arises from the interaction of the microwave electric field vector with electric dipoles in the cavity. Hence the placement of the sample needs to avoid overlapping with the electric field. In Figure 8.1 can be seen that there is a nodal plane in the center of the cavity (between the two “peaks” of the electric field) where the electric field is at its minimum and the magnetic field at its maximum. Confining the sample to this plane

overcomes the problem of interaction with the electric field. This is achieved in a standard EPR flat cell which has a rectangular flat section with a thickness of about 250 µm. The cell is placed in the center of the cavity with the flat section perpendicular to the incoming microwaves so that the sample is lined up with the nodal plane. The disadvantage of employing such cell is that the electrochemistry needs to be performed in a thin layer cell which unavoidably entail large ohmic losses. Further attention needs to be paid to the vertical placement of the sample as the sensitivity of the cavity is spatially discriminating, i.e. the magnetic field distribution within the cavity along the vertical axis has a \sin^2 dependency with zero sensitivity at the edges and maximum sensitivity in the center. The result is that even for a homogeneous solution of radicals in a flat cell, about 80% of the signal comes from spins within 5 mm of the cavity center [56]. This means that for an electrolytic experiment, where radicals are generated at the electrode surface, placement of the electrode within the flat section of the cell within the cavity is a crucial parameter that influences the sensitivity.

To summarize the aforementioned issues, it is obvious that there are some conflicting requirements for good quality EPR measurements and good quality electrochemical measurements. The EPR setup requires the electrochemistry to take place in a thin layer cell which has its influence on the electrochemistry. It requires a complex electrode construction to achieve acceptable electrochemical performance. Furthermore, considering the dielectric loss, the greater the relative permittivity² of the sample, the greater the loss. Thus solvents with a low relative permittivity are preferred for EPR which is the contrary for electrochemistry which requires sufficient conduction and often uses solvents with significantly high relative permittivity. A good in situ EPR spectroelectrochemical experiment is about finding the balance between the needs for the two techniques which unavoidably means some compromises on either side. One issue that is common for both techniques is the removal of oxygen. Where dissolved oxygen often disturbs electrochemical

² Relative permittivity is commonly known as the dielectric constant. The latter term is considered obsolete and its use is discouraged by IUPAC recommendations and the IEEE Standards Board.

measurements, the singlet oxygen state is paramagnetic and can cause loss of resolution in the EPR spectrum. It is therefore advised to properly deoxygenize the sample.

8.2 Applications

The application of *in situ* EPR spectroelectrochemical experiments is versatile. Since EPR allows the detection of organic radicals, the combination of both techniques is often applied to identify important intermediates and the obtained information is used in turn to establish or confirm reaction schemes. In such studies if the electrochemical behavior is uncomplicated, there is no need to precisely control the working electrode potential as long as secondary reactions are avoided. Application of a potential corresponding to a point on the limiting current plateau is sufficient. The resulting current quickly decays so the desired potential is approached. The resulting diffusion and the natural convection by thermal and density gradients keep the potential from shifting to a different reaction. In case the radical to detect is too short-lived and cannot be detected directly, a spin trap can be used. Spin trapping is the technique where the radical is “spin-trapped” by letting it chemically react with a spin trap agent (which is diamagnetic) to produce a relatively stable radical which in turn can be detected. The technique is well-known and more information can be found in a review by Kemp [175].

Often it is difficult to distinguish between two related reaction mechanisms and kinetic measurements are required to elucidate the situation. To be able to derive kinetics, the concentration of radicals in space and time must be known. Standard flat cells as discussed in Section 8.1.1 preclude this due to the irregular and irreproducible natural convection. As a solution, several different flow cells with well-defined and calculable hydrodynamics have been developed, some based on traditional hydrodynamic electrodes known from analytical electrochemistry. Examples of such flow cells are cells that are based on channel electrodes [176–178], tubular electrodes

[179–181], wall jet electrodes [182], coaxial flow cells [183] and other geometries [184,185]. Flow cells allow steady state measurements of the EPR signal as a function of the electrode current and flow rate to determine kinetics and radical decay mechanisms. Alternatively the electrodes can be open-circuited to record transient EPR signals and directly measure radical lifetimes. Thorough mathematical work allows deriving equations to infer rate constants for radical decay and for mechanistic discrimination (see [57]). Besides kinetic measurements flow cells are also useful for simple radical detection. In a quiescent solution there is no flow to bring fresh electroactive material to the electrode surface. The diffusion (supplemented by the natural convection) provides a small constant current so only radicals which are sufficiently long-lived will accumulate enough to be detected in the time interval of the EPR measurement. The constant replenishment of electrolyte at the electrode surface in the flow cell and the subsequent transport of the generated radicals to the most sensitive part of the cavity allows the detection of radicals with a much shorter lifetime.

8.3 Cell designs

8.3.1 The Adams cell

Continuing on the pioneering work of Maki and Geske, Adams et al. optimized the design of the cell for in situ experiments [186–188]. The cell is essentially a conventional EPR flat cell in which a platinum gauze is used as a working electrode inside the flat section (Figure 8.2). A counter electrode is placed below the flat section and a reference electrode above it. The design is straightforward, but this cell and several variants of it have been used extensively in various different studies. The simplicity of its design and its capacity to generate large amounts of radicals easily attribute to its popularity. Its success is the reason that this type of cell is the only commercially available electrolytic EPR cell to date, offered by manufacturers like Bruker (ER 164 EC-Q Electrolytic Cell Assembly) and Wilmad-Labglass (WG-810-Q

Electrolytic Cell Assembly) (Figure 8.2). In both cases the main cell is similar to a conventional EPR flat cell, but both assemblies offer additional components to mount on top of the cell by ground glass joints that give additional inlets for reference electrodes, gas bubbling and working electrodes.

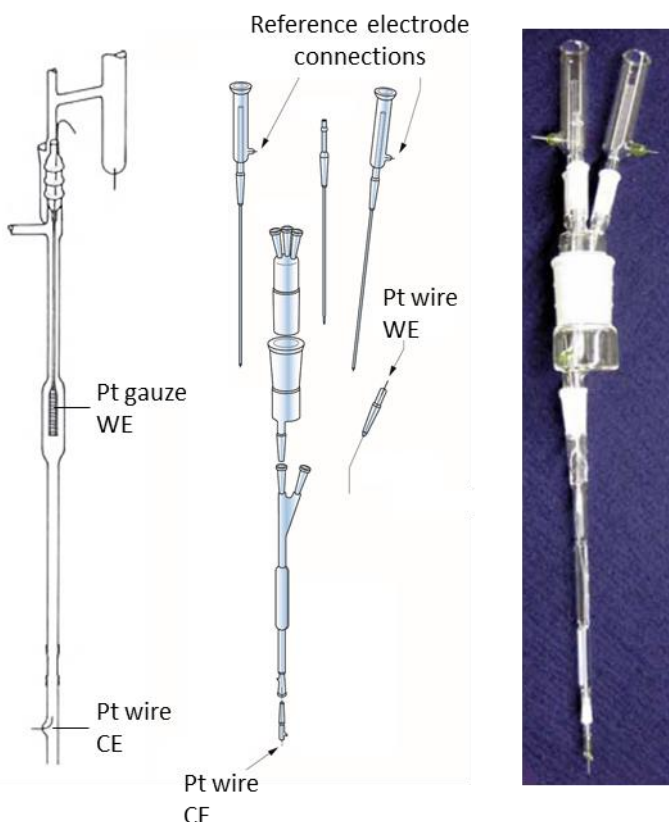


Figure 8.2: Left: the Adams cell. Center: the Wilmad-Labglass Electrolytic Cell Assembly. Right: the Bruker Electrolytic Cell Assembly.

Although often used as a tool to generate radicals, the cell suffers from poorly resolved electrochemistry as discussed in the previous section. The high ohmic drop and non-ideal electrode placement lead to inhomogeneous potential and current distributions over the working electrode and disturbed voltammetric measurements. A partial solution to this problem was given by Neudeck et al. who adapted the cell for *in situ* UV-VIS EPR spectroelectrochemistry [189]. To be suitable with the UV-VIS measurements, the working electrode needs to be optically transparent, which is

achieved by using a laminated mesh electrode [190]. The lamination provides rigidity and prevents edge effects. Because of the fine mesh, the diffusion layers of each wire superimpose resulting in a diffusion layer similar to a planar electrode so a planar diffusion profile is obtained. By using two counter electrodes (one above and one below the cavity) and a fine reference wire in a capillary close to the working electrode, acceptable voltammograms can be measured in situ. Though the cell still suffers from the consequences of the mass transfer limitations and the unavoidable natural convection. In addition in non-aqueous media the lamination often fails rendering the solution unusable. Therefore the cell is most often applied in uncomplicated identification studies and for more complex studies or kinetic studies more complex (flow cell) designs are employed.

8.3.2 The Allendoerfer cell

The Allendoerfer cell is worth mentioning because it is a stationary cell design with the highest sensitivity towards unstable radicals. The cell exists in two designs, one using a TE₀₁₁ cylindrical cavity [191,192] and one based on a loop-gap resonator [181]. The high sensitivity is a result of the cell design. The cell consists of a quartz tube (6 mm ID) in which a finely wound shallow pitched helix stands freely against the inner wall (Figure 8.3). This helix acts as the working electrode and provides the unique feature that the microwaves only “see” the portion of solution between the helix and the tube and do not penetrate the inside of the helix. A first advantage of this is that because only tiny amount of solution is seen by the microwaves, the sensitivity of the cell is high, even when using lossy solvents. A second advantage is that the inside of the helix electrode can house the counter electrode and reference electrode. Because the counter electrode can stretch over the entire length of the working electrode, a good current and potential distribution is obtained and also a very low ohmic drop. Where the cell resistance in conventional flat cell designs can be as high as several kΩ, in the Allendoerfer cell it was found to be only 13 Ω when filled with DMF (+0.1 M TBAP) [191]. The cell was also adapted to flow capabilities to study short-lived

radicals [192], though it is not applicable for kinetic studies since the flow over the helix does not have well-defined hydrodynamics.

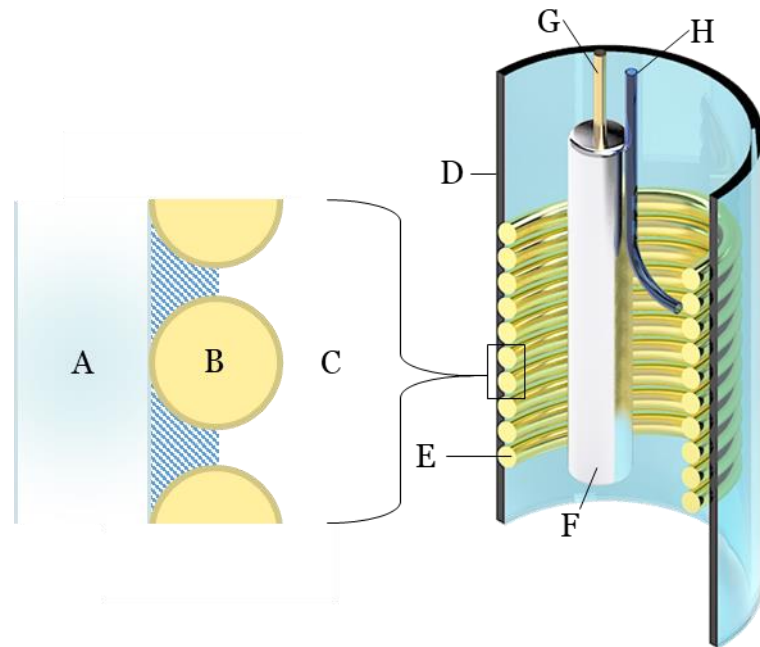


Figure 8.3: Left: schematic illustration of the quartz-metal helix-solution interface with A: the wall of the quartz tube, B: cross section of the helix wire, C: the liquid sample. The shaded portion of area C represents the portion of the sample seen by the microwaves. Right: 3D representation of a cross-section of the cell with D: the quartz tube, E: Au helical working electrode, F: Pt counter electrode, G: counter electrode lead-out wire, H: reference electrode Luggin capillary. Based on [191]

8.3.3 The channel electrode cell

The channel electrode cell is a flow cell design based on a channel electrode. Designed by Compton and Coles it is also often referred to as the Compton-Coles cell [178]. The design is simple and versatile and offers the advantages of a hydrodynamic electrode [193]. It has well-defined hydrodynamic properties that have been described and equations for the concentration profile and the limiting current have been derived [168]. The channel electrode is a non-uniform accessible electrode which offers an additional sensitivity in distinguishing between related mechanisms, such as ECE and

DISP1 [194]. This type of cell is the most used hydrodynamic cell for EPR and has been applied for kinetic studies and deducing reaction mechanisms in many studies (see [57]).

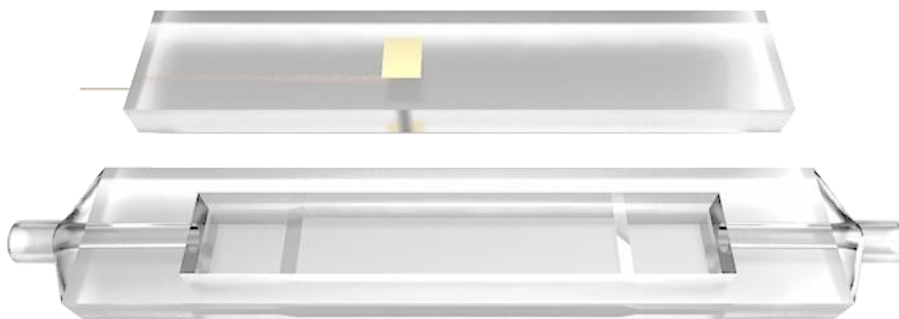


Figure 8.4: Illustration of the channel electrode cell with a copper lead-out wire and gold working electrode for in situ EPR spectroelectrochemical experiments. The deeper sections at each end of the channel serve to equalize the pressure across the full width. Redrawn from [168].

It is obvious that each cell design has its advantages and disadvantages. The best suited setup depends on the main goal of the application. If the detection and identification of intermediates is targeted, some compromises on the electrochemical performance can be made. A high as possible sensitivity is always desired, but other criteria might put restrictions on this. To obtain a cell with broad applicability in electrocatalytic research, a flat and highly reproducible surface is a main criterion. This puts limitations on the possible geometries. Additionally, to stimulate the use of cell, the setup will be built suitable for the most common spectrometer setup, which is a TE₁₀₂ cavity. This puts further implications on the geometry. The requirements and the construction of such setup is discussed in detail in Chapter 9.

CHAPTER 9

Development of a versatile *in situ* EPR spectroelectrochemistry platform for electrocatalysis

THE DESIGN AND CONSTRUCTION OF A VERSATILE SETUP FOR *IN SITU* EPR SPECTROELECTROCHEMISTRY, OPTIMIZED FOR ELECTROCATALYSIS, IS PRESENTED. THE DESIGN CRITERIA ARE DISCUSSED IN DETAIL. THE ELECTROCHEMICAL AND SPECTROSCOPIC PERFORMANCE OF THE CELL IS EVALUATED BY TWO STANDARD REACTIONS: THE ELECTROCHROMIC REDUCTION OF METHYL VIOLOGEN IN AN AQUEOUS ENVIRONMENT AND THE REDUCTION OF *P*-BENZOQUINONE IN A NON-AQUEOUS ENVIRONMENT.

This chapter is in preparation for publication as: D. Pauwels, H. Y. Vincent Ching, S. Van Doorslaer, K. De Wael, T. Breugelmans, A versatile *in situ* EPR spectroelectrochemistry platform for electrocatalysis, *Electrochemistry communications* (2018)

9.1 Introduction

A profound electrocatalytic investigation includes the possibility to investigate the influence of the electrocatalyst on the reaction mechanism, which presumes the ability to identify intermediates and determine reaction mechanisms. Hence, the first step to achieve this goal is to acquire a versatile platform for the detection of radical intermediates that allows the incorporation of different electrocatalysts. As shown in the previous chapter quite some work has been done in the development of cells and electrodes upon which can be build, however, there are some additional requirements that are not achieved by the designs available in literature. The platform should fulfill following criteria:

- Simple and inexpensive design

Preferably the design is as simple and as cheap as possible, but not less than necessary. Most often multiple repeated experiments are performed. In case different electrocatalysts are measured the same electrode cannot be reused. The more simple the design, the more easy it is to replicate which will ensure a similar performance between two different electrodes. Additionally an inexpensive design allows for many repeated experiments.

- Have a flat surface to incorporate nanostructured electrocatalysts

Common strategies to enhance catalytic activity and reduce the amount of expensive electrocatalyst materials involves alloying and creating nanostructured electrocatalysts of which the morphology is carefully tuned [171] (Figure 9.1). These alloys and nanostructured catalysts may have a significant effect on the mechanism. Therefore the in situ EPR spectroelectrochemical experiments should be conducted on these catalysts directly. However, to the best of our knowledge, all reports in literature about in situ EPR spectroelectrochemical measurements mention the use of monometallic bulk materials only. Though nanostructured catalysts can be

deposited on three-dimensional carrier structures as well, for investigations a flat surface is preferred as it offers a much more reproducible and controllable deposition. In addition it is also easier to correlate the results with experiments performed in regular batch setups which commonly use flat substrates.

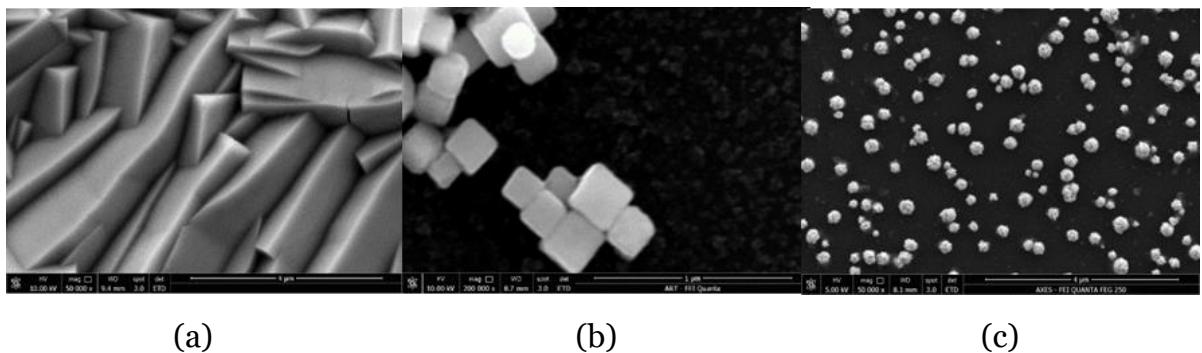


Figure 9.1: Examples of nanostructured catalysts: (a) layer deposition, (b) cubic nanoparticles, (c) spherical nanoparticles.

- Provide a reproducible surface

This criterion is inseparably connected to the previous one. Any form of repeated measurements require a reproducible base situation and this is even more the case with (electrodeposited) nanostructured electrocatalysts. The surface roughness, morphology and material of the substrate have an influence on the deposited catalysts. Therefore it is of utmost importance to have a reproducible substrate. In regular batch electrochemistry this is ensured by thoroughly mechanically polishing the substrate electrodes, which is not possible for the extremely thin and small electrodes necessary for *in situ* EPR spectroelectrochemistry. The flat surface of the electrode substrate has to be constructed in such way that it provides a reproducible surface. It is also obvious that an electrode substrate on which nanoparticles were deposited cannot be reused for a subsequent new deposition as is the case in batch electrochemistry. This is an additional incentive for the first criterion.

- Applicable in both aqueous and non-aqueous environments

The standard solvent for electrochemistry is water and consequently a lot of electrochemistry proceeds in an aqueous environment. In organic electrochemistry however, non-aqueous environments are very common due to the solubility problems of several organic compounds in water. This criterion might seem straightforward, but the implementation not necessarily is. It requires the electrode construction to use materials that are both chemically resistant to a wide range of solvents and EPR inactive. Polyether ether ketone (PEEK) for example is a polymer with excellent chemical resistance, but its production process involves a radical polymerization and as a result, PEEK has a significant EPR response and is unsuitable for this application.

- Display reasonably defined electrochemical behavior

As discussed in the previous chapter, the nature of the EPR cells and the technique itself encompass some drawbacks for electrochemistry. These can be alleviated to some extent by smart design as shown by Neudeck et al. and Allendoerfer et al. As the main target is the identification of intermediates to elucidate reaction pathways the voltammetric response need not be equal to that in a batch experiment. However, a good electrochemical behavior will allow identifying correct voltammetric peaks *in situ* and will help performing accurate potential-controlled electrolysis. This is particularly important when complex reactions are studied.

9.2 Construction of the electrode

To achieve a simple design, the platform will be based on the common TE₁₀₂ cavity and consist of a flat cell and an innovative electrode construction. The Allendoerfer design discussed in the previous chapter might be the best solution for sensitivity, but is not applicable in this case as it does not fulfill the first two criteria. The solution of

Neudeck et al. (laminated electrodes) offers an acceptable electrochemical performance but also lacks to fulfill the second and fourth requirement.

To achieve a design that meets all criteria, the working electrode part is made by physical vapor deposition (PVD) of a metallic film onto an EPR inactive substrate. Sputter deposition is an easy and (relatively) inexpensive process. It offers a great deal of versatility as several different metals and even carbon can be sputtered. The resulting surfaces can be controlled accurately in size, shape and thickness and are reproducible. Figure 9.2 (a) shows different shapes and sizes of sputter deposited silver on polypropylene.

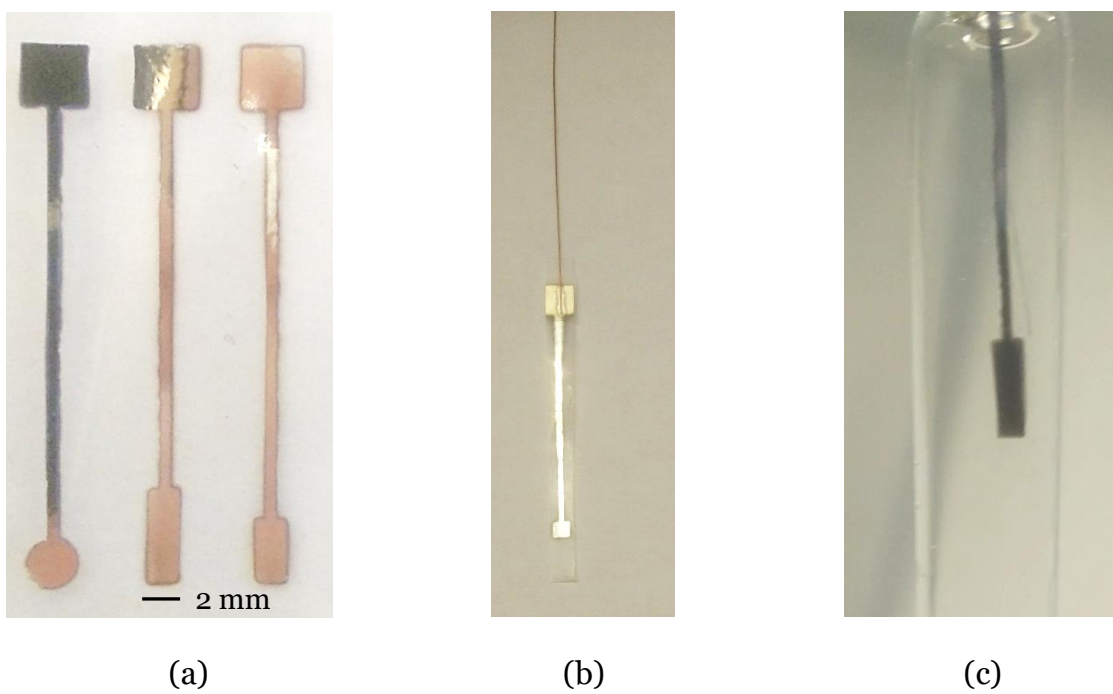


Figure 9.2: (a) Ag sputtered on PP creating different working electrode surfaces.
(b) Connection wire attached to a single working electrode tip.
(c) Close-up of an electrode in the flat section of an EPR flat cell.

To construct the electrode the required metal is sputter deposited onto a thin polypropylene film. Polypropylene (PP) is resistant to most common solvents in electrochemistry and does not give an EPR signal. Polytetrafluoroethylene (Teflon®)

is a commonly used polymer for EPR cells as it also offers a great chemical resistance and is EPR inactive, but in practice the adhesion of sputtered layers on Teflon is inferior compared to a PP substrate and can cause problems. The substrate thickness is a parameter that can vary within a certain margin. The substrate needs to be thick enough to provide sufficient rigidness to be able to insert it in the flat section of the EPR cell, but at the same time be thin enough to leave at least 100 µm of solution at the electrode surface to ensure proper diffusion [195]. The PP substrate used has a thickness of 30 µm which is rigid enough to easily insert it in and remove it out of the flat section. The metallic coating thickness can be controlled down to the nanometer level. A thickness of 100 nm ensures sufficient conductivity [196] and because of the large ratio of the surface area to the thickness edge effects can be neglected.

After a working electrode tip is sputtered, a connection wire is attached to the top. The reference electrode is added by securing a Teflon insulated silver wire (75 µm diameter) to the electrode tip which is stripped near the working electrode. The distance between the working electrode surface and the reference electrode is less than 1 mm. The top of the electrode tip is then inserted in a PP tube covering the connection and heat sealed. This sealed tip is subsequently attached to a glass tube which leads the connection wires out of the cell and also offers a rigid structure for better handling of the electrode. Figure 9.3 shows an illustration of a finished working electrode tip. A counter electrode is added by finely wounding an uncoated platinum wire around the base of the glass tube. The three wires (working electrode, reference electrode and counter electrode) are soldered to a cable which has 2 mm banana jack connectors for easy connection to the potentiostat. The top of the tube is sealed with a silicon stopper. This provides an airtight closure of the flat cell, but the electrode can still be moved vertically to adjust the height of the working electrode in the cavity.

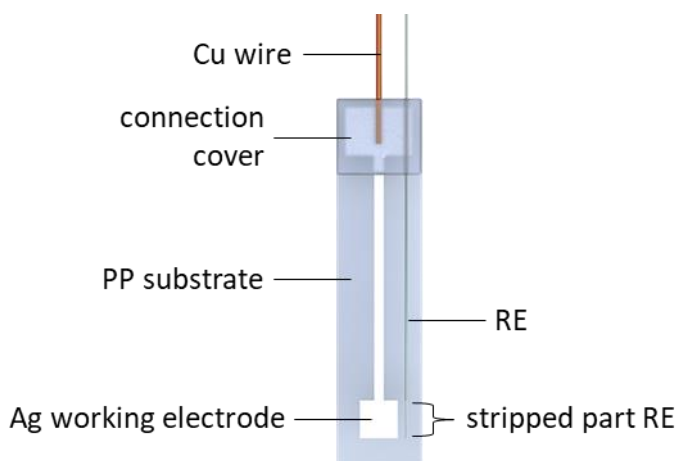


Figure 9.3: Illustration (not to scale) of a finished electrode tip. The wires are inserted in a glass tube which is then sealed.

9.3 Electrochemical and spectroscopic validation

The electrode's performance is evaluated by means of a standard reaction that is commonly used in both electrochemistry and EPR studies [185,197–199]: the reduction of methyl viologen (MV). Methyl viologen in solution is a divalent cation MV^{2+} that after reduction yields the paramagnetic active radical cation $MV^{\bullet+}$, a second reduction yields the diamagnetic MV^0 [200,201]. A useful property of MV is that the reversible reaction is an electrochromic reaction, i.e. there is a color change associated with its oxidation state. The divalent cation is colorless while the radical cation has a blue color and the neutral species MV^0 has a yellow color. Besides being able to visually follow the reaction by the color changes in solution this is very useful to check the electrode's construction and performance. The color shows where the reaction takes place and can be used to check if the connections are sealed properly. It also shows the electrode's accessibility by the difference in color intensity or the gradual color change over the electrode for large electrodes.

For the measurements, an electrode with an Ag working electrode surface was constructed as described in Section 9.2. Since the electrode has to be applicable in both aqueous and non-aqueous environments, the reaction was performed in both

environments in a standard batch setup and in the EPR flat cell. Methyl viologen dichloride hydrate (98 %) and the supporting electrolytes tetrabutylammonium perchlorate ($n\text{-Bu}_4\text{NClO}_4$, electrochemical analysis grade, $\geq 99.0 \%$) and sodium sulphate (Na_2SO_4 , $\geq 99.0 \%$) was obtained from Sigma-Aldrich. The water used for the aqueous environment is ultrapure water ($18.2 \text{ M}\Omega \text{ cm}$) purified in the laboratory (Milli-Q, Millipore, USA). Acetonitrile (ACN, HPLC gradient grade) was obtained from Chem-Lab (Belgium). For the measurements in ACN the methyl viologen dichloride hydrate was converted to the hexafluorophosphoric salt which is soluble in ACN. Figure 9.4 and Figure 9.5 show the results for the electrochemical validation.

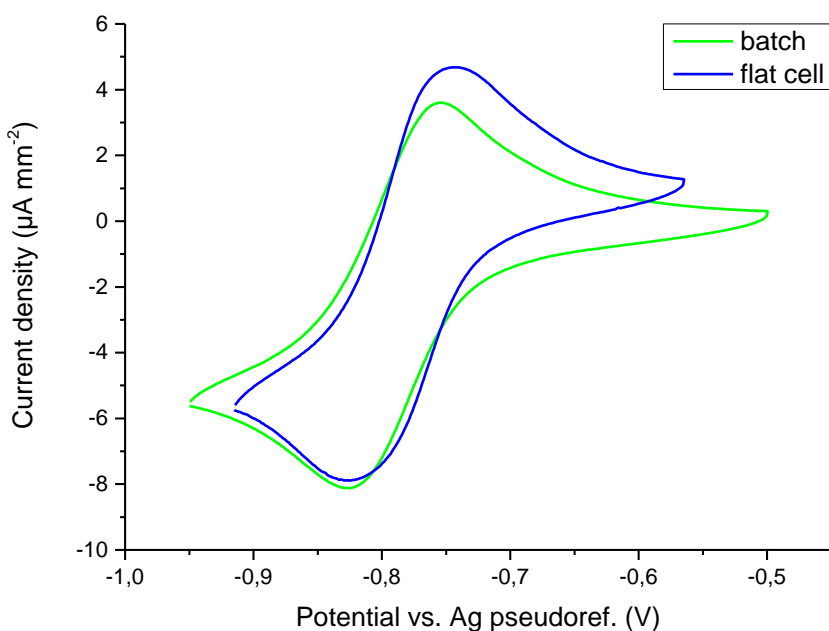


Figure 9.4: Cyclic voltammogram for the reduction of methyl viologen in aqueous environment on a PVD Ag electrode constructed as described in Section 9.2. Electrolyte = $\text{H}_2\text{O} + 0.2 \text{ M Na}_2\text{SO}_4$. Recorded at 50 mV s^{-1} .

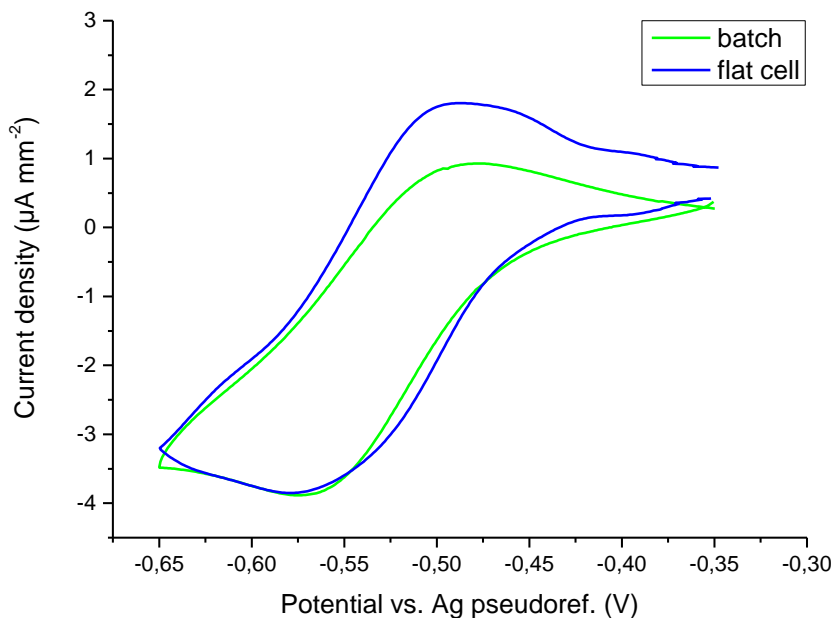


Figure 9.5: Cyclic voltammogram for the reduction of methyl viologen in acetonitrile on a PVD Ag electrode constructed as described in Section 9.2. Electrolyte = ACN + 0.1 M *n*-Bu₄NClO₄. Recorded at 50 mV s⁻¹.

From visual observation during the experiments it was clear that electrode was well-constructed and the reaction proceeded only at the working electrode surface. In all experiments (both setups in both environments) the blue discoloration was noticeable when the potential approached the reduction peak value (Figure 9.6). The discoloration also occurred immediately at the entire electrode surface, even in the flat cell. This means there is no significant potential difference over the electrode surface, an effect of the short distance between working electrode and reference electrode and the small thickness of the electrode tip which provides a linear diffusion profile.

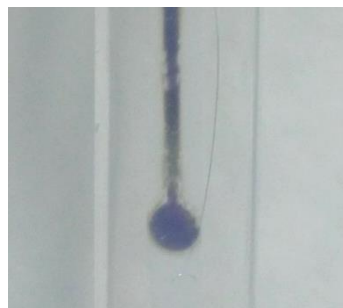


Figure 9.6: Blue discoloration of the methyl viologen radical cation resulting from the MV reduction on a Ag electrode in an EPR flat cell.

In both environments the CVs obtained in the batch setup are similar to those measured in the flat cell showing the excellent electrochemical response of the electrode construction. In the aqueous environment the peak-to-peak separation is 71 mV in the batch cell and 86 mV in the flat cell, close to the 59 mV in the ideal case of a one-electron reversible reaction. The peak-to-peak separation in ACN is 96 mV in the batch cell and 92 mV in the flat cell. The slightly higher peak separation values are expected due to the larger uncompensated resistance. An interesting observation is that in both environments the anodic peak current is slightly higher than the corresponding peak current in the batch cell. This implies that geometry of the flat cell and the electrode influence the diffusion and causes deviation from a semi-infinite linear diffusion situation. This deviation of the ideal case is also visible in the series of voltammograms recorded at different scan rates in Figure 9.7. The shift of the peak potentials at higher scan rates show the effects of the relatively high uncompensated resistance. Likewise, the inset of Figure 9.7 shows deviation from the linear correlation between the peak current and the square root of the scan rate for a diffusion controlled process.

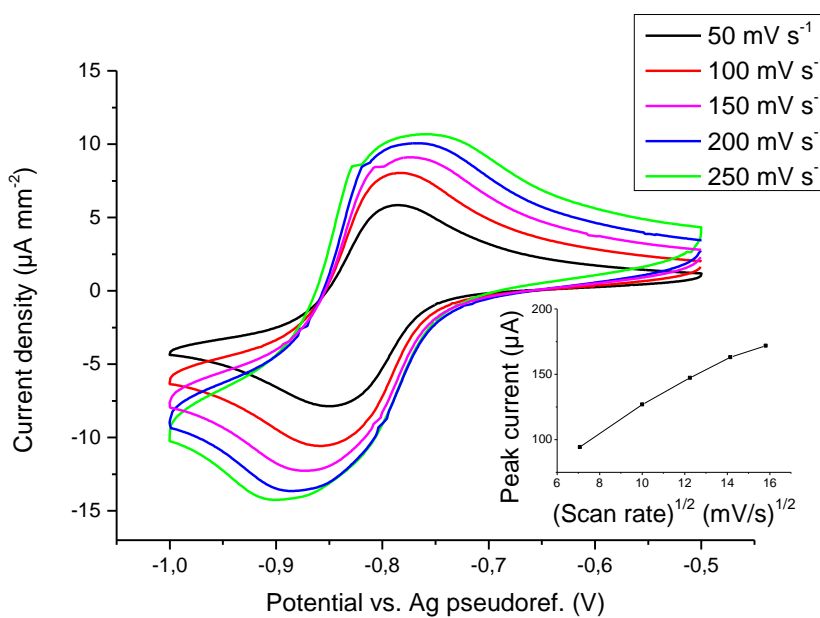


Figure 9.7: Cyclic voltammograms at different scan rates for the reduction of methyl viologen aqueous environment on a PVD Ag electrode constructed as described in Section 9.2. Electrolyte = $\text{H}_2\text{O} + 0.2 \text{ M Na}_2\text{SO}_4$. Inset: peak current versus $\sqrt{\nu}$.

The relatively high uncompensated resistance of this type of cell also becomes obvious during the measurements by the placement of the reference electrode. For a proper constructed electrode the distance between reference electrode and working electrode is less than 1 mm and a good electrochemical response is obtained. In the odd case that the reference electrode is loosened during the insertion and shifts position for a couple of millimeters, a significant distorted signal or even no signal at all is obtained.

To check the spectroscopic response, an EPR spectrum is recorded in both aqueous and non-aqueous environment during electrolysis of a 5 mM solution of the electroactive reactant. In the aqueous environment the reduction of methyl viologen is used. For the non-aqueous environment a different standard reaction is used: the reduction of *p*-benzoquinone which yields the EPR active semiquinone radical anion [182,202–205]. To perform the measurements, the cell was set up in the spectrometer and a CV was recorded to find the peak potential of the reduction. A

chronoamperometry was started at 100 mV more negative than the peak potential and simultaneously EPR spectra were recorded. The recorded spectra are shown in Figure 9.8. In both cases the expected spectrum was quickly discernible [182,197,199].

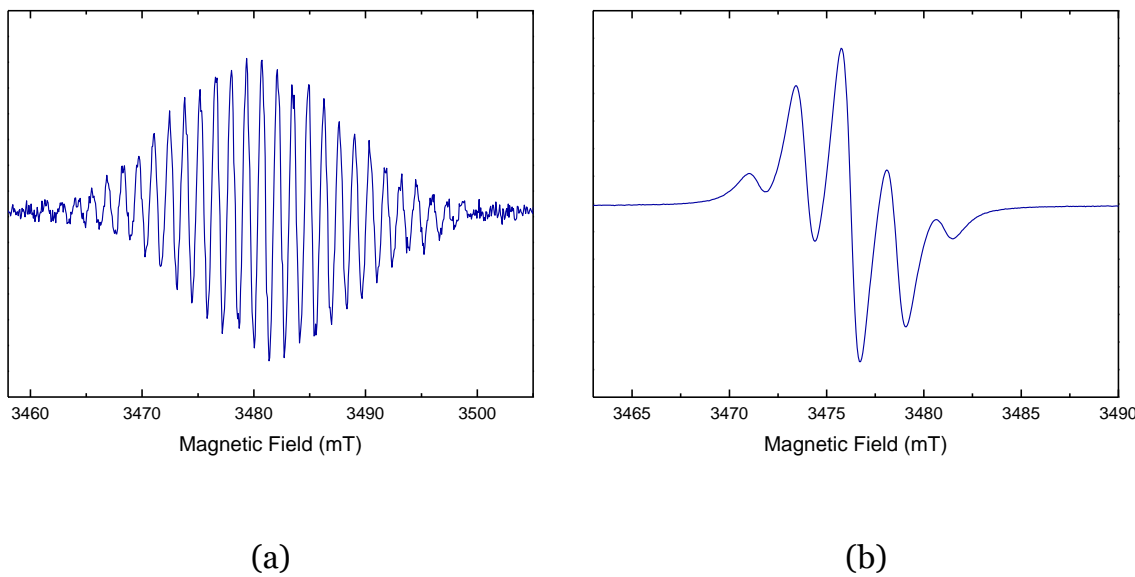


Figure 9.8: EPR spectrum recorded during in situ electrolysis of (a) 5 mM methyl viologen in $\text{H}_2\text{O} + 0.2 \text{ M Na}_2\text{SO}_4$ and (b) 5 mM *p*-benzoquinone in ACN + 0.1 M *n*-Bu₄NClO₄.

9.4 Conclusions

A versatile electrode construction for in situ EPR spectroelectrochemical experiments was developed. The setup showed a reasonably-defined electrochemical response in both an aqueous and non-aqueous environment. Subsequently the setup was used to measure EPR spectra in both environments which in both cases was achieved without difficulties. These results validate the applicability of the setup.

9.5 Supplementary Information

In this section a brief overview is given of other types of electrode constructions for in situ spectroelectrochemical experiments which are commonly found in literature. The construction and the performance is described and compared to the sputter coated electrode construction.

9.5.1 Mesh-electrode

The term mesh-electrode is used to refer to an electrode construction that uses a fine metal mesh as a working electrode. Such types of electrode have been used since the first EPR spectroelectrochemical experiments, but have become increasingly popular since the improved design of Neudeck et al. was reported [190,206–213]. A mesh-electrodes offers an optically transparent electrode. This is useful in EPR spectroscopy as the electrode does not block the radicals from the microwaves in the cavity and hence, a high sensitivity is obtained. Because of its optical transparency, such design can also be used together with other spectroscopic techniques such as UV-VIS. The mesh also offers a good electrochemical performance. If the timescale of the experiment is long enough (or a low scan rate is used), the diffusion layers at each wire superimpose and a planar diffusion profile perpendicular to mesh is obtained, giving it an electrochemical response similar to a sheet electrode. The scan rates or timescales for which this happens depends on the wire density and wire thickness of the mesh. Finer meshes permit a shorter experiment time, which can be useful in flat cells to prevent natural convection.

The fine metal meshes that are used are not mechanically stable enough by themselves to be used in solution as an electrode. Often this problem was solved by using special cell designs or different sorts of glue depending on the solvent. To expand the applicability, Neudeck et al. made a laminated design in which the mesh and the connection wire is thermally laminated with a laminating foil in which a hole is cut to provide an active electrode area. This adds rigidity to the electrode and

ensures that the active part of the electrode is confined to the hole so it can be placed in the most sensitive part of the cavity.

9.5.1.1 Construction of the mesh-electrode

To construct the mesh-electrode, a platinum mesh is used with the following specifications (Table 9.1).

Table 9.1: Specifications of the platinum mesh working electrode.

Aperture (mm)	0.25
Diameter (mm)	0.06
# wires (inch ⁻¹)	82
Open area (%)	65

Assumed that the wires are completely accessible this yields an active surface area of approximately $1.2 \text{ cm}^2/\text{cm}^2$ mesh. This is a minor overestimation as the wires are not 100 % accessible. A planar sheet electrode with both sides accessible has an active surface area of $2 \text{ cm}^2/\text{cm}^2$ sheet, but if only one side is accessible this is of course only 1 cm^2 . Since the mesh is optically transparent it offers a slightly bigger active surface area than a one sided sheet electrode for the same geometrical area.

A connection is made to the working electrode mesh with a thin copper wire and the construction is laminated between two laminating foils of $38 \mu\text{m}$ thickness which results in a total thickness of $76 \mu\text{m}$. This is thin enough to ensure proper diffusion around the electrode. Holes are made in the laminating foils before the lamination process to provide a working electrode surface area. Typically rectangular holes of $\sim 10 \text{ mm}^2$ or less are used. The reference electrode is provided by a coated silver wire of which the coating is removed at the tip near the working electrode. As explained in the previous sections of this chapter, this results in a low ohmic drop between working and reference electrode. To keep the reference electrode in place, the wire is attached to the connection wire of the working electrode and included in the lamination foil

(besides the bottom tip which provides the active reference electrode surface area). To complete the three-electrode design, a counter electrode is added by attaching a thicker platinum wire which extends from the top of the construction until right above the thin section of the flat cell. The electrode construction is finished by fixing a stopper to the top of the laminated electrode so the cell is sealed airtight when the electrode is put in place. FIGURE SHOWS AN ELECTRODE

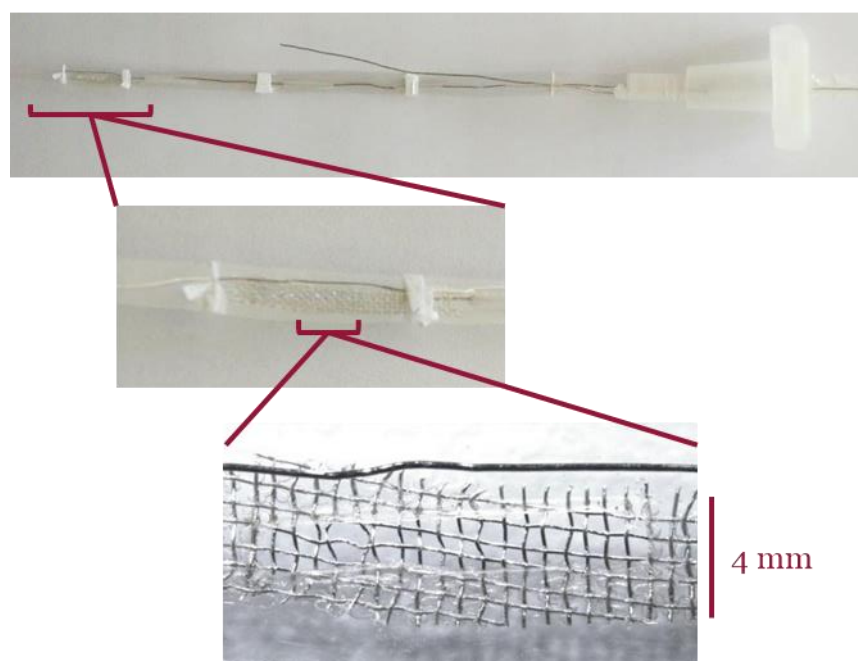


Figure 9.9: Picture of a platinum mesh-electrode. The largest magnification shows the laminated platinum mesh working electrode with a hole of approximately $2 \times 8 \text{ mm}^2$. The wire is a $75 \mu\text{m}$ silver wire that serves as reference electrode.

9.5.1.2 Performance of the mesh-electrode

This type of electrode has been used in several studies and several reports can be found in literature (see references listed in Section 9.5.1). Considering the criteria for the platform listed in Section 9.1 the electrode was evaluated on its performance in both aqueous and non-aqueous media. For the aqueous environment the reduction of methyl viologen was used and for the non-aqueous environment both the oxidation

of hydroquinone and the reduction of benzoquinone was attempted which both result in the semiquinone anion radical (Figure 9.10).

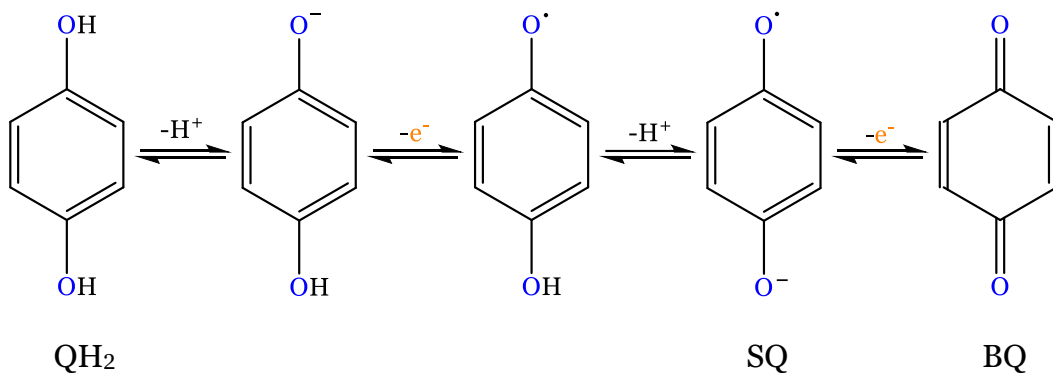


Figure 9.10: Oxidation of hydroquinone (QH₂) to benzoquinone (BQ) (left to right) and reduction of benzoquinone to hydroquinone (right to left) in a protic solvent (in an aprotic solvent the quinone dianion is obtained) with the semiquinone radical anion intermediate (SQ).

For the reduction of methyl viologen in aqueous environment the mesh-electrode exhibits an excellent electrochemical response in the flat cell, similar to the response in a batch cell (Figure 9.11 (a)). The peak-to-peak separation is 62 mV in the batch setup and 96 mV in the flat cell. Thanks to the blue color of the methyl viologen radical anion it could be seen that the reaction only proceeded at the part of the mesh which was accessible via the hole in the lamination foil. To record the EPR spectrum, a chronoamperometry was started at the peak potential of an *in situ* CV and simultaneous the EPR spectrum was recorded. The resulting spectrum shown in Figure 9.11 (b) is the expected spectrum for methyl viologen.

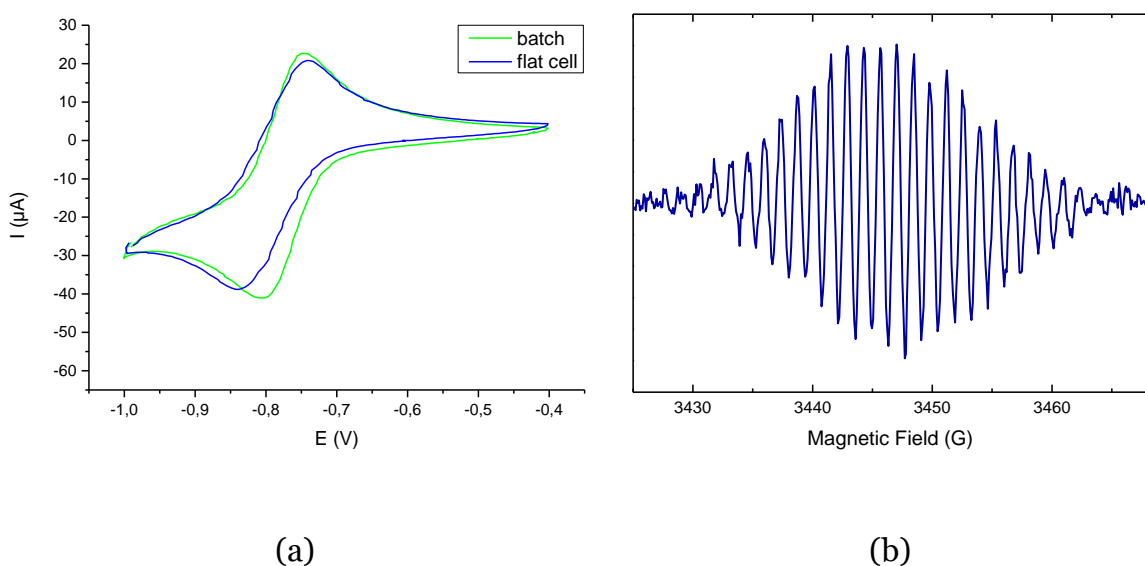


Figure 9.11: (a) Cyclic voltammogram for the reduction of methyl viologen in aqueous environment on a platinum mesh-electrode in both a standard batch setup and in an EPR flat cell. Recorded at 100 mv s^{-1} . (b) EPR spectrum recorded during in situ electrolysis of 5 mM methyl viologen in $\text{H}_2\text{O} + 0.2 \text{ M Na}_2\text{SO}_4$. The potential was set at the peak potential of the reduction peak during an in situ CV.

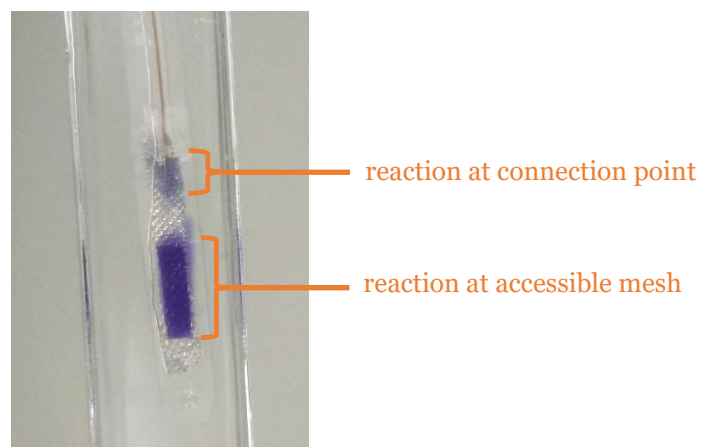


Figure 9.12: Example of a failure of the mesh-electrode after usage in a non-aqueous environment. The intense blue discoloration due to the methyl viologen radical anion shows that the reaction not only proceeds at the cut out hole (lower, intense blue color) but also between the lamination foil at the connection point (upper, less intense blue color).

In the non-aqueous environment however, the laminated mesh-electrode showed its major disadvantage. Initial scans showed the expected voltammograms but in subsequent scans, distortions became noticeable until eventually no decent voltammogram could be acquired anymore. Using the methyl viologen as a redox indicator it became clear that the lamination failed which caused the solvent to reach larger areas of the mesh and the connection (Figure 9.12). This caused the reaction to proceed at the connection wire itself as well. At this stage the lamination failed and was easily dismantled. The reason of the failure is that thermal lamination is actually gluing two polymer sheets together with a thermally activated glue. If the glue is not resistant to the solvent, it will dissolve and the lamination will fail. In acetonitrile this stage is reached after only minutes, making the laminated mesh-electrode unsuitable for use in non-aqueous solvents.

9.5.2 Wire-electrode

Another type of electrode commonly reported in literature is the wire-electrode. Though several electrode designs are constructed with wires (such as the helix electrode of Allendoerfer et al.), this term is usually used for electrode constructions using a straight wire as working electrode [185,197,202,214–217]. An advantage of a wire-electrode is that the construction is less complex compared to that of the mesh-electrode. It is also a scalable design as very thin wires can be used, making the design applicable for Q- and W-band EPR spectroscopy [216]. The electrode construction can be achieved in several ways. Usually coated wires are used of which the ends are stripped to provide the electrode surface area. Cutting the wires at different heights prevents short circuiting. Since the wires offer little mechanical stability they have to be attached to some sort of rigid body to be able to repeatedly and properly insert them in a flat cell. The diameter of the wires can vary a lot and usually a thicker wire is desired for additional mechanical strength and a larger surface area. However, if the diameter of the wire approaches the height of the flat section in the EPR cell (for example >150 µm wires in a <250 µm flat cell), the voltammograms become distorted or it might even be impossible to make an

electrochemical measurement. As with the sputter coated electrode (and the mesh-electrode), at least 100 µm of solution should be left to distribute around the wire to allow proper diffusion.

9.5.2.1 Construction of the wire-electrode

To construct the wire-electrode silver and platinum wires of 75 µm diameter are used. The silver wire is Teflon coated and the platinum wire is uncoated. The silver wire is used to construct the working and reference electrode and the platinum wire serves as counter electrode. The coating is removed by carefully holding the wires near a flame which causes the coating to smolder away. This should be done carefully as the flame is hot enough to melt the silver wire. In case platinum is used, the coating can be burned off as the flame cannot melt platinum. For the working electrode approximately 2 cm of coating is removed, for the reference electrode only a couple of millimeters suffice.

The wires are inserted through a glass tubing to offer mechanical stability to the construction. The wires extend from the end of the tube so that when the glass tubing is brought into the flat cell until right above the flat section, the working electrode extends to about the center of the flat section, which is the most sensitive part of the cavity. The reference electrode is drawn out of the bottom of the tube until right above the uncoated part of the working electrode. This results in a small distance between working and reference electrode and prevents contact between them. The counter electrode is drawn out further and bend upwards and then finely wound around the base of the glass tubing. This provides a large surface area close to the flat section. The wires are fixed in place by closing the bottom of the tube with a small amount of fast-drying epoxy. This also ensures that no solvent enters the tubing. At the top of the tubing the wires are soldered to connections and a stopper is attached to provide an airtight sealing when the electrode is inserted in the flat cell.

9.5.2.2 Performance of the wire-electrode

Many reports can be found in literature that use this type of electrode (see the references in Section 9.5.2). The mesh-electrode offers a performant platform for aqueous environments but is not suited for non-aqueous environments. Therefore the focus for the wire-electrode was put on the applicability in non-aqueous environments. Similar to previous tests the reduction of benzoquinone was used. Figure 9.13 (a) shows a CV of the reduction of BQ in ACN on a silver wire-electrode and Figure 9.13 (b) shows the resulting EPR spectrum measured in situ during electrolysis at the peak potential of an in situ CV. The resulting spectrum is the spectrum as expected. Contrary to the mesh-electrode, prolonged or repeated use of the wire-electrode in non-aqueous solvents showed no adverse effect on the electrochemical performance.

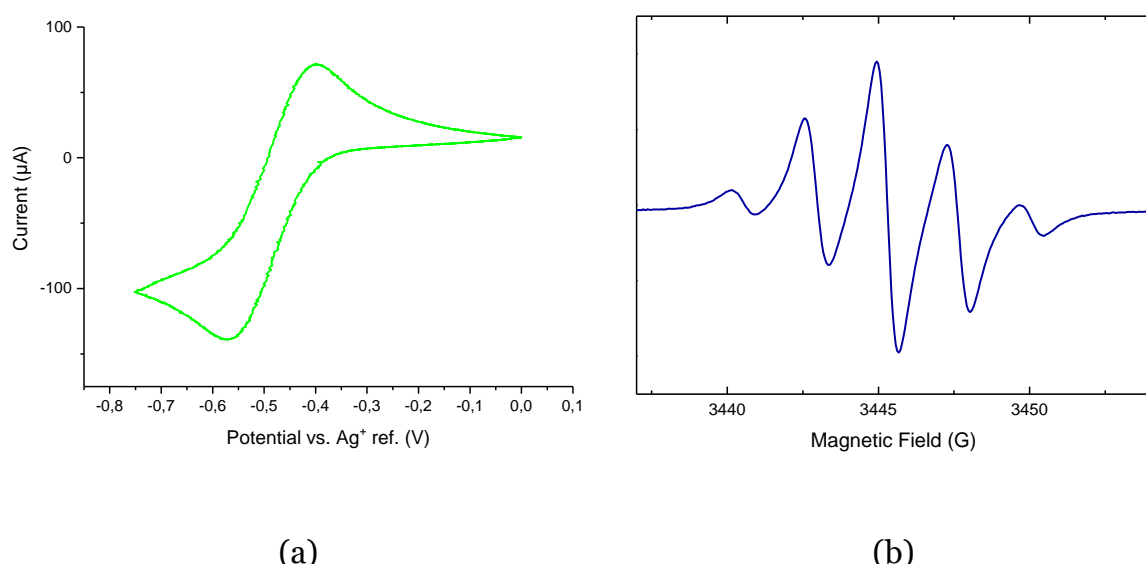


Figure 9.13: (a) Cyclic voltammogram for the reduction of benzoquinone in acetonitrile on a silver wire-electrode in a standard batch setup. (b) EPR spectrum recorded during in situ electrolysis of 5 mM benzoquinone in $\text{ACN} + 0.1 \text{ M } n\text{-Bu}_4\text{NClO}_4$. The potential was set at the peak potential of the reduction peak during an in situ CV.

The reduction of methyl viologen was also used as a visual indicator to check the electrode. Figure 9.14 shows the results of this reaction on the electrode in a flat cell. Above the flat section, in the bulk part of the flat cell, the bottom of the glass tube through which the electrode wires run, can be seen.



Figure 9.14: Picture of the reduction of methyl viologen on a wire-electrode in an EPR flat cell. The blue color is due to the methyl viologen radical anion and shows the active surface area of the working electrode.

CHAPTER 10

Elucidation of the mechanism of the electrosynthetic intramolecular cyclisation of allyl 2-bromobenzyl ether

THE SETUP DEVELOPED IN THE PREVIOUS CHAPTER IS USED TO INVESTIGATE AN INDUSTRIAL RELEVANT CASE STUDY: THE ELECTROSYNTHETIC INTRAMOLECULAR REDUCTION OF ALLYL 2-BROMOBENZYL ETHER TO 4-METHYLISOCHROMANE. TO ELUCIDATE THE REACTION MECHANISM, THE INTERMEDIATES ARE DETECTED AND IDENTIFIED BY DENSITY FUNCTIONAL THEORY COMPUTATIONS. THE GEOMETRY-OPTIMIZED MODELS OF THE SPIN-TRAPPED RADICALS ARE PROVIDED.

This chapter is submitted for publication as: D. Pauwels, H. Y. Vincent Ching, M. Samanipour, S. Neukermans, J. Hereijgers, S. Van Doorslaer, K. De Wael, T. Breugelmans, Elucidation of the mechanism of the intramolecular cyclisation of allyl 2-bromobenzyl ether by *in situ* EPR spectroelectrochemistry and DFT calculations, *Electrochimica Acta* (2018).

10.1 Introduction

In Chapter 3 the advantages of combining electrochemical techniques and EPR spectroscopy for electrocatalytic research have been discussed. Being able to detect and identify the radicals that are formed during the reaction, will provide essential information on the chemical nature and electronic structure of the different intermediates and the influence of the catalyst. This in turn allows an optimal tuning of the electrocatalyst. In the previous chapter the development of a generic setup for *in situ* EPR spectroelectrochemistry adapted specifically for electrocatalytic research was shown. Standard reactions were used to validate both the electrochemical and spectroscopic response of the constructed electrode. As a proof of concept, the setup is used to investigate the intermediates in an industrial relevant reaction: the reductive cyclisation of allyl 2-bromobenzyl ether, which to the best of our knowledge, has not been reported in the literature.

The electrosynthetic reduction of organic halides has attracted extensive interest and accompanying research [23,218]. This interest has been sparked by the many important applications associated with these reactions, such as reduction of environmental pollutants, investigation of the DET mechanism (dissociative electron transfer), carbon fixation and upgrading of organics through activation of the R-X bond [219–223]. Of specific interest is the synthesis of heterocyclic compounds due to important applications in pharmaceuticals [224–226], pesticides [227], dyes [228] and synthetic applications [229]. An industrially relevant and interesting case is the cyclisation of allyl 2-bromobenzyl ether to 4-methylisochromane (a benzopyran derivate). On the one hand it is considered a model reaction [230,231] and, on the other hand, it is of importance for the pharmaceutical industry as benzopyran is an essential building block for numerous drugs.

Conventional synthesis of heterocycles is complex and requires a large number of reaction steps and the use of auxiliaries which results in a low selectivity [218]. The reductive radical cyclisation of aryl halides onto an unsaturated bond is frequently used to construct fused aromatics in heterocyclic organic synthesis [230,232]. However, a major drawback of using organic halides in electrosynthesis is that the electrochemical activation of C-X bonds, especially in chlorides and bromides, requires very negative electrode potentials, which is impractical for industrial production processes due to exuberant energy costs. To reduce the large overpotentials and increase selectivity, research has been directed towards improving the catalytic activity of the electrode materials [233–236]. The strategies that have been employed include: investigating different bulk materials that have shown potential for the carbo-halogen bond rupture such as Ag, Pd, Ni and Cu [234,237–239], tuning the morphology and geometrical characteristics of the electrode [235,240] and using a homogeneous electrocatalysis route with mainly transition-metal complexes [230,241–244]. In order to select the best electrocatalytic material and optimally tune the catalysts, a profound knowledge of the complex reaction mechanism and the effect of the catalyst is required. Figure 10.1 shows a proposed mechanism for the cyclisation of allyl 2-bromobenzyl ether [236].

The reduction of aryl halides occurs through a dissociative electron transfer leading to the scission of the carbon-halogen bond [222,237]. There are two possible pathways for this: a stepwise mechanism or a concerted mechanism. The former is shown by reactions (1) and (2) with the formation of an intermediate radical anion, the latter is presented by reaction (3) leading directly to the allyl benzyl ether radical. This radical can then undergo an intramolecular cyclisation reaction (4) after which it is reduced (5). Alternatively, the allyl benzyl ether radical can also be reduced directly (6). Since the product of interest is the benzopyran derivate obtained in reaction (5), the optimization of the electrocatalyst will also include preventing reaction (6) from taking place.

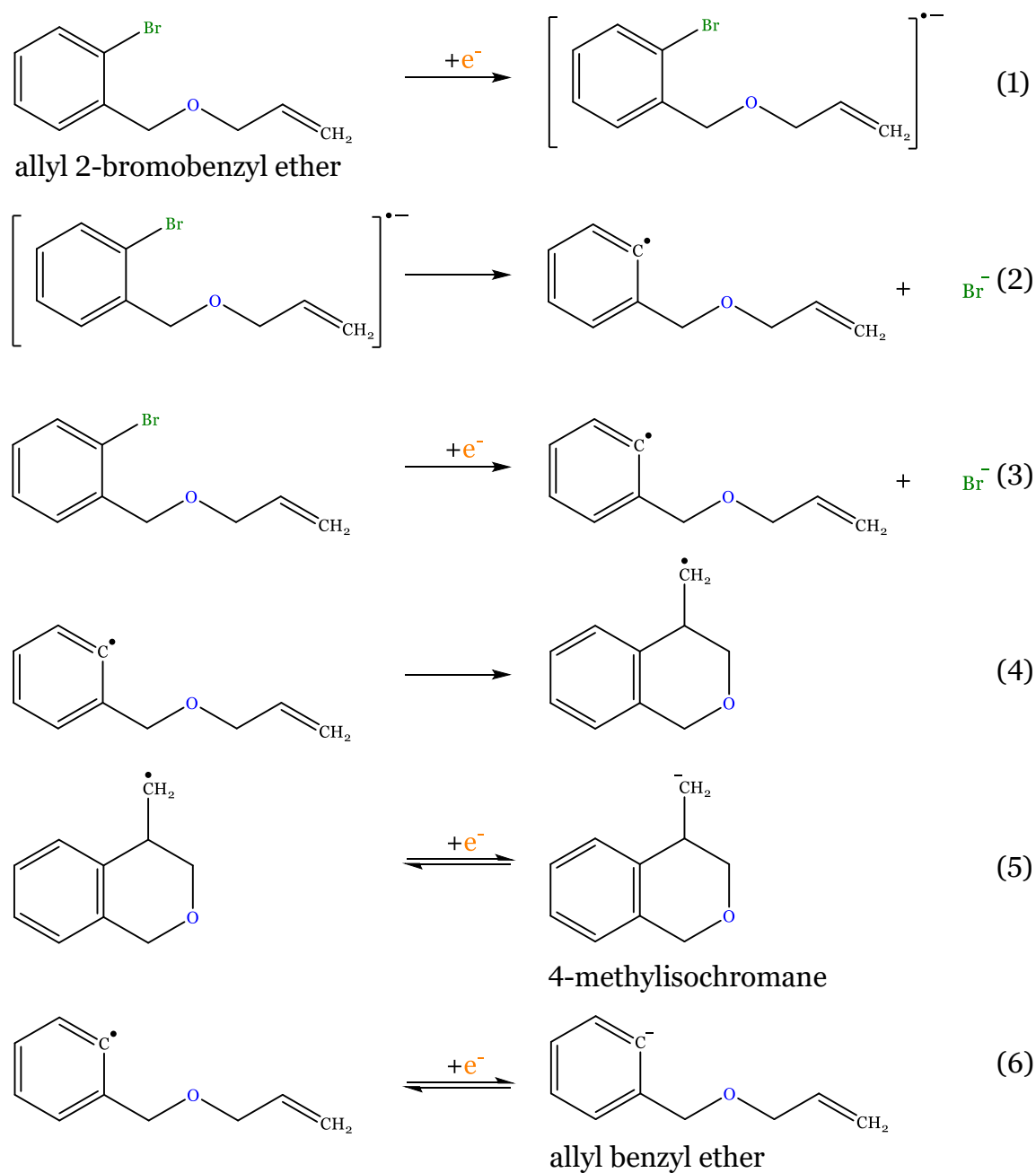


Figure 10.1: Possible reaction pathways to construct fused aromatic molecules starting from allyl 2-bromobenzyl ether in an aprotic solvent [236].

10.2 Experimental

10.2.1 Chemicals

Acetonitrile (ACN, HPLC gradient grade, $\geq 99.9\%$) was purchased from Chem-Lab (Belgium). Allyl 2-bromobenzyl ether (ABBE, 95 %), (2,2,6,6-tetramethylpiperidin-1-yl)oxyl (TEMPO), the spin trapping agent *N*-tert-Butyl- α -phenylnitronone (PBN, for ESR-spectroscopy, $\geq 99.5\%$) and the supporting electrolyte tetrabutylammonium perchlorate (TBAP, *n*-Bu₄NClO₄, 99.0 %) were purchased from Sigma-Aldrich (Belgium).

10.2.2 Setup and procedure

The combined EPR and electrochemical experiments were performed in a Wilmad WG-810 Suprasil® (quartz) electrolytic flat cell. The cell was positioned in a TE₁₀₂ cavity in a Bruker E580 Elexsys spectrometer and a custom-constructed electrode as described in Chapter 9 with a silver working electrode and a platinum counter electrode was used.

Experimental solutions were prepared with 0.1 M *n*-Bu₄NClO₄, 5 mM of the analyte and 15 mM of PBN. Prior to measurements, the solutions were extensively flushed with argon. To fill the cell, approximately 1.5-2 ml is pipetted under inert atmosphere. The filled cell is further flushed with argon, creating an argon blanket on top of the solution. The cell is closed by inserting the electrode construction from the top and is then transferred to the spectrometer and connected to the potentiostat. A PAR VersaSTAT 3 is used to apply and measure the electrochemical signal. Firstly, CVs are measured to determine the exact potential of the reduction peak versus the pseudo-reference electrode in this cell. Then the experiment is performed by applying a constant potential set at the cathodic peak potential. The EPR spectra are recorded simultaneously at X-band in continuous-wave (CW) mode (~ 9.7 GHz) at room

temperature with 5 mW microwave power 0.1 mT modulation amplitude and 100 kHz modulation frequency.

10.2.3 EPR simulations and density functional theory (DFT) computations

The EPR spectra were simulated using the EasySpin-5.1.11 module [245] running in Matlab 2017a. Spin-unrestricted (UKS) DFT computations were performed with the ORCA package [246–249] for PBN-Ox, PBN-allyl benzyl ether and PBN-4-methylisochromane in ACN, and TEMPO, and (5,5-dimethyl-2-hydroxyl-pyrrolin-1-yl)oxyl (DMPO-OH) in water. To simulate the solvent, a dielectric surrounding with the dielectric constant of the respective solvents according to the COSMO model was used [250]. For the geometry optimizations, the Becke-Perdew density functional (BP86) [251–253] and the split-valence plus polarization (SVP) basis set [254] were used for all atoms. The energy was converged to 1×10^{-8} Hartree (Eh) and the convergence tolerances in the geometry optimization were 3×10^{-4} Eh/Bohr for the gradient and 5×10^{-6} Eh for the total energy. The coordinates of the optimized geometries are given in Table S2. For benchmarking, single-point calculations with the B3LYP/EPR-II, B3LYP/6-31+G**, and PWPPB95/EPR-II functional/basis sets [255–258] were used to predict the EPR spectral parameters from the optimized geometries.

10.3 Results and discussion

10.3.1 Electrochemical validation

In previous work from our laboratory ([236]), several cathode materials were investigated as potential electrocatalyst for the electrochemical cyclisation of allyl 2-bromobenzyl ether to 4-methylisochromane (4-methyl-3,4-dihydro-1*H*-2-benzopyran) and an activity scale of bulk materials was determined. It was shown that out of the selected materials, silver exhibits the best activity with a very high selectivity towards the product of interest. It was also shown that on silver, two

distinct reduction waves were observable, corresponding with one or two electrons being transferred. Setting the potential to the first reduction peak (least negative potential) exclusively yields 4-methylisochromane, while at the second reduction peak the major product is the undesired allyl benzyl ether (((allyloxy)methyl)benzene). Since 4-methyl-isochromane is the desired product, the reaction at the first reduction peak will be investigated. A CV study was performed to find the potential of the reduction peak versus the pseudo-reference electrode. This was done in both a standard batch setup and in the EPR flat cell so electrochemical behavior of the electrode in both situations could be compared (Figure 10.2).

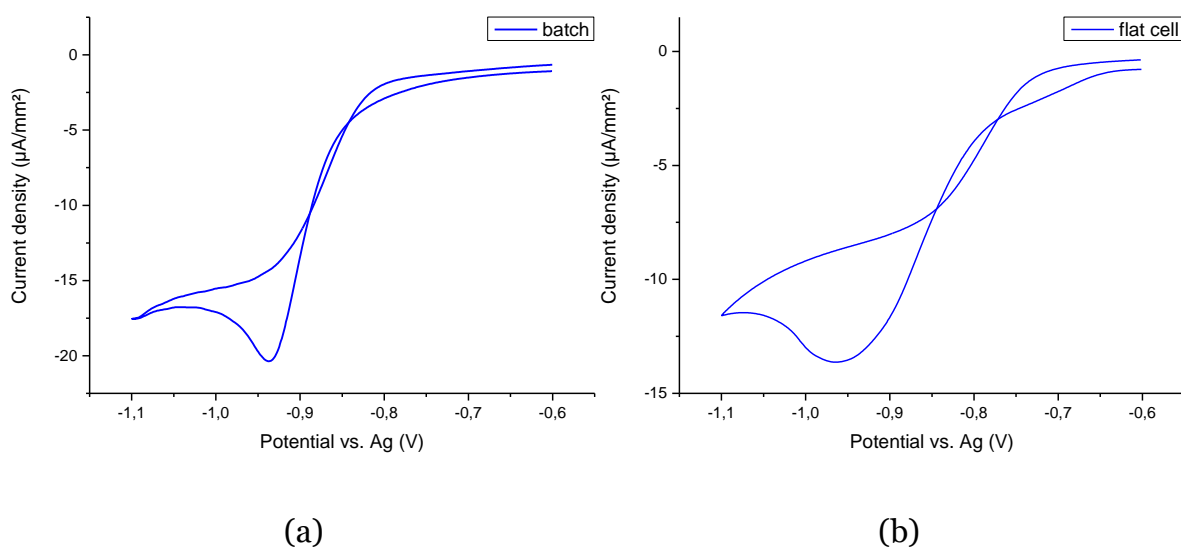


Figure 10.2: Cyclic voltammetry of ABLE in ACN + 0.1 M TBAP on a Ag working electrode constructed as described in Chapter 9 in (a) a standard batch setup and (b) an EPR flat cell. CVs recorded at 100 mV s⁻¹.

Both voltammograms clearly show the reduction peak with a slight shift of the peak potential in the flat cell. The flat compartment of the spectroscopic cell wherein the working electrode resides is $\leq 250 \mu\text{m}$ and entails a high ohmic drop, hence the shift is to be expected. However, due to the very thin electrode thickness of $\sim 30 \mu\text{m}$, semi-infinite linear diffusion is approximated and the response is less distorted than previous electrochemical measurements in cells of similar dimensions [259]. The peak shapes of both voltammograms are also comparable, but the peak in the flat cell

experiment is slightly less pronounced and more spread out as a consequence of the diffusion limitations. The voltammogram in the flat cell shows a good response which allows identifying the peaks and deriving the peak potential. The presence of PBN in the electrolyte gave a comparable voltammogram which is expected as PBN is not electroactive in the potential window of the measurements [260].

10.3.2 In situ EPR spectroelectrochemical study of the cyclisation reaction

Using the in situ setup, controlled-potential electrolysis experiments with simultaneous EPR measurements were performed on samples containing allyl 2-bromobenzyl ether in ACN with *n*-Bu₄NClO₄. However, no EPR signals were observed, most probably due to the high reactivity of the radical intermediates in the proposed mechanism (Figure 1) such that they did not accumulate to detectable concentrations. Consequently, PBN was introduced in excess to the experiments as a spin-trap. Spin-traps react with short-living radicals and convert them to more stable, EPR-detectable radical species. The current response of the experiment is shown in Figure 10.3.

In the first quarter of the total experiment time up until 1800 s, the current is rather unstable, slowly increasing over time and exhibiting some peaks towards more negative currents. At first sight, this appeared random, but repeated experiments under the same conditions confirm that this is reproducible and thus, can be linked to the processes taking place. After about 2700 s the current more or less stabilizes, after which the current slightly decreases. It is known that Br⁻ resulting from the C-X bond cleavage can adsorb onto Ag, blocking the surface [261]. A decreasing current as seen from 2700 s onwards can be expected, even at steady state electrolysis.

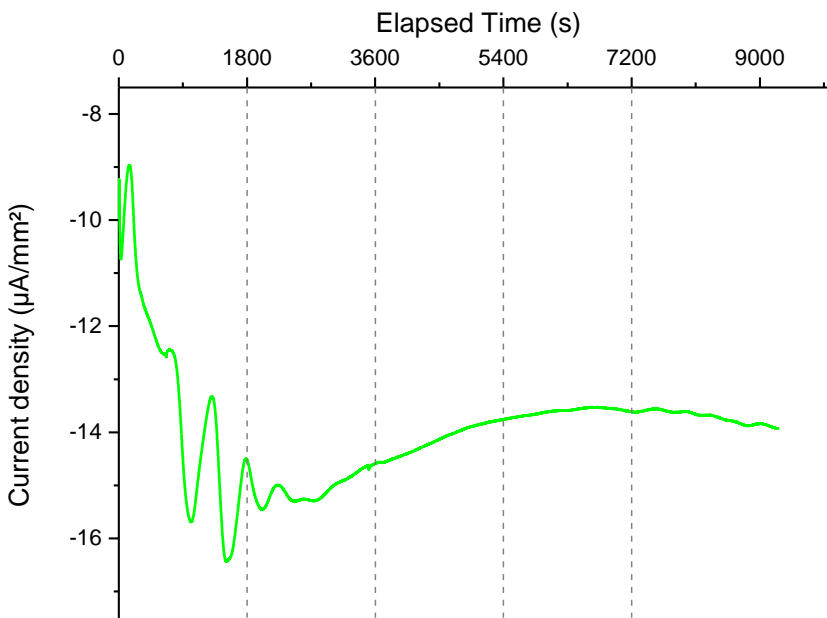


Figure 10.3: Current response of the controlled-potential electrolysis of ABBE in the EPR flat cell. Ag WE, electrolyte = 5 mM ABBE and 15 mM PBN in ACN + 0.1 M TBAP. Potential set at the peak potential of the reduction wave in the EPR flat cell, checked by in situ CV. The dashed lines mark the 30 min (20 scan) periods over which the EPR scans are accumulated.

In correlation with the current response, a change in the CW-EPR spectrum over time is also observed. The scans were accumulated over a time period of 30 min or 20 scans at four points during the experiment (marked by the dashed lines in Figure 10.3). 20 scan accumulations were chosen due to the poor signal-to-noise (S/N) of the initial spectra, and this was maintained for consistency. Clear changes in the spectral features over time can be observed in the CW-EPR spectra (normalized) (Figure 10.4). In the corresponding unnormalized spectra (Figure 10.7) an increase in the signal intensities over time is also observed. Also depicted in Figure 10.7, is the unnormalized spectrum of a potential controlled electrolysis experiment on a solution containing only PBN in ACN with $n\text{-Bu}_4\text{NClO}_4$ after 75 min. In this control experiment a small EPR signal of an unknown radical is also observed, but it was not present in the allyl 2-bromobenzyl ether experiments.

As the changes in features and amount of splitting in the spectra suggests, all spectra are convoluted spectra of more than one species. All spectra agree with the features expected for nitroxide radicals formed by trapping of a reactive organic radical with PBN [262]. The formed nitroxide radicals have a longer lifetime than the original radicals, which decayed too fast to be detected with CW EPR. The spectra can be interpreted in terms of an isotropic g value and the hyperfine interactions (A) between the unpaired electron and the magnetic nuclei in its vicinity. These parameters can be used as a unique fingerprint of the trapped radical. Due to the interaction of the unpaired electron with the nitroxide ^{14}N nucleus ($I=1$), the room-temperature CW-EPR spectra of all nitroxide radicals consist of at least a triplet signal. Subsequent splitting of the three signals can occur through resolved hyperfine interaction with protons in the vicinity of the unpaired electron.

The spectrum depicted in Figure 10.4 (a) is a sum of a triplet (radical 1) and a triplet of doublets (radical 2) (Figure 10.5 (a) and (b) respectively). In the following spectrum, Figure 10.4 (b), the contribution of a third species emerges (radical 3, see Figure 10.5 (c)). The EPR features of radical 3 are more pronounced in the third (Figure 10.4 (c)) and fourth (Figure 10.4 (d)) spectrum. All EPR spectra can be simulated in terms of these three contributions for which the parameters are listed in Table 10.1. From the simulations, the EPR spectrum of radical 3 was found to be a triplet of doublets of doublets. The individual EPR contributions are shown in Figure 10.5.

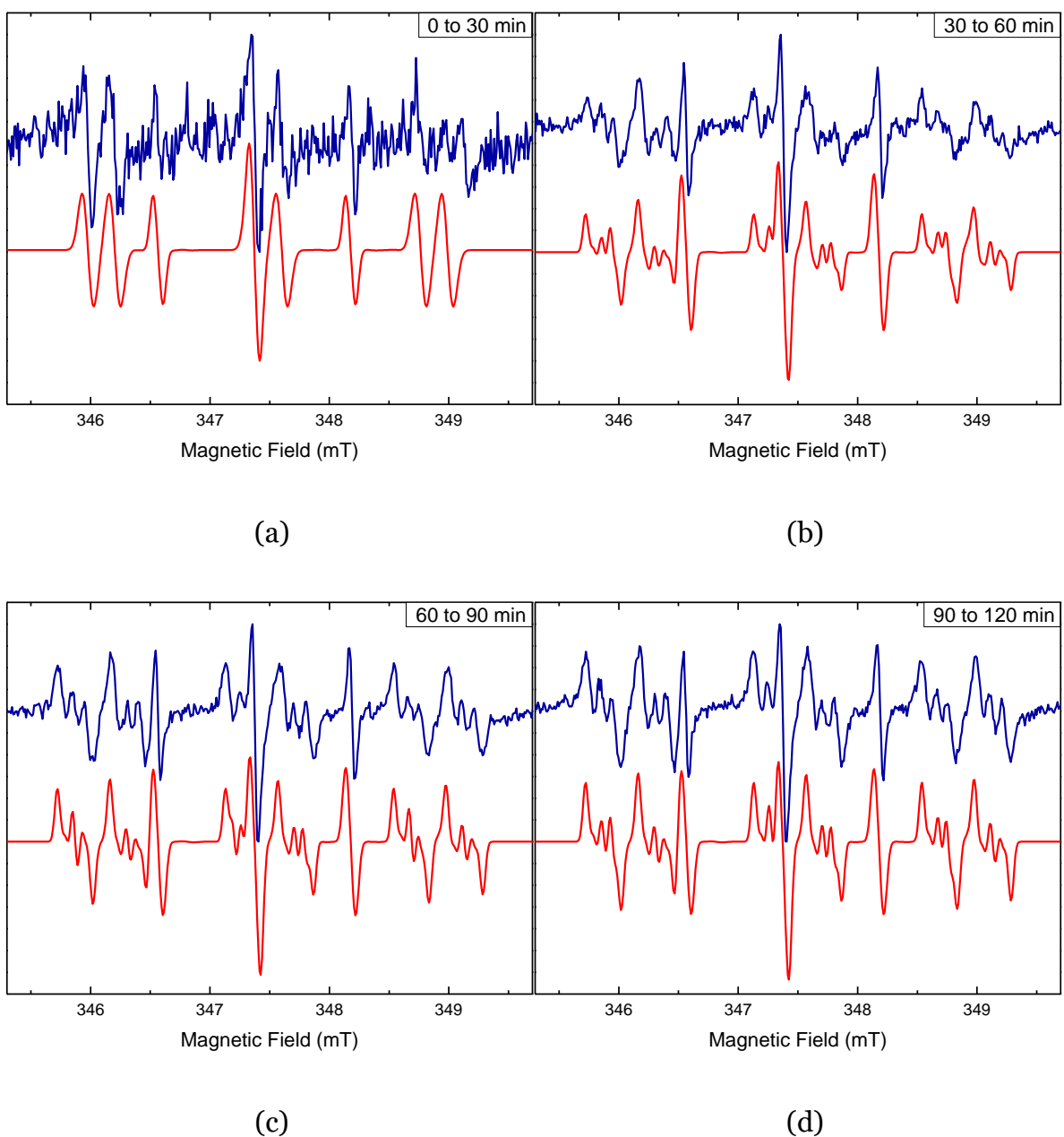


Figure 10.4: Accumulated experimental EPR spectra (blue line) and corresponding simulations (red line) of the controlled-potential electrolysis of ABBE in the EPR flat cell. Ag WE, electrolyte = 5 mM ABBE and 15 mM PBN in ACN + 0.1 M TBAP (potential set at the peak potential of the reduction wave in the EPR flat cell, checked by in situ CV) at different time intervals: (a) 0-30 min, (b) 30-60 min, (c) 60-90 min and (d) 90-120 min and the simulated spectra. The spectra are shown normalized to allow easy comparison.

Table 10.1: Experimental (*exp*) and calculated (*cal*) isotropic *g* and hyperfine coupling constants of the three spin-trapped radicals during the electrolysis ABBE.

	radical 1		radical 2		radical 3	
	<i>exp</i>	<i>cal</i>	<i>exp</i>	<i>cal</i>	<i>exp</i>	<i>cal</i>
<i>g_{iso}</i>	2.0069	2.0067	2.0063	2.0053	2.0062	2.0054
<i>A_{N-iso}</i> [MHz]	22.66	22.53	39.09	40.35	39.53	43.17
<i>A_{H^B}</i> [MHz]	-	-	6.46	5.61	12.43	12.18
<i>A_H</i> [MHz]	-	-	-	-	4.03	-0.82 (<i>A_{H_a}</i> ^v)/
<i>A_H</i> [MHz]	-	-	-	-	2.19	-0.94 (<i>A_{H_b}</i> ^v) ^a

^a Possible assignments (see main text for details)

Based on the isotropic ¹⁴N hyperfine coupling constant (22.66 MHz) of radical 1, it is assigned to benzoyl-*tert*-butyl nitroxide (PBN-Ox) (Figure 10.5 (a)) [262]. This species is often observed in PBN spin-trapping experiments, especially in the presence of oxygen [263]. Although the electrolyte was extensively deoxygenated during sample preparation and was under an argon atmosphere during the experiment, there still can be residual dioxygen in the electrolyte due to its high solubility in ACN (8.1 mM [264]). Alternatively, residual water in the ACN solvent (<150 ppm) can be oxidized at the counter electrode and the generated dioxygen can diffuse to the working electrode part of the cell. Radicals 2 and 3, displayed ¹⁴N and ¹H hyperfine couplings that are suggestive of carbon-centered radicals that have been spin-trapped such as the expected radical intermediates from reactions (3) and (4) in Figure 10.1. In order to assign radicals 2 and 3, DFT was used to compute the EPR parameters of the PBN spin-trapped allyl benzyl ether and 4-methylisochromane

radicals. The computational method (appropriate choice of basis sets and functionals) was benchmarked using standard nitroxide radicals TEMPO and 5,5-dimethyl-1-pyrroline *N*-oxide (DMPO)-OH as well as PBN-Ox (see Table 10.2). All three functional/basis sets that were tested reasonably predicted the g_{iso} values. The B3LYP/(6-31+G**) was found to be most accurate for calculating the hyperfine interactions (Figure 10.8), and thus was chosen for calculating the EPR parameters of the spin-trap radicals. Variations between different functional/basis sets and deviations from the exact experimental values are normal for DFT computations, but the observed trends are generally followed [265].

The geometry-optimized models of PBN-Ox, PBN-allyl benzyl ether, and PBN-4-methylisochromane are depicted in Figure 10.5. Compared to PBN-Ox, the latter two PBN-adducts have greater degrees of freedom. To account for this, selected bonds close to the nitroxide moiety were manually rotated. Rotation around the N-C β bond had the most significant impact on the EPR parameters calculated from the molecular models (Figure 10.9). Averaging the values of the thermally allowed ($kT = 25.7$ meV at 298 K) N-C β bond rotamers, yielded EPR parameters for PBN-4-methylisochromane and PBN-allyl benzyl ether that are comparable to radical 2 and 3, respectively (Table 10.1), and thus are assigned accordingly. The calculations reasonably predicted the g_{iso} values for both radicals. For radical 2, the experimental and calculated hyperfine coupling values are in good agreement (Table 10.1). These are assigned to the expected isotropic ^{14}N interaction, and the interactions between the unpaired electron and the H β proton (see Figure 10.5 for proton assignment).

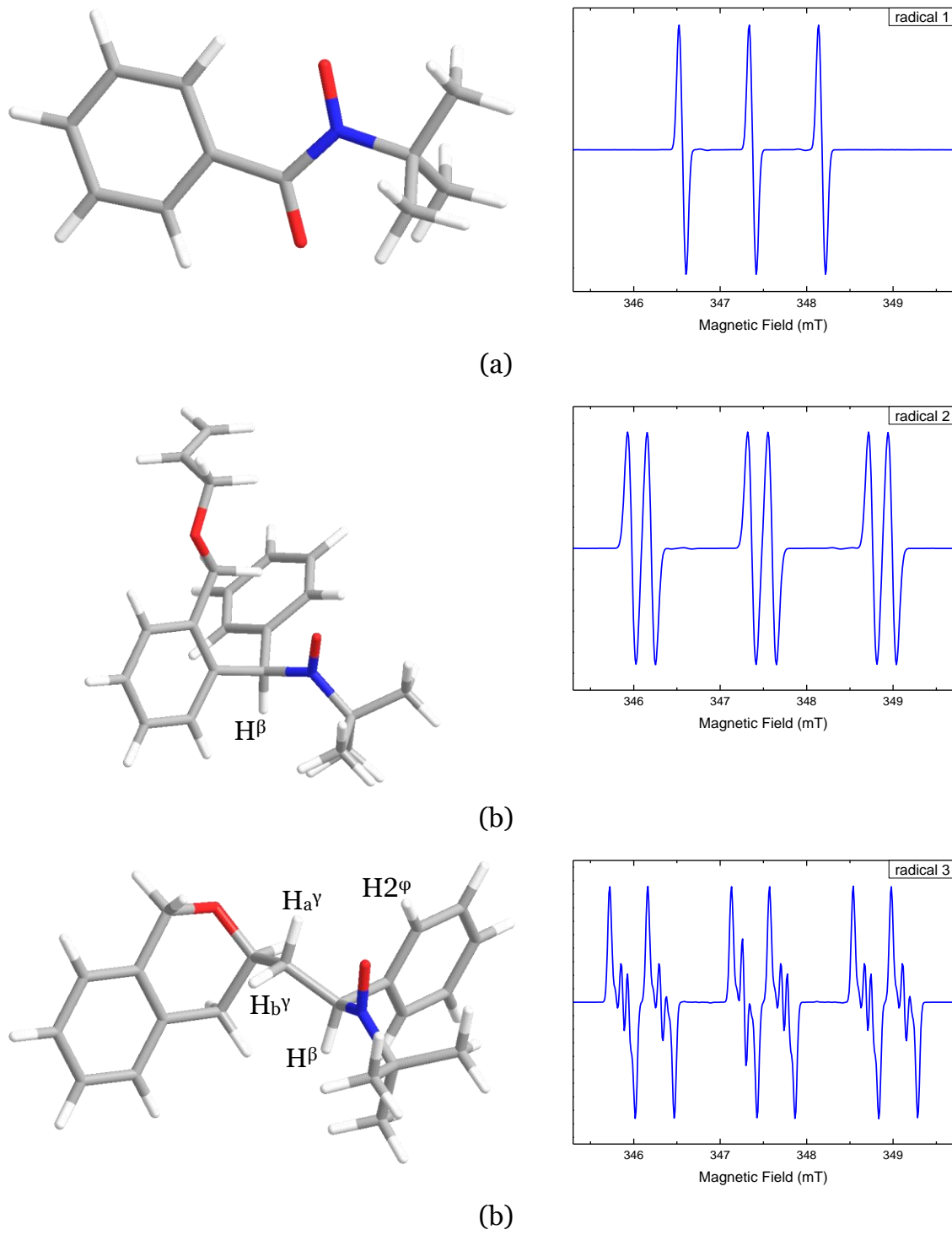


Figure 10.5: Molecular models derived from DFT computations and the contributions in the spectra of (a) radical 1/PBN-Ox, (b) radical 2/PBN-allyl benzyl ether, (c) radical 3/PBN-4-methylisochromane.

For radical 3, the experimental and calculated values for the isotropic ^{14}N and H^β proton hyperfine interactions are also in good agreement. Two further ^1H interactions (4.03 and 2.19 MHz) are also used in the simulation of the spectrum of radical 3. After the isotropic ^{14}N and H^β proton, the next largest calculated hyperfine interactions are H_2^φ (1.43 MHz), $A_{\text{H}_b^\gamma}$ protons (-0.94 MHz) and $A_{\text{H}_a^\gamma}$ (-0.82 MHz). Two of these are likely candidates for the unattributed couplings in the spectrum of radical 3. However, the calculated values are close in magnitude and somewhat smaller than the experiment preventing definitive assignments.

As shown in Figure 10.4, the three PBN-trapped radicals are not all present at each time interval. The relative weight of each radical in the spectrum correlates linearly with their relative concentration and can be plotted versus the elapsed time to visualize their evolution (Figure 10.6).

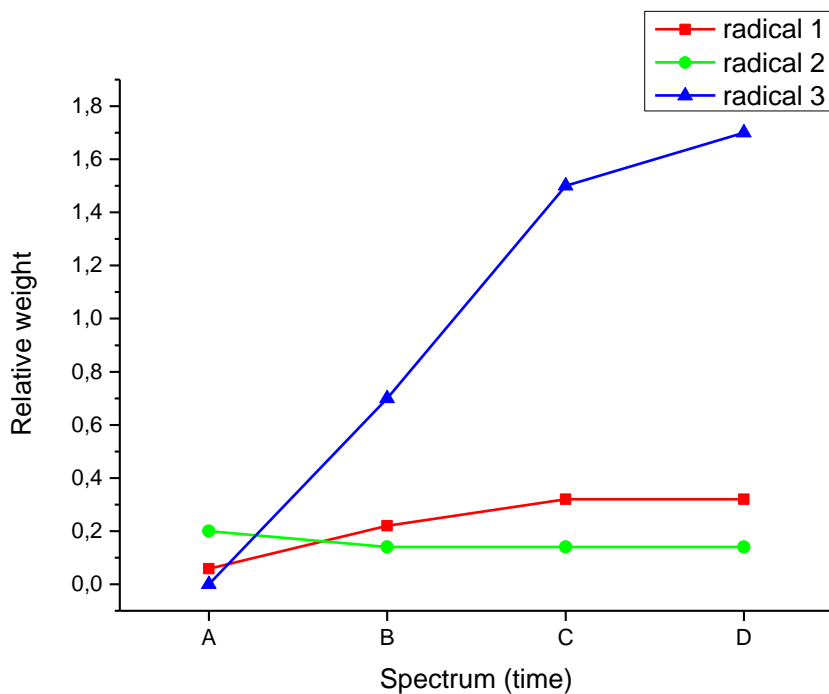


Figure 10.6: Relative weight of each radical in the different spectra of Figure 10.4.

The presence of the PBN-Ox increases with time then plateaus, suggesting that the electrolytic generation of this species is exhaustive, or that it reaches steady-state

between PBN-Ox decay and spin-trapping reactions. Considering the very low concentration of residual oxygen/water, exhaustive electrolysis is plausible. The concentration of PBN-allyl benzyl ether appears to decrease between the first and second time intervals. This change is small and maybe due to the poor S/N of the first spectrum. From the second time interval to the remainder of the experiment the concentration of PBN-allyl benzyl ether remains constant. PBN-4-methylisochromane, which arises from the spin-trapping of the radical intermediate from the intramolecular cyclisation of the allyl benzyl ether radical is the most abundant product over time. This is expected as the experimental conditions favored its formation. There is strong increase in the concentration of PBN-4-methylisochromane in the beginning which starts to plateaus in the last time interval. The data suggests that the cyclisation intermediate (4-methylisochromane radical) is not present during the first time interval, which is unexpected considering the precursor intermediate (allyl benzyl ether radical) is formed. However, it should be noted that the intermediates are not detected directly, and that an extra spin-trapping reaction step is needed for detection. The reactivity of PBN with different radicals can vary [266] and thus the formation of certain radicals can be masked. It is possible that PBN-Ox is formed much more easily than PBN-4-methylisochromane. Alternately, the 4-methylisochromane radical generated is reacting with the fast diffusing residue oxygen in the initial stages, which yields PBN-Ox after subsequent decay/reaction steps. Due to the geometry of the thin cell, natural convection quickly sets in. Over time the oxygen species becomes exhausted and more of the target radical will be spin-trapped and becomes detectable in the spectra. This appears to follow the course of the current in Figure 10.3 where after the first time interval, the current starts to stabilize (no longer strongly influenced by the oxygen/water species), after which PBN-4-methylisochromane emerges in the subsequent spectra. In addition, the S/N is lower in the beginning, possibly masking the spectral features of a low amount of the PBN-4-methylisochromane. This correlates with the previous results of a electrochemical investigation [236] which shows that product distribution is not time dependent and that the cyclisation

product is formed at any point during the electrolysis. The concentration of the allyl benzyl ether radical remaining constant throughout the experiment also corresponds with the earlier results. At the applied potential, the radical is expected to completely undergo the intramolecular cyclisation to 4-methylisochromane which presumably is faster than the spin-trapping reaction.

10.4 Conclusions

Employing a platform for combined EPR and electrochemical measurements to elucidate mechanisms remains underexploited in electrocatalytic research. In this work this approach is validated on a model reaction and for the first time, the proposed mechanism for the reductive cyclisation of allyl 2-bromobenzyl ether to 4-methylisochromane was confirmed. Both the allyl benzyl ether radical and the 4-methylisochromane radical intermediates could be detected by spin-trapping and identified with the help of DFT computations. As expected, the target cyclic radical was the most abundant product. To this end, a simple, inexpensive and versatile electrode setup for *in situ* EPR and electrochemical experiments has been constructed. The setup is suitable for both aqueous and non-aqueous environments and shows both a good electrochemical as a good EPR response and can be used in an EPR flat cell in a TE₁₀₂ cavity. These results show the strength of combined EPR and electrochemical measurements in electrocatalytic research. Currently a similar setup is developed for flow cell experiments to expand the applicability of the platform. A flow cell will allow deriving kinetic information such as the radical decay rates and offers an increased sensitivity for short-lived radicals. The cell design is based on a channel electrode [168] which is adapted to fulfill the requirements to incorporate nanostructured electrocatalysts, similar to the setup in this work. The possibility of adapting the setup for rapid-scan EPR methods [267,268], which will greatly decrease the acquisition time and thus improve the detection sensitivity of the setup, is also explored.

10.5 Supplementary information

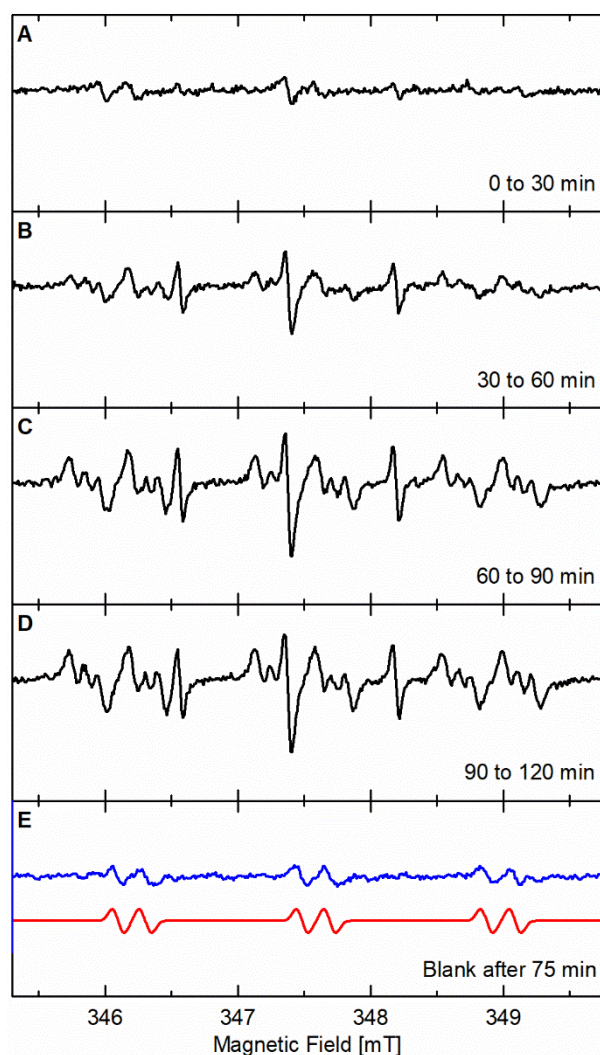


Figure 10.7: Accumulated experimental EPR spectra (black, 20 scans) of the controlled-potential electrolysis of ABBE in the EPR flat cell and of a blank sample. Ag WE, electrolyte = 5 mM ABBE and 15 mM PBN in ACN + 0.1 M TBAP (potential set at the peak potential of the reduction wave in the EPR flat cell, checked by in situ CV) at different time intervals: 0-30 min, (A), 30-60 min (B), 60-90 min (C) and 90-120 min (D), and the spectrum (blue, 50 scans) and simulation (red) of a blank sample containing only PBN in ACN with $n\text{-Bu}_4\text{NClO}_4$ collected after 75 min of controlled potential electrolysis in the same setup at the same potential (E). The parameters for the simulation were $g_{iso} = 2.0057$, $A_{\text{N-iso}} = 39.00$ MHz, $A_{\text{H}} = 5.8$ MHz.

Table 10.2: Experimental and numerical EPR parameters from DFT calculations using different functional/basis sets combinations.

		PBN-Ox ^a	TEMPO ^a	DMPO-OH ^b
experimental	g_{iso}	2.0069	2.0059	2.0056
	$A_{N\text{-iso}}$ [MHz]	22.66	48.63	41.76
	A_{H^β} [MHz]			41.76
B3LYP/EPR-II	g_{iso}	2.0063	2.0057	2.0056
	$A_{N\text{-iso}}$ [MHz]	15.14	37047	25.90
	A_{H^β} [MHz]			37.03
B3LYP/6-31+G**	$A_{CH_3}^{\text{AVG}}$ [MHz] ^c	0.46	-0.54,-0.66	
	g_{iso}	2.0067	2.0055	2.0057
	$A_{N\text{-iso}}$ [MHz]	22.53	45.85	42.52
	A_{H^β} [MHz]			35.30
PWPB95/EPRII	$A_{CH_3}^{\text{AVG}}$ [MHz] ^c	0.46	-0.53,-0.53	
	g_{iso}	2.0070	2.0062	2.0060
	$A_{N\text{-iso}}$ [MHz]	21.07	48.32	35.96
	A_{H^β} [MHz]			35.44
	$A_{CH_3}^{\text{AVG}}$ [MHz] ^c	-0.03	-1.32,-0.79	

^a this work

^b values from [269]

^c In solution the hyperfine coupling of protons on methyl and tert-butyl groups are generally small and unresolved owing to the free rotation around Sp^3 C-C bonds that averages their contributions.

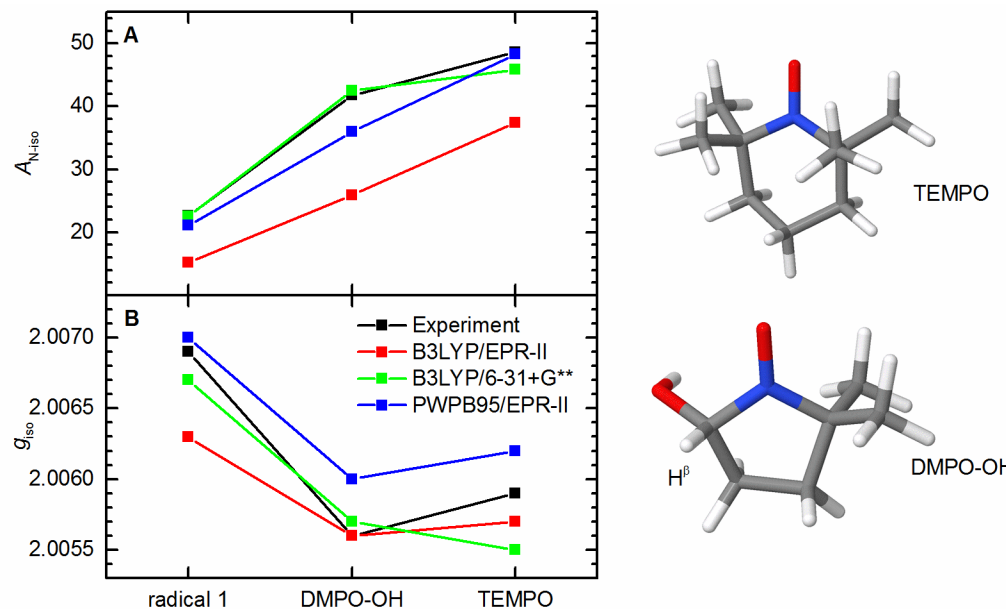


Figure 10.8: Comparisons of the trends in the $A_{N\text{-iso}}$ (A) and g_{iso} (B) between the experimental and calculated values using different functional/basis sets combinations, and molecular models of TEMPO and DMPO-OH.

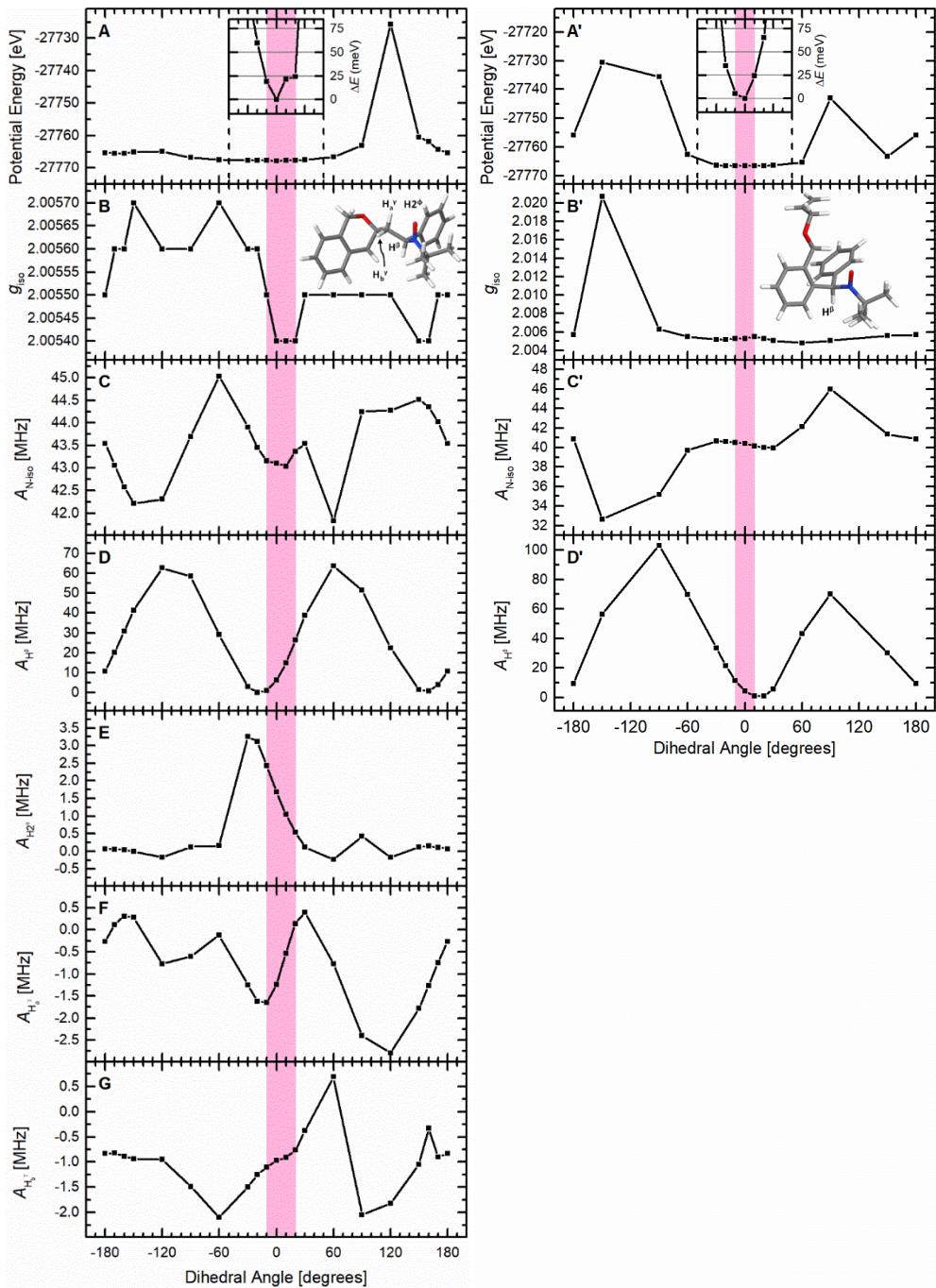


Figure 10.9: Evolution of the potential energy (A), and EPR parameters g_{iso} (B), A_{N-iso} (C), A_{H^B} (D), $A_{H^{2\phi}}$ (E), $A_{H^a\gamma}$ (F) and $A_{H^b\gamma}$ (G) as a function of the dihedral angle manually rotated around the N-C^B bond for PBN-4-methylisochromane from calculations using B3LYP/EPR-II functional/basis set; the corresponding values for PBN-allyl benzyl ether (A' to D'); magnification of the region near the lowest energy (insets). The bands shade in pink indicates the dihedral angles which are thermally allowed at 298 K.

Table 10.3: XYZ coordinates of optimized geometries (in Å).

PBN-Ox (radical 1)

C	0.83334	-2.426262	-0.000411
C	0.895578	-1.006943	-0.000527
C	2.174021	-0.391232	-0.000153
C	1.997887	-3.203026	0.000096
C	3.259871	-2.579733	0.000441
C	3.338673	-1.176829	0.000271
C	-0.451269	-0.333573	-0.001141
O	-1.496104	-0.993588	-0.001771
N	-0.559165	1.101218	-0.00001
C	-1.940367	1.791462	0.00011
C	-1.676918	3.303862	-0.000052
C	-2.704507	1.395495	-1.280183
C	-2.704139	1.395717	1.280703
O	0.472418	1.837996	0.000573
H	-0.156123	-2.905361	-0.000743
H	2.25197	0.699955	-0.00026
H	1.921916	-4.301354	0.00021
H	4.178483	-3.186983	0.000789
H	4.321506	-0.680507	0.000506
H	-2.656334	3.821441	0.00002
H	-1.112402	3.623102	0.896748
H	-1.1126	3.622948	-0.897032
H	-3.653936	1.966699	-1.319184
H	-2.115311	1.652011	-2.183901
H	-2.940829	0.316997	-1.29867
H	-3.653841	1.966473	1.319615
H	-2.939906	0.317119	1.299747
H	-2.114911	1.652897	2.184207

PBN-allylbenzyl ether (radical 2)

C	-1.999244	-2.590714	-0.623569
C	-1.322674	-3.819311	-0.551555
C	0.575746	-2.837148	-1.705074
C	-0.102943	-1.606905	-1.777797
C	-1.396132	-1.469735	-1.23584
C	-0.029883	-3.947076	-1.092506
C	-2.204354	-0.168406	-1.333117
N	-1.507217	0.872787	-2.131364
O	-0.572078	1.543117	-1.565699
C	-1.967652	1.346505	-3.496559

C	-0.701397	1.537489	-4.356
C	-2.896556	0.321029	-4.165216
C	-2.690403	2.696601	-3.296703
C	-2.720381	0.395246	0.001701
C	-4.073652	0.800754	0.028638
C	-4.659674	1.365138	1.172769
C	-3.879482	1.531001	2.327447
C	-2.53527	1.124859	2.321832
C	-1.934144	0.554602	1.178473
C	-0.486531	0.108942	1.263722
O	0.146417	0.71219	2.388048
C	1.479255	0.246629	2.604443
C	1.540408	-1.16308	3.140231
C	2.29907	-2.148155	2.625763
H	-3.012265	-2.500717	-0.199136
H	-1.80967	-4.683119	-0.072223
H	1.587621	-2.924628	-2.130949
H	0.384777	-0.741622	-2.249483
H	0.502247	-4.909479	-1.036303
H	-3.1111	-0.422548	-1.911981
H	-0.976739	1.977366	-5.33468
H	0.011204	2.212838	-3.847177
H	-0.198372	0.566285	-4.53978
H	-3.092964	0.648486	-5.205524
H	-2.432332	-0.684722	-4.213019
H	-3.880662	0.239882	-3.661939
H	-2.977374	3.128117	-4.276737
H	-3.610141	2.571377	-2.69004
H	-2.021006	3.410168	-2.777067
H	-4.686147	0.666893	-0.877968
H	-5.717662	1.669372	1.158394
H	-4.315735	1.972601	3.237295
H	-1.916169	1.247546	3.221519
H	-0.442263	-1.004911	1.340613
H	0.040277	0.391157	0.325433
H	2.088526	0.333601	1.672538
H	1.908433	0.947289	3.353383
H	0.917401	-1.354475	4.034246
H	2.331162	-3.151807	3.080199
H	2.924723	-1.983313	1.731315

PBN-4-methylisochromane

C	1.029692	-2.261271	0.3991
---	----------	-----------	--------

C	2.268594	-2.901064	0.212957
C	3.45504	-2.147474	0.199326
C	3.394384	-0.75154	0.372131
C	2.156528	-0.112893	0.55197
C	0.958219	-0.861919	0.567668
C	-0.394969	-0.17193	0.752759
N	-0.427219	0.627878	2.011185
O	0.13645	1.780305	1.991813
C	-0.739444	0.044523	3.373153
C	-1.582753	1.099006	4.118574
C	-1.528269	-1.267224	3.25178
C	0.598942	-0.190914	4.107334
C	-0.781084	0.752297	-0.423631
C	-0.894741	0.03061	-1.77923
O	-0.850553	0.958022	-2.879584
C	-1.923663	1.893188	-2.907748
C	-3.290633	1.288273	-2.641088
C	-3.398169	-0.030511	-2.140025
C	-2.142538	-0.855888	-1.933229
C	-4.457181	2.052966	-2.854473
C	-5.726021	1.517944	-2.584164
C	-5.837667	0.205917	-2.084677
C	-4.679813	-0.555803	-1.863606
H	0.104368	-2.860466	0.409223
H	2.30487	-3.993674	0.079537
H	4.426392	-2.646057	0.055706
H	4.320303	-0.154994	0.366532
H	2.111856	0.976447	0.703593
H	-1.16653	-0.957325	0.859053
H	-1.766782	0.767998	5.159822
H	-1.050432	2.068492	4.13983
H	-2.562187	1.245524	3.619278
H	-1.791869	-1.615486	4.270334
H	-2.476236	-1.130048	2.692877
H	-0.938803	-2.073825	2.772907
H	0.410988	-0.524163	5.147816
H	1.203376	-0.966435	3.595797
H	1.183072	0.749678	4.135476
H	-1.738916	1.251236	-0.164393
H	-0.01493	1.547707	-0.516457
H	0.01169	-0.592944	-1.921862
H	-1.899091	2.352613	-3.9183
H	-1.746265	2.725994	-2.182091

H	-1.988091	-1.520737	-2.811397
H	-2.264625	-1.531852	-1.060743
H	-4.367131	3.081633	-3.241671
H	-6.628707	2.123216	-2.762056
H	-6.828544	-0.221592	-1.865074
H	-4.764909	-1.581438	-1.468032

TEMPO

O	-1.800226	-1.132621	-0.472929
N	-0.661718	-0.60076	-0.20991
C	1.666463	0.780404	0.803625
C	0.963651	1.29515	-0.454318
C	-0.516899	0.863658	-0.556201
C	-1.009538	1.037832	-2.005168
C	-1.416636	1.68662	0.396025
C	1.626497	-0.749195	0.809137
C	0.194541	-1.330567	0.799828
C	-0.475953	-1.214895	2.189241
C	0.237989	-2.809874	0.372815
H	1.190085	1.192066	1.719654
H	1.50674	0.912547	-1.346284
H	1.000674	2.403196	-0.514011
H	-0.411231	0.414324	-2.700363
H	-2.072079	0.745116	-2.096981
H	-0.901593	2.098603	-2.307779
H	-1.469191	2.739192	0.05155
H	-2.440495	1.263117	0.396767
H	-1.037051	1.686763	1.436632
H	2.15739	-1.164908	1.691202
H	2.166456	-1.121856	-0.08891
H	-0.4303	-0.184333	2.592734
H	-1.53996	-1.514502	2.113256
H	0.030433	-1.887046	2.911126
H	0.874197	-3.380327	1.078693
H	-0.777283	-3.248412	0.370553
H	0.667862	-2.911851	-0.644458
H	2.719175	1.131556	0.819474

DMPO-OH

C	-0.633335	-0.460217	-0.246221
C	1.595974	0.104601	-0.676498
C	0.996299	1.155199	0.284662
C	-0.538597	0.979566	0.17485

O	-1.734518	-1.102487	-0.294704
C	-1.165221	1.851591	-0.932568
C	-1.282213	1.169225	1.504292
C	0.667086	-1.100501	-0.543121
O	1.096065	-1.927972	0.52455
H	2.638645	-0.169745	-0.4257
H	1.581804	0.464877	-1.724934
H	1.313278	2.187701	0.039681
H	1.320053	0.939172	1.323004
H	-0.600809	1.767745	-1.88328
H	-2.208875	1.527098	-1.118988
H	-1.176157	2.916552	-0.625247
H	-1.224142	2.226905	1.830504
H	-2.349515	0.894595	1.386594
H	-0.842199	0.530911	2.296843
H	0.540963	-1.690375	-1.47894
H	0.457416	-2.66744	0.589222

Part IV

Conclusions and future perspectives

CHAPTER 11

Conclusions and future perspectives

11.1 Conclusions

Organic electrosynthesis offers a viable alternative to many traditional chemical routes, but it is too often not considered when new pathways or improvements of existing pathways are sought-after. Many reasons contribute to the lack of the industry to venture into this area of which a major one is the requirement of the particular combination of knowledge in the different research areas of (chemical) engineering, electrochemistry and organic synthesis, which is not commonly found in one place. Recognizing this problem, the goal of this work was to develop a multi-aspect screening methodology to help further closing the gap between these different domains, more specifically between the engineering aspect and fundamental electrochemistry. To reach this goal both an engineering approach and a mechanistic approach for the investigation and development of an electrosynthetic pathway were embarked upon and completed by means of industrial relevant case studies. The combination of these two approaches constitute the general multi-aspect screening methodology.

11.1.1 Engineering approach for an electrochemical study towards industrial implementation

In the first part of this dissertation, the aldol reaction of acetone to diacetone alcohol was used as a case study in the engineering approach. As shown in the literature review in Chapter 4, this type of reaction and specifically this specific case exhibits several drawbacks that are insufficiently solved by the current solutions, which made it an ideal candidate for this investigation. Of primary importance is identifying key parameters for the electrosynthetic pathway and mapping their influence. Thus, in Chapter 5, an electrochemical screening was performed to evaluate the potential of and to provide insights into the electrochemical route. Electrochemical techniques were combined with traditional analytical techniques to monitor the reaction and quantitatively describe the parameters. Since in this stage, the goal was not to develop

the most optimal electrocatalyst but to acquire an understanding of the electrochemical route of the reaction, a selected range of promising electrode materials were screened of which platinum exhibited the best activity. The reaction showed excellent performance and even in a simple batch setup it was possible to obtain the same equilibrium concentration of about 15 m% as is obtained in the traditional process. Furthermore a high selectivity of >90 % was easily reached and the reaction proceeded with high current efficiencies that ran into the thousands of percent. Additionally, the behavior of the reaction at different electrolysis conditions was described and quantified, which gave insights into the course and nature of the reaction. A substantial amount of information was obtained that allowed further development of this route without an in-depth fundamental study of the electrode reactions, as intended by the engineering approach.

The information obtained in the electrochemical screening was subsequently used in the conversion of the reaction to a continuous flow process. As shown in the literature review in Chapter 4, flow chemistry is becoming increasingly important in the chemical industry, making this a logical follow-up step. In Chapter 6 a modular continuous flow microreactor setup was developed that was used to valorize the information obtained in the previous step and to investigate the flow process conditions. The influence of the spacer design and inter-electrode distance on the performance of the flow process were described. The nature of the reaction showed to be particularly suited for a flow process and the excellent performance earlier obtained, could be reproduced. Furthermore, considerations on the process design, such as the incorporation of a membrane were also discussed. Although promising results were obtained, the optimization of the complete process was limited by practical issues. Nevertheless, the applicability of this engineering approach was demonstrated and the beginning for the development of a continuous flow electrochemical pathway for the aldol reaction has been made.

The success in the screening and development of this particular case study validates the approach, but the true strength is the ability to extend this to other reactions and reaction types. The modular reactor setup and targeted screening allows quantifying key parameters of an electrosynthetic process to improve the process and the results obtained in a fundamental mechanistic investigation can easily be incorporated in this approach. Thanks to the modularity, the platform is readily applied to other (electro)organic synthesis. An example is given in the application of this approach on the electrochemical cross-coupling reactions of arenes [270]. In a batch setup these reactions experience problems such as over-reduction of the products, passivation of the electrodes and problems due to the significant amount of supporting electrolyte that is required. To address these problems, conversion of the batch process to a flow process on microreactor scale was proposed. To this end the setup and approach presented in this work were applied and the first results have shown to be promising.

Despite that the screening in Chapter 5 and Chapter 6 do not comprise fundamental research towards electrode reactions and reaction mechanisms, valuable information on the elementary mechanism was obtained. As discussed in Chapter 4, little research has been devoted to unraveling the fundamental mechanism of the electrosynthetic aldol reactions and few mechanisms have been proposed in literature. Therefore in Chapter 7 a concise investigation towards the mechanism of the reaction was performed which yielded information that allowed an evaluation of these proposals of which the most probable could be selected.

11.1.2 Mechanistic approach for an electrochemical study by *in situ* EPR spectroelectrochemistry.

In the second part of the dissertation, the intramolecular reductive cyclisation of allyl 2-bromobenzyl ether to 4-methylisochromane was used as a case study for the mechanistic approach which consists of an *in situ* study combining EPR and electrochemistry. A profound knowledge of the reaction mechanism, the important intermediates and the influence of the catalyst allows a thorough optimization of the

electrocatalyst and the reaction. As was evident from the literature review discussed in Chapter 8, combining these techniques is not a trivial task. Useful cell designs that are relevant for the development of an *in situ* platform tailored for electrocatalytic research were selected from literature and discussed. In Chapter 9 a versatile platform that consisted of an electrolytic EPR flat cell and a custom-constructed electrode was developed. The electrochemical and spectroscopic response in both aqueous and non-aqueous environment was evaluated by standard reactions: the electrochromic reduction of methyl viologen and the reduction of *p*-benzoquinone. The setup displayed both a good electrochemical as a good spectroscopic response in all cases. The construction also satisfies the demands listed for a versatile platform for electrocatalytic research.

Subsequently the setup was applied in the investigation of the intermediates of the reductive cyclisation of allyl 2-bromobenzyl ether in Chapter 10. Both the allyl benzyl ether radical and the 4-methylisochromane radical intermediates could be detected by spin-trapping and identified with the help of DFT calculations. The DFT calculations also allowed deriving the geometry optimized models of the spin-trapped intermediates. As expected, the target cyclic radical was the most abundant product.

Besides confirming the proposed mechanism for the reductive cyclisation of allyl 2-bromobenzyl ether, the strength of using EPR in electrocatalytic research has been demonstrated. A direct detection of the intermediates and subsequent confirmation of proposed mechanisms provides a powerful method to validate electrocatalytic performance. The information obtained can be used to optimally tune the electrocatalyst which then can be incorporated in the engineering approach for a complete investigation of an organic electrosynthesis.

11.2 Future perspectives

After concluding the work presented in this dissertation, a multi-aspect methodology that can be applied for the screening and development of an electrosynthetic alternative route is obtained. However, a research path is not a closed loop and in this work many opportunities for further research or for new ventures present themselves. Additionally improvements of the applied procedures and developed setups can also be proposed.

The results of the screening and the concise mechanistic investigation of the electrosynthetic aldol reaction of acetone revealed the initiation of the reaction by deprotonation of the substrate. However, the exact nature of the EGB, whether it is the radical anion or a dianion species could not be discerned. To elucidate this mechanism which has not been confirmed in literature to date, *in situ* mass spectrometry could be of great use. This can be achieved by a DEMS (Differential Electrochemical Mass Spectrometry) setup which enables the detection of negative ions provided some adaptions to the standard instrumentation. In-depth understanding of the mechanism would assist the further development of the reaction and help extrapolating the obtained results to other reactions and even different types of reactions that are closely related. Furthermore, it was shown that reaction proceeded with very high current efficiencies, attributed to the propagation step in the pathway. This is huge advantage over the traditional route and offers a true viability for an economic feasible process. Adapting the modular reactor setup to fully quantify the flow process performance will allow a thorough techno-economic evaluation of this route.

Although the modular reactor setup allows for a large degree of freedom in reaction channel design, electrolysis setup, incorporation of membranes, electrode material and so on, it also had a limited optimization window as shown in Chapter 6. To further improve the setup and expand its ability, the principles could be transferred

to smaller, interconnecting setups which provide a much larger range of residence times and electrode surface areas. In addition the design could be adapted to include accessories often used in industrial setups such as non-conducting static mixers or even innovative conductive static mixers employed as electrodes [271]. This would provide an even more thorough screening ability.

As outlined in Chapter 2, the scope of Part II was not to develop the most optimal electrocatalyst in that stage. However, the potential brought to light in the screening calls for a further development of the reaction as explained in the previous paragraph. In this stage it becomes interesting to turn to electrocatalysis to maximize the economic feasibility by reducing the amount of an expensive material as platinum. Common strategies include alloying and using nanostructured catalysts.

Looking at the *in situ* EPR spectroelectrochemical platform that has been constructed and validated in this work, a plethora of opportunities emerge. A straightforward step is expanding the use of the setup to other interesting reactions such as the cross-coupling of arylhalides. Another interesting follow-up step to take, is the development of a flow cell based on the same principle as the constructed device to expand the capabilities of the platform. This would allow inferring kinetic information about the intermediates which enables identifying rate determining steps and discriminating between closely-related reaction mechanisms. Additionally a flow cell offers a higher sensitivity towards short-lived radicals. As the possibility to incorporate nanostructured catalysts is provided by the design, venturing into this area also offers an interesting direction for further research. The first experiments to obtain electrodeposited nanoparticles on the custom-constructed electrode have been performed in the laboratory and show promising results. Besides performing the *in situ* electrolysis directly on the state-of-the-art nano-electrocatalysts, this also offers the opportunity to study adsorbed species. Achieving this feat allows a direct evaluation of the catalyst's influence which would be a major benefit in electrocatalytic research.

As evident from this disquisition of opportunities, many different directions for future research can be identified and the list above is by no means exhaustive. To conclude, a general perspective is provided: thanks to the ever-growing use of electricity in our society and the accompanying increasing production and availability to satisfy the demand, the future for electricity-based production processes and the related research is bright. And as electrosynthesis helps increasing the sustainability in the chemical industry, stimulation of further research is paramount

List of figures

Figure 1.1 :	The first organic electrolysis, reported by Faraday.....	7
Figure 1.2 :	Reaction scheme of the Kolbe electrolysis.....	7
Figure 1.3 :	The direct relationship of organic electrosynthesis to the twelve principles of green chemistry [31].	9
Figure 1.4 :	Possible pathways and intermediates of organic electrosynthesis. The radical anion and cation formed after the first oxidation or reduction step can also react directly. Additionally the radical R [•] can also react in a radical disproportionation or add to unsaturated bonds. Based on [24].	11
Figure 1.5 :	Electrochemically one-step in situ umpolung to couple two electrophiles or two nucleophiles [27].....	12
Figure 1.6 :	The Monsanto process: the electrohydrodimerization of acrylonitrile to adiponitrile.....	13
Figure 1.7 :	Scheme of the industrial electrosynthesis process for the electrohydrodimerization of acrylonitrile. ACN = acrylonitrile, ADN = adiponitrile, QS = quaternary ammonium salt [24].	14
Figure 1.8 :	The BASF paired electrosynthesis process: (1) cathodic reduction of phthalic acid dimethyl ester to phthalide, (2) anodic oxidation of 4- <i>tert</i> -butyltoluene to 4- <i>tert</i> -butylbenzaldehyde dimethyl acetal.....	16
Figure 2.1 :	Schematic outline of this dissertation.	25
Figure 3.1 :	Possible reaction steps during a general electrochemical reaction. Redrawn from [40].	29
Figure 3.2 :	CE mechanism example: reduction of acetic acid.	30
Figure 3.3 :	EC mechanism example: electrohydrodimerization of an alkene.	31
Figure 3.4 :	EEC mechanism example: reduction of alkyl halides to alkanes.....	31
Figure 3.5 :	ECE mechanism example: reduction of benzoquinone in a protic solvent. A: 1,4-benzoquinone, BH: semiquinone, CH ₂ hydroquinone.	32

- Figure 3.6 :** DISP mechanism example: reduction of aromatic halides 32
- Figure 3.7 :** Current-potential curves at different times (increasing from t_1 to t_5) during a stirred controlled-potential bulk electrolysis at potential E_c . The current at the applied potential drops as time passes. Redrawn from [40]. 42
- Figure 3.8 :** Current-potential curves at different times (increasing from t_1 to t_6) during a stirred bulk electrolysis with an applied constant current I_{app} . The potential to maintain I_{app} shifts from E_1 to E_6 as time passes. The largest shift between E_3 and E_4 occurs when I_{app} is equal to the limiting current. Redrawn from [40]..... 43
- Figure 3.9 :** Top: example of an H-type cell. The clamp holds the two parts together between which the membrane is inserted. Models with an incorporated glass frit are also available. Bottom: Concentric bulk electrolysis cell. The counter electrode is positioned in the center in a concentric tube with a glass frit. 45
- Figure 3.10 :** Representation of parallel planer electrodes (left) and concentric cylindrical electrodes (right). 47
- Figure 3.11 :** Left: variation of the applied potential with time in cyclic voltammetry, showing the initial potential E_i , switching potentials E_{min} and E_{max} and the final potential E_f . Right: Cyclic voltammogram of a reversible system, showing the peak potentials $E_{p,c}$ and $E_{p,a}$ and the corresponding peak currents $I_{p,c}$ and $I_{p,a}$ 53
- Figure 3.12 :** Visual representation of a free unpaired electron in space. Its spin is represented by the black arrow, the resulting magnetic moment by the blue arrow pointing up..... 56
- Figure 3.13 :** Left: Precession of the spin vector S about the magnetic field B_0 . Note that the direction of the μ_S is opposite to that of S [55]. Right: Visual representation of the minimum and maximum energy orientations of μ_S with respect to the magnetic field B_0 58

Figure 3.14 :	Electron Zeeman splitting as a function of the magnetic field B_0 and the corresponding spin state energies.	59
Figure 3.15 :	(a) Energy-level diagram of an unpaired electron in a magnetic field. (b) Absorption signal when the resonance condition is fulfilled. (c) Resulting first derivative of the absorption curve, recorded by the detector. [56].....	61
Figure 3.16 :	Schematic representation of the phase sensitive detection. As the magnetic field is swept a small oscillating magnetic field is applied (commonly 100 KHz) in the same direction as the main field. As the modulation B_m increases from B_{m1} to B_{m2} the detector output increases from i_1 to i_2 . If the magnitude of B_m is sufficiently small relative to the line width, the detector current's peak-to-peak value approximates the slope of the absorption curve and consequently, the first derivative of the absorption curve is obtained [60].....	62
Figure 3.17 :	Splitting of an EPR signal by hyperfine interactions between the unpaired electron and a nucleus with spin quantum number (a) $I = 1/2$ and (b) $I = 1$ and the anticipated EPR spectra for both cases [57].....	65
Figure 3.18 :	Schematic illustration of an EPR spectrometer. The flow of the microwaves is represented by the green arrows. Redrawn from [59].	67
Figure 3.19 :	Left: part of the waveguide and a TE_{102} cavity. Right: schematic illustration of the microwaves entering the cavity. The iris screw is used to adjust the iris to achieve critical coupling [66].	68
Figure 4.1 :	Base mediated aldol addition and aldol condensation of an enolate (aldehyde enolate if $R_1 = H$, ketone enolate if $R_1 \neq H$) and a carbonyl compound (aldehyde if R_3 or $R_4 = H$, ketone if R_3 and $R_4 \neq H$). The red bond depicts the resulting carbon-carbon bond.	75
Figure 4.2 :	Scheme of the pathways in the self-condensation of acetone [71].....	76
Figure 4.3 :	Self-aldol addition of acetone to diacetone alcohol and subsequent dehydration to mesityl oxide to complete the aldol condensation.	77

Figure 4.4 : Comparison of the current distribution (a), mass transfer (b) and heat transfer (c) of conventional batch (STR) and micro electrochemical reactors [106].	83
Figure 4.5 : Classification of electrochemical microsystems with respect to the distance relationship $Sv = dxdy$. The dashed lines mark an Sv of 10^{-3} , 1 and 10^3 respectively [109].	85
Figure 4.6 : (a) Principle of a parallel plate flow-through electrochemical microreactor. (b) Serpentine reaction channel design to increase the channel length [136].....	87
Figure 4.7 : Electrochemical microreactor designed by Green et al. for preparative synthesis. 1. Central bolt. 2. Washer. 3. Insulating tube. 4. Peripheral bolt. 5. Perspex top plate. 6. Cu backing plate. 7. Carbon/polymer anode plate. 8. Perfluoroelastomer gasket. 9. Insulating tube around central bolt. 10. Stainless steel cathode plate with spiral groove. 11. Al base plate. (b) Photograph of reactor with Perspex top. (c) Photograph of reactor with gasket fitted into cathode plate to create the spiral channel [128].....	88
Figure 4.8 : Mechanism of the acid-catalyzed aldol reaction (enol mechanism)... 90	
Figure 4.9 : Mechanism of the base-catalyzed aldol reaction (enolate mechanism).	91
Figure 4.10 : Formation (1) and protonation (2) of a radical anion EGB derived from a carbonyl compound as PB [152].....	92
Figure 4.11 : Formation of the diol by reaction of two radicals or between a radical and a radical anion.	93
Figure 4.12 : Direct reduction (1) and reduction by disproportionation (2) of the radical to the alkoxide. Protonation of the alkoxide to the alcohol (3)....	93
Figure 4.13 : Formation of the dimer dianion or carbonyl dianion by reaction of two ketyl radicals.....	94

Figure 4.14 :	Disproportionation of superoxide anion with a proton donor (1) and termination reactions of the hydroperoxyl radical (2).....	95
Figure 4.15 :	Mechanism of the electrochemical aldol by direct activation of the reactant as proposed by Tsai [102].	96
Figure 4.16 :	Mechanism of the electrochemical aldol reaction by reaction of independently formed radical anion and enolate as proposed by Kumar et al. [99]. Reformatted and errors corrected.....	97
Figure 4.17 :	Mechanism of the electrochemical aldol reaction by generation of an EGB derived from the reactant as proposed by Shono et al. [98].....	98
Figure 5.1 :	Concentration of DAA (m%) per hour of electrolysis (black line, left y-axis) and corresponding selectivity (blue line, right y-axis) during a batch electrolysis in the standard setup. WE and CE: 8 cm ² platinum sheet, potential: -2.5 V, runtime: 7 h.....	103
Figure 5.2 :	Cyclic voltammetry of 10 mM acetone in DMF + 0.1 M TBAP and of blank DMF (+ 0.1 M TBAP). Scanned at 100 mV s ⁻¹	104
Figure 5.3 :	Current densities of separate batch electrolysis experiments at different potentials of WE versus RE in the standard setup. WE and CE: 8 cm ² platinum sheet, runtime: 2 h.	106
Figure 5.4 :	The concentration of DAA (m%) after 1 h of electrolysis (black columns) and after 2 h of electrolysis (red columns) in separate experiments in the standard setup with a different potential applied each experiment. WE and CE: 8 cm ² platinum sheet, runtime: 2 h.....	107
Figure 5.5 :	The selectivity towards DAA after 1 h of electrolysis (black line) and 2 h of electrolysis (blue line) in separate experiments in the standard setup with a different potential applied in each experiment. WE and CE: 8 cm ² platinum sheet, runtime: 2 h.	109
Figure 5.6 :	Relative (pseudo) current efficiencies for DAA formation after 1 h of electrolysis (black columns) and 2 h of electrolysis (red columns) in separate experiments in the standard setup with a different potential	

applied each experiment. WE and CE: 8 cm² platinum sheet, runtime: 2 h. 110

Figure 5.7 : The concentration of DAA (m%) versus different amounts of water added to the electrolyte in separate experiments, after 1 h of electrolysis (black columns) and after 2 h of electrolysis (red columns). WE and CE: 8 cm² platinum sheet, runtime: 2 h..... 111

Figure 5.8 : Relative (pseudo) current efficiencies for DAA formation versus different amounts of water added to the electrolyte in separate experiments, after 1 h of electrolysis (black columns) and after 2 h of electrolysis (red columns). WE and CE: 8 cm² platinum sheet, runtime: 2 h 112

Figure 5.9 : (a) Current densities of the anode (black line) and cathode (red line) in separate experiments and (b) resulting DAA concentration after 1 h (black columns) and 2 h (red columns). Experiments in divided setup with respectively -2.5 V and +2.5 V applied to the cathode and anode in separate experiments. WE: 0.156 cm² platinum wire, CE: 8 cm² platinum sheet, runtime: 2 h. 113

Figure 5.10 : DAA concentration (a) and surface area normalized yield (b) after 1 h (black columns), 2 h (red columns) and 4 h (blue columns) of electrolysis in separate experiments with different working electrodes: 0.287 cm² glassy carbon disk, 0.156 cm² platinum wire and 0.133 cm² gold disk, CE: 8 cm² platinum sheet. Potential: -2.5 V..... 115

Figure 5.11 : The DAA concentration (black line, left y-axis) and corresponding selectivity (blue line, right y-axis) during a 1 h experiment in the divided setup, sampling each 10 min. WE: 0.156 cm² platinum wire, CE: 8 cm² platinum sheet. Potential: -2.5 V. Runtime: 1 h. 117

Figure 5.12 : DAA concentration for a Pt sheet electrode (a) and Pt wire electrode (b) after 1 h (black columns) and 2 h (red columns) of electrolysis in a divided and standard (undivided) setup. CE: 8 cm² Pt sheet. Potential: -2.5 V. 118

Figure 6.1 :	Exploded view of the electrochemical microreactor. 1 Aluminium housing with holes for the in- and outlet tubing, electrode connections and reference electrode (1b only). 2 PEEK housing in which the electrodes are embedded with epoxy with in- and outlet ports, reference electrode port (2b only), hole for the electrode connection and groove for the EPDM O-ring. 3 Glassy carbon counter electrode. 4 POM spacer with serpentine reaction channel. 5 Working electrode consisting of a copper substrate with a deposited platinum layer on top.....	124
Figure 6.2 :	Comparison of a deposited platinum electrode (Pt deposition) and a solid platinum electrode (Pt solid). DAA concentration after two hours of electrolysis in batch setup. Electrolyte = 50 ml acetone + 0.1 M TBAP, E = -2.35 V vs. Ag/Ag ⁺ , S _{electrodes} : 0.28 cm ² . Experiments performed in triplicate.....	129
Figure 6.3 :	SEM images for the platinum layer deposition on copper and a solid platinum electrode. Constant potential deposition in Pt 5Q plating solution with T: 365 K, pH: 10.5, E: -720 mV vs. Ag/AgCl, Q: 1 C cm ⁻²	130
Figure 6.4 :	Comparison of the DAA concentration in the product stream in the reactor setup with no membrane (left) and membrane employed (right). Electrolyte = acetone + 0.1 M TBAP, E = -2.35 V vs Ag/Ag ⁺ , GC working and counter electrode, V = 0.5 ml min ⁻¹ , v = 0.18 mm s ⁻¹ . Experiments performed in triplicate.....	132
Figure 6.5 :	SEM picture (20k magnification) of the Celgard® 2500 membrane.	133
Figure 6.6 :	Representation of the spacer design, outer dimensions = 50 x 150 mm. Spacer A: rectangular channel with channel length 130 mm and channel surface area 1252 mm ² . Spacer B: serpentine channel with channel length 318 mm and channel surface area 971 mm ² . The dots represent the electrolyte inlet and outlet.	134
Figure 6.7 :	Current-potential plots of the limiting current region for the reduction of ferricyanide in the reactor with spacer A.	136

- Figure 6.8 :** *Sh* versus *Re* plot for the two spacers. Squares connected by solid line: spacer A, dots connected by dashed line: spacer B. The horizontal lines mark the area of equal *Re*, which is referred to in Figure 6.9138
- Figure 6.9 :** *Sh* versus *Gz – 1* plot for both spacers. Squares and solid line: experimental values and fitted curve for spacer A. Dots and dashed line: experimental values and fitted curve for spacer B. The horizontal lines represent the points of equal *Re* on both curves and correspond to the values marked by the vertical lines on Figure 6.8.139
- Figure 6.10 :** (a): DAA concentration at different flow rates in the divided reactor setup with Pt (black columns) or GC (red columns) WE, GC CE, electrolyte = acetone + 0.1 M TBAP, E = -2.35 V vs Ag/Ag⁺, inter-electrode distance = 4 mm. Experiments performed in triplicate. (b): normalised DAA concentration as a function of residence time for a platinum working electrode in a commercial thin layer cell employed as ECMR.141
- Figure 6.11 :** The DAA production rate versus volumetric flow rate for the divided reactor setup for a Pt (black columns) and GC (red columns) WE, GC CE, electrolyte = acetone + 0.1 M TBAP, E = -2.35 V vs Ag/Ag⁺, inter-electrode distance = 4 mm. Experiments performed in triplicate.142
- Figure 6.12 :** Adjusted ECMR with a smaller working electrode and adapted spacer leading to a smaller reactor volume, but equal specific electrode area compared to the larger volume setup.143
- Figure 6.13 :** Experiments in the smaller divided ECMR with Pt WE, GC CE, electrolyte = acetone + 0.1 M TBAP, E = -2.35 V vs Ag/Ag⁺, inter-electrode distance = 4 mm. Experiments performed in triplicate. DAA concentration in the product stream at different flow rates (a) and versus the corresponding residence times (b). Experiments performed in triplicate.144
- Figure 6.14 :** Apparent current efficiency (yield per charge passed) versus volumetric flow rate for the experiments shown in Figure 6.10 and Figure 6.11. 147

Figure 7.1 :	Protonation of an acetone ketyl radical by the tetrabutyl ammonium cation of the supporting electrolyte.....	154
Figure 7.2 :	CVs for acetone with and without dissolved oxygen present. Pt WE and Ag/AgCl RE. Supporting electrolyte 0.1 M TBAP. $v = 100 \text{ mV s}^{-1}$	156
Figure 7.3 :	CVs for acetone with 10 mM PhPh added (no dissolved oxygen). Pt WE and Ag/AgCl RE. Supporting electrolyte 0.1 M TBAP. $v = 100 \text{ mV s}^{-1}$...	
	157
Figure 7.4 :	Relative concentrations of DAA for the controlled-potential electrolysis of acetone + 0.1 M TBAP at -1.6 V vs. Ag/AgCl with and without dissolved oxygen present and with PhPh added.	158
Figure 7.5 :	Purple discoloration noticeable at the working electrode due to the disprotonation of PhPh during the controlled-potential electrolysis of acetone + 0.1 M TBAP at -1.6 V vs. Ag/AgCl with dissolved oxygen present.....	158
Figure 7.6 :	Relative concentrations of DAA for the controlled-potential electrolysis of acetone + 0.1 M TBAP at -2.1 V vs. Ag/AgCl with and without dissolved oxygen present and with PhPh added.	159
Figure 7.7 :	Oxidation of the perchlorate ion and reaction with solvent in an ACN/TBAP system [63].	161
Figure 8.1 :	(a) schematic representation of the magnetic and electric field vector (redrawn from [66]) and (b) 3D representation of the field distribution inside a TE ₁₀₂ cavity (redrawn from [174])......	167
Figure 8.2 :	Left: the Adams cell. Center: the Wilmad-Labglass Electrolytic Cell Assembly. Right: the Bruker Electrolytic Cell Assembly.....	171
Figure 8.3 :	Left: schematic illustration of the quartz-metal helix-solution interface with A: the wall of the quartz tube, B: cross section of the helix wire, C: the liquid sample. The shaded portion of area C represents the portion of the sample seen by the microwaves. Right: 3D representation of a cross-section of the cell with D: the quartz tube, E: Au helical working	

electrode, F: Pt counter electrode, G: counter electrode lead-out wire, H: reference electrode Luggin capillary. Based on [191]	173
Figure 8.4 : Illustration of the channel electrode cell with a copper lead-out wire and gold working electrode for in situ EPR spectroelectrochemical experiments. The deeper sections at each end of the channel serve to equalize the pressure across the full width. Redrawn from [168].....	174
Figure 9.1 : Examples of nanostructured catalysts: (a) layer deposition, (b) cubic nanoparticles, (c) spherical nanoparticles.....	177
Figure 9.2 : (a) Ag sputtered on PP creating different working electrode surfaces. (b) Connection wire attached to a single working electrode tip. (c) Close-up of an electrode in the flat section of an EPR flat cell.	179
Figure 9.3 : Illustration (not to scale) of a finished electrode tip. The wires are inserted in a glass tube which is then sealed.	181
Figure 9.4 : Cyclic voltammogram for the reduction of methyl viologen in aqueous environment on a PVD Ag electrode constructed as described in Section 9.2. Electrolyte = $H_2O + 0.2\text{ M Na}_2SO_4$. Recorded at 50 mV s^{-1}	182
Figure 9.5 : Cyclic voltammogram for the reduction of methyl viologen in acetonitrile on a PVD Ag electrode constructed as described in Section 9.2. Electrolyte = $ACN + 0.1\text{ M }n\text{-Bu}_4NClO_4$. Recorded at $50\text{ mV}\text{ s}^{-1}$	183
Figure 9.6 : Blue discoloration of the methyl viologen radical cation resulting from the MV reduction on a Ag electrode in an EPR flat cell.	184
Figure 9.7 : Cyclic voltammograms at different scan rates for the reduction of methyl viologen aqueous environment on a PVD Ag electrode constructed as described in Section 9.2. Electrolyte = $H_2O + 0.2\text{ M Na}_2SO_4$. Inset: peak current versus v	185

- Figure 9.8 :** EPR spectrum recorded during in situ electrolysis of (a) 5 mM methyl viologen in H₂O + 0.2 M Na₂SO₄ and (b) 5 mM *p*-benzoquinone in ACN + 0.1 M *n*-Bu₄NClO₄.....186
- Figure 9.9 :** Picture of a platinum mesh-electrode. The largest magnification shows the laminated platinum mesh working electrode with a hole of approximately 2 × 8 mm². The wire is a 75 µm silver wire that serves as reference electrode.....189
- Figure 9.10 :** Oxidation of hydroquinone (QH₂) to benzoquinone (BQ) (left to right) and reduction of benzoquinone to hydroquinone (right to left) in a protic solvent (in an aprotic solvent the quinone dianion is obtained) with the semiquinone radical anion intermediate (SQ).....190
- Figure 9.11 :** (a) Cyclic voltammogram for the reduction of methyl viologen in aqueous environment on a platinum mesh-electrode in both a standard batch setup and in an EPR flat cell. Recorded at 100 mv s⁻¹. (b) EPR spectrum recorded during in situ electrolysis of 5 mM methyl viologen in H₂O + 0.2 M Na₂SO₄. The potential was set at the peak potential of the reduction peak during an in situ CV.....191
- Figure 9.12 :** Example of a failure of the mesh-electrode after usage in a non-aqueous environment. The intense blue discoloration due to the methyl viologen radical anion shows that the reaction not only proceeds at the cut out hole (lower, intense blue color) but also between the lamination foil at the connection point (upper, less intense blue color).191
- Figure 9.13 :** (a) Cyclic voltammogram for the reduction of benzoquinone in acetonitrile on a silver wire-electrode in a standard batch setup. (b) EPR spectrum recorded during in situ electrolysis of 5 mM benzoquinone in ACN + 0.1 M *n*-Bu₄NClO₄. The potential was set at the peak potential of the reduction peak during an in situ CV.....194
- Figure 9.14 :** Picture of the reduction of methyl viologen on a wire-electrode in an EPR flat cell. The blue color is due to the methyl viologen radical anion and shows the active surface area of the working electrode.195

Figure 10.1 : Possible reaction pathways to construct fused aromatic molecules starting from allyl 2-bromobenzyl ether in an aprotic solvent [236].....	200
Figure 10.2 : Cyclic voltammetry of ABBE in ACN + 0.1 M TBAP on a Ag working electrode constructed as described in Chapter 9 in (a) a standard batch setup and (b) an EPR flat cell. CVs recorded at 100 mV s ⁻¹	203
Figure 10.3 : Current response of the controlled-potential electrolysis of ABBE in the EPR flat cell. Ag WE, electrolyte = 5 mM ABBE and 15 mM PBN in ACN + 0.1 M TBAP. Potential set at the peak potential of the reduction wave in the EPR flat cell, checked by in situ CV. The dashed lines mark the 30 min (20 scan) periods over which the EPR scans are accumulated...	205
Figure 10.4 : Accumulated experimental EPR spectra (blue line) and corresponding simulations (red line) of the controlled-potential electrolysis of ABBE in the EPR flat cell. Ag WE, electrolyte = 5 mM ABBE and 15 mM PBN in ACN + 0.1 M TBAP (potential set at the peak potential of the reduction wave in the EPR flat cell, checked by in situ CV) at different time intervals: (a) 0-30 min, (b) 30-60 min, (c) 60-90 min and (d) 90-120 min and the simulated spectra. The spectra are shown normalized to allow easy comparison.	207
Figure 10.5 : Molecular models derived from DFT computations and the contributions in the spectra of (a) radical 1/PBN-Ox, (b) radical 2/PBN-allyl benzyl ether, (c) radical 3/PBN-4-methylisochromane.	210
Figure 10.6 : Relative weight of each radical in the different spectra of Figure 10.4...	211
Figure 10.7 : Accumulated experimental EPR spectra (black, 20 scans) of the controlled-potential electrolysis of ABBE in the EPR flat cell and of a blank sample. Ag WE, electrolyte = 5 mM ABBE and 15 mM PBN in ACN + 0.1 M TBAP (potential set at the peak potential of the reduction wave in the EPR flat cell, checked by in situ CV) at different time intervals:	

0-30 min, (A), 30-60 min (B), 60-90 min (C) and 90-120 min (D), and the spectrum (blue, 50 scans) and simulation (red) of a blank sample containing only PBN in ACN with *n*-Bu₄NClO₄ collected after 75 min of controlled potential electrolysis in the same setup at the same potential (E). The parameters for the simulation were $g_{iso} = 2.0057$, $A_{N\text{-iso}} = 39.00$ MHz, $A_H = 5.8$ MHz. 214

Figure 10.8 : Comparisons of the trends in the $A_{N\text{-iso}}$ (A) and g_{iso} (B) between the experimental and calculated values using different functional/basis sets combinations, and molecular models of TEMPO and DMPO-OH. ... 215

Figure 10.9 : Evolution of the potential energy (A), and EPR parameters g_{iso} (B), $A_{N\text{-iso}}$ (C), A_H^β (D), A_{H2^φ} (E), A_{Ha^γ} (F) and A_{Hb^γ} (G) as a function of the dihedral angle manually rotated around the N-C^β bond for PBN-4-methylisochromane from calculations using B3LYP/EPR-II functional/basis set; the corresponding values for PBN-allyl benzyl ether (A' to D'); magnification of the region near the lowest energy (insets). The bands shade in pink indicates the dihedral angles which are thermally allowed at 298 K. 216

List of tables

Table 4.1 :	Equilibrium conversions of acetone to DAA.....	79
Table 9.1 :	Specifications of the platinum mesh working electrode.....	188
Table 10.1 :	Experimental (<i>exp</i>) and calculated (<i>calc</i>) isotropic <i>g</i> and hyperfine coupling constants of the three spin-trapped radicals during the electrolysis ABBE.....	208
Table 10.2 :	Experimental and numerical EPR parameters from DFT calculations using different functional/basis sets combinations.....	215
Table 10.3 :	XYZ coordinates of optimized geometries (in Å).....	217

Bibliography

- [1] European Commission, Climate change - Eurobarometer Report, 2011.
- [2] United Nations, Kyoto Protocol to the United Nations Framework Convention on Climate Change, 1998.
- [3] M. Doble, A.K. Kruthiventi, Green Chemistry & Engineering, Elsevier Science & Technology Books, 2007.
- [4] EPA - Office of pollution prevention and toxics, Green Chemistry Program Fact Sheet, (2002) 2.
<https://nepis.epa.gov/Exe/ZyPDF.cgi/P1004H5E.PDF?Dockey=P1004H5E.PDF>.
- [5] P.T. Anastas, M.M. Kirchhoff, Origins, current status, and future challenges of green chemistry, *Acc. Chem. Res.* 35 (2002) 686–694. doi:10.1021/ar010065m.
- [6] P.T. Anastas, J.C. Warner, Green chemistry: theory and practice, Oxford University Press, 1998.
- [7] A.P. Dicks, A. Hent, Green Chemistry Metrics A Guide to Determining and Evaluating Process Greenness, Springer, 2015.
- [8] P. Anastas, J. Zimmerman, Design Through the 12 Principles of Green Engineering, *Environ. Sci. Technol.* 37 (2003) 94–101.
<http://ieeexplore.ieee.org/document/4296421/>.
- [9] K. Jüttner, Technical Scale of Electrochemistry, in: D.D. Macdonald, P. Schmuki (Eds.), *Encycl. Electrochem. Vol. 5 Electrochem. Eng.*, Wiley-VCH, 2007: pp. 1–22.
- [10] A. Volta, On the electricity excited by the mere contact of conducting substances of different kinds, *Philos. Trans. R. Soc. London.* 90 (1800) 403–431. doi:10.1080/14786440008562590.
- [11] W. Nicholson, Account of the new Electrical or Galvanic Apparatus of Sig. Alex. Volta and experiments performed with the same., *J. Nat. Philos. Chem. Arts.* 4 (1801) 179–187.

- [12] M. Faraday, Experimental Researches in Electricity, Philos. Trans. R. Soc. London. 124 (1834) 77–122. doi:10.1098/rstl.1832.0006.
- [13] H. Kolbe, Beobachtungen über die oxydirende Wirkung des Sauerstoffs, wenn derselbe mit Hülfe einer elektrischen Säule entwickelt wird, J. Fur Prakt. Chemie. 41 (1847) 137–139.
- [14] H. Kolbe, Zersetzung der Valeriansäure durch den elektrischen Strom, Ann. Der Chemie Und Pharm. 64 (1848) 339–341.
- [15] H. Kolbe, Untersuchungen über die Elektrolyse organischer Verbindungen, Ann. Der Chemie Und Pharm. 69 (1849) 257–372.
- [16] H. Lund, A Century of Organic Electrochemistry, J. Electrochem. Soc. 149 (2002) S21. doi:10.1149/1.1462037.
- [17] W. Löb, Electrochemistry of Organic Compounds, 1st ed., John Wiley & Sons, Inc., 1906.
- [18] M.M. Baizer, R.D. Little, N. Weinberg, Electroorganic Synthesis, Marcel Dekker, Inc., 1991.
- [19] H. Lund, O. Hammerich, Organic Electrochemistry, 4th ed., Marcel Dekker, Inc., 1991.
- [20] J. Volke, F. Liška, Electrochemistry in Organic Synthesis, 1st ed., Springer-Verlag, 1994.
- [21] J. Grimshaw, Electrochemical Reactions and Mechanisms in Organic Chemistry, 1st ed., Elsevier, 2000. doi:10.1017/CBO9781107415324.004.
- [22] T. Fuchigami, M. Atobe, S. Inagi, Fundamentals and Applications of Organic Electrochemistry, John Wiley & Sons, Inc., 2015.
- [23] H.J. Schäfer, Contributions of organic electrosynthesis to green chemistry, Comptes Rendus Chim. 14 (2011) 745–765. doi:10.1016/j.crci.2011.01.002.
- [24] D.S.P. Cardoso, B. Šljukić, D.M.F. Santos, C.A.C. Sequeira, Organic Electrosynthesis: From Laboratorial Practice to Industrial Applications, Org. Process Res. Dev. (2017) acs.oprd.7b00004. doi:10.1021/acs.oprd.7b00004.

- [25] H.J. Schäfer, Anodic and Cathodic CC \square Bond Formation, *Angew. Chemie Int. Ed. English.* 20 (1981) 911–934. doi:10.1002/anie.198109111.
- [26] F. Tang, C. Chen, K.D. Moeller, Electrochemistry and umpolung reactions: New tools for solving synthetic challenges of structure and location, *Synthesis (Stuttg.)*. (2007) 3411–3420. doi:10.1055/s-2007-990835.
- [27] R.D. Little, K.D. Moeller, Organic Electrochemistry as a Tool for Synthesis, *Electrochem. Soc. Interface.* Winter 2002. (2002) 36–42.
- [28] K. Jüttner, U. Galla, H. Schmieder, Electrochemical approaches to environmental problems in the process industry, *Electrochim. Acta.* 45 (2000) 2575–2594. doi:10.1016/S0013-4686(00)00339-X.
- [29] C.A.C. Sequeira, D.M.F. Santos, Electrochemical Routes for Industrial Synthesis, *J. Braz. Chem. Soc.* 20 (2009) 387–406.
- [30] D. Simonsson, Electrochemistry for a Cleaner Environment, *Chem. Soc. Rev.* 26 (1997) 181–189. doi:10.1039/cs9972600181.
- [31] B.A. Frontana-Uribe, R.D. Little, J.G. Ibanez, A.A. Palma, R. Vasquez-Medrano, Organic electrosynthesis: a promising green methodology in organic chemistry, *Green Chem.* 12 (2010) 2099–2119. doi:10.1039/c0gc00382d.
- [32] J. Yoshida, K. Kataoka, R. Horcajada, A. Nagaki, Modern Strategies in Electroorganic Synthesis, *Chem. Rev.* 108 (2008) 2265–2299.
- [33] H. Pütter, Industrial Electroorganic Chemistry, in: H. Lund, O. Hammerich (Eds.), *Org. Electrochem.*, Marcel Dekker, Inc., 1991.
- [34] D. Pletcher, F.C. Walsh, *Industrial Electrochemistry*, 2nd ed., Chapman and Hall, London, 1990.
- [35] M.M. Baizer, Electrolytic hydrodimerization process and extraction procedure, 1962.
- [36] M.M. Baizer, Electrolytic Reductive Coupling 1. Acrylonitrile, *J. Electrochem. Soc.* 111 (1964) 215. doi:10.1149/1.2426086.
- [37] M.M. Baizer, Electrochemical Route to Adiponitrile .1. Discovery, *Chemtech.* 10 (1980) 161–164.

- [38] L. Albright, Albright's Chemical Engineering Handbook, 1st ed., CRC Press, 2008.
- [39] V.S. Bagotsky, Fundamentals of Electrochemistry, 2nd ed., John Wiley & Sons, Inc., 2006.
- [40] A.J. Bard, L.R. Faulkner, Electrochemical methods: Fundamentals and Applications, 2nd ed., John Wiley & Sons, Inc., 2001.
- [41] C.M.A. Brett, A.M.O. Brett, Electrochemistry: Principles, Methods, and Applications, Oxford University Press, 1994.
- [42] J. Newman, K.E. Thomas-Alyea, Electrochemical Systems, John Wiley & Sons, Inc., 2004.
- [43] P.A. Christensen, A. Hamnett, Techniques and Mechanisms in Electrochemistry, Chapman and Hall, 1994.
- [44] A.J. Bard, M. Stratmann, Encyclopedia of Electrochemistry, Wiley-VCH, 2007.
- [45] R. Francke, R.D. Little, Redox catalysis in organic electrosynthesis: basic principles and recent developments, *Chem. Soc. Rev.* 43 (2014) 2492–2521. doi:10.1039/c3cs60464k.
- [46] V.G. Levich, Physicochemical Hydrodynamics, Prentice-Hall, 1962.
- [47] C.A. Paddon, M. Atobe, T. Fuchigami, P. He, P. Watts, S.J. Haswell, G.J. Pritchard, S.D. Bull, F. Marken, Towards paired and coupled electrode reactions for clean organic microreactor electrosyntheses, *J. Appl. Electrochem.* 36 (2006) 617–634. doi:10.1007/s10800-006-9122-2.
- [48] H.J. Schäfer, Volume 8: Organic Electrochemistry, in: A.J. Bard, M. Stratmann (Eds.), *Encycl. Electrochem.*, Wiley-VCH, 2004.
- [49] A.M. Couper, D. Pletcher, F.C. Walsh, Electrode Materials for Electrosynthesis, *Phys. Rev.* 174 (1968) 1020–1026.
- [50] G. Inzelt, A. Lewenstam, F. Scholz, Handbook of Reference Electrodes, Springer-Verlag, 2013.
- [51] J.R. Selman, C.W. Tobias, mass-transfer measurements by the limiting-current

- technique, *Adv. Chem. Eng.* 10 (1978) 211–318.
- [52] J. Wilk, A review of measurements of the mass transfer in minichannels using the limiting current technique, *Exp. Therm. Fluid Sci.* 57 (2014) 242–249. doi:10.1016/j.expthermflusci.2014.04.019.
- [53] D.A. Szántó, S. Cleghorn, C. Ponce de León, F.C. Walsh, The Limiting Current for Reduction of Ferricyanide Ion at Nickel: The Importance of Experimental Conditions, *AICHE J.* 54 (2008) 802–810. doi:10.1002/aic.
- [54] R.J. Gale, *Spectroelectrochemistry, theory and practice*, Plenum Press, New York, 1988.
- [55] F. Gerson, W. Huber, *Electron Spin Resonance Spectroscopy of Organic Radicals*, 2003. doi:10.1002/3527601627.
- [56] P.T. Kissinger, W.R. Heineman, *Laboratory techniques in electroanalytical chemistry*, 2nd ed., Marcel Dekker, Inc., 1996.
- [57] J.D. Wadhawan, R.G. Compton, EPR Spectroscopy in Electrochemistry, in: E.J. Calvo (Ed.), *Encycl. Electrochem.* Vol. 2 Kinet. Mass Transp., Wiley-VCH, 2004: pp. 170–220.
- [58] V. Chechik, E. Carter, D. Murphy, *Electron Paramagnetic Resonance*, Oxford University Press, 2016.
- [59] W.R. Hagen, *Biomolecular EPR Spectroscopy*, CRC Press, 2008.
- [60] G.R. Eaton, S.S. Eaton, D.P. Barr, R.T. Weber, *Quantitative EPR*, Springer, 2010.
- [61] G. Gabrielse, D. Hanneke, Precision pins down the electron's magnetism, *Cern Cour.* 46 (2006) 35–37. cerncourier.com/cws/article/cern/29724 (accessed October 23, 2017).
- [62] D.E.G. Austen, P.H. Given, D.J.E. Ingram, M.E. Peover, Electron Resonance Study of the Radicals Produced by Controlled Potential Electrolysis of Aromatic Substances, *Nature*. 182 (1958) 1784–1786. doi:10.1038/1821784a0.
- [63] A.H. Maki, D.H. Geske, Detection of Electrolytically Generated Transient Free Radicals by Electron Spin Resonance, *J. Chem. Phys.* 30 (1959) 1356. doi:10.1063/1.1730187.

- [64] A.H. Maki, D.H. Geske, Electron-Spin Resonance of Electrochemically Generated Free Radicals. Isomeric Dinitrobenzene Mononegative Ions, *J. Chem. Phys.* 33 (1960) 825. doi:10.1063/1.1731269.
- [65] A.H. Maki, D.H. Geske, Electron Spin Resonance and Polarographic Investigation of Substituted Nitrobenzene Negative Ions, *J. Am. Chem. Soc.* 83 (1961) 1852–1860. doi:10.1021/ja01469a019.
- [66] Duin Laboratory, EPR manual: Practical Aspects, Auburn University College of Sciences and Mathematics, n.d.
- [67] R. Mahrwald, Modern Aldol Reactions. Vol. 1: Enolates, Organocatalysis, Biocatalysis and Natural Product Synthesis, 2004.
- [68] F.A. Carey, Organic Chemistry, 7th ed., McGraw-Hill, 2008.
- [69] J.P. Richard, R.W. Nagorski, Mechanistic imperatives for catalysis of aldol addition reactions: Partitioning of the enolate intermediate between reaction with bronsted acids and the carbonyl group, *J. Am. Chem. Soc.* 121 (1999) 4763–4770. doi:10.1021/ja9900297.
- [70] E.M. Arnett, F.J. Fisher, M.A. Nichols, A.A. Ribeiro, Thermochemistry of a structurally defined aldol reaction, *J. Am. Chem. Soc.* 111 (1989) 748–749. doi:10.1021/ja00184a062.
- [71] G.S. Salvapati, K. V. Ramanamurty, M. Janardanarao, Selective Catalytic Self-condensation of Acetone, *J. Mol. Catal.* 54 (1989) 9–30.
- [72] H. Arpe, S. Hawkins, Industrial Organic Chemistry, 5th ed., Wiley-VCH, 2010.
- [73] E.M. Kirschner, Environment, Health Concerns Force Shift In Use Of Organic Solvents, *Chem. Eng. News.* 72 (1994) 13. doi:10.1021/cen-v072n025.p013.
- [74] W.K.O. Keefe, M. Jiang, F.T.T. Ng, G.L. Rempel, Liquid phase kinetics for the selective hydrogenation of mesityl oxide to methyl isobutyl ketone in acetone over a Pd / Al₂O₃ catalyst, *Chem. Eng. Sci.* 60 (2005) 4131–4140. doi:10.1016/j.ces.2005.02.049.
- [75] F.A. Carey, R.J. Sundberg, Advanced Organic Chemistry, 5th ed., Springer, 2007.
- [76] J. Braithwaite, Ketones, in: Kirk-Othmer Encycl. Chem. Technol., 4th ed.,

- Wiley, 1995: pp. 485–506.
- [77] N.B. Lorette, Ketone Condensations Using a Sulfonic Acid Ion Exchange Resin, 22 (1957) 346–347.
- [78] G.J. Kelly, F. King, M. Kett, Waste elimination in condensation reactions of industrial importance Green Context, *Green Chem.* 4 (2002) 392–399. doi:10.1039/b201982p.
- [79] K. Tanabe, W.F. Ho, Industrial application of solid acid ± base catalysts, *Appl. Catal. A Gen.* 181 (1999) 399–434.
- [80] E.C. Craven, The alkaline condensation of acetone, *J. Biochem. Toxicol.* 13 (1963) 71–77. doi:10.1002/jbt.2570130205.
- [81] G.G. Podrebarac, F.T.T. Ng, G.L. Rempel, A kinetic study of the aldol condensation of acetone using an anion exchange resin catalyst, *Chem. Eng. Sci.* 52 (1997) 2991–3002. doi:10.1016/S0009-2509(97)00098-5.
- [82] S. Lippert, W. Baumann, K. Thomke, Secondary reactions of the base-catalyzed aldol condensation of acetone, *J. Mol. Catal.* 69 (1991) 199–214. doi:10.1016/0304-5102(91)80145-S.
- [83] P. Kustrowski, D. Sułkowska, R. Pytlowany, R. Dziembaj, Kinetics of self-condensation of acetone over heterogeneous Ba(OH)₂ and Sr(OH)₂ catalysts, *React. Kinet. Catal. Lett.* 81 (2004) 3–11.
- [84] G. Zhang, H. Hattori, K. Tanabe, Aldol Addition of Acetone , Catalyzed by Solid Base Catalysts : Magnesium Oxide , Calcium Oxide , Strontium Oxide , Barium Oxide , Lanthanum (III) Oxide and Zirconium Oxide, *Appl. Catal.* 36 (1988) 189–197.
- [85] M. Paulis, M. Martín, D.B. Soria, A. Díaz, J.A. Odriozola, M. Montes, Preparation and characterization of niobium oxide for the catalytic aldol condensation of acetone, *Appl. Catal. A Gen.* 180 (1999) 411–420.
- [86] G. Zhang, H. Hattori, K. Tanabe, Aldol Condensation of Acetone / Acetone d6 over Magnesium Oxide and Lanthanum Oxide, *Appl. Catal.* 40 (1988) 183–190.
- [87] C.H. Du, Y. Shen, L.P. Sun, X.C. Meng, Condensation of Acetone to Diacetone Alcohol over Structured MgO/Al₂O₃-Al Catalyst Packing, *Adv. Mater. Res.* 347–353 (2011) 3050–3053. doi:10.4028/www.scientific.net/AMR.347-

353.3050.

- [88] K. Tanabe, G. Zhang, H. Hattori, Addition of Metal Cations to Magnesium Oxide Catalyst for the Aldol Condensation of Acetone, *Appl. Catal.* 48 (1989) 63–69.
- [89] S. Ordóñez, E. Díaz, M. León, L. Faba, Hydrotalcite-derived mixed oxides as catalysts for different C – C bond formation reactions from bioorganic materials, *Catal. Today.* 167 (2011) 71–76. doi:10.1016/j.cattod.2010.11.056.
- [90] L. Faba, E. Díaz, S. Ordó, Gas phase acetone self-condensation over unsupported and supported Mg – Zr mixed-oxides catalysts, *Appl. Catal. B Environ.* 143 (2013) 387–395. doi:10.1016/j.apcatb.2013.05.043.
- [91] P. Kustrowski, D. Sułkowska, L. Chmielarz, A. Rafalska-łasocha, B. Dudek, R. Dziembaj, Influence of thermal treatment conditions on the activity of hydrotalcite-derived Mg – Al oxides in the aldol condensation of acetone, *Microporous Mesoporous Mater.* 78 (2005) 11–22. doi:10.1016/j.micromeso.2004.09.011.
- [92] D. Tichit, M. Naciri Bennani, F. Figueras, R. Tessier, K. J, Aldol condensation of acetone over layered double hydroxides of the meixnerite type, *Appl. Clay Sci.* 13 (1998) 401–415.
- [93] G.G. Podrebarac, F.T.T. Ng, G.L. Rempel, The production of diacetone alcohol with catalytic distillation Part I: Catalytic distillation experiments, *Chem. Eng. Sci.* 53 (1998) 1077–1088. doi:10.1016/S0009-2509(97)00428-4.
- [94] W. Nicol, Comparing catalytic distillation to separate reaction and distillation for the production of diacetone alcohol, *Chem. Eng. Des.* 81 (2003) 1026–1032.
- [95] S. Thotla, V. Agarwal, S.M. Mahajani, Simultaneous production of diacetone alcohol and mesityl oxide from acetone using reactive distillation, *Chem. Eng. Sci.* (2007).
- [96] S. Thotla, V. Agarwal, S.M. Mahajani, Aldol condensation of acetone with reactive distillation using water as a selectivity enhancer, *Ind. Eng. Chem. Res.* 46 (2007) 8371–8379. doi:10.1021/ie061658+.
- [97] C. Huang, F.T.T. Ng, G.L. Rempel, Application of catalytic distillation for the aldol condensation of acetone : the effect of the mass transfer and kinetic rates on the yield and selectivity, *Chem. Eng. Sci.* 55 (2000) 5919–5931.

- [98] T. Shono, S. Kashimura, K. Ishizaki, Electroinduced aldol condensation*, *Electrochim. Acta.* 29 (1984) 603–605.
- [99] S. Kumar, L.K. Sharma, R.K.P. Singh, Electroinduced aldol condensation on platinum electrode, *J. Indian Chem. Soc.* 83 (2006) 1160–1162.
- [100] M.-L. Tsai, C. Tse-Chuan, Aldol condensation of acetone in an undivided cell via electrochemical catalyzed reaction.pdf, *J. Chinese Institut Chem. Eng.* (1997).
- [101] M.-L. Tsai, T.-C. Chou, Electrolysis of acetone in a divided cell.pdf, *J. Chinese Institut Chem. Eng.* (1998).
- [102] M. Tsai, The production of Diacetone Alcohol via paired electrolysis in a undivided cell.pdf, *J. Chinese Institut Chem. Eng.* (2005).
- [103] J. Wegner, S. Ceylan, A. Kirschning, Flow chemistry - A key enabling technology for (multistep) organic synthesis, *Adv. Synth. Catal.* 354 (2012) 17–57. doi:10.1002/adsc.201100584.
- [104] G. Jas, A. Kirschning, Continuous Flow Techniques in Organic Synthesis, *Chem. - A Eur. J.* 9 (2003) 5708–5723. doi:10.1002/chem.200305212.
- [105] D. Webb, T.F. Jamison, Continuous flow multi-step organic synthesis, *Chem. Sci.* 1 (2010) 675–680. doi:10.1039/c0sc00381f.
- [106] M. Küpper, V. Hessel, H. Löwe, W. Stark, J. Kinkel, M. Michel, H. Schmidt-Traub, Micro reactor for electroorganic synthesis in the simulated moving bed-reaction and separation environment, *Electrochim. Acta.* 48 (2003) 2889–2896. doi:10.1016/S0013-4686(03)00353-0.
- [107] S. Rode, A. Attour, F. Lapicque, M. Matlosz, Thin-Gap Single-Pass High-Conversion Reactor for Organic Electrosynthesis, *J. Electrochem. Soc.* 155 (2008) 193–200. doi:10.1149/1.2996568.
- [108] F.J. Del Campo, Miniaturization of electrochemical flow devices: A mini-review, *Electrochim. Commun.* 45 (2014) 91–94. doi:10.1016/j.elecom.2014.05.013.
- [109] A. Ziogas, G. Kolb, M. O'Connell, A. Attour, F. Lapicque, M. Matlosz, S. Rode, Electrochemical microstructured reactors: Design and application in organic synthesis, *J. Appl. Electrochem.* 39 (2009) 2297–2313. doi:10.1007/s10800-

009-9939-6.

- [110] K.F. Jensen, Microreaction engineering — is small better?, *Chem. Eng. Sci.* 56 (2001) 293–303. doi:10.1016/S0009-2509(00)00230-X.
- [111] R.L. Hartman, K.F. Jensen, Microchemical systems for continuous-flow synthesis, *Lab Chip.* 9 (2009) 2495. doi:10.1039/b906343a.
- [112] B.P. Mason, K.E. Price, J.L. Steinbacher, A.R. Bogdan, D.T. Mcquade, Greener Approaches to Organic Synthesis Using Microreactor Technology, *Chem. Rev.* 107 (2007) 2300–2318.
- [113] H. Pennemann, V. Hessel, H. Löwe, Chemical microprocess technology—from laboratory-scale to production, *Chem. Eng. Sci.* 59 (2004) 4789–4794. doi:10.1016/j.ces.2004.07.049.
- [114] H. Wendt, G. Kreysa, *Electrochemical Engineering*, Springer-Verlag, Berlin, 1999.
- [115] R.J. Marshall, F.C. Walsh, A review of some recent electrolytic cell designs, *Surf. Technol.* 24 (1985) 45–77. doi:10.1016/0376-4583(85)90015-9.
- [116] D.J. Pickett, *Electrochemical Reactor Design*, 2nd ed., Elsevier, Amsterdam., 1979.
- [117] R. Green, R. Brown, D. Pletcher, Understanding the Performance of a Microfluidic Electrolysis Cell for Routine Organic Electrosynthesis, *J. Flow Chem.* 5 (2014) 31–36. doi:10.1556/JFC-D-14-00027.
- [118] O. Scialdone, C. Guarisco, A. Galia, Oxidation of organics in water in microfluidic electrochemical reactors: Theoretical model and experiments, *Electrochim. Acta*. 58 (2011) 463–473. doi:10.1016/j.electacta.2011.09.073.
- [119] M. Küpper, V. Hessel, H. Löwe, W. Stark, J. Kinkel, M. Michel, H. Schmidt-Traub, Micro reactor for electroorganic synthesis in the simulated moving bed-reaction and separation environment, *Electrochim. Acta*. 48 (2003) 2889–2896. doi:10.1016/S0013-4686(03)00353-0.
- [120] C.A. Paddon, G.J. Pritchard, T. Thiemann, F. Marken, Paired electrosynthesis: micro-flow cell processes with and without added electrolyte, *Electrochim. Commun.* 4 (2002) 825–831.

- [121] R. Horcajada, M. Okajima, S. Suga, J. Yoshida, Microflow electroorganic synthesis without supporting electrolyte, *Chem. Commun.* (2005) 1303–1305. doi:10.1039/b417388k.
- [122] C.A. Paddon, M. Atobe, T. Fuchigami, P. He, P. Watts, S.J. Haswell, G.J. Pritchard, S.D. Bull, F. Marken, Towards paired and coupled electrode reactions for clean organic microreactor electrosyntheses, *J. Appl. Electrochem.* 61 (2006) 617–634. doi:10.1007/s10800-006-9122-2.
- [123] D. Horii, T. Fuchigami, M. Atobe, A New Approach to Anodic Substitution Reaction Using Parallel Laminar Flow in a Micro-Flow Reactor, *J. Am. Chem. Soc.* (2007) 11692–11693.
- [124] K. Watts, A. Baker, T. Wirth, Electrochemical Synthesis in Microreactors, *J. Flow Chem.* 4 (2014) 2–11. doi:10.1556/JFC-D-13-00030.
- [125] A. Attour, P. Dirrenberger, S. Rode, A. Ziogas, M. Matlosz, F. Lapicque, A high pressure single-pass high-conversion electrochemical cell for intensification of organic electrosynthesis processes, *Chem. Eng. Sci.* 66 (2011) 480–489. doi:10.1016/j.ces.2010.11.002.
- [126] O. Scialdone, A. Galia, S. Sabatino, M. Vaiana, D. Agro, A. Busacca, C. Amatore, Electrochemical Conversion of Dichloroacetic Acid to Chloroacetic Acid in Conventional Cell and in Two Microfluidic Reactors, *ChemElectroChem.* 5 (2014) 116–124. doi:10.1002/celec.201300216.
- [127] H. Löwe, W. Ehrfeld, State-of-the-art in microreaction technology: concepts, manufacturing and applications, *Electrochim. Acta.* 44 (1999) 3679–3689. doi:10.1016/S0013-4686(99)00071-7.
- [128] R.A. Green, R.C.D. Brown, D. Pletcher, B. Harji, A Microflow Electrolysis Cell for Laboratory Synthesis on the Multigram Scale, *Org. Process Res. Dev.* 19 (2015) 1424–1427. doi:10.1021/acs.oprd.5b00260.
- [129] C. Gütz, A. Stenglein, S.R. Waldvogel, Highly Modular Flow Cell for Electroorganic Synthesis, *Org. Process Res. Dev.* 21 (2017) 771–778. doi:10.1021/acs.oprd.7b00123.
- [130] J. Kuleshova, J.T. Hill-Cousins, P.R. Birkin, R.C.D. Brown, D. Pletcher, T.J. Underwood, A simple and inexpensive microfluidic electrolysis cell, *Electrochim. Acta.* 56 (2011) 4322–4326. doi:10.1016/j.electacta.2011.01.036.
- [131] G.P. Roth, R. Stalder, T.R. Long, D.R. Sauer, S.W. Djuric, Continuous-Flow

- Microfluidic Electrochemical Synthesis: Investigating a New Tool for Oxidative Chemistry, *J. Flow Chem.* 3 (2013) 34–40. doi:10.1556/JFC-D-13-00002.
- [132] S. Suga, M. Okajima, K. Fujiwara, “Cation Flow” Method: A New Approach to Conventional and Combinatorial Organic Syntheses Using Electrochemical Microflow Systems, *J. Am. Chem. Soc.* 131 (2001) 7941–7942.
- [133] S. Suga, M. Okajima, K. Fujiwara, J. Yoshida, Electrochemical Combinatorial Organic Syntheses Using Microflow Systems, *QSAR Comb. Sci.* 24 (2005). doi:10.1002/qsar.200440003.
- [134] D. Horii, M. Atobe, T. Fuchigami, F. Marken, Self-Supported Methoxylation and Acetoxylation Electrosynthesis Using a Simple Thin-Layer Flow Cell, *J. Electrochem. Soc.* 153 (2006) 143–147. doi:10.1149/1.2209565.
- [135] F.F. Rivera, C.P. De León, J.L. Nava, F.C. Walsh, The filter-press FM01-LC laboratory flow reactor and its applications, *Electrochim. Acta* 163 (2015) 338–354. doi:10.1016/j.electacta.2015.02.179.
- [136] J. Kuleshova, J.T. Hill-Cousins, P.R. Birkin, R.C.D. Brown, D. Pletcher, T.J. Underwood, The methoxylation of N-formylpyrrolidine in a microfluidic electrolysis cell for routine synthesis, *Electrochim. Acta* 69 (2012) 197–202. doi:10.1016/j.electacta.2012.02.093.
- [137] O. Scialdone, A. Galia, S. Sabatino, D. Mira, Electrochemical Conversion of Dichloroacetic Acid to Chloroacetic Acid in a Microfluidic Stack and in a Series of Microfluidic Reactors, (2015) 684–690. doi:10.1002/celc.201402454.
- [138] F.F. Rivera, C.P. De León, F.C. Walsh, J.L. Nava, The reaction environment in a filter-press laboratory reactor: The FM01-LC flow cell, *Electrochim. Acta* 161 (2015) 436–452. doi:10.1016/j.electacta.2015.02.161.
- [139] M. Griffiths, C.P. De León, F.C. Walsh, Mass transport in the rectangular channel of a filter-press electrolyzer (the FM01-LC reactor), *AIChE J.* 51 (2005) 682–687. doi:10.1002/aic.10311.
- [140] C.J. Brown, D. Pletcher, F.C. Walsh, J.K. Hammond, D. Robinson, Studies of space-averaged mass transport in the FM01-LC laboratory electrolyser, *J. Appl. Electrochem.* 23 (1993) 38–43. doi:10.1007/BF00241573.
- [141] I. Carlsson, B. Sandegren, D. Simonsson, Design And Performance Of A Modular, Multi-Purpose Electrochemical Reactor, *J. Electrochem. Soc.* 130 (1983) 342–346.

- [142] A. Montillet, J. Comiti, J. Legrand, Application of metallic foams in electrochemical reactors of the filter-press type: Part II Mass transfer performance, *J. Appl. Electrochem.* 24 (1994) 384–389. doi:10.1007/BF00254149.
- [143] C. Bengoa, A. Montillet, P. Legentilhomme, J. Legrand, Flow visualization and modelling of a filter-press type electrochemical reactor, *J. Appl. Electrochem.* 27 (1997) 1313–1322. doi:10.1023/A:1018456609059.
- [144] ElectroCell A/S, High quality electrochemical cells and systems, Website. (2017). www.electrocell.com (accessed January 1, 2017).
- [145] J.E. Lira-Teco, F. Rivera, O. Farías-Moguel, J. Torres-González, Y. Reyes, R. Antaño-López, G. Orozco, F. Castañeda-Zaldivar, Comparison of experimental and CFD mass transfer coefficient of three commercial turbulence promoters, *Fuel.* 167 (2016) 337–346. doi:10.1016/j.fuel.2015.11.053.
- [146] a. N. Colli, J.M. Bisang, Evaluation of the hydrodynamic behaviour of turbulence promoters in parallel plate electrochemical reactors by means of the dispersion model, *Electrochim. Acta.* 56 (2011) 7312–7318. doi:10.1016/j.electacta.2011.06.047.
- [147] T.R. Ralph, M.L. Hitchman, J.P. Millington, F.C. Walsh, Mass transport in an electrochemical laboratory filterpress reactor and its enhancement by turbulence promoters, *Electrochim. Acta.* 41 (1996) 591–603. doi:10.1016/0013-4686(95)00346-0.
- [148] M. Matlosz, Electrochemical engineering analysis of multisected porous electrodes, *J. Electrochem. Soc.* 142 (1995) 1915–1922. doi:10.1149/1.2044214.
- [149] C. Vallières, M. Matlosz, A Multisected Porous Electrode for Synthesis of D-Arabinose, *J. Electrochem. Soc.* 146 (1999) 2933. doi:10.1149/1.1392031.
- [150] J.H.P. Utley, M.F. Nielsen, Electrogenerated Bases, in: H. Lund, O. Hammerich (Eds.), *Org. Electrochem.*, 4th ed., Marcel Dekker, Inc., 1991.
- [151] M.F. Nielsen, Electrogenerated Acids and Bases, in: H. Schäfer (Ed.), *Encycl. Electrochem.* Vol. 8 *Org. Electrochem.*, Wiley-VCH, 2004: pp. 451–488.
- [152] J. Grimshaw, Carbonyl Compounds, in: H. Lund, O. Hammerich (Eds.), *Org. Electrochem.*, Marcel Dekker, Inc., 1991: pp. 411–434.

- [153] J. Simonet, J.-F. Pilard, Electrogenerated Reagents, in: H. Lund, O. Hammerich (Eds.), *Org. Electrochem.*, 4th ed., Marcel Dekker, Inc., 1991: pp. 1163–1226.
- [154] C.P. Andrieux, M. Grzeszczuk, J.M. Saveant, Electrochemical generation and reduction of organic free radicals. α -Hydroxybenzyl radicals from the reduction of benzaldehyde, *J. Am. Chem. Soc.* 113 (1991) 8811–8817. doi:10.1021/ja00023a032.
- [155] P.J. Elving, J.T. Leone, Mechanism of the Electrochemical Reduction of Phenyl Ketones, *J. Am. Chem. Soc.* 80 (1958) 1021–1029. doi:10.1021/ja01538a002.
- [156] L. Nadjo, J.M. Savéant, Dimerization, disproportionation and ECE mechanisms in reduction of aromatic carbonyl compounds in alkaline media, *J. Electroanal. Chem.* 33 (1971) 419.
- [157] M.F. Nielsen, S. Spriggs, J.H.P. Utley, Y. Gao, The Formation of Relatively Stable Protonated Anion-radicals in the Cathodic Hydrogenation of Quinonemethides, *J. Chem. Soc. Chem. Commun.* (1994) 1395–1397.
- [158] M. Kimura, T. Kurata, T. Yamashita, Y. Sawaki, Electrocatalyzed addition of dialkyl phosphonates to aromatic carbonyl compounds. A convenient preparation of phosphoric esters via an efficient rearrangement, *Electrochim. Acta*. 42 (1997) 2225–2231.
- [159] J.C. Gard, B. Hanquet, L. Rouiller, Y. Mugnier, J. Lessard, Electrochemically induced chain reactions: The addition of fluorene and indene to aromatic aldehydes initiated by electrochemical reduction, *Can. J. Chem.* 74 (1996) 55–62.
- [160] E.M. Abbot, A.J. Bellamy, J.B. Kerr, I.S. Mackirdy, Cyanomethylation during the Electroreduction of Aromatic Carbonyl Compounds in Acetonitrile, *J. Chem. Soc. Perkin Trans. 2.* (1982).
- [161] D.T. Sawyer, J.S. Valentine, How Super Is Superoxide?, *Acc. Chem. Res.* 14 (1981) 393–400. doi:10.1021/ar00072a005.
- [162] K. Izutsu, Nonaqueous Solutions Related Titles from WILEY-VCH Encyclopedia of Electrochemistry , Volume VI Supramolecular Electrochemistry Semiconductor Electrochemistry Handbook of Analytical Techniques, 2002.
- [163] W.J. Basirun, D. Pletcher, A. Saraby-Reintjes, Studies of platinum

- electroplating baths Part IV: Deposits on copper from Q bath, *J. Appl. Electrochem.* 26 (1996) 873–880. doi:10.1007/BF00683750.
- [164] O.B. Ergu, O.N. Sara, S. Yapici, M.E. Arzutug, Pressure drop and point mass transfer in a rectangular microchannel, *Int. Commun. Heat Mass Transf.* 36 (2009) 618–623. doi:10.1016/j.icheatmasstransfer.2009.03.015.
- [165] L.F. Arenas, C.P. de Leon, F.C. Walsh, Mass transport and active area of porous Pt/Ti electrodes for the Zn-Ce redox flow battery determined from limiting current measurements, *Electrochim. Acta* 221 (2016) 154–166. doi:10.1016/j.electacta.2016.10.097.
- [166] K. Scott, J. Lobato, Determination of a Mass-Transfer Coefficient Using the Limiting-Current Technique, *Chem. Educ.* 7 (2002) 214–219. doi:10.1007/s00897020579a.
- [167] L.F. Arenas, C.P. de León, R.P. Boardman, F.C. Walsh, Electrodeposition of Platinum on Titanium Felt in a Rectangular Channel Flow Cell, *J. Electrochem. Soc.* 164 (2017) D57–D66. doi:10.1149/2.0651702jes.
- [168] R.G. Compton, P.R. Unwin, Channel and tubular electrodes, *J. Electroanal. Chem. Interfacial Electrochem.* 205 (1986) 1–20. doi:10.1016/0022-0728(86)90219-6.
- [169] J.L. Plawsky, Transport phenomena fundamentals, 2001.
- [170] D. Pauwels, J. Hereijgers, K. Verhulst, K. De Wael, T. Breugelmans, Investigation of the electrosynthetic pathway of the aldol condensation of acetone, *Chem. Eng. J.* 289 (2016) 554–561. doi:10.1016/j.cej.2016.01.018.
- [171] B. Geboes, New routes towards efficient electrocatalyst development, (2016).
- [172] L. Eberson, S.S. Shaik, Electron-Transfer Reactions of Radical Anions: Do They Follow Outer- or Inner-Sphere Mechanisms?, *J. Am. Chem. Soc.* 112 (1990) 4484–4489.
- [173] H. Lund, Electrochemical preparation of strong bases, in: *Electrochemical Soc. Proc. Mech. Synth. Asp. Org. Biol. Electrochem.*, 2003: pp. 25–28.
- [174] Users Service Training Course: EPR Resonators, Bruker, n.d.
- [175] T.J. Kemp, Kinetic aspects of spin trapping, *Prog. React. Kinet. Mech.* 24 (1999)

287–358.

- [176] A.J. Wain, R.G. Compton, R. Le Roux, S. Matthews, A.C. Fisher, Microfluidic channel flow cell for simultaneous cryoelectrochemical electron spin resonance, *Anal. Chem.* 79 (2007) 1865–1873. doi:10.1021/ac061910n.
- [177] A.J. Wain, R.G. Compton, R. Le Roux, S. Matthews, K. Yunus, A.C. Fisher, A microfluidic channel flow cell for electrochemical ESR, *J. Phys. Chem. B.* 110 (2006) 26040–26044.
- [178] B.A. Coles, R.G. Compton, Photoelectrochemical ESR, *J. Electroanal. Chem. Interfacial Electrochem.* 144 (1983) 87–98. doi:10.1016/S0022-0728(83)80146-6.
- [179] W.J. Albery, R.G. Compton, C.C. Jones, A novel electrode for electrochemical ESR and its application to modified electrodes, *J. Am. Chem. Soc.* 106 (1984) 469–473.
- [180] A.J. Wain, M. Thompson, O. V Klymenko, R.G. Compton, An improved configuration for simultaneous electrochemical ESR studies: a tubular electrode in a cylindrical cavity, *Phys. Chem. Chem. Phys.* 6 (2004) 4018–4027.
- [181] R.D. Allendoerfer, W. Froncisz, C.C. Felix, J.S. Hyde, Electrochemical generation of free radicals in an EPR loop-gap resonator, *J. Magn. Reson.* 76 (1988) 100–105. doi:10.1016/0022-2364(88)90204-1.
- [182] R.G. Compton, C.R. Greaves, A.M. Waller, A wall-jet electrode for in-situ electrochemical ESR, *J. Electroanal. Chem.* 211 (1990) 83–92.
- [183] R.G. Compton, A.M. Waller, An improved cell for in-situ electrochemical ESR, *J. Electroanal. Chem. Interfacial Electrochem.* 195 (1985) 289–297. doi:10.1016/0022-0728(85)80049-8.
- [184] J. Zeitouny, V. Jouikov, Reversed redox generation of silyl radicals in a four-electrode flow-through EPR spectroelectrochemical cell., *Phys. Chem. Chem. Phys.* 11 (2009) 7161–7170. doi:10.1039/b905072h.
- [185] R.N. Bagchi, A.M. Bond, F. Schulz, A newly designed variable temperature stationary and flow-through cell for in situ ESR-electrochemical experiments in solvents having either low or high dielectric constants, *J. Electroanal. Chem.* 252 (1988) 259–267. doi:10.1016/0022-0728(88)80215-8.

- [186] L.H. Piette, P. Ludwig, R.N. Adams, Electron Paramagnetic Resonance and Electrochemistry. Studies of Electrochemically Generated Radical Ions in Aqueous Solution., *Anal. Chem.* 34 (1962) 916–921. doi:10.1021/ac60188a013.
- [187] L.H. Piette, P. Ludwig, R.N. Adams, Electron Paramagnetic Resonance of Aromatic and Aliphatic Nitro Anions in Aqueous Solution, *J. Am. Chem. Soc.* 84 (1962) 4212–4215.
- [188] L.H. Piette, R.N. Adams, P. Ludwig, Electrolytic generation of radical ions in aqueous solution, *J. Am. Chem. Soc.* 83 (1961) 3909–3910.
- [189] A. Petr, L. Dunsch, A. Neudeck, In situ UV-vis ESR spectroelectrochemistry, *J. Electroanal. Chem.* 412 (1996) 153–158. doi:10.1016/0022-0728(96)04582-2.
- [190] A. Neudeck, L. Kress, Laminated micro-meshes - A new kind of optically transparent electrode, *J. Electroanal. Chem.* 437 (1997) 141–156. <http://www.scopus.com/inward/record.url?eid=2-s2.0-0031269541&partnerID=40&md5=fd05526d829ea0eb3ebd1da86de205ca>.
- [191] R.D. Allendoerfer, G. a Martinchek, S. Bruckenstein, Simultaneous Electrochemical-Electron Spin Resonance Measurements with a Coaxial Microwave Cavity, *Anal. Chem.* 47 (1975) 890. doi:10.1021/ac60356a023.
- [192] R.D. Allendoerfer, J.B. Carroll, A coaxial microwave cavity for improved electron paramagnetic resonance sensitivity with lossy solvents, *J. Magn. Reson.* 37 (1980) 497–508. doi:10.1016/0022-2364(80)90054-2.
- [193] R.G. Compton, D.J. Page, G.R. Sealy, In-situ electrochemical ESR: First-order kinetics and transient signals, *J. Electroanal. Chem.* 163 (1984) 65–75.
- [194] R.G. Compton, P.J. Daly, P.R. Unwin, A.M. Waller, In-situ electrochemical ESR: ECE versus DISP1, *J. Electroanal. Chem.* 191 (1985) 15–29.
- [195] L. Dunsch, Simultaneous ESR-electrochemical investigations at solid electrodes, in: A. Ivaska, A. Lewenstam, R. Sara (Eds.), *Contemp. Electroanal. Chem.*, Springer Science + Business Media, 1990: pp. 59–68.
- [196] S.P. Murarka, R.f. diode sputtered platinum films, *Thin Solid Films.* 23 (1974) 323–336.
- [197] M. a. Tamski, J. V. Macpherson, P.R. Unwin, M.E. Newton, Electrochemical electron paramagnetic resonance utilizing loop gap resonators and micro-

- electrochemical cells, *Phys. Chem. Chem. Phys.* 17 (2015) 23438–23447. doi:10.1039/C5CP04259C.
- [198] J.A. Cooper, R.G. Compton, Channel Electrodes — A Review, *Electroanalysis*. 10 (1998) 141–155. doi:10.1002/(SICI)1521-4109(199803)10:3<141::AID-ELAN141>3.3.CO;2-6.
- [199] R.D. Webster, R.A.W. Dryfe, J.C. Eklund, C.-W. Lee, R.G. Compton, In situ electrochemical ESR studies of reactive radicals: the reductions of bromo-anthraquinone and methyl viologen, *J. Electroanal. Chem.* 402 (1996) 167–174. doi:10.1016/0022-0728(95)04351-9.
- [200] N. Aristov, A. Habekost, Electrochromism of Methylviologen (Paraquat), *World J. Chem. Educ.* 3 (2015) 82–86. doi:10.12691/wjce-3-4-1.
- [201] L. Xiao, G.G. Wildgoose, R.G. Compton, Investigating the voltammetric reduction of methylviologen at gold and carbon based electrode materials. Evidence for a surface bound adsorption mechanism leading to electrode “protection” using multi-walled carbon nanotubes, *New J. Chem.* 32 (2008) 1628. doi:10.1039/b804842h.
- [202] S. Klod, L. Dunsch, A combination of in situ ESR and in situ NMR spectroelectrochemistry for mechanistic studies of electrode reactions: The case of p-benzoquinone, *Magn. Reson. Chem.* 49 (2011) 725–729. doi:10.1002/mrc.2819.
- [203] H. Park, M.S. Won, C. Cheong, Y.B. Shim, In-situ ESR detection of radical species of p-benzoquinone in aqueous media, *Electroanalysis*. 14 (2002) 1501–1507. doi:10.1002/1521-4109(200211)14:21<1501::AID-ELAN1501>3.0.CO;2-B.
- [204] X. Zhang, J.W. Zwanziger, Design and applications of an in situ electrochemical NMR cell, *J. Magn. Reson.* 208 (2011) 136–147. doi:10.1016/j.jmr.2010.10.013.
- [205] M.A. Tamaki, M.W. Dale, B.G. Breeze, J.V. Macpherson, P.R. Unwin, M.E. Newton, Quantitative measurements in electrochemical electron paramagnetic resonance, *Electrochim. Acta*. 213 (2016) 802–810. doi:10.1016/j.electacta.2016.07.114.
- [206] P. Damlin, C. Kvarnström, A. Petr, P. Ek, L. Dunsch, A. Ivaska, In situ resonant Raman and ESR spectroelectrochemical study of electrochemically synthesized poly(p-phenylenevinylene), *J. Solid State Electrochem.* 6 (2002) 291–301. doi:10.1007/s100080100240.

- [207] B. Gadgil, P. Damlin, E. Dmitrieva, T. Ääritalo, C. Kvarnström, ESR/UV-Vis-NIR spectroelectrochemical study and electrochromic contrast enhancement of a polythiophene derivative bearing a pendant viologen, *RSC Adv.* 5 (2015) 42242–42249. doi:10.1039/C5RA04618A.
- [208] A. Goux, D. Pratt, L. Dunsch, The reaction mechanism of p-toluenediamine anodic oxidation: An in situ ESR-UV/Vis/NIR spectroelectrochemical study, *ChemPhysChem.* 8 (2007) 2101–2106. doi:10.1002/cphc.200700235.
- [209] G. Armendáriz-Vidales, C. Frontana, Insights into dissociative electron transfer in esterified shikonin semiquinones by in situ ESR/UV-Vis spectroelectrochemistry, *Phys. Chem. Chem. Phys.* 17 (2015) 29299–29304. doi:10.1039/C5CP04306A.
- [210] A. Petr, V. Kataev, B. Büchner, First direct in situ EPR spectroelectrochemical evidence of the superoxide anion radical, *J. Phys. Chem. B.* 115 (2011) 12036–12039. doi:10.1021/jp206540c.
- [211] R.T. Boeré, A.M. Bond, T. Chivers, S.W. Feldberg, T.L. Roemmele, Identification of the Radical Anions of C₂N₄S₂ and P₂N₄S₂ Rings by In Situ EPR Spectroelectrochemistry and DFT Calculations, *Inorg. Chem.* 46 (2007) 5596–5607. doi:10.1021/ic070243t.
- [212] R.D. Webster, R. a. W. Dryfe, B. a. Coles, R.G. Compton, In Situ Electrochemical EPR Studies of Charge Transfer across the Liquid/Liquid Interface, *Anal. Chem.* 70 (1998) 792–800. doi:10.1021/ac9708147.
- [213] M. Zalibera, P. Machata, T.T. Clikeman, M. Rosenkranz, S.H. Strauss, O. V. Boltalina, A.A. Popov, ¹⁹F NMR-, ESR-, and vis-NIR-spectroelectrochemical study of the unconventional reduction behaviour of a perfluoroalkylated fullerene: dimerization of the C₇₀(CF₃)₁₀ – radical anion, *Analyst.* 140 (2013) 7209–7216. doi:10.1039/C5AN01129A.
- [214] R. a. W. Dryfe, R.D. Webster, B. a. Coles, R.G. Compton, In situ EPR studies of electron transfer across a polarised liquid/liquid interface, *Chem. Commun.* (1997) 779–780. doi:10.1039/a700640c.
- [215] R.N. Bagchi, A.M. Bond, R. Colton, Simultaneous in-situ electron spin resonance and voltammetric studies in high resistance solvents at low temperature using a newly designed small volume electrolysis cell, *J. Electroanal. Chem.* 199 (1986) 297–309.
- [216] P.R. Murray, D. Collison, S. Daff, N. Austin, R. Edge, B.W. Flynn, L. Jack, F. Leroux, E.J.L. McInnes, A.F. Murray, D. Sells, T. Stevenson, J. Wolowska, L.J.

- Yellowlees, An in situ electrochemical cell for Q- and W-band EPR spectroscopy., J. Magn. Reson. 213 (2011) 206–9. doi:10.1016/j.jmr.2011.09.041.
- [217] C. Frontana, I. González, The role of intramolecular hydrogen bonding in the electrochemical behavior of hydroxy-quinones and in semiquinone stability, J. Braz. Chem. Soc. 16 (2005) 299–307.
- [218] E. Duñach, M. José Medeiros, S. Olivero, Intramolecular reductive cyclisations using electrochemistry: development of environmentally friendly synthetic methodologies, New J. Chem. 30 (2006) 1534–1548. doi:10.1039/B608228A.
- [219] C. Durante, B. Huang, A.A. Isse, A. Gennaro, Electrocatalytic dechlorination of volatile organic compounds at copper cathode. Part II: Polychloroethanes, Appl. Catal. B Environ. 126 (2012) 355–362. doi:10.1016/j.apcatb.2012.07.003.
- [220] C. Durante, V. Perazzolo, A.A. Isse, M. Favaro, G. Granozzi, A. Gennaro, Electrochemical Activation of Carbon-Halogen Bonds: Electrocatalysis at Palladium-Copper Nanoparticles, ChemElectroChem. 1 (2014) 1370–1381. doi:10.1002/celc.201402032.
- [221] C. Durante, A.A. Isse, G. Sandonà, A. Gennaro, Electrochemical hydrodehalogenation of polychloromethanes at silver and carbon electrodes, Appl. Catal. B Environ. 88 (2009) 479–489. doi:10.1016/j.apcatb.2008.10.010.
- [222] A.A. Isse, S. Gottardello, C. Durante, A. Gennaro, Dissociative electron transfer to organic chlorides: electrocatalysis at metal cathodes., Phys. Chem. Chem. Phys. 10 (2008) 2409–2416. doi:10.1039/b719936h.
- [223] D.F. Niu, L.P. Xiao, A.J. Zhang, G.R. Zhang, Q.Y. Tan, J.X. Lu, Electrocatalytic carboxylation of aliphatic halides at silver cathode in acetonitrile, Tetrahedron. 64 (2008) 10517–10520. doi:10.1016/j.tet.2008.08.093.
- [224] M.M. Burbuliene, V. Jakubkiene, G. Mekuskiene, E. Udrėnaitė, R. Smicius, P. Vainilavicius, Synthesis and anti-inflammatory activity of derivatives of 5-[(2-disubstitutedamino-6-methyl-pyrimidin-4-yl)-sulfanyl methyl]-3H-1,3,4-oxadiazole-2-thiones, Farm. 59 (2004) 767–774. doi:10.1016/j.farmac.2004.05.007.
- [225] L. Pieters, S. Van Dyck, M. Gao, R. Bai, E. Hamel, a Vlietinck, G. Lemière, Synthesis and biological evaluation of dihydrobenzofuran lignans and related compounds as potential antitumor agents that inhibit tubulin polymerization., J. Med. Chem. 42 (1999) 5475–5481. doi:10.1021/jm990251m.

- [226] H.F. Roaiah, S.S. El-Nakkady, W.S. El-Serwy, M.A.A. Ali, A.H.A. El-Rahman, Z. El-Bazza, Studies on some benzopyran derivatives with expected antimicrobial and antiviral activity, *Nat. Sci.* 8 (2010) 20–29.
- [227] E. Ayrancı, N. Hoda, Adsorption kinetics and isotherms of pesticides onto activated carbon-cloth, *Chemosphere.* 60 (2005) 1600–1607. doi:10.1016/j.chemosphere.2005.02.040.
- [228] A.S. Shawali, Synthesis and tautomerism of aryl- and hetaryl-azo derivatives of bi- and tri-heterocycles, *J. Adv. Res.* 1 (2010) 255–290. doi:10.1016/j.jare.2010.07.002.
- [229] K.C. Majumdar, G. V. Karunakar, B. Sinha, Formation of five- and six-membered heterocyclic rings under radical cyclization conditions, *Synth.* 44 (2012) 2475–2505. doi:10.1055/s-0032-1316566.
- [230] E. Duñach, A.P. Esteves, M.J. Medeiros, C.S. dos Santos Neves, S. Olivero, Radical-type reactions in protic and aprotic media: Comparisons in nickel-catalysed electrochemical reductive cyclisations, *Comptes Rendus Chim.* 12 (2009) 889–894. doi:10.1016/j.crci.2008.09.025.
- [231] E. Duñach, A.P. Esteves, A.M. Freitas, M.J. Medeiros, S. Olivero, Electroreductive cyclisation of unsaturated halides catalysed by nickel macrocyclic complexes, *Tetrahedron Lett.* 40 (1999) 8693–8696.
- [232] W.R.L. and L.D.R. Sowell C.G., Electroreductive cyclization reaction, stereoselectino creation of quaternary centres in bicyclic frameworks and a formal total synthesis of quadrone, *Tetrahedron Lett.* 31 (1990) 95–98.
- [233] V. Jouikov, J. Simonet, The one-electron cleavage of benzylic bromides at palladium and palladized cathodes: Benzyl radicals generation and immobilization onto solid interfaces, *Electrochem. Commun.* 12 (2010) 331–334. doi:10.1016/j.elecom.2009.12.009.
- [234] C. Bellomunno, D. Bonanomi, L. Falciola, M. Longhi, P.R. Mussini, L.M. Doubova, G. Di Silvestro, Building up an electrocatalytic activity scale of cathode materials for organic halide reductions, 50 (2005) 2331–2341. doi:10.1016/j.electacta.2004.10.047.
- [235] B. Geboes, B. Vanrenterghem, J. Ustarroz, D. Pauwels, S. Sotiropoulos, A. Hubin, T. Breugelmans, Influence of the morphology of electrodeposited nanoparticles on the activity of organic halide reduction, 2014. doi:10.3303/CET1441013.

- [236] B. Vanreenterghem, T. Breugelmans, An activity scale of cathode materials for the electrochemical cyclisation of allyl 2-bromobenzyl ether, *Electrochim. Acta.* 234 (2017) 28–36. doi:10.1016/j.electacta.2017.03.016.
- [237] A.A. Isse, G. Berzi, L. Falciola, M. Rossi, P.R. Mussini, A. Gennaro, Electrocatalysis and electron transfer mechanisms in the reduction of organic halides at Ag, *J. Appl. Electrochem.* 39 (2009) 2217–2225. doi:10.1007/s10800-008-9768-z.
- [238] P. Poizot, J. Monnerie, Silver-palladium cathode: Selective one-electron scission of alkyl halides: Homo-coupling and cross-coupling subsequent reactions, *Electrochim. Acta.* 56 (2010) 15–36. doi:10.1016/j.electacta.2010.09.020.
- [239] J. Monnerie, The one-electron reduction of primary alkyl iodides at palladium and palladiated surfaces: a facile source of alkyl radicals?, *Electrochim. Commun.* 7 (2005) 74–80. doi:10.1016/j.elecom.2004.10.006.
- [240] B. Vanreenterghem, B. Geboes, S. Bals, J. Ustarroz, A. Hubin, T. Breugelmans, Influence of the support material and the resulting particle distribution on the deposition of Ag nanoparticles for the electrocatalytic activity of benzyl bromide reduction, *Appl. Catal. B Environ.* 181 (2016) 542–549. doi:10.1016/j.apcatb.2015.08.026.
- [241] A.P. Esteves, A.M. Freitas, M.J. Medeiros, D. Pletcher, Reductive intramolecular cyclisation of unsaturated halides by Ni(II) complexes, *J. Electroanal. Chem.* 499 (2001) 95–102. doi:10.1016/S0022-0728(00)00494-0.
- [242] X. Chaminade, E. Duñach, A.P. Esteves, M.J. Medeiros, C.S. Neves, S. Olivero, Electrosynthesis of nitrogen heterocycles using environmentally friendly methodologies, *Electrochim. Acta.* 54 (2009) 5120–5126. doi:10.1016/j.electacta.2009.01.004.
- [243] S. Olivero, J.C. Clinet, E. Duñach, Electrochemical intramolecular reductive cyclisation catalysed by electrogenerated Ni(cyclam)²⁺, *Tetrahedron Lett.* 36 (1995) 4429–4432. doi:10.1016/0040-4039(95)00782-8.
- [244] E. Duñach, A.P. Esteves, M.J. Medeiros, D. Pletcher, S. Olivero, The study of nickel(II) and cobalt(II) complexes with a chiral salen derivative as catalysts for the electrochemical cyclisation of unsaturated 2-bromophenyl ethers, *J. Electroanal. Chem.* 566 (2004) 39–45. doi:10.1016/j.jelechem.2003.10.045.
- [245] S. Stoll, A. Schweiger, EasySpin, a comprehensive software package for spectral simulation and analysis in EPR, *J. Magn. Reson.* 178 (2006) 42–55. doi:10.1016/j.jmr.2005.08.013.

- [246] F. Neese, Prediction of electron paramagnetic resonance g values using coupled perturbed Hartree-Fock and Kohn-Sham theory, *J. Chem. Phys.* 115 (2001) 11080–11096. doi:10.1063/1.1419058.
- [247] F. Neese, Theoretical Study of Ligand Superhyperfine Structure. Application to Cu(II) Complexes, *J. Phys. Chem. A.* 105 (2001) 4290–4299. doi:10.1021/jp003254f.
- [248] F. Neese, Metal and ligand hyperfine couplings in transition metal complexes: The effect of spin-orbit coupling as studied by coupled perturbed Kohn-Sham theory, *J. Chem. Phys.* 118 (2003) 3939–3948. doi:10.1063/1.1540619.
- [249] F. Neese, Efficient and accurate approximations to the molecular spin-orbit coupling operator and their use in molecular g-tensor calculations, *J. Chem. Phys.* 122 (2005). doi:10.1063/1.1829047.
- [250] S. Sinnecker, A. Rajendran, A. Klamt, M. Diedenhofen, F. Neese, Calculation of solvent shifts on electronic g-tensors with the conductor-like screening model (COSMO) and its self-consistent generalization to real solvents (direct COSMO-RS), *J. Phys. Chem. A.* 110 (2006) 2235–2245. doi:10.1021/jp056016z.
- [251] J.P. Perdew, Density-functional approximation for the correlation energy of the inhomogeneous electron gas, *Phys. Rev. B.* 33 (1986) 8822–8824.
- [252] J.P. Perdew, Erratum: Density-functional approximation for the correlation energy of the inhomogeneous electron gas, *Phys. Rev. B.* 34 (1986) 7406.
- [253] A.D. Becke, Density-functional exchange-energy approximation with correct asymptotic behavior, *Phys. Rev. A.* 38 (1988) 3098–3100. doi:10.1103/PhysRevA.38.3098.
- [254] A. Schäfer, H. Horn, R. Ahlrichs, Fully optimized contracted Gaussian basis sets for atoms Li to Kr, *J. Chem. Phys.* 97 (1992) 2571–2577.
- [255] P.J. Stephens, F.J. Devlin, C.F. Chabalowski, M.J. Frisch, Ab Initio Calculation of Vibrational Absorption and Circular Dichroism Spectra Using Density Functional Force Fields, *J. Phys. Chem.* 98 (1994) 11623–11627. doi:10.1021/j100096a001.
- [256] D. Moran, A.C. Simmonett, F.E. Leach, W.D. Allen, P.V.R. Schleyer, H.F. Schaefer, Popular theoretical methods predict benzene and arenes to be nonplanar, *J. Am. Chem. Soc.* 128 (2006) 9342–9343. doi:10.1021/ja0630285.

- [257] L. Goerigk, S. Grimme, Efficient and accurate double-hybrid-meta-GGA density functionals- evaluation with the extended GMTKN30 database for general main group thermochemistry, kinetics, and noncovalent interactions, *J. Chem. Theory Comput.* 7 (2011) 291–309. doi:10.1021/ct100466k.
- [258] V. Barone, Structure, Magnetic properties and Reactivities of Open-Shell Species from Density Functional and Self-Consistent Hybrid Methods, in: D.P. Chong (Ed.), *Recent Adv. Density Funct. Methods*, 1st ed., World Scientific, 1995: pp. 287–334.
- [259] I.B. Goldberg, A.J. Bard, S.W. Feldberg, Resistive Effects in Thin Electrochemical Cells: Digital Simulations of Electrochemistry in Electron Spin Resonance Cells, *J. Phys. Chem.* 76 (1972) 2550–2559.
- [260] G.L. McIntire, H.N. Blount, H.J. Stronks, R. V. Shetty, E.G. Janzen, Spin trapping in electrochemistry. 2. Aqueous and nonaqueous electrochemical characterizations of spin traps, *J. Phys. Chem.* 84 (1980) 916–921. doi:10.1021/j100445a026.
- [261] T. Wandlowski, J.X. Wang, B.M. Ocko, Adsorption of bromide at the Ag(100) electrode surface, *J. Electroanal. Chem.* 500 (2001) 418–434. doi:10.1016/S0022-0728(00)00380-6.
- [262] G.R. Buettner, Spin Trapping - Electron-Spin-Resonance Parameters of Spin Adducts, *Free Radic. Bio. Med.* 3 (1987) 259–303. doi:10.1016/s0891-5849(87)80033-3.
- [263] M.C.R. Symons, E. Albano, A. Tomasi, T.F. Slater, Radiolysis of tetrachloromethane, *J. Chem. Soc. Faraday Trans. 1.* 78 (1982) 2205. doi:10.1039/f19827802205.
- [264] J.M. Achord, C.L. Hussey, Determination of dissolved oxygen in nonaqueous electrochemical solvents Determination of Dissolved Oxygen in Nonaqueous Electrochemical Solvents, *Anal. Chem.* 52 (2002) 601–602. doi:10.1021/ac50053a061.
- [265] F. Neese, Prediction of molecular properties and molecular spectroscopy with density functional theory: From fundamental theory to exchange-coupling, *Coord. Chem. Rev.* 253 (2009) 526–563. doi:10.1016/j.ccr.2008.05.014.
- [266] P.B. Mccays, E.K. Lai, J.L. Poyer, C.M. Dubose, G. Janzenll, Oxygen- and Carbon-centered Free Radical Formation during Carbon Tetrachloride Metabolism, *J. Biol. Chem.* 259 (1984) 2135–2143.

- [267] D.G. Mitchell, G.M. Rosen, M. Tseitlin, B. Symmes, S.S. Eaton, G.R. Eaton, Use of rapid-scan EPR to improve detection sensitivity for spin-trapped radicals, *Biophys. J.* 105 (2013) 338–342. doi:10.1016/j.bpj.2013.06.005.
- [268] D.G. Mitchell, M. Tseitlin, R.W. Quine, V. Meyer, M.E. Newton, A. Schnegg, B. George, S.S. Eaton, G.R. Eaton, X-band rapid-scan EPR of samples with long electron spin relaxation times: A comparison of continuous wave, pulse and rapid-scan EPR, *Mol. Phys.* 111 (2013) 2664–2673. doi:10.1080/00268976.2013.792959.
- [269] G.M. Rosen, A. Beselman, P. Tsai, S. Pou, C. Mailer, K. Ichikawa, B.H. Robinson, R. Nielsen, H.J. Halpern, A.D. MacKerell, Influence of Conformation on the EPR Spectrum of 5,5-Dimethyl-1-hydroperoxy-1-pyrrolidinyloxy: A Spin Trapped Adduct of Superoxide, *J. Org. Chem.* 69 (2004) 1321–1330. doi:10.1021/jo0354894.
- [270] I. Gallardo, S. Soler, Electrochemically promoted arylation of iodoaromatics, *J. Electroanal. Chem.* 799 (2017) 9–16. doi:10.1016/j.jelechem.2017.05.034.
- [271] J. Lölsberg, O. Starck, S. Stiefel, J. Hereijgers, T. Breugelmans, M. Wessling, 3D-Printed Electrodes with Improved Mass Transport Properties, *ChemElectroChem.* (2017) 1–6. doi:10.1002/celc.201700662.

Personal information

Publications in international peer-reviewed journals included in the Web of Science™

1. B. Geboes, B. Vanrenterghem, J. Ustarroz, D. Pauwels, S. Sotiropoulos, A. Hubin, T. Breugelmans, Influence of the Morphology of electrodeposited nanoparticles on the activity of organic halide reduction, *Chemical Engineering Transactions*, 41 (2015) 73-78.
2. D. Pauwels, J. Hereijgers, K. Verhulst, K. De Wael, T. Breugelmans, Investigation of the electrosynthetic pathway of the aldol condensation of acetone, *Chemical Engineering Journal*, 289 (2016) 554-561.
3. D. Pauwels, S. Pilehvar, B. Geboes, A. Hubin, K. De Wael, T. Breugelmans, A new multisine-based impedimetric aptasensing platform, *Electrochemistry Communications*, 71 (2016) 23-27.
4. D. Pauwels, B. Geboes, J. Hereijgers, D. Choukroun, K. De Wael, T. Breugelmans, The application of an electrochemical microflow reactor for the electrosynthetic aldol reaction of acetone to diacetone alcohol, *Chemical Engineering Research & Design*, 128 (2017) 205-2013.

Publications in review in international peer-reviewed journals

1. D. Pauwels, H. Y. V. Ching, M. Samanipour, S. Neukermans, J. Hereijgers, S. Van Doorslaer, K. De Wael, T. Breugelmans, Elucidation of the mechanism of the intramolecular cyclisation of allyl 2-bromobenzyl ether by in situ EPR spectroelectrochemistry, *Electrochimica Acta* (2018)

Publications in proceedings of international conferences without peer-review

1. E. Van Aert, K. Baert, D. Pauwels, B. Geboes, T. Breugelmans, A. Hubin, Des mesures d'impédance électrochimique dans une base de données intelligente pour la corrosion, *Actes du 24ème Forum sur les Impédances Electrochimiques* (2013).

Lectures on international conferences

1. B. Geboes, D. Pauwels, J. Ustarroz, S. Sotiropoulos, A. Hubin, T. Breugelmans, Influence of the morphology of electrodeposited nanoparticles on the mechanism of organic halide reduction, *10th European Symposium on Electrochemical Engineering*, 28 September – 04 October, 2014, Sardinia, Italy.
2. D. Pauwels, J. Hereijgers, K. Verhulst, K. De Wael, T. Breugelmans, Design of a microflow reactor for the electrosynthetic aldol reaction of acetone, *7th Kurt-Schwabe-Symposium*, 04 – 07 September, 2016, Mittweida, Germany.
3. J. Hereijgers, R. Vervecken, D. Pauwels, V. Meynen, T. Breugelmans, On the geometrical features of the electrolyzer for CO₂ reduction, *67th Annual Meeting of the International Society of Electrochemistry*, 24 – 26 August, 2016, The Hague, The Netherlands.

4. D. Pauwels, S. Neukermans, A. Hubin, S. Van Doorslaer, T. Breugelmans, Combining EPR and electrochemical techniques to study electrocatalytic systems, 68th Annual Meeting of the International Society of Electrochemistry, 27 August – 1 September, 2017, Providence, Rhode Island, USA.

Lectures on national conferences

1. D. Pauwels, J. Hereijgers, K. Verhulst, K. De Wael, T. Breugelmans, Investigation of the electrosynthetic pathway of the aldol condensation of acetone, Chemical Research in Flanders (CRF-1), 24 – 26 October, 2016, Blankenberge, Belgium.
2. M. Samanipour, H. Y. V. Ching, D. Pauwels, T. Breugelmans, S. Van Doorslaer, Studying the electrochemical cyclisation of allyl 2-bromobenzylether by EPR, 16th Young Belgian Magnetic Resonance Scientist, 04 – 05 December, 2017, Blankenberge, Belgium

Poster presentations on international conferences

1. E. Van Aert, K. Baert, D. Pauwels, B. Geboes, T. Breugelmans, A. Hubin, Des mesure d'impédance électrochimique dans une base de données intelligente pour la corrosion, 24ème Forum sur les Impédances Electrochimiques, 12 March, 2013, Paris, France.
2. B. Geboes, J. Ustarroz, D. Pauwels, S. Sotiropoulos, A. Hubin, T. Breugelmans, Influence of the morphology of electrodeposited nanoparticles on the electrocatalytic activity towards organic halide reduction, 65th Annual Meeting of the International Society of Electrochemistry, 31 August – 5 September, 2014, Lausanne, Switzerland.

3. D. Pauwels, B. Geboes, P. Vanderauwera, K. De Wael, A. Hubin, T. Breugelmans, Investigation of the electrosynthetic pathway of the aldol condensation of acetone, 65th Annual Meeting of the International Society of Electrochemistry, 31 August – 5 September, 2014, Lausanne, Switzerland.
4. D. Pauwels, B. Geboes, P. Vanderauwera, K. De Wael, A. Hubin, T. Breugelmans, Investigation of the electrosynthetic pathway of the aldol condensation of acetone, 10th European Symposium on Electrochemical Engineering, 28 September – 04 October, 2014, Sardinia, Italy.
5. D. Pauwels, J. Hereijgers, K. Verhulst, K. De Wael, T. Breugelmans, Investigation of the electrosynthetic pathway of the aldol condensation of acetone, 67th Annual Meeting of the International Society of Electrochemistry, 24 – 26 August, 2016, The Hague, The Netherlands